LBNL-46525

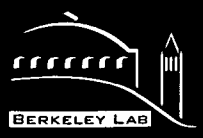

ERNEST ORLANDO LAWRENCE
BERKELEY NATIONAL LABORATORY

The Geochemistry of Gold, Arsenic, and Antimony in the Carlin-Type Gold Deposits and the Mechanics of Geologic Fractures

Brad Bessinger

Earth Sciences Division

May 2000

Ph.D. Thesis

DISCLAIMER

LBNL-46525

The Geochemistry of Gold, Arsenic, and Antimony in the Carlin-Type Gold Deposits and the Mechanics of Geologic Fractures

Brad Bessinger
Ph.D. Thesis

Department of Materials Science and Mineral Engineering
University of California, Berkeley

and

Earth Sciences Division
Ernest Orlando Lawrence Berkeley National Laboratory
University of California
Berkeley, CA 94720

May 2000

This work was supported by the Director, Office of Science, Office of Basic Energy Sciences, Materials Sciences Division, of the U.S. Department of Energy under Contract No. DE-AC03-76SF00098, and by the Donald H. McLaughlin Chair Account and Jane Lewis Fellowship in Mineral Engineering.

Abstract

The Geochemistry of Gold, Arsenic, and Antimony

in the Carlin-Type Gold Deposits

and

The Mechanics of Geologic Fractures

by

Brad Alan Bessinger

Doctor of Philosophy in Materials Science and Mineral Engineering

University of California, Berkeley

Dr. John Apps, Co-Chair

Professor Fiona Doyle, Co-Chair

Because geologic fractures often control the location and grade of an orebody, the ability to understand their occurrence and mineralogy is a significant step in assessing the economic viability of a deposit. In *Part I* of this dissertation, the geochemistry of gold, arsenic, and antimony in the fractured, Carlin-type gold deposits of Nevada is investigated. In *Part II*, a tribute to the late Dr. Neville G. W. Cook is paid with three independent geomechanics studies designed to understand the conditions leading to fracture, as well as develop methods to detect their presence.

Part I of this dissertation begins with a review of the geology and geochemistry of the Carlin-type gold deposits necessary to constrain the geochemical model developed in the study (**Chapter 1**). Following this introduction, the HKF equation of state is shown to inadequately describe the derivative thermodynamic properties of neutral aqueous species (**Chapter 2**). Despite these reservations, the HKF equation of state parameters for aqueous

gold, arsenic, and antimony species are calculated in **Chapter 3**. Given the available geologic data for the Carlin-type gold deposits, antimony and arsenic solubility in the system are found to be controlled by their hydroxide species, and gold by its sulfide complexes (**Chapter 4**). These results imply that sulfidation of host rock iron is a process which could selectively precipitate gold, pyrite, and arsenian pyrite; however, phase and solubility diagrams also suggest that the oxidation state of the system is a key variable, and additional research is required.

After a brief prologue to *Part II* (**Chapter 5**), far field compressive stresses are shown to be responsible for jointing at a field site on Vancouver Island, British Columbia (**Chapter 6**). Despite the prevalence given to "tensile" mechanisms in the geologic literature, these are found to be secondary effects. In the next geomechanics study (**Chapter 7**), a method to predict the occurrence of fractures in rock using seismic amplitude measurements at various orientations to bedding is investigated. Finally, in **Chapter 8**, a new, nondilatational fracturing mechanism which likely contributes to sand production in oil and natural gas reservoirs is identified.

Dedication

This dissertation is dedicated to the late Dr. Neville G. W. Cook (1938-1998) who allowed me the opportunity to come to Berkeley and study under him. Dr. Cook was not only one of the world's greatest educators in the field of rock mechanics, but also taught those of us fortunate to know him how to lead an exemplary life. Dr. Cook was always generous with his praise and eager to offer advice and support in times of stress. His own enthusiasm inspired everyone around him to challenge conventional wisdom and the results are evidenced by the great body of literature authored by him and his students. Although faced with a terminal condition, the courage that he showed during his battle will always be remembered. My thoughts of Neville are some of my most cherished. He is greatly missed.

Acknowledgments

This dissertation would not have been possible without all of the people listed below. As mentioned in the Dedication, Dr. Cook was the guiding force behind the research. In addition, his wife Jennifer formed the other half of the Cook team. Dr. Larry Myer, Dr. Kurt Nihei, and Professor Ronald Gronsky were all instrumental in helping me complete my work after Neville passed away. I cannot thank them enough for always taking the time to talk with me and for providing any assistance they could. Dr. John Apps and Professor Fiona Doyle, the two co-chairs of this dissertation, particularly aided me when I wanted to switch my focus from rock mechanics to geochemistry. Fiona ensured that I cleared the academic hurdles, and provided me a forum to discuss my results. John took me "under his wing" and taught me how to tackle the challenging problems in geochemistry.

The many graduate students I worked with not only provided friendship and camaraderie, but many aided in the experiments and provided necessary input on the results. This group of friends include: Pascual Benito; Jianli Fang; Galen Hesler; Brun Hilbert; Pingan Huang; Taylor Hwong; Mike Kowalski; Seiji Nakagawa; Grace Su; and Weidong Yi. Of these, I would especially like to thank Dr. Seiji Nakagawa for always helping me whenever I had a question or problem.

Finally, I would like to thank my family. Thanks Mom and Dad for always encouraging me and supporting my decisions, and thanks Trina for providing the emotional support during all of my trials and tribulations. I could not have done it without you.

Table of contents

CHAPTER 1. Introduction to the Geology and Geochemistry of the Carlin-Type Gold Deposits

1.1 Introduction

The first four chapters of this dissertation explore the water-rock interactions responsible for the transport and precipitation of gold, arsenic, and antimony in the fractured, Carlin-type gold deposits of the Great Basin of North America (Figure 1.1). In **Chapter 1,** the geological system, geochemical system, and current theories on mineralization are introduced. This is followed in **Chapter 2** by an evaluation of different equations of state for minerals, gases, and aqueous species necessary to predict the importance of various reactions at the elevated pressures and temperatures. In **Chapter 3,** the standard state thermodynamic properties and Helgeson-Kirkham-Flowers (HKF) equation of state parameters for gold, arsenic, and antimony minerals and aqueous species are subsequently calculated from regression analysis. Finally, given the geologic constraints and calculated thermodynamic properties, the relative importance of different metal depositional mechanisms are examined in **Chapter 4**. These results allow insight into the geologic conditions favorable to mineralization.

In the first section of this introductory chapter (*Section 1.2*), the geologic setting of the Carlin-type gold deposits, including their location, structural environment, host rock lithologies, observed hydrothermal alteration patterns, and metal associations is summarized. This discussion is followed by a review of the geologic history of the region and the temporal and spatial link between the deposits and possible Cretaceous and Tertiary volcanism (*Section 1.3*). Geochemical isotopic and fluid inclusion analyses are then discussed in *Section 1.4* in the context of possible origins for the metals, leading to geochemical models of different ore-forming scenarios (*Section 1.5*). Although several important water-rock interactions controlling gold mineralization are identified in this latter section, key issues remain (*Section 1.6*). A thorough description of the methodology used to identify and resolve the principal

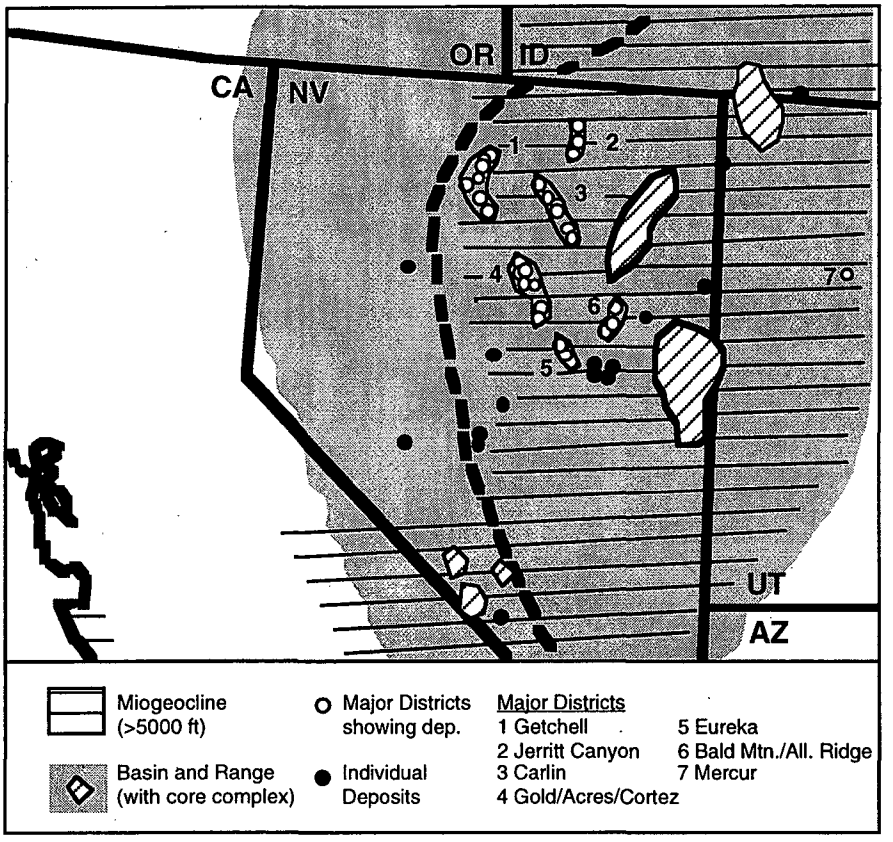

Figure 1.1 Location of the Carlin-type gold deposits within the Great Basin of North America relative to miogeoclinal sedimentary rocks (horizontal lines), Basin and Range faulting and core complexes (shaded region), and the eastern limit of Mesozoic, early Cenozoic batholiths (heavy dashed line) (from Ilchik and Barton, 1997). The deposits have been divided into districts based on proximity and trends.

chemical processes controlling Au, As, and Sb transport and deposition is elaborated in *Section 1.7.*

1.2 Geologic setting

1.2.1 Location

The Carlin-type gold deposits are a unique suite of gold deposits named for the Carlin mine in northeastern Nevada after it was recognized that this deposit shared many of the same geologic characteristics as the previously discovered, but unclassified Getchell, Mercur, and Gold Acres deposits of the region (Bagby and Berger, 1985). The characteristics which define this class of gold deposits are: 1) the occurrence of fine-grained disseminated gold associated with arsenian pyrite or jasperoids; 2) a metal association of Au-As-Sb-Hg-Ag-Ba-Tl; 3) a lack of base metals; and 4) a sedimentary host rock.

Most of the Carlin-type gold deposits are located in northeastern Nevada, localized along one of the six major trends in Figure 1.1. Although similar deposits have also been discovered in the Guizhou and Liaoning provinces of China (Cunningham, et al., 1988; Ashley, et al., 1991; Cheng, et al., 1994), in the Yauricocha district of Peru (Alvarez and Noble 1988), and in the Ratatotok district of Indonesia (Turner, et al., 1994), the North American deposits are the most extensively studied and provide the largest geologic database. Consequently, they are the focus of this dissertation.

1.2.2 Structural controls

An important feature of Figure 1.1 is the alignment of the Carlin-type gold deposits along northwestern and northeastern regional trends. Although it is possible that the trends merely represent selective exposure, additional geophysical and isotopic surveys suggest that mineralization may be localized over crustal weaknesses. Shawe (1991) showed that positive magnetic anomalies associated with Tertiary intrusives were subparallel to the Cortez, Eureka, Carlin, and Alligator ridge trends. Wooden, et al. (1997) also found a similar

alignment with isotopic boundaries. Finally, Rodriguez (1997) interpreted magnetotelluric soundings across the Eureka and Carlin trends to indicate the presence of deep crustal faults and large intrusive bodies underlying each.

At the deposit-scale, ore is localized vertically along high-angle normal or reverse faults and laterally within favorable host lithologies (i.e. silty carbonates, calcareous siltstones, and calcareous shales) (Arehart, 1996). Because the structure and lithology of any particular deposit is unique, a wide variety of ore styles have been observed. Deposits which lack favorable host rock are primarily mineralized next to fault zones (e.g. Pinson) (Madrid, et al., 1988), but favorable lithologies more often support stratiform orebodies (e.g. Carlin) (Bakken and Einaudi, 1986).

Folds and hydrothermal breccias are also essential structural features of many Carlin-type gold deposits. Kuehn and Rose (1995) used evidence of two types of fluid inclusions to hypothesize that the episodic throttling of overpressurized fluids through the Tuscarora anticline at the Carlin deposit mixed hydrothermal fluids with cooler, oxidized fluids, resulting in gold deposition. Brecciated sedimentary rock not only hosts significant gold mineralization, but evidence at the Post/Betze gold deposit suggests that at least some localized breccia is directly related to hydrothermal alteration and mineralization processes (Peters, et al., 1997).

1.2.3 Host lithologies

The primary hosts for Carlin-type gold deposits are Cambrian through Mississippian-aged sedimentary rocks. Figure 1.2 shows the lithologies and distribution of gold deposits for the Carlin trend. The bulk of the ore deposits are located below the Roberts Mountain Thrust Fault within an assemblage of silty and fossiliferous limestones. At the Carlin deposit itself, three distinct lithologies are present: 1) laminated argillaceous dolomitic limestone and calcareous siltstone; 2) massive carbonates; and 3) medium- to coarse-grained carbonates with bioclastic debris (Kuehn and Rose, 1992). The most intensely altered and mineralized layers

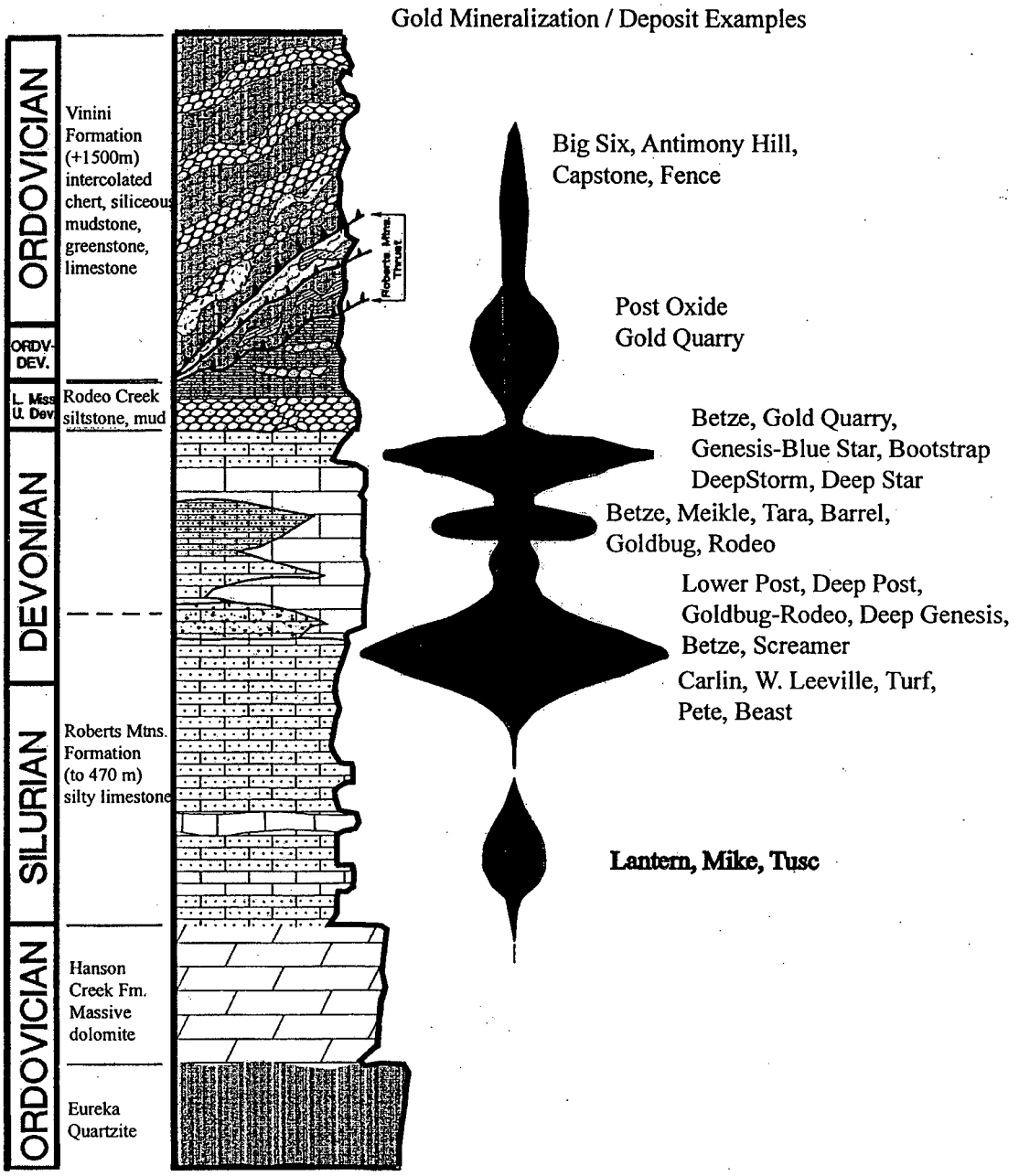

Figure 1.2 Idealized stratigraphic column and gold mineralization in the Carlin trend of Nevada (from Teal and Jackson, 1997).

are the coarser-grained siltstone and bioclastic interbeds. Multiple dikes and stocks of dioritic to granodioritic composition also host gold mineralization, but they are generally less enriched than the surrounding sedimentary rocks (Arehart, et al., 1993).

Early studies of Carlin-type gold deposits noted a positive correlation between carbonaceous host rock and gold mineralization, even suggesting an "active" role for carbonaceous sediments in gold precipitation (Radtke and Scheiner, 1970). This notion has subsequently been dispelled, with more detailed studies indicating that gold is not correlated with organic matter (Hausen and Park, 1985). Ilchik, et al. (1986) discussed evidence that the organic matter at Alligator Ridge was generated during a pre-ore hydrocarbon stage within the host rock. Structural traps such as the folds in the Paleozoic sequences also may have concentrated it in the vicinity of the gold.

1.2.4 Alteration assemblages

Figure 1.3 shows an idealized cross-section for the Carlin deposit (Kuehn and Rose, 1992), which is considered to reflect the general patterns of hypogene alteration found in other deposits (Arehart, 1996). Nearest to the feeder fault on the right side of the figure are jasperoid replacement bodies characterized by fine-grained quartz, followed by siliceous/argillic alteration where dickite/kaolinite and sericite have replaced K feldspar and illite. More distal alteration includes dedolomitization and finally decalcification. Where pre-existing dikes are present in the figure, sericitic and argillic alteration has also occurred. Although late-stage calcite/ barite/ stibnite/ quartz veins crosscut pre-existing alteration, they are not shown in Figure 1.3.

1.2.5 Metal associations

Figure 1.4 summarizes the temporal relationship between gold and other metal and nonmental-bearing minerals for a number of Carlin-type gold deposits (Arehart, 1996). According to the figure, the bulk of the gold was deposited with arsenian pyrite prior to most

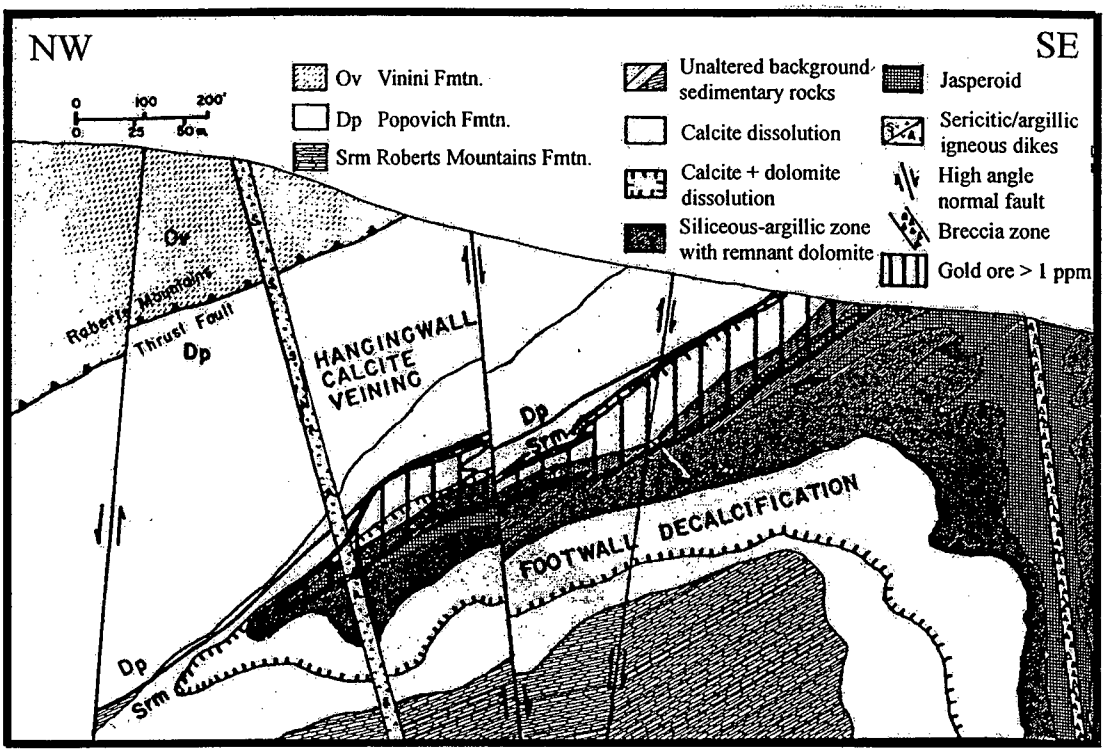

Figure 1.3 Schematic cross section of the Carlin pit showing the spatial relationships of hypogene alteration and mineralization features (Kuehn and Rose, 1992).

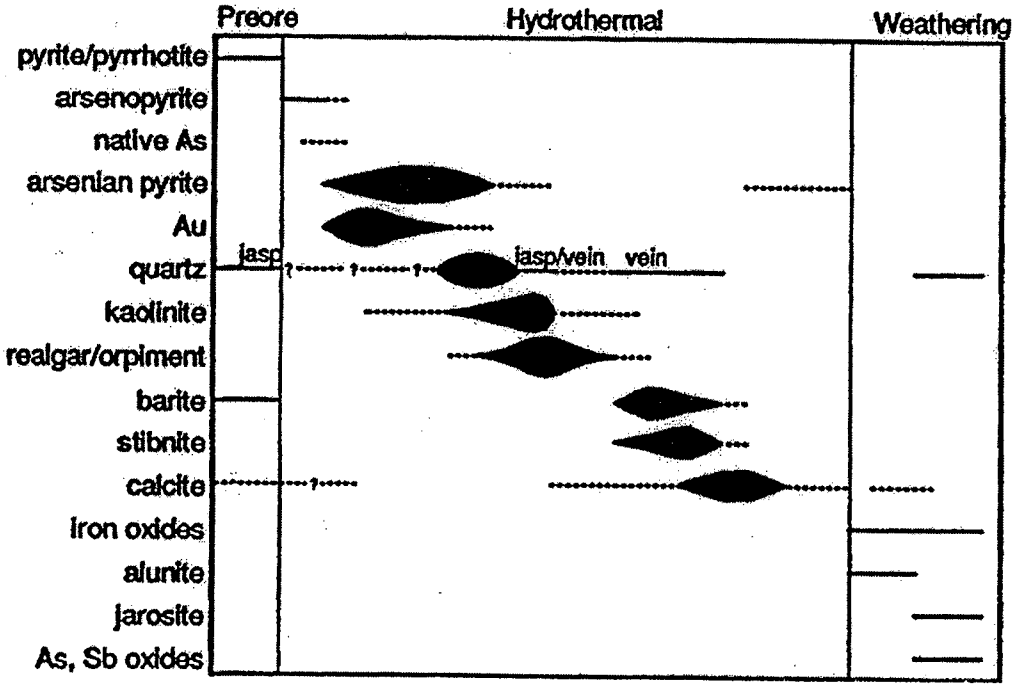

Figure 1.4 Generalized paragenetic sequence based on descriptions from the Getchell, Carlin, Cortez, Jerritt Canyon, Chimney Creek, Rabbit Creek, and Post/Betze deposits (from Arehart, 1996).

hydrothermal alteration. In the Carlin deposit, this deposition is most commonly associated with pyrite in the dedolomitized alteration zone (Kuehn and Rose, 1995); however, in the Post/Betze deposit, Au is most commonly associated with a later argillic alteration stage (Ferdock, et al., 1997). Deposition of orpiment/realgar, barite, and stibnite all occurred after main-stage gold mineralization. Sb, Hg, and Ag are not shown in Figure 1.4, but Sb and Hg are found either on pyrite grains or as dispersed stibnite or cinnabar grains, respectively, and Ag is commonly found as inclusions in base metal sulfides such as galena, sphalerite, and chalcopyrite (Radtke, 1985).

Although Figure 1.4 indicates that gold deposition preceded jasperoid development, in some deposits gold is predominantly hosted by jasperoids. Consequently, Bagby and Berger (1985) have categorized the Carlin-type gold deposits into two subclasses based on the location of gold within the deposit. An example of their "jasperoid" subclass is the Preble deposit in the Getchell trend and an example of the pyrite-hosted subclass is the Carlin deposit. In addition to differences in location of the gold within different deposits, the relative abundance of the major elements in each deposit led Bagby and Berger (1985) to further divide the Carlin-type gold deposits into Au-rich and Ag-rich endmembers. Figure 1.5 reports the abundance of Au, Ag, As, Sb, Ba, and Hg for eight different deposits. The Carlin gold deposit (CA in the figure) is enriched in Au-Ba relative to the Taylor deposit (TA in the figure) which is enriched in Ag-Sb.

1.3 Geologic history

1.3.1 Paleozoic history

Nevada lay submerged along a passive tectonic margin when deposition of the Paleozoic sequences hosting the Carlin-type gold deposits occurred (Stewart, 1980). An idealized section illustrating the distribution of the observed Devonian facies along the Carlin trend is shown in Figure 1.6 (Armstrong, et al., 1997). The Bootstrap limestone is part of the Roberts Mountain Formation of Figure 1.2 and represented platform carbonates which were

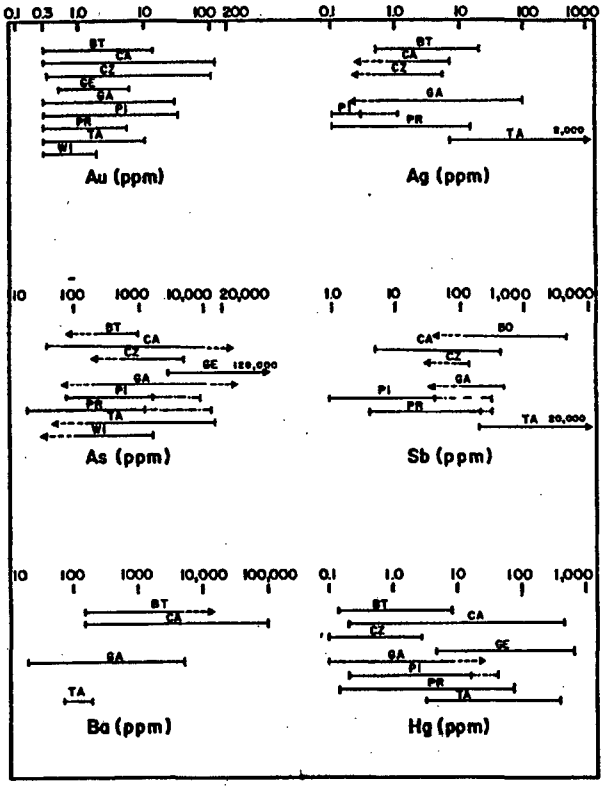

Figure 1.5 Summary of trace element variations in the Carlin-type gold deposits (from Bagby and Berger, 1985). The symbols refer to the Bootstrap (BT), Carlin (CA), Cortez (CZ), Getchell (GE), Gold Acres (GA), Pinson (PI), Preble (PR), Taylor (TA), and Windfall (WI) deposits.

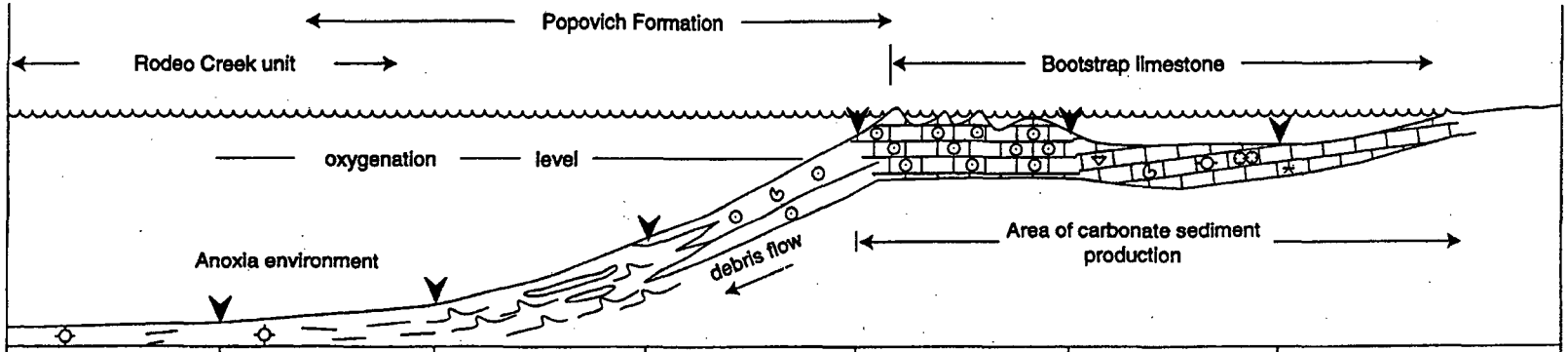

	Basin	Deep open self	Toe of slope	Foreslope	Sand on edge of platform	Open platform	Restricted platform
Facies	a) Fine clastics b) Carbonates c) Cherts	a) Carbonates b) Clastics c) Cherts	a) Carbonates b) Clastics	a) Bedded fine grained with slump b) Foreset debris and lime sands c) Lime mud masses	a) Shoal ooid lime sands-grapestone bioclastic sands b) Island with dune sands	a) Marine, limited fauna b) Wackstone-mudstone	to supratidal a) Bioclastic wackestones to algal stromatolite mats
Lithology	Radiolarian cherts Micritic limestones and dolomicrite Quartz siltstones	Cherts, micrite, dolomicrite, quartz siltstone	Micrites, dolomicrite quartz siltstone chert. Thin debris beds of oolites and fossil	Debris flows of oolitic and fossil sands, sedimentary breccias	Oolite sands and fossils	Variable fossils and mudlumps wackestone and packstone - some dolomites	Fossilferous wackestones to lime mudstones - irregularly laminated dolomites

Figure 1.6 Idealized distribution of Paleozoic facies (from Armstrong, 1997).

later overlain by deeper slope and basin deposits represented by the Popovich and Rodeo Creek deposits, respectively. The Ordovician Vinini Formation represented a eugeosynclinal assemblage of interbedded chert, sandstone, and siltstone originating from an offshore magmatic arc.

Near the close of the Devonian (360-340 Ma), it is believed that the magmatic arc collided with continental crust of western North America, producing the Antler orogeny (Fiero, 1986). Subsequent thrust faulting along the Roberts Mountain fault displaced the western eugeoclinal assemblage of sediments over the eastern miogeoclinal assemblages, deeply burying the latter. Despite constraints on the timing of the Antler orogeny, rocks represented by the accreted arc have not been found and the fate of the Antler island arc remains a geologic mystery. Subsequent to this orogeny, erosion occurred to sea level followed by deposition of an overlap sequence.

A second accretionary episode occurred in the Permian (286-254 Ma) and is known as the Sonomia orogeny. This orogenic episode uplifted much of western Nevada, creating a highland where erosion occurred. A second overlap sequence developed on either side of this uplift and remained active throughout much of the Triassic (King, 1977).

1.3.2 Mesozoic history

Near the beginning of the Jurassic (195 Ma) a shift in the motion of crustal plates changed the transform boundary west of North America and its newly-accreted Sonomia terrane into a subduction zone, and initiated a major mountain-building sequence known as the Cordilleran orogeny along western North America. The first phase of this deformation is called the Nevadan orogeny (195-80 Ma), and reflects the generation of magmas within the Sierra Nevada (it has been suggested that the Tuscarora anticline of the Carlin trend may have also developed at this time (Madrid, 1987)). The second phase of cordilleran development was the Sevier orogeny (150-80 Ma), which is a subset of the Nevadan orogeny and resulted in the eastward propagating thrust faults and folds which are now expressed in the

Mercur district of Utah (the Goldstrike stock in the Carlin trend is also believed to reflect associated magmatic activity (Arehart, et al., 1993)). Finally, the Laramide orogeny, which is described below, occurred from 80-40 Ma, creating widespread deformation well into the Tertiary.

1.3.3 Cenozoic history

It is believed that the Laramide orogeny was characterized by a decrease in subduction angle due to a warmer, more buoyant Farallon plate which was being subducted along the western coast of North America. One possible explanation for Laramide deformation is that subduction rates increased during the Late Cretaceous, decreasing the density contrast between the subsequently warmer, subducting slab and mantle (Fiero, 1986). Evidence for this mechanism is provided by the widening of magnetic stripes away from the mid-Atlantic ridge during this time interval. An alternative explanation is that the Yellowstone hot spot migrated below the subducting Farallon Plate, increasing its temperature and providing a buoyant lift (Figure 1.7.a) (Murphy, et al., 1999). Timing for this event is approximately 55 Ma, but it is suggested that the swell associated with the hotspot may have been elongated up to 1800 kilometers in the direction of plate motion, and could have arrived 15 Ma sooner.

Whichever of these scenarios is accepted, the Laramide orogeny ceased around 40 Ma, and was replaced by extension and widespread volcanism in the Great Basin. This change in structural styles may reflect reduced spreading along the mid-Atlantic ridge which would have had the effect of increasing the rate that the North American plate moved relative to the Farallon plate, and thus steepening the angle of subduction (Coney, 1979). Another explanation is that thermal relaxation and gravitational spreading occurred in response to overthickening during the previous compressional regimes (Coney and Harms, 1984). Finally, a third hypothesis is that the invasion of basaltic magmas into the crust (possibly due to the migrating Yellowstone hotspot) thermally-weakened and extended it (Gans, et al., 1989).

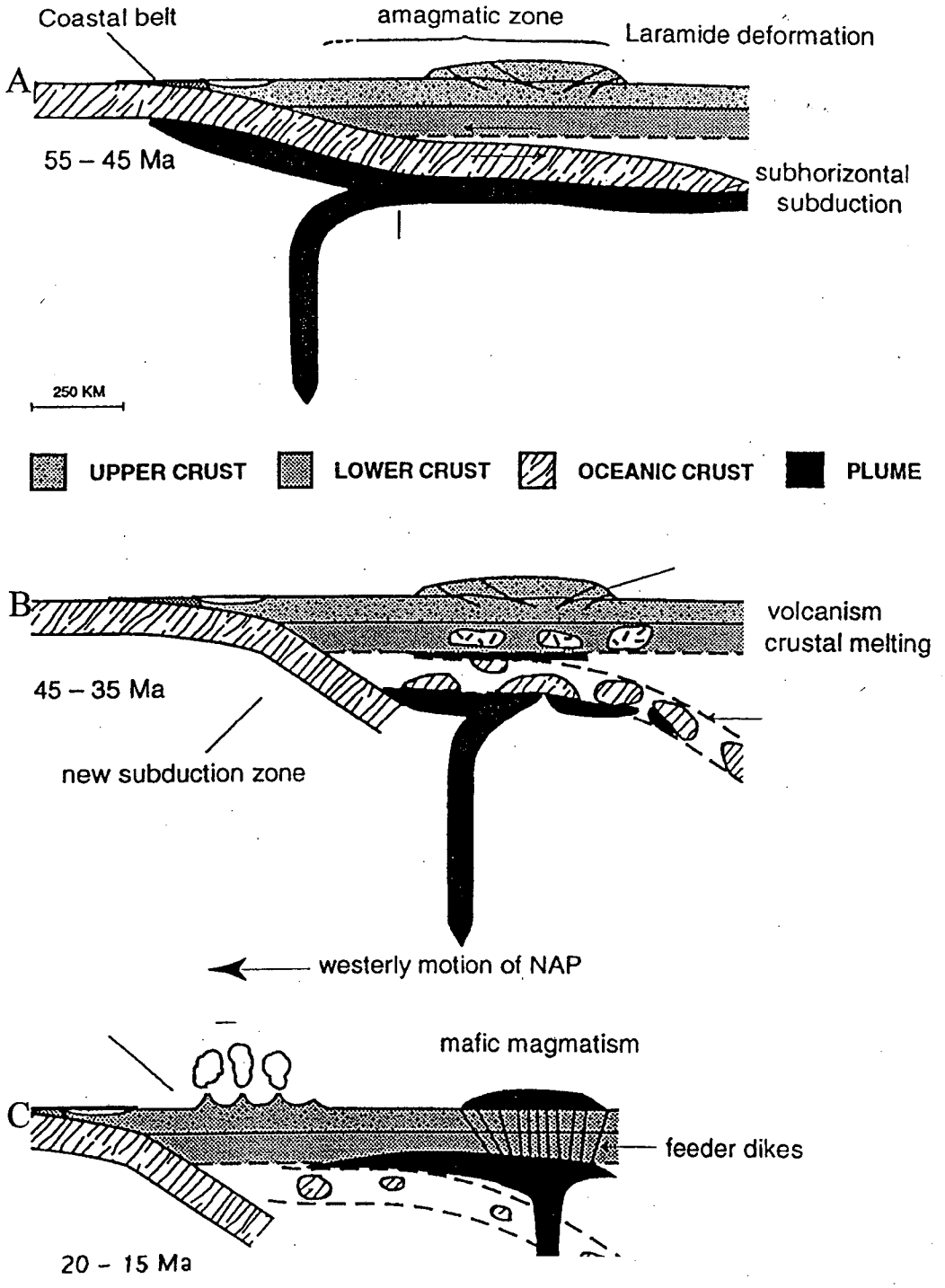

Figure 1.7 Geologic history of the Yellowstone hotspot (Opplinger, et al., 1997).

Seedorff (1991) summarized both the dates of Cenozoic igneous rocks in the Great Basin region and the dates believed to represent crustal extension, and subsequently showed that both extension and volcanism migrated outward from northern Nevada in tandem, with the volcanic intrusions and extrusions slightly pre-dating extension. Murphy, et al. (1999) suggested that the Yellowstone hotspot may have begun to break through the subducted Farallon plate between 45-35 Ma (Figure 1.7.b), producing the silicic magmas and tuffs emplaced at this time. Later, from 20-15 Ma, basaltic magmas in the crust may have extruded along crustal weaknesses (Figure 1.7.c), generating the more mafic magmas preserved in the rock record. Their explanation for the migration of extension over time was that crustal thicknesses and temperatures eventually became more uniform.

1.3.4 Relationship of mineralization to volcanism

The main periods of volcanism during the Tertiary included: a silicic ash-flow tuff phase (43-34 Ma); a calc-alkaline bimodal phase consisting of alternating andesites and rhyolites/dacites (34-17 Ma); and a bimodal basalt phase (17-6 Ma). Seedorff (1991) also compared the dates of igneous rocks to inferred and measured dates of mineralization of various ore deposits in the Great Basin and showed that the Carlin-type gold deposits were likely deposited during the earliest stages of extension and volcanism, between 35-40 Ma. Opplinger, et al. (1997) have suggested that the Yellowstone hotspot, which may have also produced the syngenetic extension, could have provided the metals for the deposits on the fact that lamprophyres may contain 10-100 times the content of Au, As, Sb, and Te as average crustal rocks (Rock and Groves, 1988). An alternative explanation was given by Ilchik and Barton (1997), who hypothesized that mineralization was amagmatic and that the role of extension-related magmatism was only to act as a source of heat (see *Section 1.5.5*).

Although a Tertiary origin for the Carlin-type gold deposits is generally consistent with the regional geology of the Great Basin discussed above, $^{40}Ar/^{39}Ar$ and K/Ar dating instead indicate that some of Carlin-type gold deposits are Cretaceous-aged. Arehart, et al. (1993a)

dated sericite which they believed to be hydrothermal in the Post/Betze orebody to be approximately 118 Ma, and additionally questioned previously reported Tertiary ages because isotopic analyses were either performed on alunite (which is interpreted to be supergene (Arehart, et al. (1992)), or on biotite and feldspars which are normally altered by hydrothermal activity. Although some sericites in other Carlin-type gold deposits give Tertiary-ages (e.g. the Twin Creeks deposit (Hall, et al., 1997)), corroborating evidence for Cretaceous mineralization include the results of Parry, et al. (1997) at the Mercur deposit. The exact timing of Carlin-type gold deposition remains a very important unresolved issue because it greatly affects which geologic provenances are favorable to mineralization (extensional versus compressional regimes).

1.4 Geochemistry of ore-stage fluids

1.4.1 Fluid inclusion results

Fluid inclusions from several deposits were used to estimate the temperature of formation of the hydrothermal events and the composition of the volatile phases. For example, Kuehn and Rose (1995) studied inclusions from the Carlin gold deposit using standard heating and freezing and crushing techniques, and Raman microprobe analyses to determine the composition of the inclusions and their homogenization temperatures. Calculations of phase relations between H_2O, CO_2, and NaCl were also used to establish constraints on the pressure of entrapment of the inclusions.

The results of their study are displayed in Table 1.1, with the identification of three different types of fluid inclusions: an early, saline, hydrocarbon stage (HC); a low-salinity, CO_2-rich main gold ore stage (MGO); and a low-salinity, CO_2-poor late gold ore stage (LGO). Based on freezing point depression, the maximum salinities of MGO fluids was approximately 3 weight percent, with a significant CO_2 concentration and minor $CH_4 + H_2S + SO_2$. This high level of CO_2 in Table 1.1 implies that local fluid immiscibility may have occurred during gold deposition at Carlin. The temperature and pressure of the MGO fluids were estimated at 215

Deposit	Temperature [°C]	Salinity [wt. % NaCl]	Gas Composition
Carlin HC[1]	155±20	16±4	Major CH_4; Minor CO_2, H_2S
Carlin Main Gold	185-245	2-4	Major CO_2; Minor CH_4, H_2S, SO_2
Carlin Late Gold	175-250	< 1.5	Minor CO_2; Trace H_2S, SO_2
Jerritt I	200-250	3-10	4% CO_2; 1% H_2S± SO_2±HC±Ar
Jerritt II	< 200	< 0.1	< 0.5% CO_2± H_2S± SO_2±HC±Ar
Chimney Creek I	250-300	6.4-9.2	CO_2 present
Chimney Creek II	250-300	2.8	n.d.
Mercur	220-270	4.4-7.4	CO_2 present
Getchell Main	n.d.	n.d.	Major CO_2; Minor N_2± H_2S±HC
Getchell Late	n.d.	n.d.	Minor CO_2± N_2± H_2S±HC

[a]HC = short chain hydrocarbon

Table 1.1 Summary of fluid inclusion studies from various deposits (as summarized by Arehart (1996)).

± 30° Celsius and 800 ± 400 bars, respectively. This pressure translates into a depth of formation for the Carlin deposit of 2.5-3 km under lithostatic conditions and 6-8 km under hydrostatic conditions, clearly distinguishing them from shallower epithermal deposits.

The late gold stage fluids (LGO) identified in their study were less saline and had lower CO_2-content than their MGO counterparts. The fact that the minerals hosting the MGO and LGO fluids were often interpreted to be syngenetic led Kuehn and Rose (1995) to speculate that the two fluids were present together during mineralization and that fluid mixing may have resulted in gold deposition.

Studies of fluid inclusions at other Carlin-type gold deposits include the Jerritt Canyon (Hofstra, et al., 1991), Chimney Creek (Osterberg, 1990), and Mercur deposit (Jewell and Parry, 1988), as reviewed by Arehart (1996) (Table 1.1). The Jerritt Canyon and Chimney Creek inclusions both had a pre-ore hydrothermal stages and evidence for two different fluids (CO_2-rich and CO_2-poor) during the gold stage similar to the Carlin deposit (Table 1.1). Mercur by contrast had only one identified type of inclusion. Most recently, Cline, et al. (1997) reported fluid inclusions at Getchell which had very similar compositions as the Carlin deposit, with elevated levels of CO_2 and trace H_2S gas.

1.4.2 Sulfur Isotopes

Sulfur isotopes were used to deduce the origin of sulfur in both sulfide and sulfate minerals at various Carlin-type ore deposits. The commonly measured value for sulfur isotopes is the $\delta^{34}S$ ratio, which is determined from the following calculation:

$$\delta^{34}S = \left[\frac{\left({}^{34}S/{}^{32}S\right)_{sample}}{\left({}^{34}S/{}^{32}S\right)_{standard}} - 1 \right](1000) \qquad (1.1)$$

where the standard can be any known value that has been measured against 0‰ for iron meteorites (Faure, 1986). Reported values for hydrothermal sulfides in the Carlin-type gold

deposits are compared in Figure 1.8.a to possible geologic processes. To interpret these results, fractionation factors expressed as:

$$\alpha = \frac{\left({}^{34}S/{}^{32}S\right)_{sample}}{\left({}^{34}S/{}^{32}S\right)_{standard}} \qquad (1.2)$$

between the minerals hosting the sulfur and their aqueous fluids must be accounted for. For example, pyrite preferentially concentrates $\delta^{34}S$ from the fluid phase by up to 5‰ near 25° Celsius, but by only 2‰ at 200°C. In some cases, interpreted $\delta^{34}S$ values must also account for chemical systems being open or closed with respect to sulfur.

According to Figure 1.8.a, sedimentary processes leading to the generation of the H_2S in ore fluids could have included breakdown of organosulfur compounds at temperatures greater than 50°C, thermochemical, organic sulfate reduction between 75°-175°C, and finally inorganic sulfate reduction at temperature exceeding 250°C. Because the bulk of the ore-stage sulfide minerals have $\delta^{34}S$ values that range between 0‰ and 20‰, either a metasedimentary pyrite source or breakdown of organosulfur compounds is indicated (Hofstra, 1997); however, the highest values for ore-stage sulfides may also reflect thermochemical and inorganic sulfate reduction, and the lowest values could reflect leaching of magmatic stock or introduction of magmatic fluids.

Although most of the deposits are consistent with either a sedimentary or metasedimentary origin, deposits in the Getchell district have values similar to the associated Osgood Mountain intrusion, suggesting a magmatic source. Also, the Lone Tree and Melco deposits exhibit magmatic $\delta^{34}S$ ratios (Hofstra, 1997).

1.4.3 Carbon Isotopes

Carbon isotopes of $\delta^{13}C$ also inherit values indicative of their source region. The reference for $\delta^{13}C$ is 0‰ is for CO_2 gas from the Pedee Formation, and typical values observed geologically are: -25‰ for reduced carbon; 0±4‰ for oxidized carbonates; -30‰

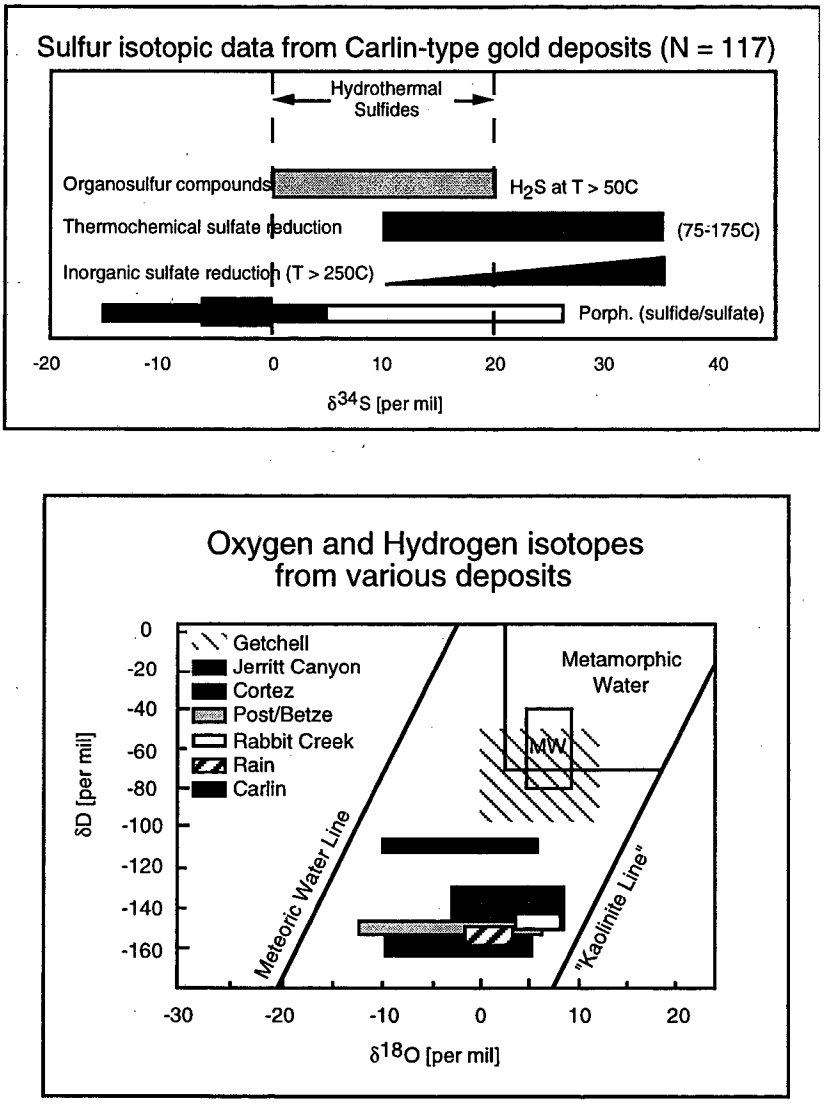

Figure 1.8 Results of isotopic studies. a) Sulfur isotopic data from hydrothermal cinnabar, stibnite, realgar, orpiment, pyrite, maracsite, and arsenopyrite in the Carlin-type gold deposits (after Hofstra, 1997). The vertical dashed lines correspond to the range of reported values. The horizontal bars represent the isotopic signatures expected from various source regions (see discussion in the text). b) Calculated oxygen and hydrogen isotopic compositions from ore stage fluids from the summary of Arehart (1996) and the data of Cline, et al. (1997). The lower cluster likely represents evolved meteoric waters. The Getchell deposit exhibited values consistent with magmatic/meteoric fluids.

for reduced igneous rocks; and -10‰ for more oxidized igneous rocks (Faure, 1986). CO_2 may be introduced into hydrothermal systems in three ways (1) from magmas; 2) the oxidation of or hydrolysis by organic carbon compounds; and/or 3) the dissolution of marine carbonates. Because the bulk of the $\delta^{13}C$ ratios of main-stage calcite at Carlin clusters around 0‰ ± 2‰, carbon was most-likely derived from oxidized carbon in country-rock carbonates (Kuehn and Rose, 1995). The lack of change in the isotopic values for $\delta^{13}C$ also indicates that reduction by organic matter was a minor process during deposition.

Kuehn and Rose (1995) hypothesized that the high CO_2 gas content of MGO fluids was from an exotic source (i.e. either the result of a magmatic contribution or the thermal breakdown of carbonates during metamorphism) because the amount of acid necessary to produce it has no hydrothermal equivalent. The $\delta^{13}C$ ratios generally support this hypothesis, although some CO_2 may have been derived from thermochemical sulfate reduction:

$$2\ CH_2O(s) + SO_4^{2-} + 2\ H^+ = H_2S + 2\ CO_2 + 2\ H_2O, \qquad (1.3)$$

(Gammons, 1997), based on the sulfur isotopes presented above.

1.4.4. Oxygen and Hydrogen Isotopes

Oxygen and hydrogen isotopes in the Carlin-type gold deposits were used to obtain additional evidence for the source of hydrothermal fluids. Typical geologic values for $\delta^{18}O$ and δD are: $\delta^{18}O$ = +6‰ to +8‰ and δD = -50‰ to -80‰ for magmatic sources; $\delta^{18}O$ = +18‰ to +25‰ for clays; $\delta^{18}O$ = +25‰ to +30‰ for carbonates; $\delta^{18}O$ = +8‰ to +13‰ for typical sandstones; and $\delta^{18}O$ = +5‰ to +25‰ and δD = -20‰ to -65‰ for metamorphic rocks (Faure, 1986). Figure 1.8.b shows the results for several different Carlin-type gold deposits determined from inclusions in quartz and jasperoid minerals. Because a fluid of meteoric origin has little chemical interaction except with hydrous minerals, its δD

value should be relatively constant. The wide range in $\delta^{18}O$ and small variation in δD suggests that the fluids in most deposits were dominantly evolved meteoric water.

A very different picture of ore stage fluids is presented by fluid inclusions at the Getchell deposit (Cline. et al., 1997). Figure 1.8.b shows that $\delta^{18}O$ from fluid inclusions within main ore-stage quartz, fluorite, and orpiment ranged from +12‰ to 0‰, and δD ranged from -50‰ to -97‰. These results are consistent with the sulfur isotope data from the same deposits, indicating that fluids were related to igneous activity.

4.4.5 Summary of geological and geochemical data

Carlin-type gold deposits exhibit the following characteristics:

1) Gold deposition is localized near feeder faults in Paleozoic carbonate rocks.
2) Cross-cutting relationships of veins in the Carlin deposit indicate an early hydrocarbon stage, a pre-gold-ore barite ± base metals stage; a main ore stage consisting of decalcification, silicification, argillization, and introduction of gold, arsenic, and mercury (particularly on the surface of syngenetic arsenian pyrite grains), and post-ore barite, stibnite, and calcite stage.
3) Au concentrations are generally greater than Ag, although there are some exceptions.
4) Fluids evolved from a high-salinity fluid possibly related to oil generation and possible base metal migration to one or two fluids of lower salinity representative of main-stage hydrothermal events.
5) CO_2-rich main-stage fluids at Carlin indicate that the temperature of formation was 215° ± 30° Celsius and 800 ± 400 bars.
6) Sulfur isotopes suggest that sulfur was derived from reduced Paleozoic sulfates, but may have a magmatic or metamorphic component (particularly for Getchell trend deposits).
7) Carbon isotopes are indicative of an oxidized carbonate source.

8) Oxygen and hydrogen isotopes are indicative of evolved meteoric waters in many deposits, but appear to be magmatic or metamorphic in the Getchell deposit.

9) Potassium-argon dating of hydrothermal sericites related to gold mineralization gives a date of formation of 80-120 Ma, but dating of these same minerals in other deposits give a Tertiary age, and may be related to extensional tectonics.

1.5 Geochemical modeling results

1.5.1 Magmatic source fluid

One possible source for the metals which comprise the Carlin-type gold deposits is magmatic fluids or leaching of pre-existing plutons. Gammons and William-Jones (1997) explored the solubility of gold in porphyry environments and discussed fluid pathways leading to sulfide-rich aqueous fluids capable of transporting gold to the upper crust. They began their investigation by selecting the important chemical reactions listed in Table 1.2. ΣCl was set to 2.0 *m* (10 wt % NaCl equivalent), the oxidation state was set at the SO_2-H_2S isoactivity boundary above 400°C, and below this temperature at the H_2S-H_2SO_4 boundary. The relatively high oxidation state of their study was selected to reflect oxidized, I-type magmas. In most runs, solution pH was buffered by a K feldspar, muscovite, and quartz assemblage, although they also looked at the effects of more acidic alteration buffers on the solubility of gold. H_2S fugacity was calculated from the assumed coexistence of pyrite and magnetite, and an extrapolated Henry's law constant based on the results of Suleimenov and Krupp (1994). Finally, speciation calculations were performed for various scenarios, followed by gold solubility calculations based on equations (12)-(15) in Table 1.2.

Their first experiment was designed to examine the effect of gold transport from a pluton emplaced at hypozonal or mesozonal depths, and consisted of cooling the aqueous phase described above from 500°C to 300°C at 1 kbar pressure. Figure 1.9.a shows the results along two cooling trajectories (path "A" allowed Au-bisulfide complexes, path "B" did not).

Reaction
1. $HCl(aq) = H^+ + Cl^-$
2. $NaCl(aq) = Na^+ + Cl^-$
3. $KCl(aq) = K^+ + Cl^-$
4. $NaHS(aq) = Na^+ + HS^-$
5. $H_2S(aq) = H^+ + HS^-$
6. $H_2O(l) = H^+ + OH^-$
7. $H_2S(aq) = H_2S(g)$
8. $SO_2(g) + H_2O(g) = H_2S(g) + 3/2\ O_2(g)$
9. $H_2O(g) = H_2(g) + 1/2\ O_2(g)$
10. $9/16\ FeS_2(s) + H_2O(l) = 3/16\ Fe_3O_4 + H_2S + 1/8\ SO_2$
11. $3\ KAlSi_3O_8(s) + 2\ H^+ = KAl_3Si_3O_{10}(OH)_2(s) + 6\ SiO_2(s) + 2\ K^+$
12. $Au(s) + H_2S(aq) + HS^- = Au(HS)_2^- + 1/2\ H_2(g)$
13. $Au(s) + H_2S = Au(HS) + 1/2\ H_2(g)$
14. $Au(s) + Cl^- + HCl(aq) + 1/4\ O_2(g) = AuCl_2^- + 1/2\ H_2O(l)$
15. $Au(s) + 1/2\ H_2O + 1/4\ O_2(g) = Au(OH)(aq)$

Table 1.2 Reactions considered in the geochemical reaction modeling study of Gammons and Wiliams-Jones (1997).

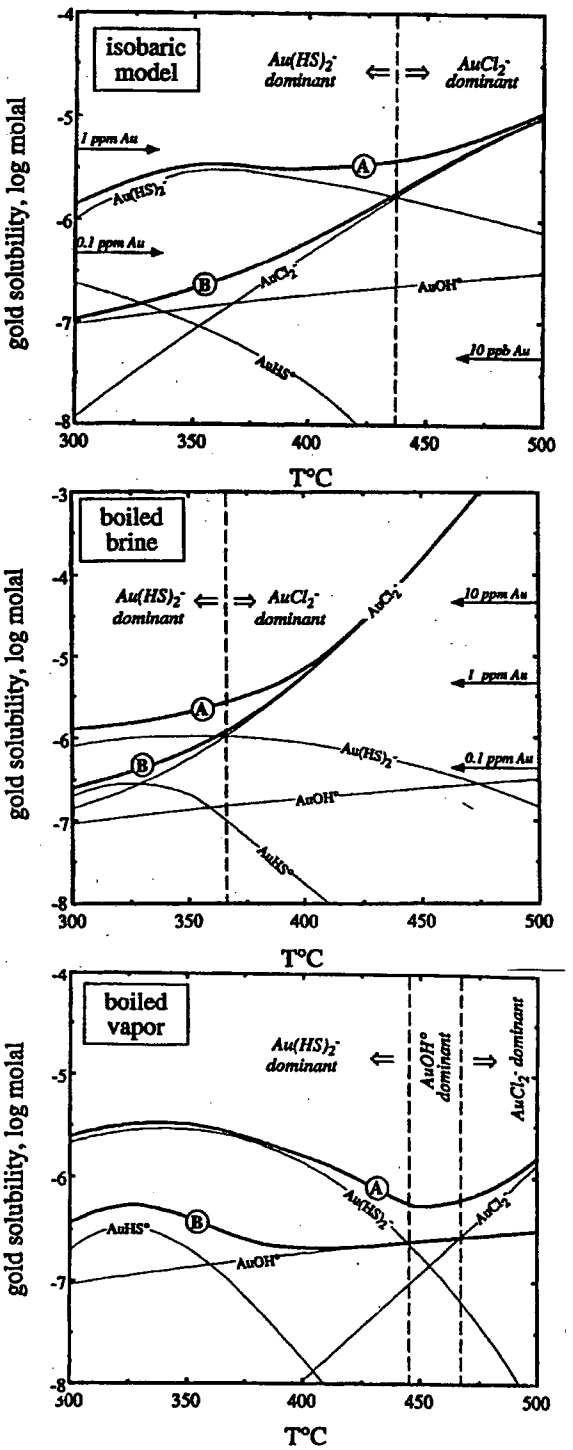

Figure 1.9 Gold solubility versus temperature for various cooling models. A and B refer to the cases where gold bisulfide complexes were included and discluded, respectively. a) Isobaric cooling at a pressure of 500 bars. Au bisulfide predominates at T < 450°C. b) Condensed phase after boiling at 500°C. The loss of H_2S(aq) decreases the solubility relative to the isobaric model. c) Vapor phase after boiling (Gammons and Williams-Jones, 1997).

Below 450°C, $Au(HS)_2^-$ became the dominant species and allowed Au to be transported away from the pluton. If insufficient H_2S was available, however, Au was found to precipitate with base metals closer to the intrusion.

Figures 1.9.b and 1.9.c display the results for a second scenario where they first boiled the fluid by dropping the pressure to 0.5 kbars at 500°C and then cooled both the liquid and vapor phases to 300°C. Two assumptions were inherent to this latter model: 1) the vapor phase was allowed to completely separate from the aqueous phase without any additional chemical interaction during cooling; and 2) the log K data for the reactions in Table 1.2 were used for the vapor phase without introducing significant errors (they cited evidence that Fe/Cl, Zn/Cl, and Pb/Cl ratios measured from vapors were nearly the same in both brine and vapor at 500°C and 0.5 kbars). According to Figure 1.9.b, at 500°C most gold remained in the boiled brine phase as $AuCl_2^-$, and rapidly decreased in solubility as the temperature declined. Gold solubility in the vapor phase, by contrast, increased with a decline in temperature (Figure 1.9.c). The parameters of their model suggest that a vapor phase will recondense at 475°C, allowing transport of Au as $Au(HS)_2^-$ in the aqueous phase away from a parent magma.

The authors concluded that distal gold deposits could form in several different ways. First of all, gold could be directly transported within the brine or aqueous phase. Another possibility is that condensation of magmatic H_2S and SO_2 could greatly increase the solubility of gold in convecting meteoric waters, at least until the pH-buffering capacity of the rock is overcome by the addition of other volatiles such as CO_2 and HCl.

Although this process may be responsible for some epithermal deposits, with low sulfidation and high sulfidation alteration assemblages reflecting the ability of the host rock to neutralize the acidity, it is not clear if magmatic degassing could occur at the depths of Carlin-type gold deposits. One scenario that may possible for the Carlin-type gold deposits which exhibit magmatic isotopic signatures is that an older, magmatic protore was leached and re-precipitated by convective fluids. H_2S-rich fluids generally precipitate H_2S as they

sulfidize ferrous minerals, but if the fluids migrated through a low-grade Au-Cu stock which was already pyritized, preferential remobilization of Au to shallower levels could occur.

1.5.2 Metamorphic source fluid

No quantitative studies have been performed on the generation of Au-bearing fluids by metamorphic processes; however, Powell (1991) and Phillips and Powell (1993) showed that low salinity, CO_2-rich fluids could be derived from devolatilization at the greenschist-amphibolite transition, with the relative quantity of CO_2-to-H_2O dependent on the source rock and the abundance of H_2S dependent on the amount of fluid produced.

1.5.3 Sedimentary source fluid

Ilchik and Barton (1997) argued against an important role for magmatic fluids on the basis of the isotope studies discussed above, the fact that regional patterns imply broad hydrologic systems rather than localized intrusive centers, a lack of enrichment in base metals or silver, and a lack of district-scale zoning which may be expected with porphyry bodies. They similarly discounted the importance of metamorphic fluids based on the inability to generate sufficient H_2O, the light δD of ore fluids, and absence of a mid-Tertiary regional metamorphic event. Their alternative scenario is that permeability anomalies and high heat flows generated by mid-Tertiary extension allowed circulating meteoric water to scavenge gold from the surrounding sedimentary rocks and precipitated it in favorable depositional environments (Figure 1.10). Evidence for this mechanism includes the various isotopic studies discussed above and the heat flow calculations of Ilchik and Barton (1997), who demonstrated that the amount of heat released during extension greatly exceeds the heat generated by magmatic or metamorphic processes.

Calculations for this sedimentary model were performed for both a source region of metamorphosed clastic rocks, and a deposit region of dominantly carbonate rocks. The

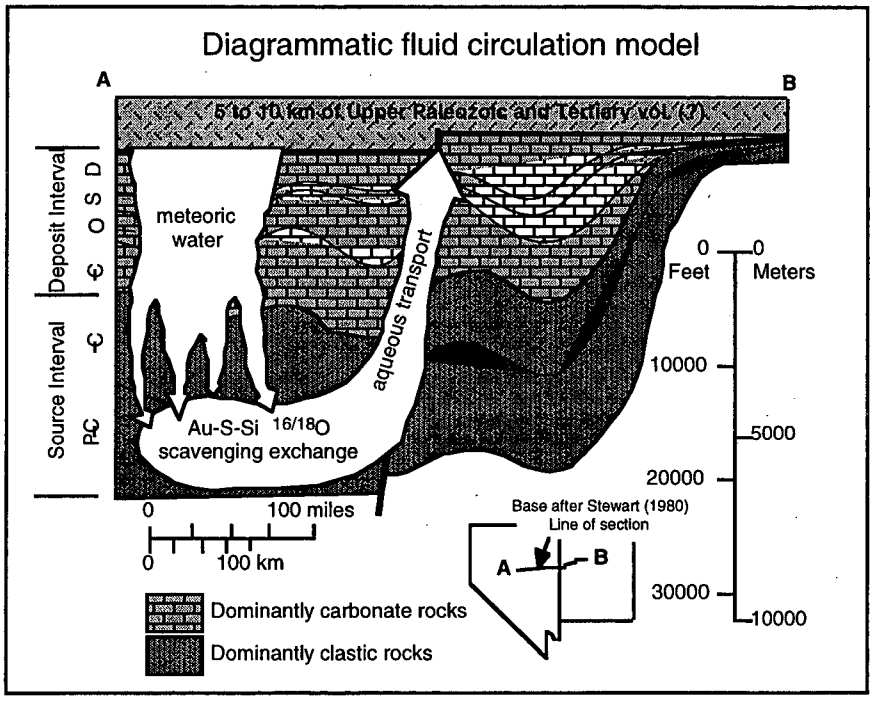

Figure 1.10 Diagrammatic fluid circulation model as proposed by Ilchik and Barton (1997). The cross-section is through central Nevada and Utah and shows the inferred sedimentary stratigraphy. Superimposed on this sequence are possible meteoric water flow paths as fluids circulated to great depths and scavenged Au. Re-precipitation occurred along crustal faults.

Arkose[1]	Graywacke[1]	Pelite[1]
Gold Quartz Low albite K feldspar Muscovite Clinozoisite Galena Sphalerite Phlogopite[2] Pyrite	Gold Quartz Paragonite Margarite Muscovite Clinozoisite Galena Sphalerite Clinochlore[2] Pyrite	Gold Quartz Paragonite Margarite Muscovite Kaolinite Galena Sphalerite Clinochlore[2] Pyrite
Magnetite + Hematite or Pyrrhotite[3] + Annite	Magnetite + Hematite or Pyrrhotite[3] + Annite or Pyrrhotite[3] + Daphnite	Magnetite + Hematite or Magnetite + Daphnite or Pyrrhotite[3] + Daphnite
Calcite or fCO_2 fixed at 10 bars	Calcite or Graphite	Calcite or Graphite

[1]Total chlorinity fixed at 1.0, 0.67, 0.33, or 0.1 m [2]Activity adjusted to coincide with fO_2 and fS_2 buffers [3]Activity = 0.6

Table 1.3 Source rock mineralogy used in the geochemical calculations of Ilchik and Barton (1997).

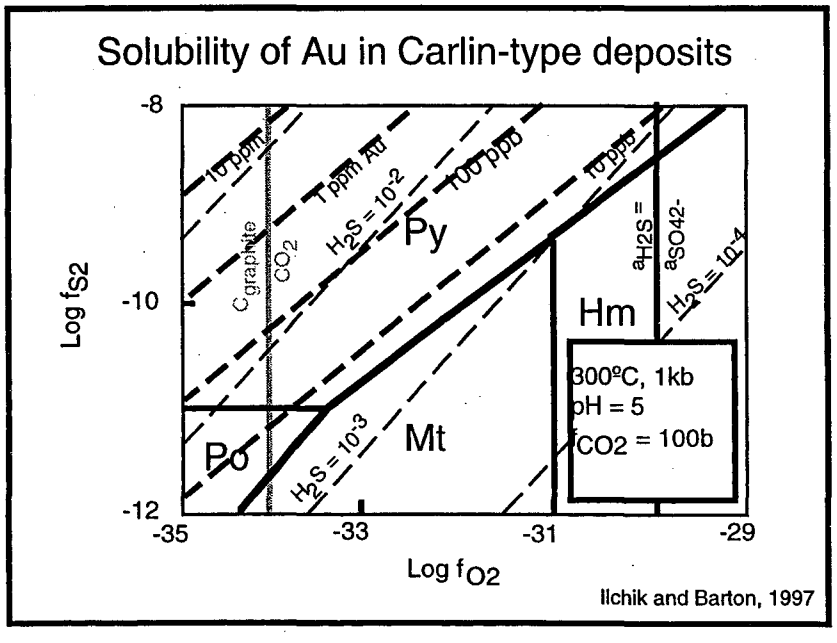

Figure 1.11 Mineralogical buffers used to fix f_{O2} and f_{S2} for a pelite (Ilchik and Barton, 1997). The greatest concentration of H_2S(aq) and gold solubility are given in the upper left of the diagram.

starting mineral assemblages for their source-rock calculations were an arkose, graywacke, and pelite shown in Table 1.3. The temperature and pressure conditions were held at 300°C and 1 kbar in their solutions, and the total chlorine content varied from 0 to 1.0 *m*. Oxygen, carbon, and sulfur were buffered by the various mineral assemblages selected to represent each rock type.

The first result of their calculations was that gold solubility increased with the total sulfur activity, but decreased with fO_2 (Figure 1.11). A graphite buffer was most favorable to gold solubility because it increased the total sulfur content. Despite the conclusions that gold was most soluble with an arkosic assemblage buffered by graphite and at a near-neutral pH, any of the source rocks in their study could have generated Au-bearing fluids if the initial fluid was reduced enough to supply H_2S. The most questionable results of the source-rock calculations were the inability to reproduce either the ΣCO_2 for an arkosic source or the ΣS for any of the rock assemblages observed in fluid inclusions.

Seedorff (1991) hypothesized that the easternmost extent of Carlin-type gold deposits in the Great Basin may be restricted by the availability of favorable sedimentary or metasedimentary host lithologies examined by Ilchik and Barton (1997) (Figure 1.10); however, no calculations have been performed on possible hydrothermal convection through the underlying carbonate assemblage in the figure, even though carbonates can host up to 3.0 ppb of Au (Wedepohl, 1978), and Emsbo, et al. (1997) reported the presence of sedimentary-exhalitive base and precious metal deposits within the Popovich and Roberts Mountain Formations of Figure 1.2.

1.5.4 Depositional mechanisms

Precipitation of gold from hydrothermal solutions is dependent on the chemical conditions of the fluid during mineralization. Hayashi and Ohmoto (1991) showed that the maximum solubility of gold complexed with sulfur at 300°C, $\Sigma S = 0.01m$, and $\Sigma Cl = 1.0m$

occurred at a pH of 7.5 and a log fO_2 = -34. Under these conditions, precipitation can occur in response to any change in the acid/redox condition. Dilution (lowering the ΣS), cooling, and sulfidation are also relevant processes.

Hofstra, et al. (1991) and Ilchik and Barton (1997) both performed geochemical reaction path modeling of gold deposition in the Carlin-type gold deposits to determine which of these scenarios was most likely. Because the calculations of Ilchik and Barton (1997) are more extensive, and produced the same general results as Hofstra, et al. (1991), they are described for illustration. At the deposit level, Ilchik and Barton (1997) re-equilibrated the same fluids generated by their source rock calculations to temperatures and pressures of 150°-225°C and 500 bars, respectively. They then examined four different precipitation mechanisms: simple cooling; cooling with wall rock reactions; sulfidation; and mixing with a second dilute fluid.

For the case of simple cooling, gold solubility was found actually to increase slightly with a drop in temperature. Quartz was also found to precipitate in most runs. The only fluid leading to supersaturation with respect to gold was one with an initially-high Cl^- constant. Precipitation in this case was due to base metal precipitation removing aqueous H_2S from solution.

In the cooling with wall rock reactions scenario, interaction was allowed to occur between the fluid and different mineral assemblages of calcite ± dolomite ± quartz ± muscovite ± kaolinite. Gold supersaturation in the presence of calcite was only found to occur in this case when there was sufficient removal of sulfur due to the precipitation of iron and base metals. The introduction of calcite generally buffered the pH, resulting in increased gold solubility. Finally, hydrothermal alteration was represented by decarbonatization and quartz precipitation. Because the volume of quartz precipitated exceeded the amount of calcite removed in this case, Ilchik and Barton (1997) surmised that massive limestone beds would tend to occlude hydrothermal fluids, and make them unfavorable host rocks.

Reaction between the fluid phase and an assemblage of dolomite and muscovite also produced quartz precipitation and gold supersaturation only when desulfidation of the fluid phase occurred; however, the volume of dolomite removed exceeded the calcite dissolved in the previous case by two to three times, and may have thus provided the necessary permeability for future mineralization. To simulate reactions with dedolomitized rocks, a mineral assemblage of quartz, muscovite, kaolinite, and the saturated sulfide phases was used. For an arkose-derived fluid, a decrease in pH of 0.8 to 1.2 units over the simple cooling-jasperoid model resulted in precipitation of 20% to 70% of the gold. For the other two initial fluids, lower levels of K^+ mediated the muscovite-to-kaolinite reaction, and pH and solubility actually increased by the reaction:

$$2\ KAl_3Si_3O_{10}(OH)_2 + 2\ H^+ + 3\ H_2O = 3\ Al_2Si_2O_5(OH)_4 + 2\ K^+. \quad (1.4)$$

Sulfidation of wall rocks by the precipitation of pyrite is a particularly attractive scenario to deposit gold based on the relationship between Au, As, and Fe in the main gold zone of the Twin Creeks deposit (Figure 1.12) (Stenger, et al., 1998). In this figure, reactive iron refers to the Fe present in minerals other than pyrite, and gold grade is indicated by the hatched areas. Gold is not only concentrated with pyrite, but apparently precipitated with it. The near consistency in the quantity of Fe present in both the mineralized and unmineralized rocks indicates that Fe has not been added from hydrothermal solution, but was likely produced by the dissolution of Fe-bearing minerals during dedolomitization. The effect of sulfidation in the experiments of Ilchik and Barton (1997) was consistent with this observation, and resulted in the precipitation of gold after 10-40% of the aqueous sulfur was removed.

The final scenario modeled by Ilchik and Barton (1997) was fluid mixing, which was simulated by incrementally reducing the concentration of all solutes. Although gold precipitated in response to dilution, the effect was partly offset by an increase in pH and fO_2 of the fluid. Mixing of fluids increased the amount of calcite leached and suppressed the amount of quartz precipitated.

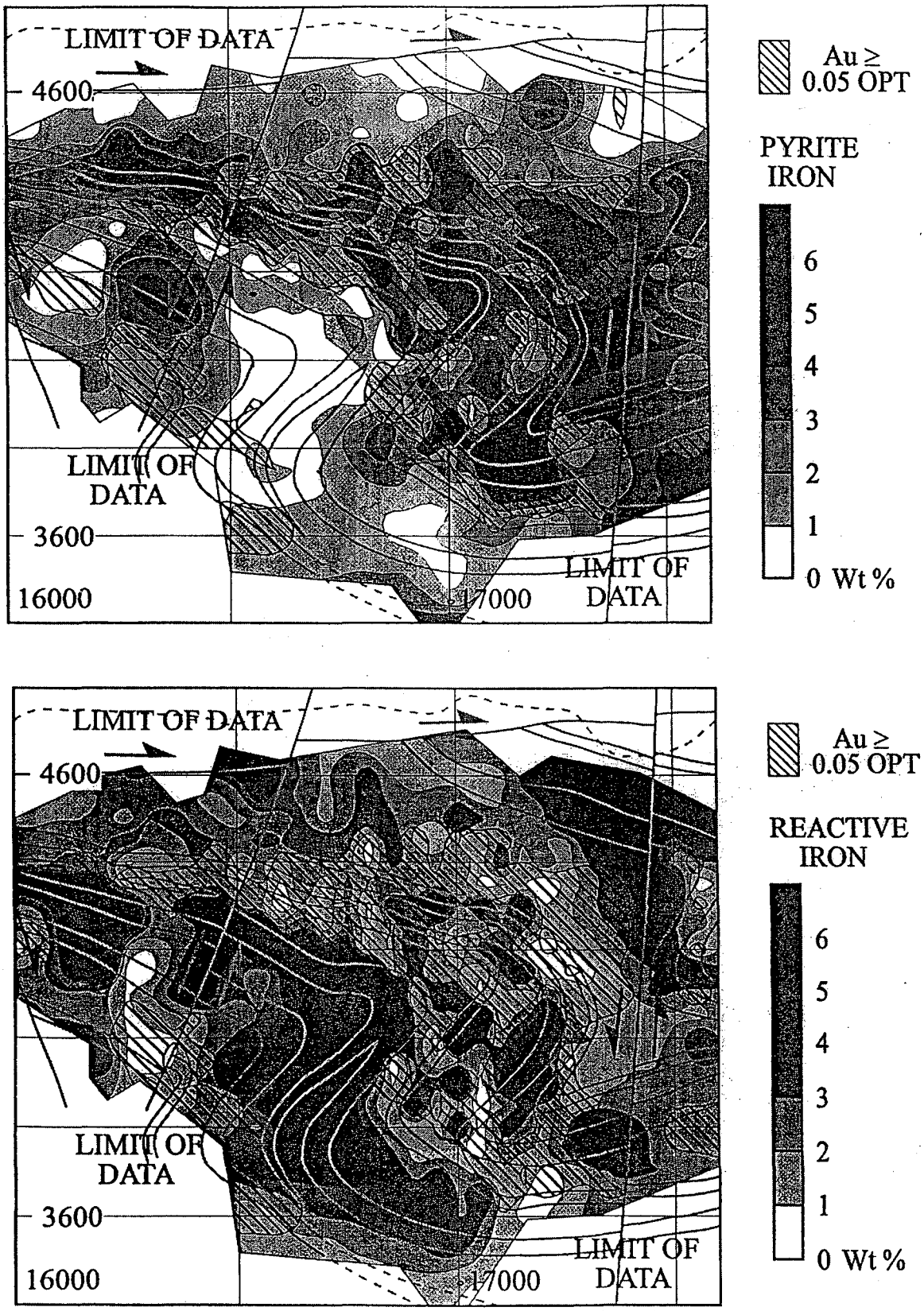

Figure 1.12 Distribution of iron in pyrite along a cross-section of the Twin Creeks deposit (Stenger, et al., 1998). a) Close association of gold with areas containing pyrite-hosted iron. b) Close association also between gold and areas depleted in reactive iron.

1.5.5 Summary of current models

Carlin-type gold deposits are different from porphyry Cu-Au deposits in that they formed at lower temperature, are not favored by high Cl^- and high fO_2 conditions, lack an obvious magmatic source, and consequently possess lower base metal abundances. Because oxygen and hydrogen isotopes in most deposits indicate that water was derived from meteoric sources, possible roles for magmatic fluids in the Carlin-type gold deposits include the production of an initial, gold-bearing protore which was later remobilized, or the production of CO_2 from skarn formation. Arehart (1996) suggested this latter mechanism on the basis that CO_2 was likely introduced close to the deposit because carbonic acid would have dissolved the carbonate fluids through which it passed. Neither sulfur nor carbon isotopes preclude magmatic involvement in either of these two ways. Because oxygen and hydrogen isotopes along the Getchell trend lie within the magmatic and/or metamorphic fields, direct magmatic introduction of fluids may also have occurred in some cases; however, these magmatic signatures may alternatively be the result of water-rock exchange dominated by intrusives.

Metamorphism may have generated ore fluids during the transition from greenschist to amphibolite metamorphic facies. Both of these facies have been observed in Paleozoic sedimentary rocks within the Ruby Mountains, and are associated with Cretaceous igneous activity (Hudec, 1992). If the K-Ar dates of Arehart, et al. (1993a) are accepted, then this mechanism may be valid.

According to Ilchik and Barton (1997) an amagmatic origin of the Carlin-type gold deposits is the most-likely explanation for the Carlin-type gold deposits. It is consistent both with the high heat flows produced by extension and the isotopic and chemical characteristics of the fluids preserved in inclusions. Gold could have been introduced in this scenario after organic carbon-buffered fluids leached sulfate and reduced it to sulfide during deep convective flow of meteoric water, with organic or inorganic desulfidation creating the observed sulfur isotope values. Their calculations indicate that gold leaching (and base metal suppression) would have been favored by a near-neutral, low chlorinity fluid buffered by the clastic rocks

which form the basement of northern Nevada. Precipitation would have been favored during dedelomitization of marl (which can also create large permeability and silica deposition), by a combination of cooling, wall-rock reaction, and mixing. Sulfidation of wall rocks is a particularly effective gold precipitation mechanism and evidence suggests it may have been important (Figure 1.15).

1.6 Unresolved geochemical issues

1.6.1 Au solubility as heteropolynuclear complexes

There are several problems with focusing geochemical modeling efforts only on the solubility of gold. The first of these is that gold has been found to increase with the addition of arsenic under the following experimental conditions: T = 200° to 300° Celsius; P = 1 kbar; ΣS = 0.065 mol/l; pH = 1.13; and a Fe-Fe_3O_4 buffer (Akhmedzhanova, et al., 1988). Figure 1.13.a shows that gold solubility is higher for 300° C than for 200° C, and that the solubility curves have two different slopes (suggesting that different complexes are responsible for solubility). The effect of solution pH and fO_2 on solubility are shown in Figure 1.13.b (Nekrasov, 1996). Solubility decreases in neutral solutions, but increases greatly in more oxidizing conditions. These data were used to infer that the predominant complex was $H_2AuAsS_3^0$, although this was based on an erroneous assumption that arsenic complexes form as dimers (Helz, 1995).

The solubility of gold has also been found to increase with antimony concentration under the following experimental conditions: T = 300°C; P = 1 kbar; ΣS = 0.065 mol/l; pH = 1.25; and a Ti-TiO_2 buffer (Nekrasov, et al., 1982). The complex proposed to explain this result was $H_2AuSbS_3^0$, based on calculations for the ratio of Au:Sb in the nucleus of the complex, and the assumption that because Au and Sb complexes are neutral in acidic solutions, the Au/Sb complex also carries zero charge. Additional experiments in more alkaline conditions

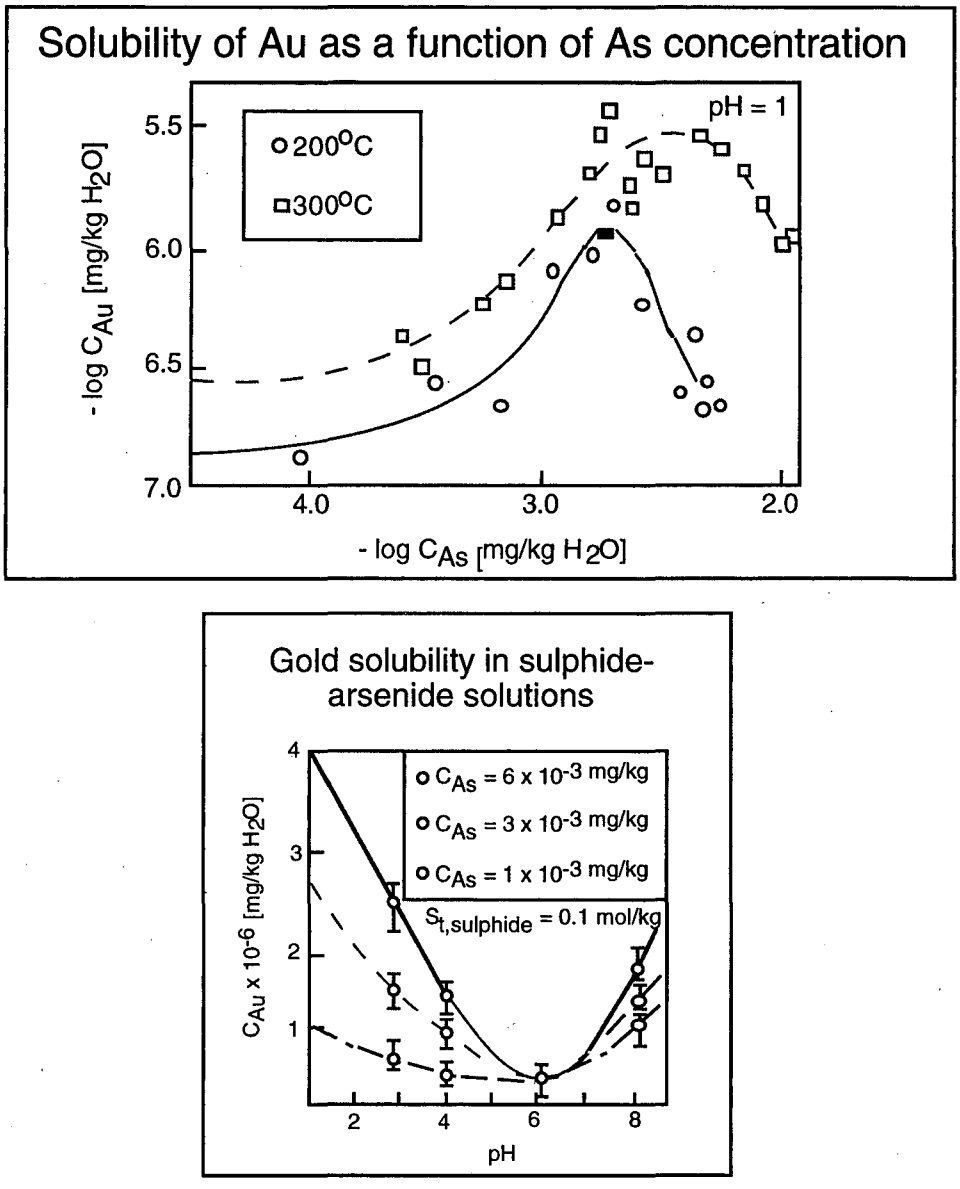

Figure 1.13 Solubility of gold as a function of temperature, pH, and As concentration (from Nekrasov, 1996).

have demonstrated that solubility is enhanced in all but the most neutral solutions (in which case $Au(HS)_2^-$ is the most important gold complex) (Nekrasov and Konyushok, 1982).

Although the existence of these Au heteropolynucleate complexes imply that gold solubility may be controlled by the amount of As and Sb in solution, no geochemical analysis has been performed on As and Sb to determine what range of conditions promotes their mobilization in the Carlin-type gold deposits. Even if this information were available, however, the thermodynamic properties of the Au-heteropolynucleate complexes would still need to be determined. The fact that Au can form complexes with As and Sb also implies that As and Sb may be similarly co-transported, but no experiments have yet been performed to examine this possibility.

1.6.2 Controls on fluid chemistry during transport

Another set of unresolved geochemical issues concerns the influence of host rock mineralogy on the composition of the ore-bearing fluids. Chief among these is determining the relevant mineral assemblage and its effect on the chemistry of the circulating hydrothermal fluids. Ilchik and Barton (1997) explored the geochemical controls in both the source and deposit region, but did not explore the consequences of traversing carbonaceous, metamorphic, or igneous wallrocks during transport. They were also unable to explain the large quantities of CO_2 found in fluid inclusions in the Carlin-type gold deposits, even though CO_2 immiscibility could partition H_2S into the volatile phase, leading to gold deposition. Finally, by limiting their investigation to the solubility of gold, they neglected valuable clues to the chemistry of hydrothermal fluids provided by the constraints that As and Sb must also be soluble.

1.6.3 Au deposition by surface reactions

A distinguishing feature of Carlin-type gold deposits is the association of microscopic gold on the surface of arsenian pyrite grains. Fleet, et al. (1989) showed that a constant

atomic percent of As + S = 66.7% was maintained in arsenopyrite from Archaen greenstone deposits, and Arehart, et al. (1993b) used this result along with their correlation between Au and As in arsenian pyrite from the Post/Betze deposit to hypothesize that As substitutes for S and Au substitutes for Fe in arsenian pyrite. They proposed an oxidation/reduction reaction of the form:

$$H_2 + H_3AsO_3(aq) + Au(HS)_2^- = AuAsS + HS^- + 3\,H_2O, \text{ or} \qquad (1.5)$$

$$3\,H_2 + H_3As_3S_6(aq) + 3\,Au(HS)_2^- = 3\,AuAsS + 6\,H_2S + 3\,HS^- \qquad (1.6)$$

to explain this process. These specific chemical reactions have recently been discounted in favor of reactions by Simon, et al. (1999a) because new experimental evidence suggested that Au exists in the Au^{+1} state on the surface of arsenian pyrite; however, two important features of the reactions remain. First of all, Au may be adsorbed even when it is undersaturated in solution. Secondly, the solubility of arsenic complexes affect the stability of Au.

1.6.4 Mineralogical differences between deposits

Ore-stage minerals within the Carlin-type gold deposits generally consist of Au, Ag, As, Sb, Ba, and Hg, but their relative abundances vary for any particular deposit. One of the most intriguing relationships is the Au/Ag ratio. Gammons and Barnes (1989) have demonstrated that one control on the relative solubility of these two elements is the H_2S concentration, with Au abundance exceeding Ag for higher concentrations of H_2S. This and other relationships between metals await experimental verification.

1.6.5 Metallogenic setting

The metallogenic setting for the Carlin-type gold deposits cannot be determined until the controversy over the ages of the deposits has been resolved. A more complete understanding of the genesis of these deposits will also benefit from probes of the stratigraphy and structure underlying each deposit. This will provide a framework for more accurate geochemical

models. In the interim, knowledge of the geochemistry of Au, As, and Sb may better constrain possible geochemical processes.

1.7 Objectives of current study

A better understanding of the genesis of Carlin-type gold deposits requires that the processes leading to the mobilization of Au be resolved; however, because Au mobilization appears to be controlled by both As and Sb, knowledge of the geochemistry of these metals is also required. The objective of this research was to identify the chemical processes which control the introduction, transport, and deposition of Au, As, and Sb by calculating the thermodynamic properties of the metal complexes for which sufficient experimental data was available, identifying the most important chemical controls on metal solubility, and determining which depositional processes might have been operative based on the geology described in this chapter.

The solubility and speciation of Au, As, and Sb in hydrothermal fluids have been determined experimentally at specified temperatures and saturated vapor pressures for a range of fluid buffered conditions. The Helgeson-Kirkham-Flowers (HKF) equations of state parameters (Helgeson, et al., 1981; Tanger and Helgeson, 1989) have additionally been derived for some of these metal complexes from the experimental solubility constants and numerous correlation algorithms (Sverjensky, et al., 1997). These parameters make it possible to predict the thermodynamic properties of a number of aqueous metal complexes at temperatures and pressures to 1000°C and 5 kbar from the limited experimental data, and therefore begin to determine which chemical processes control gold mineralization.

The first step in this research was to evaluate the validity of the HKF equation of state (**Chapter 2**). Next, the HKF parameters for important aqueous species such as $H_2S(aq)$, HS^-, and the aqueous metal complexes of Au, As and Sb were derived (**Chapter 3**). Upon adding HKF parameters for missing complexes to the SUPCRT database (Johnson, et al., 1992), this

research assessed which parameters were important for the deposition of Au, As, and Sb by generating solubility plots as a function of pressure, temperature, oxidation state, and total reduced sulfide (**Chapter 4**).

2.1 Introduction

In order to determine the relative importance of different chemical reactions in the Carlin-type gold deposits it is first necessary to know the apparent standard molal Gibbs free energies of formation [ΔG_i^o] for the minerals, gases, and aqueous species in the system. Although these values can be calculated from the following two equations:

$$\Delta G_i^o = \Delta G_{f_{\mathrm{Pr}Tr}}^o + \left(G_{PT}^o - G_{\mathrm{Pr}Tr}^o\right); \text{ and} \tag{2.1}$$

$$\Delta G_i^o = \Delta G_{f_{\mathrm{Pr}Tr}}^o - S_{\mathrm{Pr}Tr}^o\left(T - T_r\right) + \int_{Tr}^{T} C_{\mathrm{Pr}}^o dT - T\int_{Tr}^{T} C_{\mathrm{Pr}}^o d\ln T + \int_{\mathrm{Pr}}^{P} V_T^o dP; \tag{2.2}$$

where the superscript [°] denotes the standard state conventions described below and the subscript [r] denotes the reference conditions as consistent with Johnson, et al. (1992), the thermodynamic properties which appear in equation (2.2) are often unknown and must be estimated. Consequently, the objective of this chapter is to discuss different equations of state which can be used to express equation (2.2) in terms of a number of known parameters.

Section 2.2 of this chapter describes the equation of state for gases and minerals used to compile the SUPCRT database utilized in this study (Johnson, et al., 1992) (strictly speaking an equation of state refers to a function expressed in terms of temperature, pressure, and volume for which other thermodynamic properties can be calculated; however, the definition accepted in this study was that provided by the preceding database). *Section 2.3* of this chapter subsequently derives the Helgeson-Kirkham-Flowers (HKF) equation of state used for the relevant aqueous species (Helgeson, et al., 1981; Tanger and Helgeson, 1988). Although this latter equation of state has been shown to accurately predict the thermodynamic properties of ions, *Section 2.4* demonstrates that it inadequately describes the partial molal heat capacities and volumes of neutral aqueous species. This chapter thus concludes with a discussion of alternatives to the HKF equation of state.

2.2 Estimation of the thermodynamic properties of gases and minerals

2.2.1 Fugacity and the standard state of gases

The thermodynamic properties necessary to predict [ΔG_i^o] from equation (2.2) are tabulated under standard state conditions so that their meaning with respect to temperature, pressure, composition, and physical state are unambiguous (Pitzer, 1995). Although the choice of standard states is arbitrary, they are normally defined in such a way that the compositional dependence on the partial molal Gibbs free energy of the ith species (also known as the chemical potential [μ_i]) can be conveniently calculated.

The standard state for gaseous species is generally expressed in terms of the pressure of an ideal gas, which is given the special name *fugacity* [f_i]. Using this definition, the ideal gas law, and the pressure dependence of the Gibbs free energy it is possible to obtain the following relationship between fugacity and the chemical potential of the ith species:

$$\mu_i = \mu_i^o + RT\ln\left(f_i / f_i^o\right) \tag{2.3}$$

where the fugacity ratio is a dimensionless quantity called the *activity* [a_i](Anderson, 1996). Because most gases do not behave ideally, the fugacity in equation (2.3) is a fictitious quantity, only approaching real conditions as pressures approach zero; however, it can be calculated from measurable pressures through the fugacity coefficient [χ_i]:

$$f_i = \chi_i P_i \tag{2.4}$$

which is a function of a gas' compressibility (Castellan, 1983).

The standard state selected for the ith gaseous species in the SUPCRT database (Johnson, et al., 1992) is one which specifies unit fugacity of the hypothetical ideal gas at 1 bar and any temperature of interest. This standard state subsequently removes the denominator from equation (2.3) and generates the following expression for the chemical potential:

$$\mu_i = \mu_i^o + RT\ln a_i = \mu_i^o + RT\ln f_i \tag{2.5}$$

where the activity is dimensionless and equal to the fugacity (equation (2.4)) at all temperatures of interest.

2.2.2 Fugacity and the standard state of minerals

Fugacity is equally important to minerals and aqueous species because at equilibrium the chemical potential of a condensed phase is equal to the chemical potential of its coexisting vapor . Consequently, equation (2.3) also relates the chemical potential of a solid or aqueous species to fugacity (Fletcher, 1993). For minerals, the fugacity of the vapor phase is assumed to follow Raoult's law and is equal to the partial pressure of the pure vapor phase:

$$f_i = \chi_{R,i} X_i P_i^o \qquad (2.6)$$

where $[\chi_{R,i}]$ denotes a Raoultian fugacity coefficient (which can be determined from regression on a Margules-type equation (Fletcher, 1993)), $[X_i]$ is the mole fraction of $[i]$ in the condensed phase, and $[P_i^o]$ is the vapor phase pressure over the pure condensed phase.

The standard state for minerals is unit activity of a pure mineral at any pressure and temperature of interest, resulting in the following expression for chemical potential:

$$\mu = \mu^o + RT \ln a = \mu^o + RT \ln \chi_R X_i \qquad (2.7)$$

where activity is equal the product of the Raoultian fugacity coefficient $[\chi_R]$ and mole fraction $[X_i]$. This is a less restrictive standard state with only a compositional constraint.

2.2.3 Equation of state for gases and minerals

Taking account of the standard states defined above, the values of $[\Delta G_i^o]$, $[\Delta G_{f_{PrTr}}^o]$, $[S_{\mathrm{Pr}Tr}^o]$, $[C_{\mathrm{Pr}}^o]$, and $[V_T^o]$ in equation (2.2) are unambiguous, and subsequent calculation of $[\Delta G_i^o]$ can be accomplished using equation (2.2), the calculated value for $[\Delta G_{f_{PrTr}}^o]$,$[S_{\mathrm{Pr}Tr}^o]$ and expressions for the integrated properties of $[C_{\mathrm{Pr}}^o]$ and $[V_T^o]$:

$$\Delta G_i^o = \Delta G_{f_{\mathrm{Pr}Tr}}^o - S_{\mathrm{Pr}Tr}^o(T - T_r) + \sum_{i=1}^{1+\phi_T} a_i\left(T_{i+1} - T_i - T_{i+1}\ln(T_{i+1}/T_i)\right)$$

$$+ \sum_{i=1}^{1+\phi_T}\left\{\frac{\left(-c_i - b_i T_{i+1} T_i^2\right)\left(T_{i+1} - T_i^2\right)^2}{2T_{i+1}T_i^2}\right\} + V_{\mathrm{Pr}T}^o\left(P - P_r\right)$$

$$+ \sum_{i=1}^{1+\phi_T}\int_{P_{t_i}T}^{P} \Delta V_{t_i}^o dP - \sum_{i=1}^{\phi_T}\frac{\Delta H_{t_i}^o}{T_{t_i}}\left(T - T_{t_i}\right) \qquad (2.8)$$

where i=1 is the reference condition, [ϕ_T] represents the number of phase transitions (ϕ_T=0 for gases), [P_{t_i}], [T_{t_i}], and [$\Delta H_{t_i}^o$] are the pressure, temperature, and standard molal enthalpies of the phase transitions, respectively (Helgeson, et al., 1978), and the [a_i], [b_i], [c_i] terms refer to the temperature dependent parameters for [C_{Pr}^o] defined from the Maier-Kelly (1932) power function:

$$C_{\mathrm{Pr},i}^o = a_i + b_i T + c_i T^2 \qquad (2.9)$$

Because the standard molal volume of most minerals (except for quartz (Walther and Helgeson, 1977)) at a particular temperature do not change significantly, the reference standard molal volume [$\overline{V}_{t_i}^o$] is often applicable. For gases, the pressure invariance stipulated by its standard state similarly mandates that the reference value be used.

2.3 Derivation of the HKF equation of state for aqueous ions

2.3.1 Assumptions of the model

The standard state for the aqueous species in the HKF equation of state is unit activity of the species in a hypothetical one molal solution referenced to infinite dilution at any temperature and pressure. This reference to infinite dilution requires that the solute only interact with solvent molecules and that these interactions obey Henry's law, where the fugacity in the vapor phase is linearly related to the molal concentration [m_i] through the Henry's constant [k_H]:

$$f_i = k_H m_i. \tag{2.10}$$

The analogous expression of equation (2.3) for the chemical potential of an aqueous solute is:

$$\mu = \mu^o + RT \ln a = \mu^o + RT \ln \gamma_H m \tag{2.11}$$

where [γ_H] is the Henryian activity coefficient and the Henry's constant has been divided out in the fugacity ratio.

Using this standard state as a basis, the HKF equation of state was constructed on measurements of standard partial molal thermodynamic properties of aqueous electrolytes assuming that the standard partial molal thermodynamic property of the electrolyte [$\overline{\overline{\Xi}}_k^o$] is the sum of the absolute standard partial molal thermodynamic property of each aqueous ion [$\overline{\overline{\Xi}}_j^{o^{abs}}$]:

$$\overline{\overline{\Xi}}_k^o = \sum_j \nu_{j,k} \overline{\overline{\Xi}}_j^{o^{abs}} \tag{2.12}$$

where [$\nu_{j,k}$] is the stoichiometric number of moles of the jth aqueous ion in the kth electrolyte (Helgeson, et al., 1981). By additionally using the relationship between the absolute and conventional standard partial molal properties:

$$\overline{\overline{\Xi}}_j^o \equiv \overline{\overline{\Xi}}_j^{o^{abs}} - Z_j \overline{\overline{\Xi}}_{H^+}^{o^{abs}} \tag{2.13}$$

where [Z_j] is the charge of the jth ion and [$\overline{\overline{\Xi}}_{H^+}^{o^{abs}}$] is the absolute standard partial molal property of the hydrogen ion, assumed to be zero, the standard partial molal thermodynamic property of the electrolyte can be re-expressed:

$$\overline{\overline{\Xi}}_k^o = \sum_j \nu_{j,k} \overline{\overline{\Xi}}_j^o. \tag{2.14}$$

This equation allows assignment of standard partial molal thermodynamic properties to individual ions by first measuring the properties for the acid electrolyte [$H_{v(H,k)}A$] to get the properties of the anion [A] and then measuring the electrolyte [$C_{v(C,k)}A_{v(A,k)}$] to get the properties of the cation [C].

2.3.2 Solvation contributions to thermodynamic properties

The HKF equation of state decomposes the standard partial molal thermodynamic property of an electrolyte [$\overline{\Xi}_k^o$] in equation (2.14) into a nonsolvation [$\overline{\Xi}_{n,k}^o$] and solvation [$\overline{\Xi}_{s,k}^o$] component:

$$\overline{\Xi}_k^o = \overline{\Xi}_{n,k}^o + \overline{\Xi}_{s,k}^o \tag{2.15}$$

where the nonsolvation term includes both an intrinsic component and a collapse term accounting for the change in structure of the solvent surrounding the ion, and the solvation term arises from the electrostatic interactions between the ion and solvent.

The form of the solvation component is derived from the difference in the reversible electrical work required to charge a sphere in vacuo and in a medium with a bulk dielectric constant [ε] (Born, 1920; Bjerrum, 1929). Assuming that the ion is enclosed in a sphere of radius [r], this work can be expressed for one mole of ion [j] as:

$$\Delta G_{s,j}^{o,abs} = \frac{N^o e^2 Z_j^2}{2r_{e,j}}\left(\frac{1}{\varepsilon}-1\right) = \omega_j^{abs}\left(\frac{1}{\varepsilon}-1\right) \tag{2.16}$$

where [N^o] is Avogadro's number (6.02252 x 10^{23} molecules), [e] is the electronic charge (4.80298 x 10^{-10} esu), [Z_j^2] is the ionic charge, [$r_{e,j}$] is the effective electrostatic radius, and [ω_j^{abs}] is parameter known as the absolute Born parameter.

This Born parameter can also be written in conventional notation [ω_j]:

$$\Delta G_{s,j}^o = \omega_j\left(\frac{1}{\varepsilon}-1\right) \tag{2.17}$$

using the reasoning of equations (2.12) through (2.14), and its magnitude can be calculated from the properties of the electrolyte [k] using the relationship:

$$\omega_k = \sum_j \nu_{j,k}\omega_j \tag{2.18}$$

and

$$\Delta G^{o}_{s,k} = \omega_k \left(\frac{1}{\varepsilon} - 1 \right) \tag{2.19}$$

(Tanger and Helgeson, 1988).

Other solvation thermodynamic parameters such as $[\Delta \overline{S}^{o}_{s}]$, $[\Delta \overline{C}^{o}_{P,s}]$, and $[\Delta \overline{V}^{o}_{s}]$ are derivative functions of equation (2.19), and are given by:

$$\Delta \overline{S}^{o}_{s} = -\left(\frac{\partial \Delta \overline{G}^{o}_{s}}{\partial T} \right)_{P}, \tag{2.20}$$

$$\Delta \overline{C}^{o}_{P,s} = T\left(\frac{\partial \Delta \overline{S}^{o}_{s}}{\partial T} \right)_{P}, \tag{2.21}$$

and

$$\Delta \overline{V}^{o}_{s} = -\left(\frac{\partial \Delta \overline{G}^{o}_{s}}{\partial P} \right)_{T}, \tag{2.22}$$

where the complete expressions for these derivatives can be found in Appendix G of Tanger and Helgeson (1988).

2.3.3 Nonsolvation contributions to thermodynamic properties

The solvation contribution to the standard partial molal thermodynamic properties of aqueous ions does not account for local collapse of the solvent structure in the vicinity of the ion. Consequently, nonsolvation effects were incorporated into the HKF equation of state by first considering the nonsolvation contribution to the standard partial molal volume and heat capacity and then integrating over pressure and temperature to get the resultant nonsolvation standard partial molal entropy and Gibbs free energy.

The nonsolvation contribution to the standard partial molal volume $[\Delta \overline{V}^{o}_{n}]$ arises from an intrinsic component $[\sigma]$, which is believed to be proportional to the molar volume of its crystallographic counterpart, and involves an electrostriction, temperature -dependent term $[\xi]$ representing the collapse of the solvent structure in the vicinity of the solvated ion:

$$\Delta\overline{V}^{o}_{n,P_r} = \sigma + \xi\frac{1}{(T-\theta)} \tag{2.23}$$

where the subscript [P_r] denotes the reference pressure and [θ] is a structural temperature for supercooled water taken to be 228°K (Tanger and Helgeson, 1988). Figure 2.1 shows that the second derivative of the dielectric constant (as computed from the equations of Johnson and Norton, 1992) approaches minus-infinity at approximately 228°K, suggesting that this structural temperature may be related to electrostatic properties of water. To account for pressure-induced effects, Tanger and Helgeson (1988) computed the derivative of equation (2.23) to obtain the complete expression for [$\Delta\overline{V}^{o}_{n}$]:

$$\Delta\overline{V}^{o}_{n} = a_1 + \frac{a_2}{(\Psi+P)} + \frac{a_3}{(T-\theta)} + \frac{a_4}{(\Psi+P)(T-\theta)} \tag{2.24}$$

where [Ψ] was found to be equal to 2600 bars from regression on NaCl and K_2SO_4 experimental data.

The nonsolvation contribution to the standard partial molal heat capacity [$\Delta\overline{C}^{o}_{p,n}$] was derived analogously to [$\Delta\overline{V}^{o}_{n,P_r}$] starting with the following equation:

$$\Delta\overline{C}^{o}_{P_r,n} = c_1 + c_2\left(\frac{1}{(T-\theta)}\right)^2 \quad , \tag{2.25}$$

and using the relationships:

$$\left(\frac{\partial\overline{C}^{o}_{P}}{\partial P}\right) = -T\left(\frac{\partial\overline{V}^{o}}{\partial T^2}\right)_P \tag{2.26}$$

and equation (2.24), to write:

$$\Delta\overline{C}^{o}_{P,n} = c_1 + \frac{c_2}{(T-\theta)^2} - \left(\frac{2T}{(T-\theta)^3}\right)\left(a_3(P-P_r) + a_4\ln\left(\frac{(\Psi+P)}{(\Psi+P_r)}\right)\right). \tag{2.27}$$

Figure 2.2 compares the magnitude of the solvation and nonsolvation components of the volume and heat capacity of Na^+ as a function of temperature. Each of the two contributions is electrostrictive and creates negative deviations of the partial molal thermodynamic

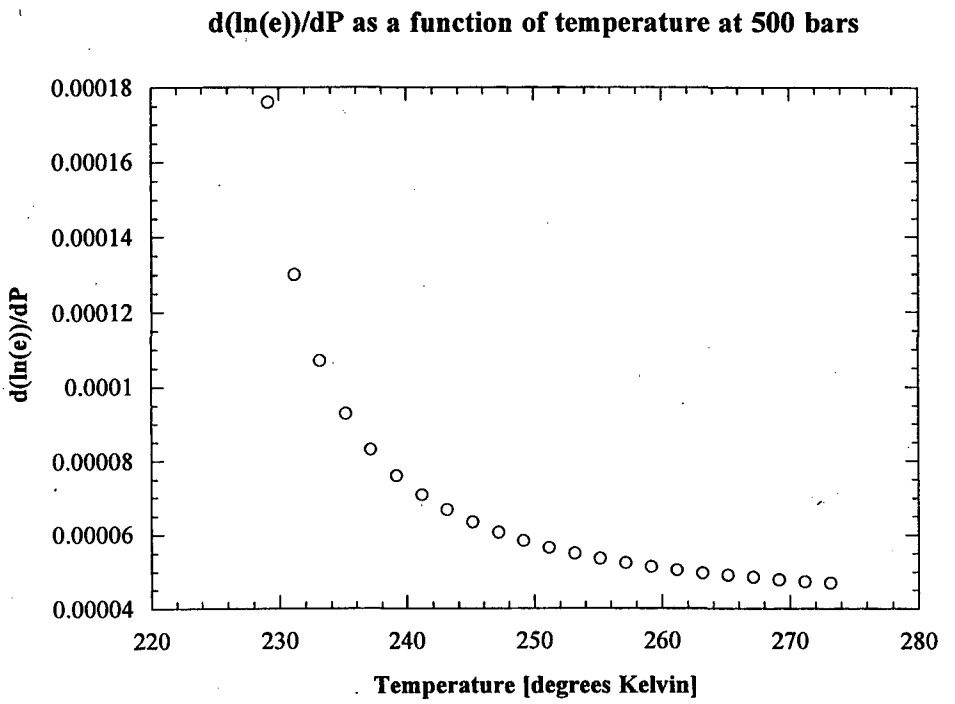

Figure 2.1 The second derivative of the natural logarithm of the dielectric constant of water as a function of temperature (degrees Kelvin). This dielectric term is used in the solvation component of the standard partial molal heat capacity for aqueous ions (equation 2.21)

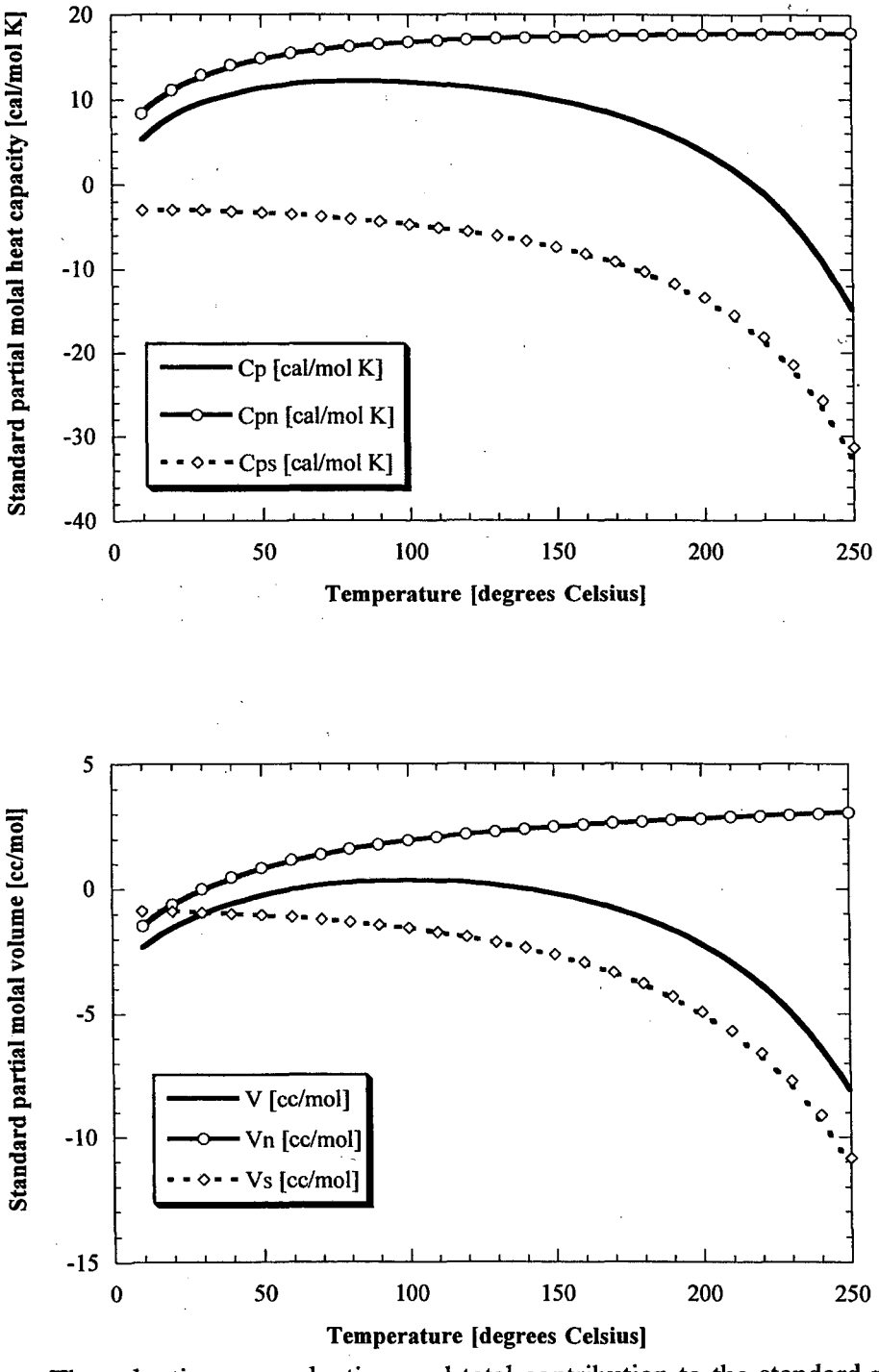

Figure 2.2 The solvation, nonsolvation, and total contribution to the standard partial molal heat capacity and volume for Na^+.

properties of the aqueous ion where their influence is greatest. For the nonsolvation component, this occurs at the lowest temperatures because as the temperatures rises, the dielectric permittivity of the solvent declines and the structural collapse contribution becomes less important. In contrast, the solvation component is greatest at higher temperatures because electrostatic interactions between the charged ion and solvent increase.

2.3.4 Solvent compressibility and dielectric saturation corrections

Tanger and Helgeson (1988) found that their predictions of $[\Delta\overline{V}^o]$ and $[\Delta\overline{C}_P^o]$ for several electrolytes underestimated experimental values at temperatures approaching the critical point of water. They subsequently proposed a correction to the original HKF equation of state to account for solvent compressibility and dielectric saturation in the vicinity of an ion at high temperatures, by including an empirical g-function correction in the effective radius term of equation (2.16):

$$\omega_j = \eta\left[Z_j^2\left(r_{x,j} + |Z_j|(k_z + g)\right)^{-1} - Z_j(3.082 + g)^{-1}\right] \qquad (2.28)$$

where $[\eta]$ = 1.66027 x 10^5 Å cal mol^{-1}, $[Z_j]$ is the ionic charge, $[r_{x,j}]$ is the crystallographic radius, $[k_z]$ is a constant equal to 0.94 Å for cations and 0.0 Å for anions, and $[g]$ is the density-temperature dependent correction function which approaches zero at the reference temperature and pressure. Shock, et al. (1992) showed that incorporation of a $[g]$-function correction into the effective radius term of equation (2.28) is equivalent to introducing a temperature/pressure-dependent relative permittivity in the vicinity of an ion $[\varepsilon_j^*]$. These latter investigators also extended equation (2.28) to 1000°C and 5 kb using the experimental log K_r for $NaCl^o$ = NaCl.

Incorporation of the temperature and pressure-dependent Born function allows $[\Delta\overline{G}^o]$, $[\overline{V}^o]$, and $[\Delta\overline{C}_P^o]$ to be written in terms of the HKF equation of state regression parameters:

$$\Delta\overline{G}^{o} = \Delta\overline{G}^{o}_{f_{\mathrm{Pr},Tr}} - \overline{S}^{o}_{\mathrm{Pr},Tr}(T-T_r) - c_1\left(T\ln\left(\frac{T}{T_r}\right) - T + T_r\right)$$

$$-c_2\left(\left[\left(\frac{1}{T-\theta}\right)-\left(\frac{1}{T_r-\theta}\right)\right]\left(\frac{\theta-T}{\theta}\right)-\frac{T}{\theta^2}\ln\left[\frac{T_r(T-\theta)}{T(T_r-\theta)}\right]\right)$$

$$+a_1(P-P_r)+a_2\ln\left(\frac{\Psi+P}{\Psi+P_r}\right)+a_3\left(\frac{P-P_r}{T-\theta}\right)+a_4\left(\frac{1}{T-\theta}\right)\ln\left(\frac{\Psi+P}{\Psi+P_r}\right)$$

$$+\omega_{\mathrm{Pr},Tr}\left[\frac{1}{\varepsilon}-\frac{1}{\varepsilon_{\mathrm{Pr}\,Tr}}+Y_{\mathrm{Pr},Tr}(T-T_r)\right]+k\left[\omega-\omega_{\mathrm{Pr},Tr}\right]\left(\frac{1}{\varepsilon}-1\right); \quad (2.29)$$

$$\overline{V}^{o} = a_1 + a_2\left(\frac{1}{\Psi+P}\right)+\left(a_3+a_4\left(\frac{1}{\Psi+P}\right)\right)\left(\frac{1}{T-\theta}\right)-\omega Q+\left(\frac{1}{\varepsilon}-1\right)\left(\frac{\partial\omega}{\partial P}\right)_T; \quad (2.30)$$

$$\overline{C}^{o}_{P} = c_1+\frac{c_2}{(T-\theta)^2}-\left(\frac{2T}{(T-\theta)^3}\right)\left(a_3(P-P_r)+a_4\ln\left(\frac{\Psi+P}{\Psi+P_r}\right)\right)$$

$$+\omega TX+2TY\left(\frac{\partial\omega}{\partial T}\right)_P-T\left(\frac{1}{\varepsilon}-1\right)\left(\frac{\partial^2\omega}{\partial T^2}\right); \quad (2.31)$$

where and $[k]$ is a switch function equal to 1 for charged species and 0 for neutral species (Sverjensky, et al., 1997), and $[Q]$, $[Y]$,and $[X]$ are given by:

$$Q \equiv -\left(\frac{\partial(1/\varepsilon)}{\partial P}\right)_T = \frac{1}{\varepsilon^2}\left(\frac{\partial\varepsilon}{\partial P}\right)_T; \quad (2.32)$$

$$Y \equiv -\left(\frac{\partial(1/\varepsilon)}{\partial T}\right)_P = \frac{1}{\varepsilon^2}\left(\frac{\partial\varepsilon}{\partial T}\right)_P; \quad (2.33)$$

$$X \equiv \left(\frac{\partial Y}{\partial T}\right)_P = \frac{1}{\varepsilon^2}\left(\left(\frac{\partial^2\varepsilon}{\partial T^2}\right)_P-\frac{2}{\varepsilon}\left(\frac{\partial\varepsilon}{\partial T}\right)_P^2\right) \quad (2.34)$$

(Tanger and Helgeson, 1988) and can be computed from equations expressing the dielectric properties of water to 1000°C and 5 kbar (Johnson and Norton, 1992).

2.3.5 HKF parameter determination from regression calculations

The nine HKF equation of state parameters required to predict the partial molal thermodynamic properties of equations (2.29) through (2.32) are [$\Delta\overline{G}^o_{f_{\mathrm{Pr},Tr}}$], [$\overline{S}^o_{\mathrm{Pr},Tr}$], [$c_1$], [$c_2$], [$a_1$], [$a_2$], [$a_3$], [$a_4$], and [$\omega_{\mathrm{Pr},Tr}$],which can be obtained by regressing these equations against experimental data. For the case of [$\Delta\overline{G}^o_{f_{\mathrm{Pr},Tr}}$], the most available reported data is often solubility or dissociation constants and equation (2.29) can be regressed against the standard partial molal Gibbs free energy of formation of the aqueous complex [$\Delta\overline{G}^o_c$] determined from:

$$\Delta\overline{G}^o_c = 2.303RT\log K_r + \sum_i \hat{n}_{i,c}\Delta\overline{G}^o_i + \sum_j \hat{n}_j\Delta G^o_j \qquad (2.35)$$

where [$\hat{n}_{i,c}$] and [$\Delta\overline{G}^o_i$] are the stoichiometric reaction coefficient and standard partial molal Gibbs free energy for the ith aqueous species, [$\hat{n}_j$] and [ΔG^o_j] are the stoichiometric reaction coefficient and standard partial molal Gibbs free energy for the jth mineral, and the activity coefficients of charged species within the equilibrium constant [K_r] are defined according to the Debye-Hückel equation, such as the form expressed by Helgeson (1969):

$$\log\gamma_i = \frac{-A|Z_i|I^{1/2}}{1+aBI^{1/2}} + B^oI \qquad (2.36)$$

where [A] and [B] are the conventional molal Debye-Hückel coefficients which vary with the dielectric constant and density of the solvent, [I] is the ionic strength, [a] is the distance of closest approach, and [B^o] is the deviation function which varies with temperature.

An alternative method for determining the HKF equation of state parameters is to regress experimental standard partial molal volume and heat capacity data against equations (2.30) or (2.31), respectively. In the former case, the standard partial molal volumes of the kth aqueous electrolyte [$\overline{V}^o_k$] must first be obtained from apparent partial molal volumes through the relationship:

$$\rho_{V,k} = \overline{V}_k^o + \frac{1}{4}\sum_j \nu_{j,k} b_{V,k} \bar{I} \tag{2.37}$$

where $[\rho_{V,k}]$ is a difference function between measured apparent molal properties and those calculated with the Hückel equation, $[\nu_{j,k}]$ is the number of moles of the j th ion in the kth electrolyte, $[b_{V,k}]$ can be calculated from appropriate derivatives of the Hückel equation (Helgeson, et al., 1981; or Shock and Helgeson, 1988), and $[\bar{I}]$ is the effective ionic strength:

$$\bar{I} \equiv \frac{1}{2}\sum_j Z_j^2 m_j \tag{2.38}$$

where $[m_j]$ is the molality of the jth ion. The analogous expression for the standard partial heat capacity $[\overline{C}_{P,k}^o]$ is:

$$\rho_{J,k} = \overline{C}_{P,k}^o - \frac{1}{4}\sum_j \nu_{j,k} b_{J,k} \bar{I}, \tag{2.39}$$

and in a completely dissociated electrolyte,

$$\bar{I} = I = \frac{1}{2}\sum_j \nu_{j,k} Z_j^2 m_k \ . \tag{2.40}$$

Plots of $[\rho_{V,k}]$ or $[\rho_{J,k}]$ versus true ionic strength $[I]$ should yield linear curves, with intercepts of $[\overline{V}_k^o]$ and $[\overline{C}_{P,k}^o]$, respectively.

2.3.6 HKF parameter determination from correlation algorithms

In the absence of sufficient experimental data, it was found that the standard partial thermodynamic properties and HKF equation of state parameters of similar aqueous species could be linearly correlated and the number of regression parameters subsequently reduced. These correlations are numerous and are summarized in Shock and Helgeson (1988), Shock, et al. (1989), Sverjensky, et al. (1997), and Shock, et al. (1997). The correlations which were

used most extensively in the regression calculations of **Chapter 3** were:

$$\sigma = (1.11)\Delta\overline{V}^{o}_{n,\mathrm{Pr},Tr} + 1.8; \tag{2.41}$$

$$a_1 = (0.013684)\Delta\overline{V}^{o}_{n,\mathrm{Pr},Tr} + 0.1765; \tag{2.42}$$

$$a_4 = -(4.134)a_2 - 27790; \tag{2.43}$$

$$c_2 = (2037)\overline{C}^{o}_{\mathrm{Pr},Tr} - 30460; \tag{2.44}$$

where

$$\Delta\overline{V}^{o}_{n,\mathrm{Pr},Tr} = \overline{V}^{o}_{\mathrm{Pr},Tr} + \omega_{\mathrm{Pr},Tr}Q_{\mathrm{Pr},Tr}; \text{ and} \tag{2.45}$$

$$\sigma = a_1 + \frac{a_2}{\Psi + P_r}. \tag{2.46}$$

These correlations can be combined with equations (2.29) and (2.30) to give:

$$\Delta\overline{G}^{o} = \Delta\overline{G}^{o}_{f_{\mathrm{Pr},Tr}} - \overline{S}^{o}_{\mathrm{Pr},Tr}(T - T_r) - \overline{C}^{o}_{\mathrm{Pr},Tr}\left[(0.5861)\left(T\ln\left(\frac{T}{T_r}\right) - T + T_r\right)\right]$$

$$-\overline{C}^{o}_{\mathrm{Pr},Tr}\left[(2037)\left(\left[\left(\frac{1}{T-\theta}\right) - \left(\frac{1}{T_r-\theta}\right)\right]\left(\frac{\theta - T}{\theta}\right) - \frac{T}{\theta^2}\ln\left[\frac{T_r(T-\theta)}{T(T_r-\theta)}\right]\right)\right]$$

$$+\overline{V}^{o}_{\mathrm{Pr},Tr}\left[(0.0137)(P - P_r) + (33.412)\ln\left(\frac{\Psi + P}{\Psi + P_r}\right) + (-0.1313)\left(\frac{P - P_r}{T - \theta}\right)\right]$$

$$+\overline{V}^{o}_{\mathrm{Pr},Tr}\left[(-138.13)\left(\frac{1}{T-\theta}\right)\ln\left(\frac{\Psi + P}{\Psi + P_r}\right)\right] + \omega_{\mathrm{Pr},Tr}\left[TX\left(T\ln\left(\frac{T}{T_r}\right) - T + T_r\right)\right]$$

$$+\omega_{\mathrm{Pr},Tr}\left[(41.8393Q)\left[(0.013684)(P - P_r) + (33.412)\left(\ln\left(\frac{\Psi + P}{\Psi + P_r}\right)\right)\right]\right]$$

$$+\omega_{\mathrm{Pr},Tr}\left[(41.8393Q)\left[(-0.1313)\left(\frac{P - P_r}{T-\theta}\right) + (-138.13)\left(\left(\frac{1}{T-\theta}\right)\ln\left(\frac{\Psi + P}{\Psi + P_r}\right)\right)\right]\right]$$

$$+\omega_{\mathrm{Pr},Tr}\left[\left(\frac{1}{\varepsilon} - \frac{1}{\varepsilon_{\mathrm{Pr},Tr}} + Y_{\mathrm{Pr},Tr}(T - T_r)\right)\right] + (-6.16)\left(T\ln\left(\frac{T}{T_r}\right) - T + T_r\right)$$

$$+(30346)\left(\left[\left(\frac{1}{T-\theta}\right)-\left(\frac{1}{T_r-\theta}\right)\right]\left(\frac{\theta-T}{\theta}\right)-\frac{T}{\theta^2}\ln\left[\frac{T_r(T-\theta)}{T(T_r-\theta)}\right]\right)+(0.1765)(P-P_r)$$

$$+(-347.18)\left(\ln\left(\frac{\Psi+P}{\Psi+P_r}\right)\right)+(7.1146)\left(\frac{P-P_r}{T-\theta}\right)+(-26355)\left(\left(\frac{1}{T-\theta}\right)\ln\left(\frac{\Psi+P}{\Psi+P_r}\right)\right)$$

$$+k\left[\omega-\omega_{\mathrm{Pr},Tr}\right]\left(\frac{1}{\varepsilon}-1\right). \qquad (2.47)$$

Equation (2.47) differs slightly from equation (38) of Sverjensky, et al. (1997), but independent calculation of $[\Delta\overline{G}^o]$ using equation (44) of Shock and Helgeson (1988) (equation (2.29) of this chapter) verifies that equation (2.47) is the correct function. Of most importance to this study is the fact that utilization of equation (2.47) allows the number of regression parameters to be reduced from nine to five. Also, for experimental data below 200 bars, the pressure terms contribute negligibly to $[\Delta\overline{G}^o]$ and the number of regression parameters in equation (2.47) can be further reduced to four (Sverjensky, et al., 1997).

An important implication of using equation (2.47) to determine the HKF equation of state parameters is that the Born parameter for charged species at the reference temperature and pressure $[\omega_{\mathrm{Pr},Tr}]$ cannot be regressed because it is dependent on $[\overline{S}^o_{\mathrm{Pr},Tr}]$. This dependence is due to the fact that for the jth charged species the Born parameter $[\omega]$ must be calculated from:

$$\omega_j=\eta Z_j\left[\frac{Z_j}{r_{e,j,\mathrm{Pr},Tr}+|Z|g}-\frac{1}{3.08+g}\right] \qquad (2.48)$$

where $[r_{e,j,\mathrm{Pr},Tr}]$ is correlated to $[\overline{S}^o_{\mathrm{Pr},Tr}]$ via:

$$r_{e,j,\mathrm{Pr},Tr}=\frac{Z_j^2\left(\eta Y_{\mathrm{Pr},Tr}-100\right)}{\overline{S}^o_{\mathrm{Pr},Tr}-\alpha_Z} \qquad (2.49)$$

and where $[\alpha_Z]$ is a charge-dependent correlation parameter equal to $71.5|Z_j|$ (Shock and Helgeson, 1988). An alternative regression approach would have been to express equation

(2.47) explicitly in terms of the effective radius of the charged species at the reference temperature and pressure [$r_{e,j,\mathrm{Pr},Tr}$]; however, this method was neither adopted by Sverjensky, et al. (1997) nor used in the regression calculations for Au, As, and Sb complexes. The correlation between [$\omega_{\mathrm{Pr},Tr}$] and [$\overline{S}^{o}_{\mathrm{Pr},Tr}$] can be calculated from equations (2.48) and (2.49) to be:

$$\omega_{j\mathrm{Pr},Tr} = -1514.2\overline{S}^{o}_{\mathrm{Pr},Tr} + \beta_Z \qquad (2.50)$$

where [β_Z] is a charge-dependent constant which again differs slightly from the values reported by Sverjensky, et al. (1997).

2.4 Assessment of the HKF equation of state for neutral aqueous species

2.4.1 Limitations of the HKF equation of state for neutral aqueous species

The extension of the HKF equation of state to neutral aqueous species was made with the assumption that nonvolatile and/or highly polar neutral molecules should attract H_2O dipoles like electrolytes, but that volatile and nonpolar molecules should repel water molecules and disrupt solvent-solvent interactions (Shock, et al., 1989). Consequently, neutral molecules could be treated as if they had an effective radius and charge with positive and negative Born parameters representing attractive and repulsive electrostatic forces, respectively.

Supporting evidence for assigning a Born parameter to neutral aqueous species was found in this study to be provided by the correlation between the coefficient of the Born parameter in equation (2.17) and the coefficient of the dipole moment [μ] in the following equation derived by Onsager (1936) to describe the free energy of solvation of a neutral aqueous species:

$$\Delta\overline{G}^{o}_{s} = \frac{\mu^2}{r^3}\left(\frac{\varepsilon - 1}{2\varepsilon + 1}\right) \qquad (2.51)$$

(Simkin and Sheikhet, 1995). Figure 2.3.a compares the temperature dependence of the Onsager coefficient to the Born parameter coefficient. The nearly perfect match implies

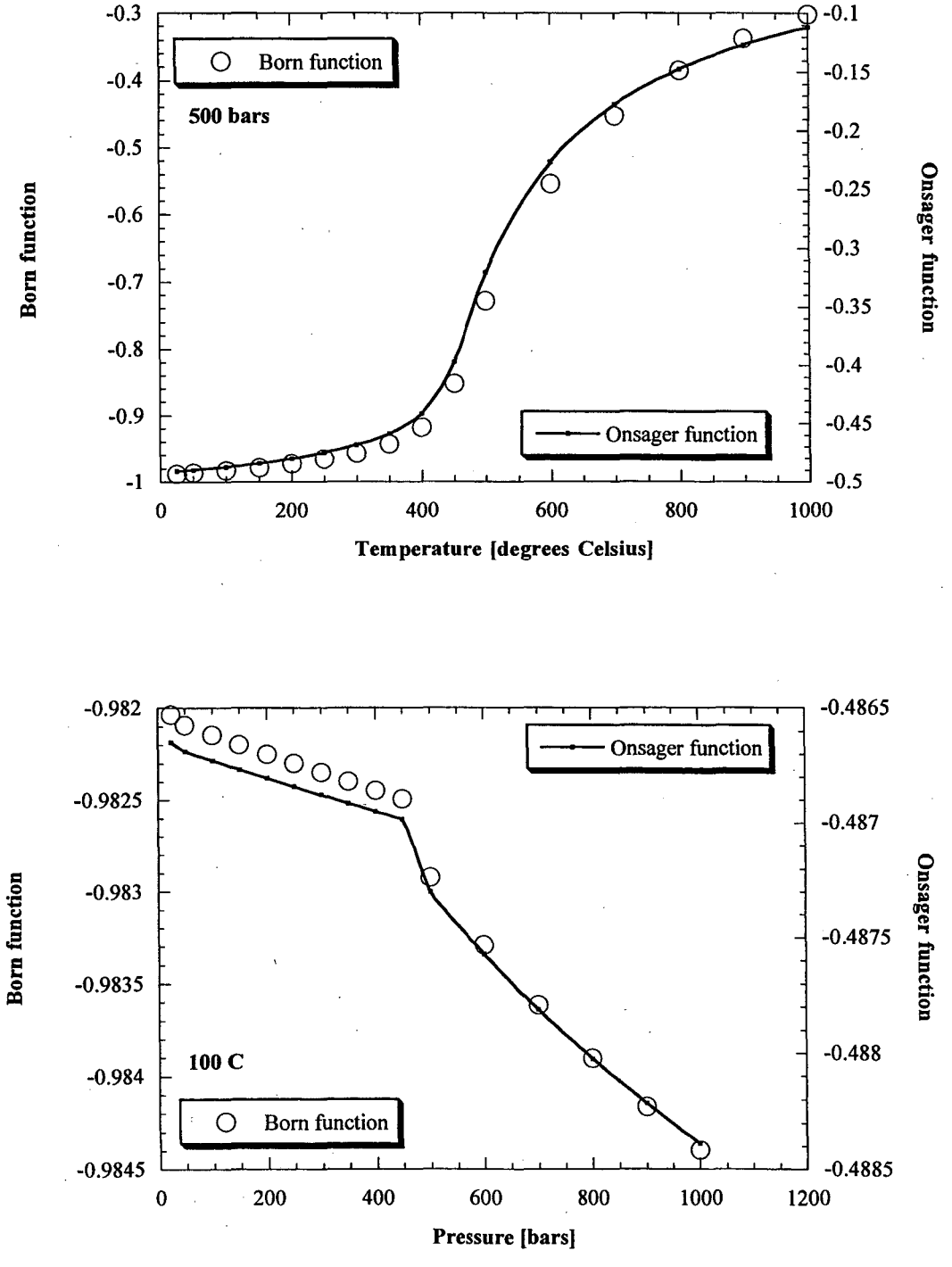

Figure 2.3 Comparison of the Born and Onsager equations as a function of a) temperature; and b) presure.

that the derivative functions with respect to temperature (i.e. $[\Delta\overline{S}_s^o]$ and $[\Delta\overline{C}_{P,s}^o]$) should be identical and will be accurately represented by a Born parameter. Figure 2.3.b additionally verifies that $[\Delta\overline{V}_s^o]$ is equally well-represented because the pressure dependence of Onsager and Born parameters are identical.

Recognition that problems existed in applying the HKF equation of state to neutral aqueous species arose with the recent experimental data on the apparent molal volumes and heat capacities of neutral volatile species to the critical point of water (Hnedkovsky, et al, 1996; Hnedkovsky and Wood, 1997). Figures 2.4.a through 2.4.h show these experimental results in relation to the heat capacities and volume of NH_3(aq), H_2S(aq), CO_2(aq), and CH_4(aq) predicted from the HKF equation of state derived from experiments at or below 100°C (Shock, et al., 1989) . There is a systematic negative deviation from the experimental results at elevated temperatures, and although one source of error may be due to the fact that the results were not extrapolated to infinite dilution, O'Connell, et al. (1996) estimated this error would only be 2% for the volumetric data, and Hnedkovsky and Wood (1997) estimated that the magnitude would be a maximum of 15% near the critical point for the heat capacity.

Table 2.1 reports the HKF equation of state parameters derived by Shock, et al. (1989) and the parameters re-derived in this study using equations (2.30) and (2.31) and the new NH_3 (aq) data to 350°C. This particular aqueous species was selected for further analysis because it was the only one which also had experimental data on $[\Delta\overline{G}^o]$ to elevated temperatures and pressures. The third column of Table 2.1 reflects the least squares fit of $[c_1]$, $[c_2]$, and $[\omega_{\mathrm{Pr},Tr}]$ to the apparent molal heat capacity data using the $[a_3]$ and $[a_4]$ values of column 4. These last two parameters were initially included in the regression but $[\overline{C}_P^o]$ was found to be relatively insensitive to them. Column 4 reports the values of $[a_1]$, $[a_2]$, $[a_3]$, $[a_4]$, and $[\omega_{\mathrm{Pr},Tr}]$ values obtained by regressing $[\sigma]$, $[\xi]$, and $[\omega_{\mathrm{Pr},Tr}]$ on the apparent molal volume data. Inspection of Table 2.1 reveals that the Born parameter is twice as large for this second scenario.

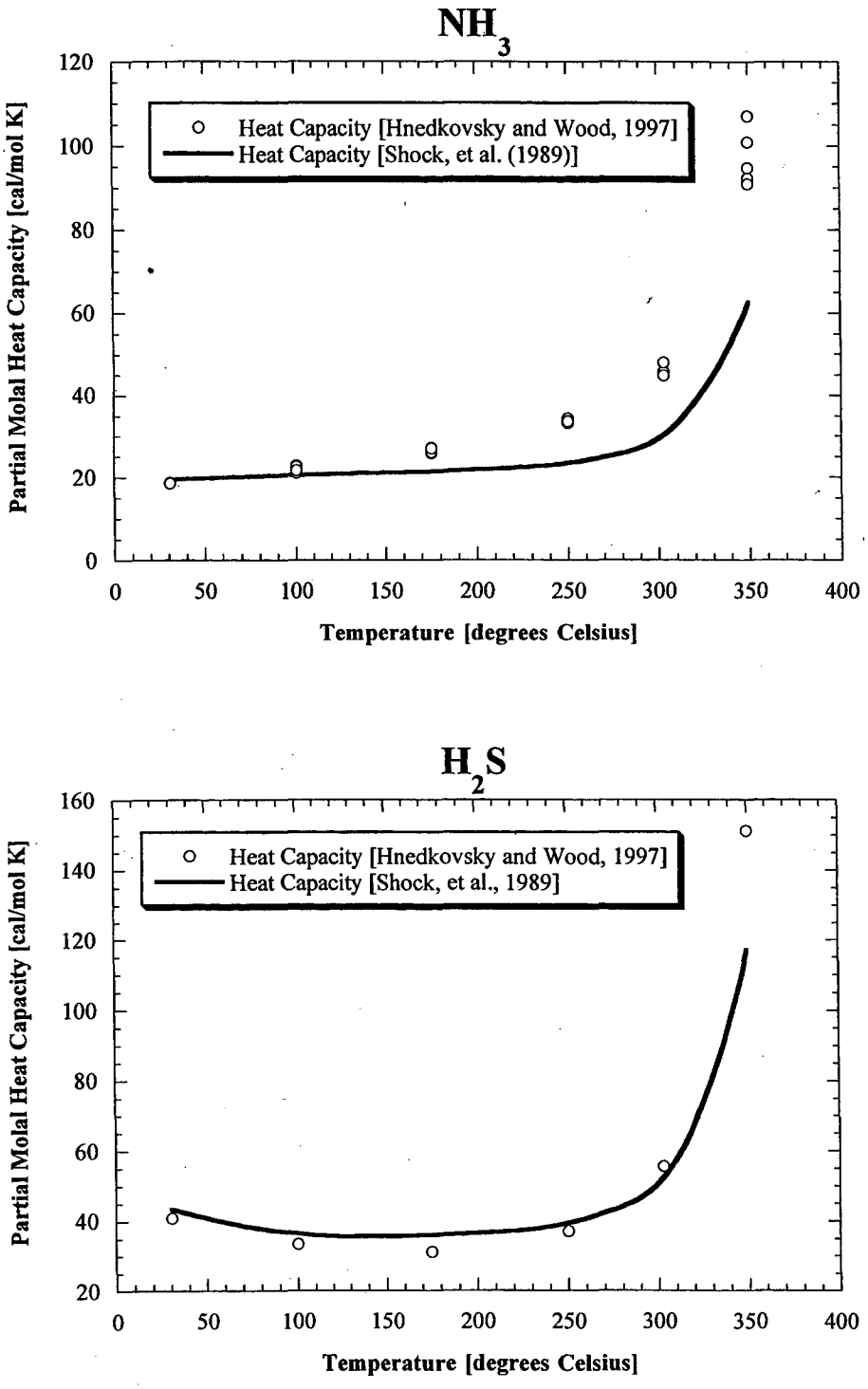

Figure 2.4 Comparison between experimental partial molal heat capacities to predictions of Shock, et al. (1989) for a) NH_3(aq) and b) H_2S(aq).

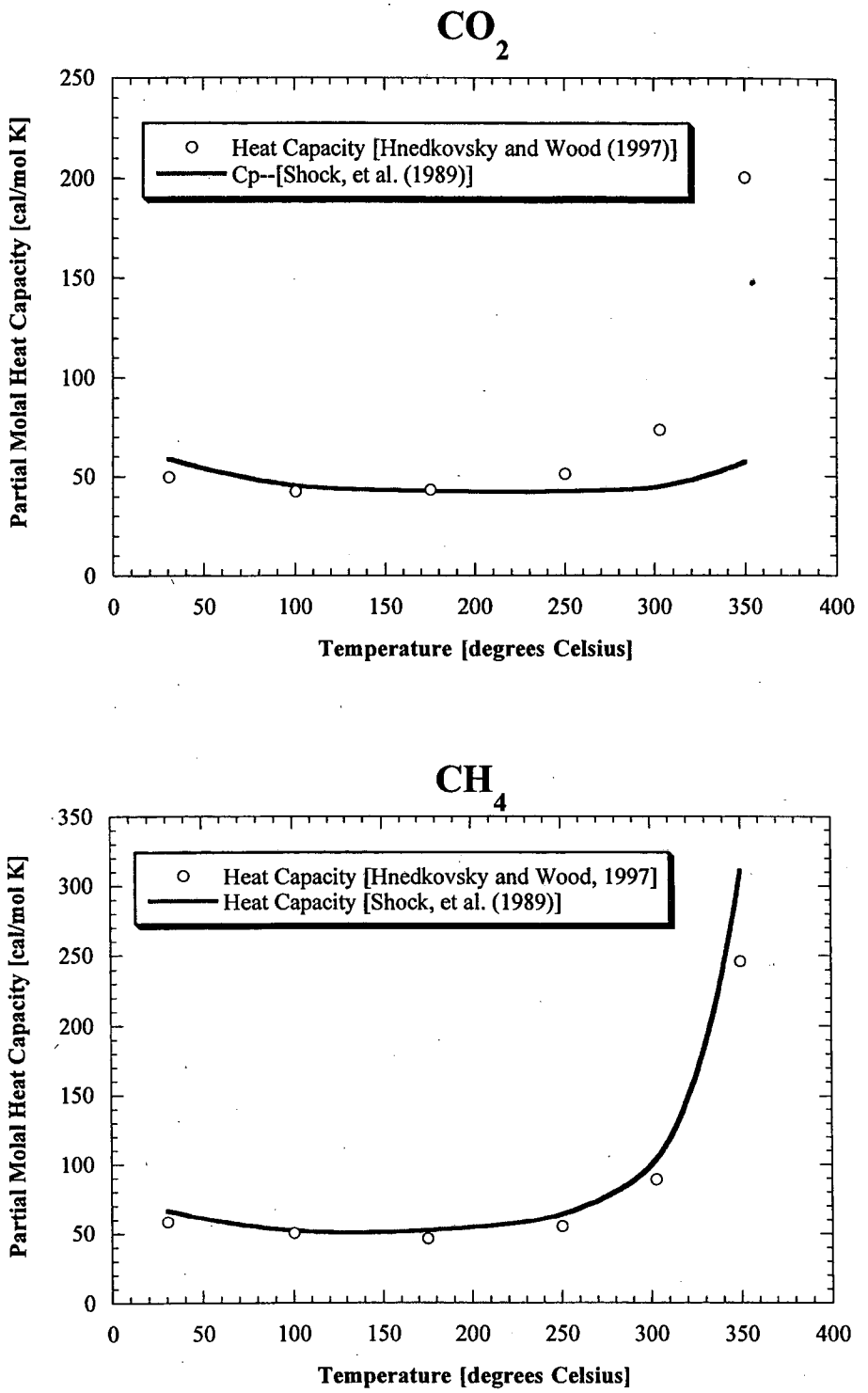

Figure 2.4 Comparison between experimental partial molal heat capacities to predictions of Shock, et al. (1989) for c) CO_2(aq) and d) CO_4(aq).

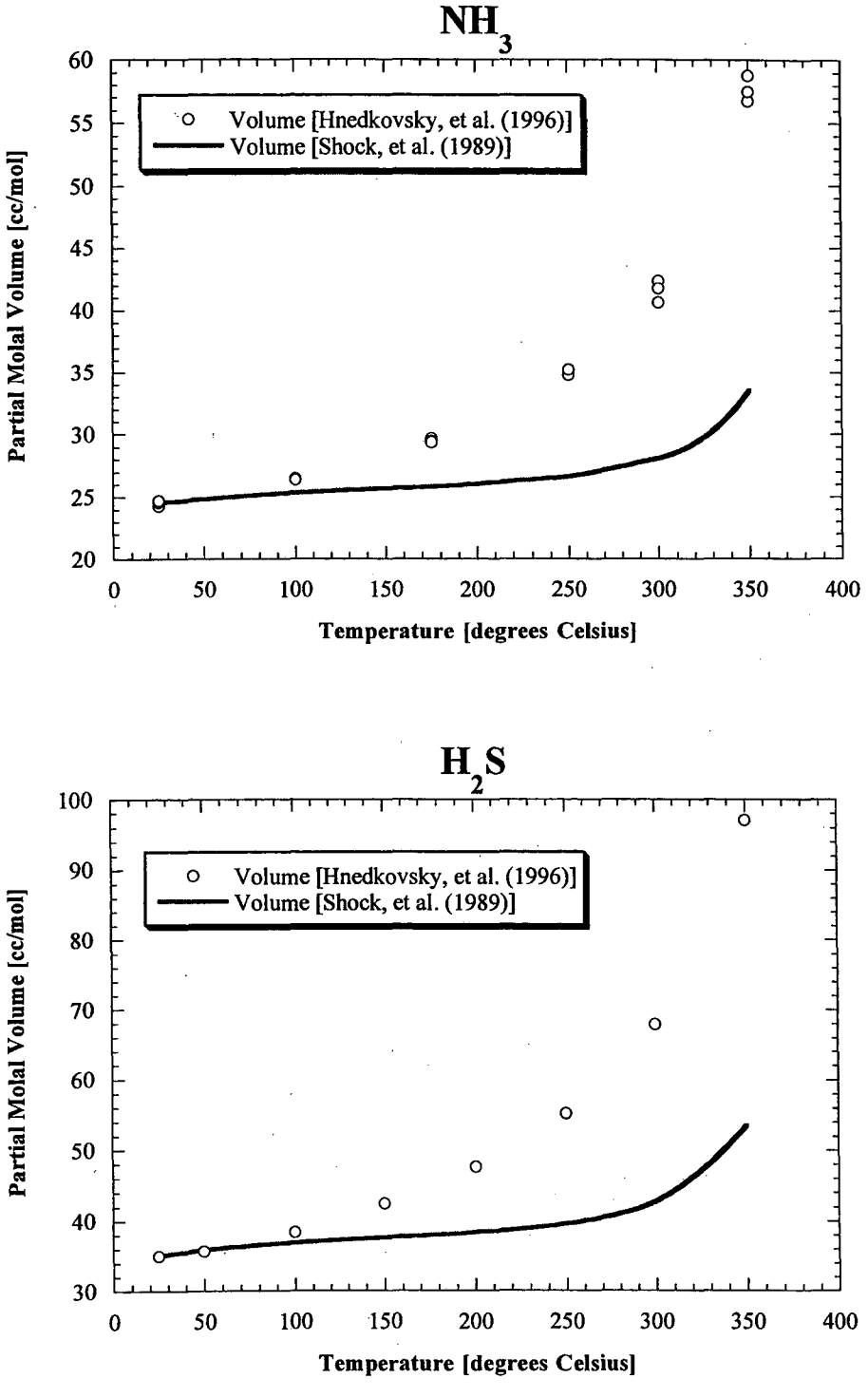

Figure 2.4 Comparison between experimental partial molal volumes to predictions of Shock, et al. (1989) for e) $NH_3(aq)$ and f) $H_2S(aq)$.

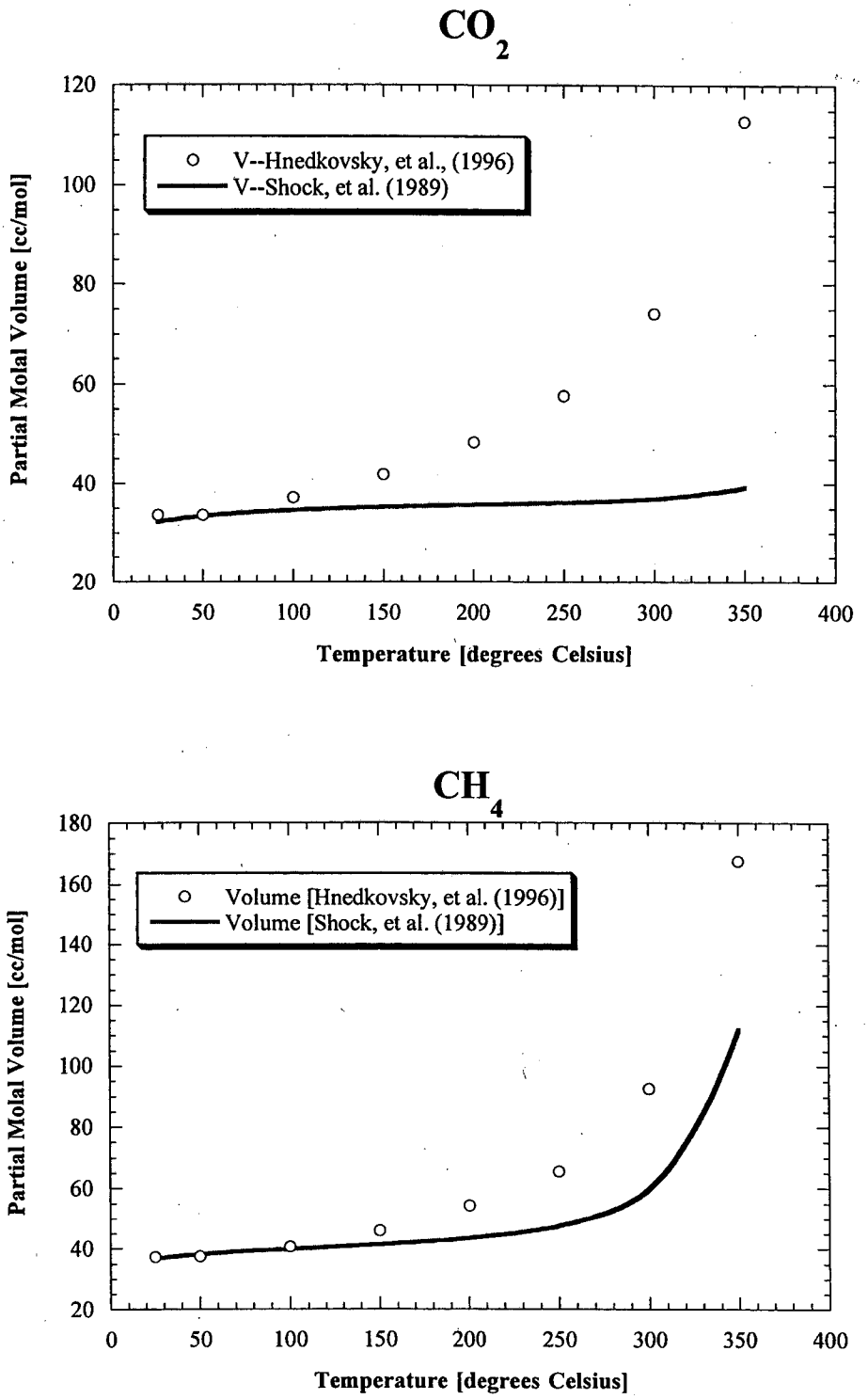

Figure 2.4 Comparison between experimental partial molal volumes to predictions of Shock, et al. (1989) for g) CO_2(aq) and h) CO_4(aq).

HKF regression parameter	Shock, et al. (1989)	This study w = -0.08	This study w = -0.16
a1	5.0911	5.029703	5.029703
a2	2.7970	6.922068	6.922068
a3	8.6248	-2.166642	-2.166642
a4	-2.8946	-3.065158	-3.065158
c1	20.3	26.722594	6.912175
c2	-1.17	-5.881137	4.650205
w	-0.05	-0.08521	-0.163632

Table 1.1 Comparison of the HKF equation of state regression parameters for NH_3(aq).

The results of the HKF regression analysis are displayed in Figures 2.5.a and 2.5.b for the apparent partial molal heat capacity and volume, respectively. The heat capacity data is well represented by the HKF equation of state parameters of Table 2.1 ($\omega_{Pr,Tr}$=-0.08), but application of these parameters to the apparent partial molal volume data resulted in a poor fit. In fact, not even the least squares fit parameters to the apparent partial molal volume data ($\omega_{Pr,Tr}$=-0.16) described this data set accurately. Although additional attempts were made to reconcile the conflicting curves generated by the HKF parameters of Table 2.1 by iterating over the volume and heat capacity equations (2.30) and (2.31) simultaneously, no satisfactory resolution was found.

2.4.2 Possible corrections to the HKF equation of state

Based on the correlation between the Born and Onsager equations (Figure 2.3) and the discrepancy between the predictions of Shock, et al. (1989) and the high temperature data of Hnedkovsky, et al. (1996) and Hnedkovsky and Wood (1997) (Figure 2.4), it was postulated that neutral aqueous species also required a correction for dielectric saturation and compressibility. To test this hypothesis, a g-correction was incorporated into the Born parameter, making it a function of the form:

$$\omega = \omega_{Pr,Tr} + g \tag{2.52}$$

where the g-function contained six regression parameters [a^{I}], [a^{II}], [a^{III}], [b^{I}], [b^{II}], and [b^{III}]:

$$g = \left(a_g^{I} + a_g^{II}T + a_g^{III}T^2\right)\left(1.0 - \hat{\rho}\right)^{\left(b_g^{I} + b_g^{II}T + b_g^{III}T^2\right)} \tag{2.53}$$

identical to the g-function proposed by Shock, et al. (1992).

Least square fits to the NH_3(aq), H_2S(aq), CO_2(aq), and CH_4(aq) data of Hnedkovsky, et al. (1996) and Hnedkovsky and Wood (1997) were calculated after first making initial guesses of the regression parameters of equations (2.52) and (2.53) using the HKF parameters of Shock, et al. (1989). Next, nonlinear regression calculations were performed using a Newton-

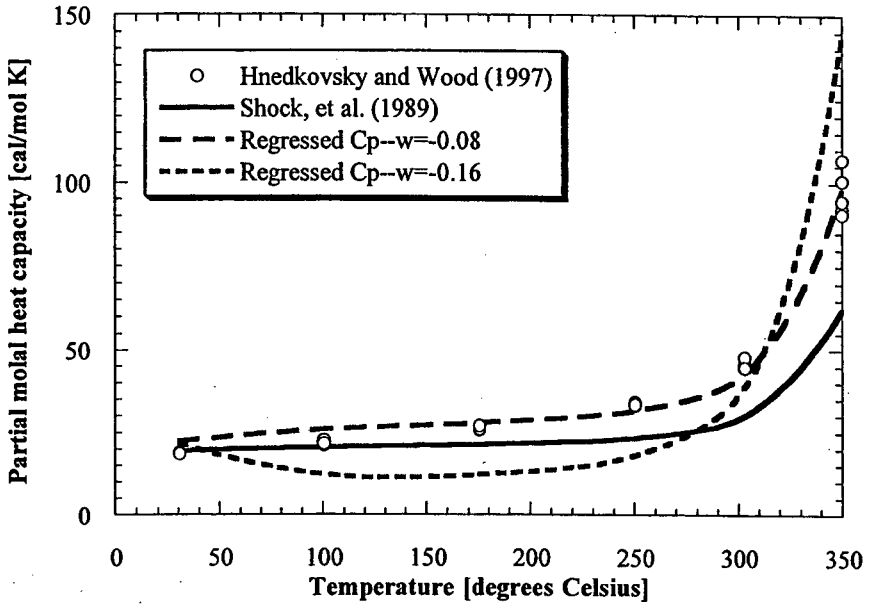

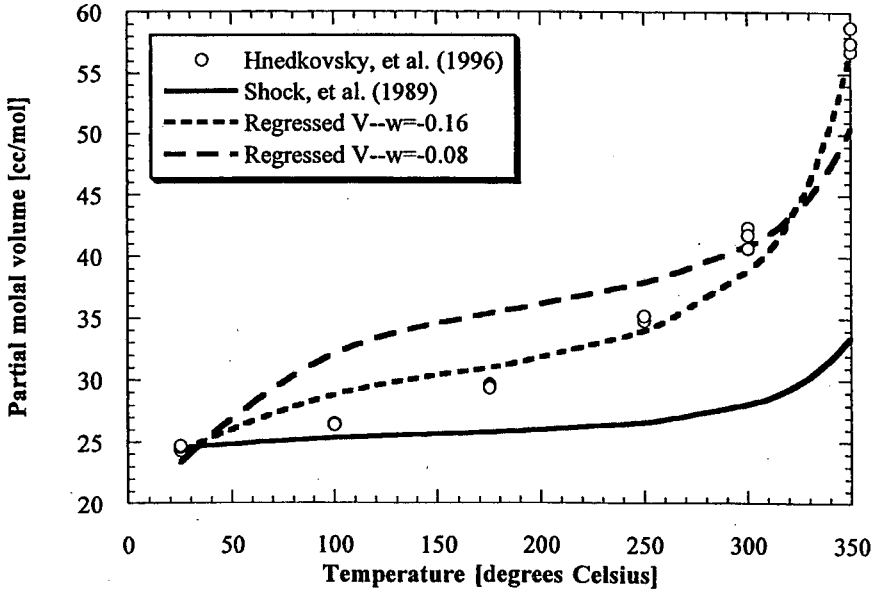

Figure 2.5 Comparison of measured partial molal thermodynamic properties for NH3(aq) to the predictions of Shock, et al. (1989) and this study. a) Partial molal heat capacity is best fit by a Born term equal to -0.08. b) Partial molal volume is best fit by a Born term equal to -0.16. Using this value to predict the partial molal heat capacity results in a poor fit to the experimental data.

Raphson technique over the apparent molal heat capacity and volume data to get least square estimates of the regression parameters consistent with experimental results. For NH_3(aq) and H_2S(aq), attempts were additionally made to reconcile the g-function correction with experimental [$\Delta\overline{G}^o$] data reported by Quist and Marshall (1968) and Suleimeniv and Krupp (1994) respectively. This was done iteratively by first calculating the regression parameters of equation (2.53) as before and then revising [$\omega_{Pr,Tr}$] using equation (2.29), [σ] and [ξ] using equation (2.30), and [c_1] and [c_2] using equation (2.31), until convergence was reached.

Unfortunately, iterations for NH_3(aq) and H_2S(aq) were terminated without ever achieving convergence. After 12 iterations, not only did finding an initial approximation for NH_3(aq) become extremely difficult, but the Born parameter [$\omega_{Pr,Tr}$] was already at 1.28 cal/mol, which is greater than Na^+ (0.33) and is nearly the same as Cl^- (1.44) (Johnson, et al., 1992). The problem with finding an initial approximation was that the solution to the equations had multiple roots and iterations often converged on a local minimum instead of the global minimum. Although alternative methods for generating an initial approximation (e.g. simulated annealing approaches (Laarhoven Aarts, 1987) could have been used, the high relative value of the Born parameter had already called into question the theoretical validity of the correction.

Figure 2.6 shows the partial molal heat capacity and volume data versus the revised HKF equation of state predictions. For the cases of NH_3(aq) and H_2S(aq) the results represent only the first iteration. The fits are generally good for the heat capacity and volume; however divergence in the predicted standard partial molal Gibbs free energy for NH_3(aq) began below 200°C at P_{sat} and approached 0.3 log units at 350°C (Figure 2.7). Despite the fact that the value of the g-function for this case was only -0.01 cal/mol at 350°C, compared to a Born parameter of -0.05 cal/mol, the divergence was due to the fact that the Gibbs free energy is more sensitive to the g-function correction because its coefficient in equation (2.29)

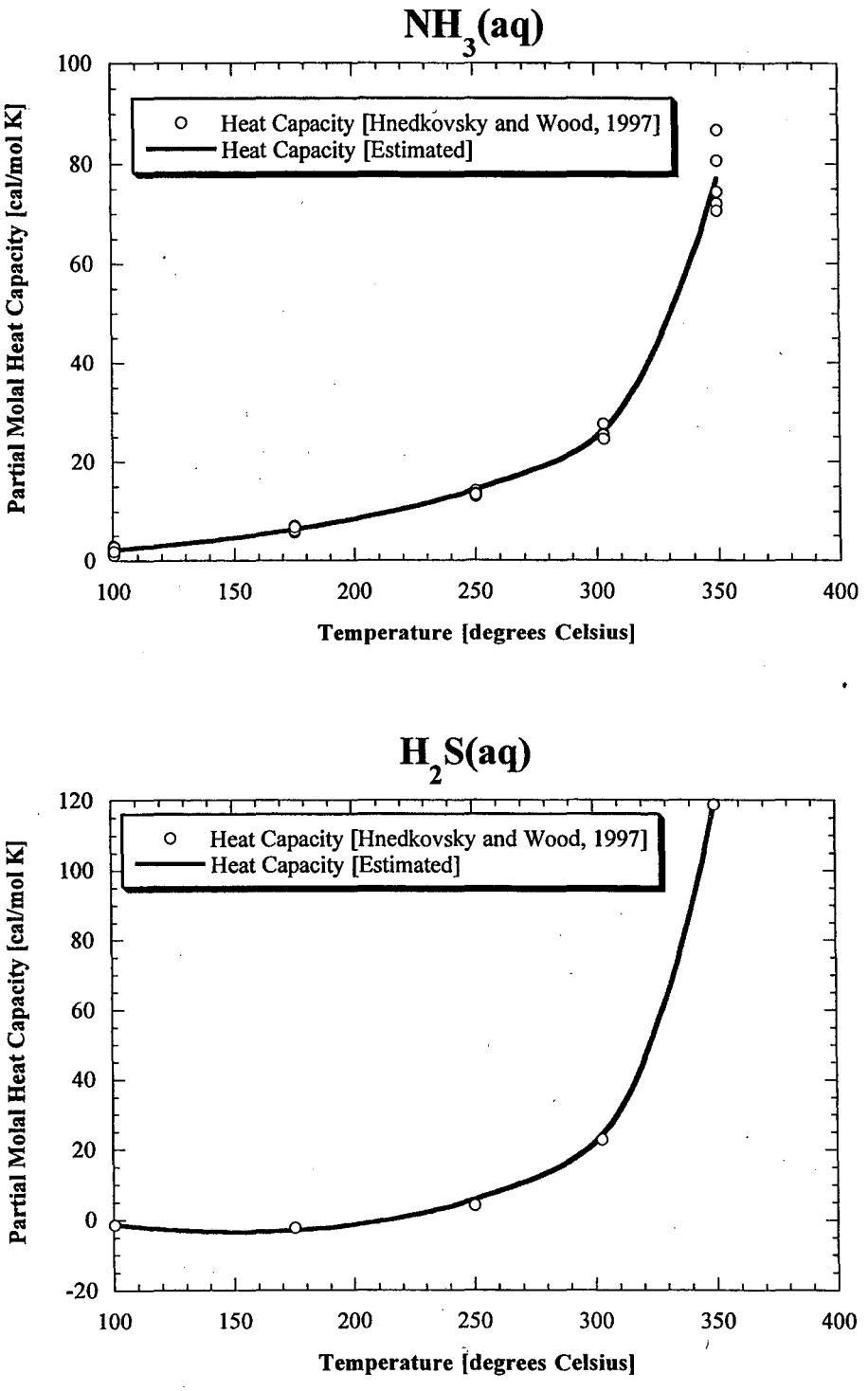

Figure 2.6 Comparison between experimental partial molal heat capacities to predictions of this study for a) $NH_3(aq)$ and b) $H_2S(aq)$.

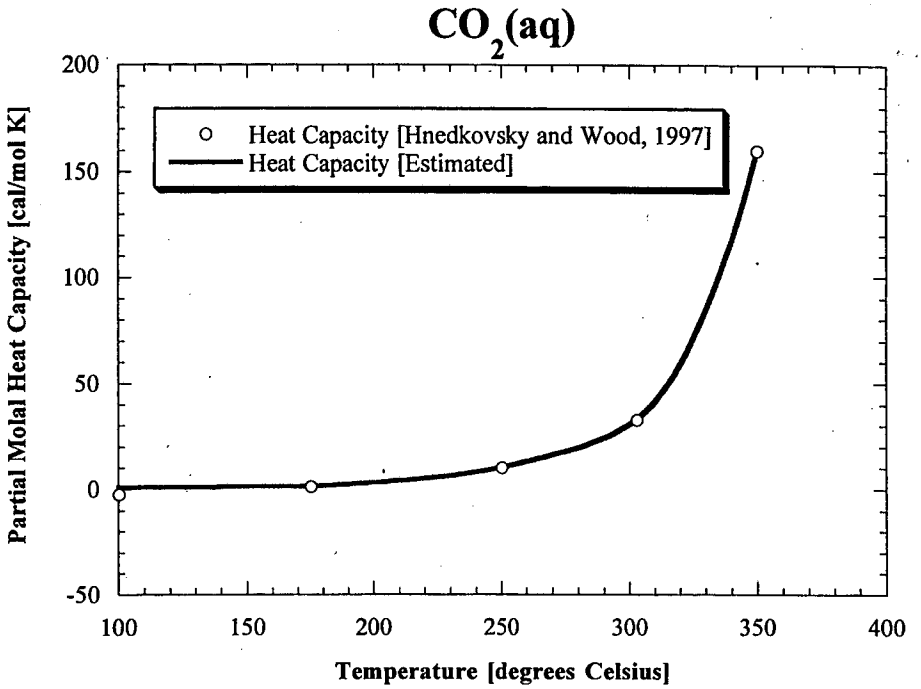

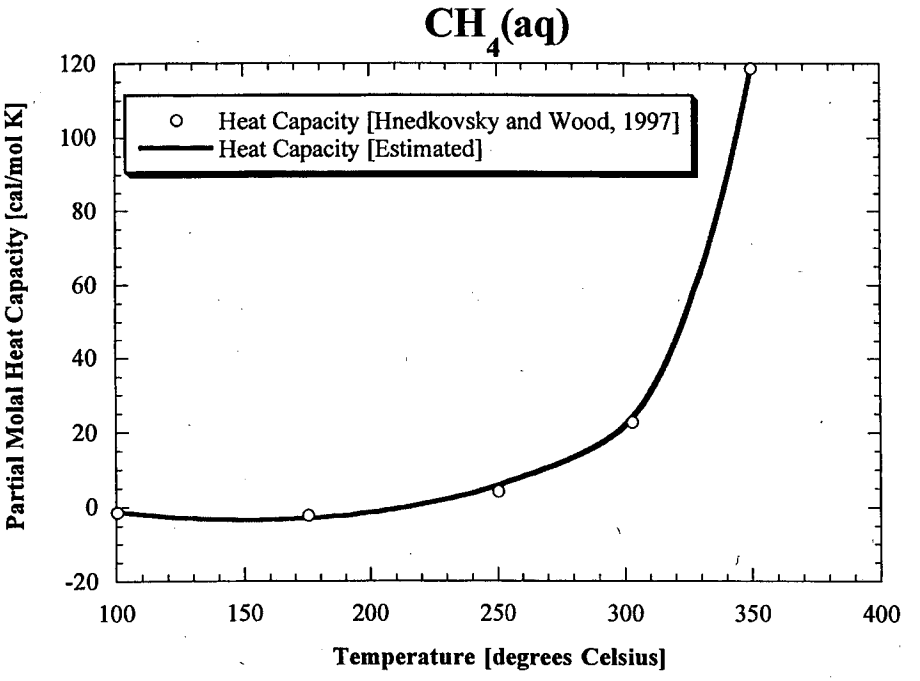

Figure 2.6 Comparison between experimental partial molal heat capacities to predictions of this study for c) CO_2(aq) and d) CO_4(aq).

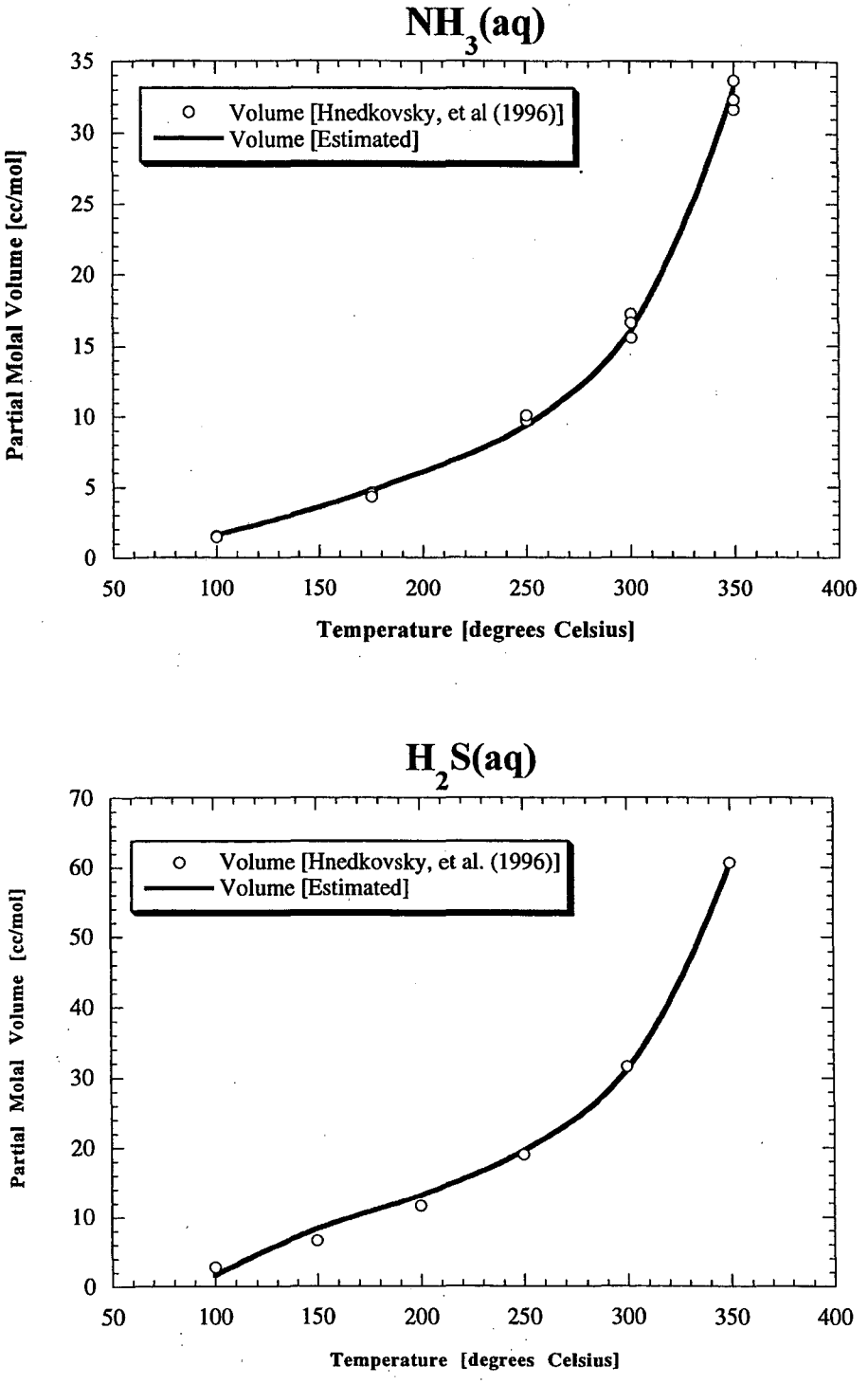

Figure 2.6 Comparison between experimental partial molal volumes to predictions of this study for e) $NH_3(aq)$ and f) $H_2S(aq)$.

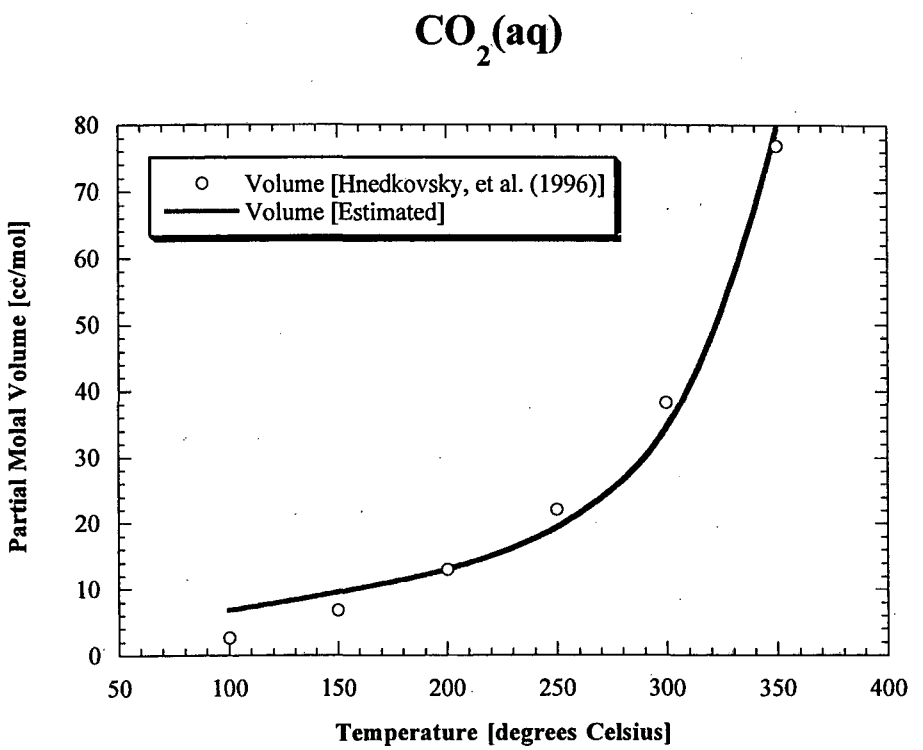

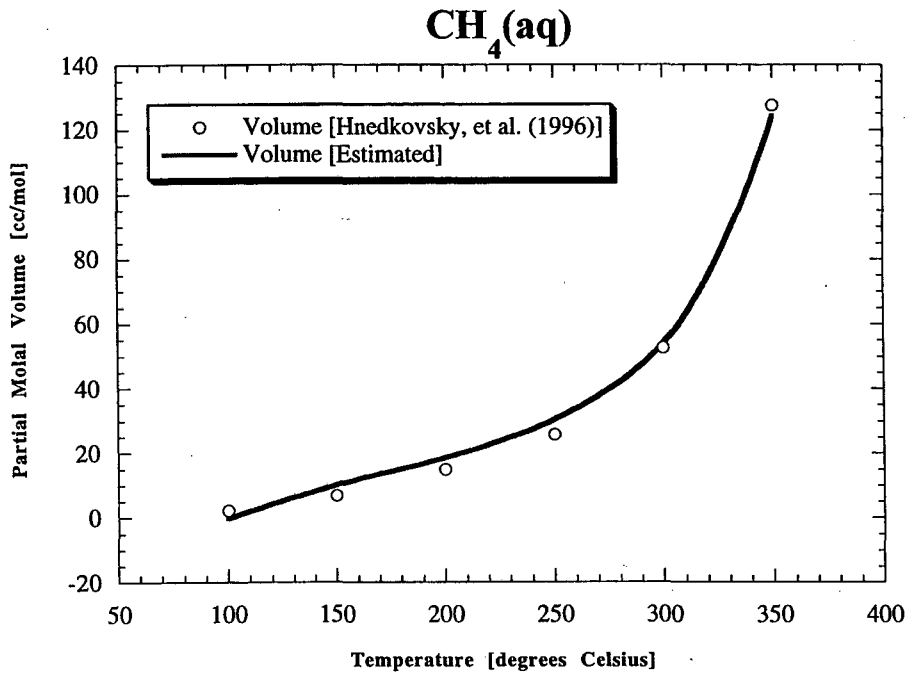

Figure 2.6 Comparison between experimental partial molal volumes to predictions of this study for g) CO_2(aq) and h) CO_4(aq).

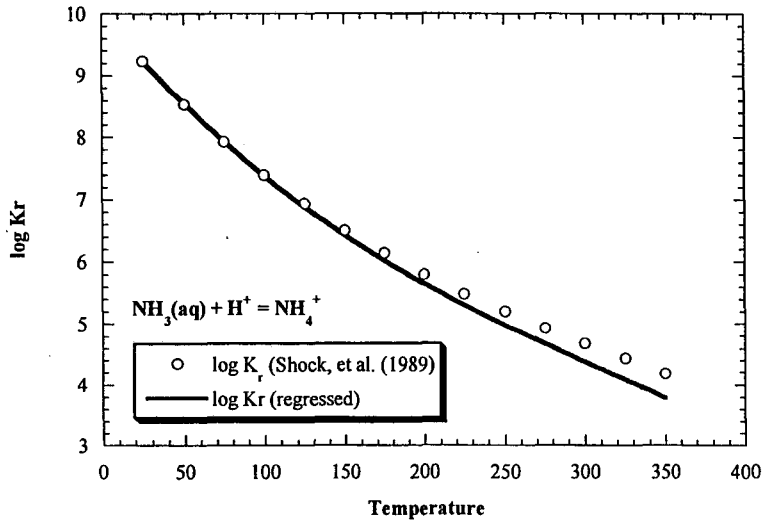

Figure 2.7 Equilibrium constant for the reaction shown in the figure. The predictions of Shock, et al. (1989) match the data of Quist and Marshall (1968) well, consequently they were used to represent a "good" fit in thi study. The prediction using the g-correction in this study underestimated the equilibrium constant.

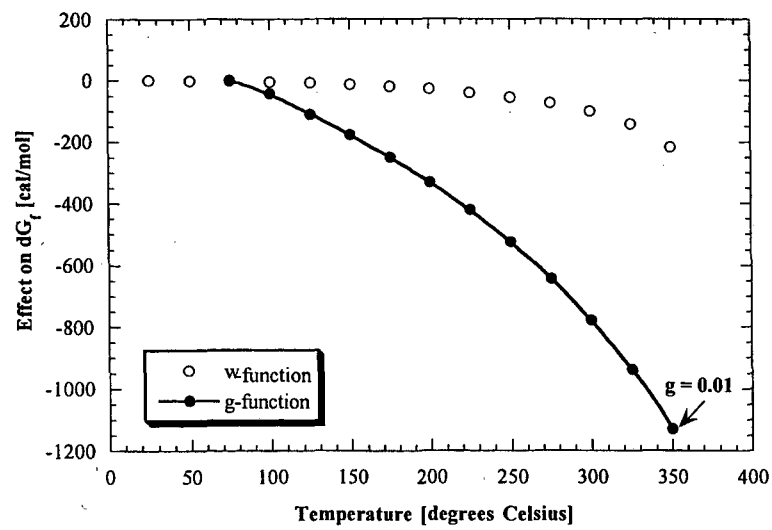

Figure 2.8 Comparison between the effect of the Born function and g-function on the standard partial molal Gibbs free energy in equation (6.29). Even though the g-function was smaller in magnitude than the Born parameter at 350 degrees Celsius, its affect on the standard partial molal Gibbs free energy was larger (see text).

(calculated by substituting equation (2.52) into it) is much larger. Figure 2.8 illustrates this result graphically.

A final problem with the g-function correction described above is that it could not be made universal. The g-function parameters for NH_3(aq), H_2S(aq), CO_2(aq), and CH_4 (aq) are listed in Table 2.2 and displayed in Figure 2.9.a and 2.9.b as a function of temperature and pressure, respectively. The values follow a general trend, so an attempt to reconcile the g-functions was made by multiplying the g-function generated from the NH_3(aq) data by a constant and comparing the results to the apparent thermodynamic properties of H_2S(aq) (Figure 2.10). The heat capacity data is matched well, but the predicted volumes are too small.

2.4.3 Alternative equations of state

An alternative equation of state for the partial molal thermodynamic properties of neutral aqueous species was provided by Harvey, et al. (1991). Their approach was to first re-write Henry's constant in equation (2.10) in terms of the molar residual Helmholtz energy (i.e. the difference between the mixture's molar Helmholtz energy and that for a mixture of ideal gases):

$$RT\ln\left(k_H/f_1\right) = A_{x_2}^{r\infty} \tag{2.54}$$

where the subscripts [1] and [2] refer to the solvent and solute respectively, the superscript [∞] indicates infinite dilution conditions, and the subscript [x_2] indicates the partial derivative of the residual Helmholtz energy with respect to the mole fraction of the aqueous species [$\left(\partial A^r/\partial x_2\right)_{V,T}$]. They next expressed the residual Helmholtz energy as a Taylor's series expansion about the solvent's critical point to obtain the equation:

$$RT\ln\left(k_H/f_1\right) = A_{x_2}^{r\infty,c} + A_{x_2,V}^{r\infty,c}\rho_c^{-2}\left(\rho_1 - \rho_{c,1}\right)+... \tag{2.55}$$

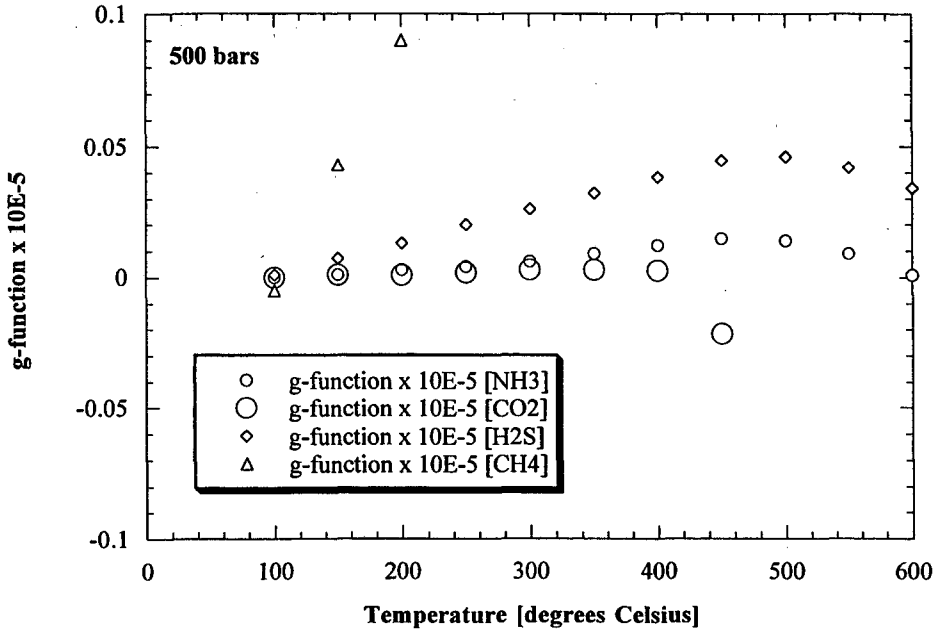

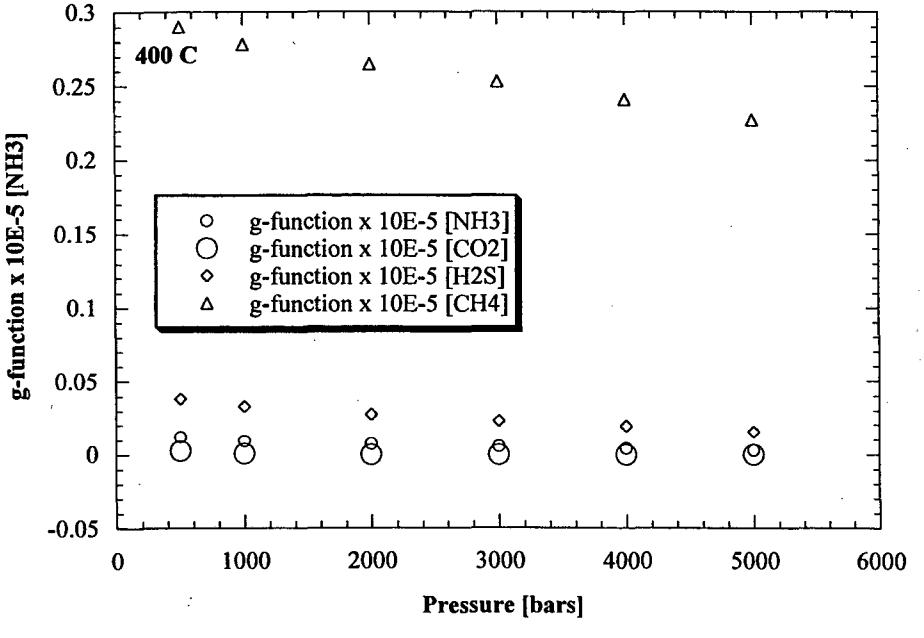

Figure 2.9 Comparison of the g-funtion for different neutral aqueous species as a: a) function of temperature at 500 bars; and b) function of pressure at 400 degrees Celsius.

	NH_3(aq)	H_2S(aq)	CO_2(aq)	CH_4(aq)
a'	-1831.7	-4002.9	2.22E+05	-12364
a''	24.647	47.558	-8.6541	119.01
a'''	-0.035309	-0.057864	-1.2475	-0.018105
b'	0.20801	0.11005	1.5619	0.022627
b''	0.004555	0.001783	0.007421	0.000261
b'''	-7.97E-06	-2.16E-06	2.39E-06	2.47E-09

Table 2.2 Regression parameters used in equation 6.53 to fit the apparent partial molal heat capacity and volume data of Hnedkovsky and Wood (1997) and Hnedkovsky, et al. (1996), respectively.

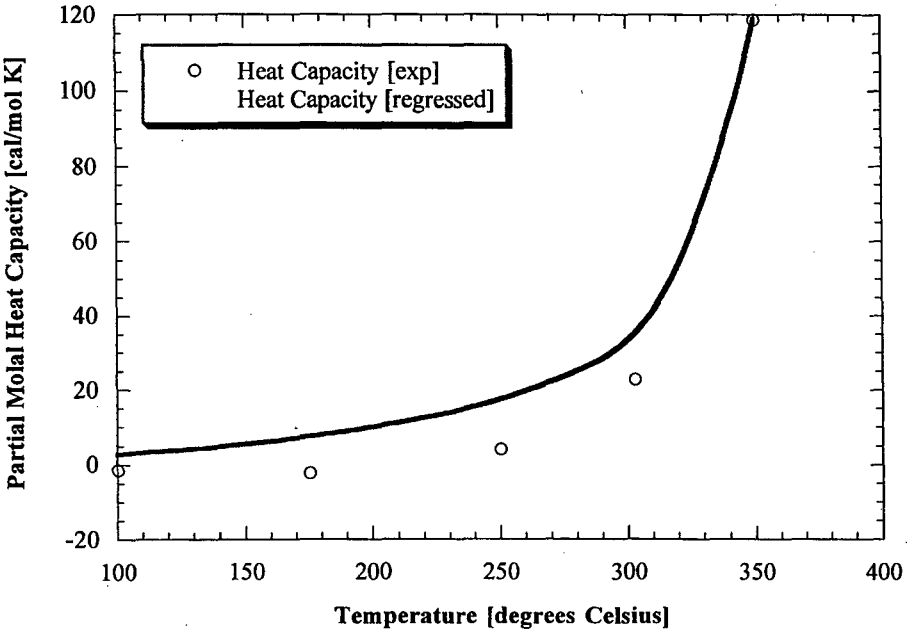

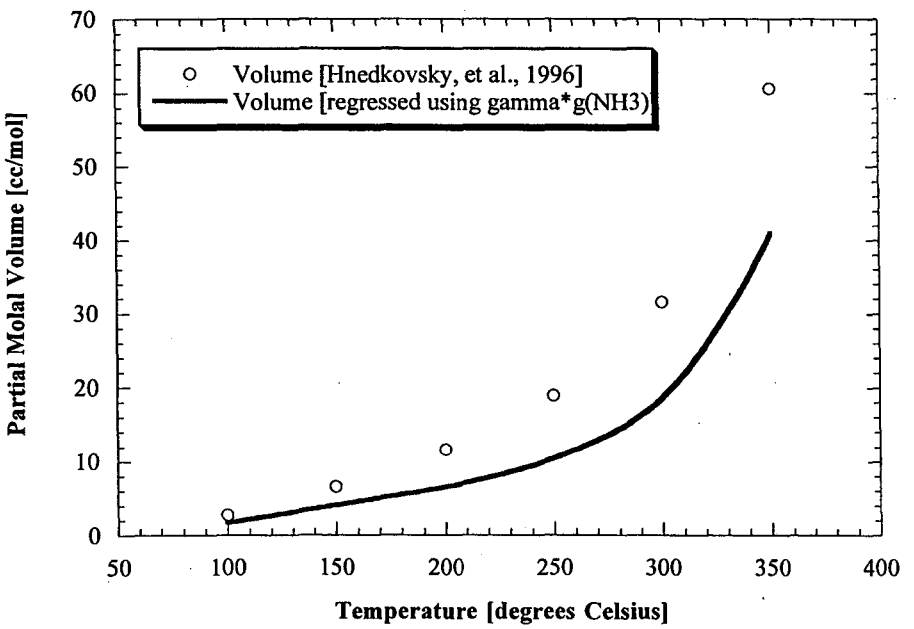

Figure 2.10 Comparison of the predicted and experimental partial molal heat capacity and volume for H_2S(aq) using the g-function for NH_3(aq) multiplied by a constant derived from a least squares fit to the data.

where the subscript $[c]$ indicates the property at its critical point. Finally, they replaced the constants in equation (2.55) by $[A]$ and $[B]$ and included an additional empirical parameter $[C]$ to account for nonsolvation effects:

$$RT\ln(k_H/f_1) = A + B(\rho_1 - \rho_{c,1}) + CT\rho_1 \exp[(273.15 - T)/50] \qquad (2.56)$$

Because the standard partial molal Gibbs free energy of hydration is given by:

$$\Delta\overline{G}^o = RT\ln k_H \qquad (2.57)$$

$[\Delta\overline{G}^o]$ was re-expressed using equation (2.56) to give:

$$\Delta\overline{G}^o = R\left[A + B(\rho_1 - \rho_{c,1}) + CT\rho_1 e^u\right] + RT\ln f_1 \qquad (2.58)$$

where $[u]$ is equal to $(273.15 - T)/50$. Of most importance to this study are the subsequent expressions for the standard partial molal volume and heat capacity:

$$\Delta\overline{V}^o = R(\partial\rho_1/\partial P)_T(B + CTe^u) + V_1; \qquad (2.59)$$

$$\Delta\overline{C}_P^o = -RT\left\{B\left(\frac{\partial^2\rho_1}{\partial T^2}\right)_T + Ce^u\left[2\left(\frac{\partial\rho_1}{\partial T}\right)_P(1 - T/50) - \left(\frac{\rho_1}{T}\right)(2 - T/50) + T\left(\frac{\partial^2\rho_1}{\partial T^2}\right)_T\right]\right.$$
$$\left. + 2\left(\frac{\partial(\ln f_1)}{\partial T}\right)_P + 2T\left(\frac{\partial^2(\ln f_1)}{\partial T^2}\right)_P\right\} \qquad (2.60)$$

To test this alternative equation of state against the experimental results of Hnedkovsky, et al. (1996) and Hnedkovsky and Wood (1997), a regression analysis was performed on equations (2.59) and (2.60). Because both of these equations required calculation of the fugacity of water, the first step in the regression calculations was to estimate the fugacity and its derivatives. This was done using the relationships:

$$RT\ln(f_1/f_1^o) = \Delta G_{T,P} - \Delta G_{T,1bar}^o \qquad (2.61)$$

where $[\Delta G_{T,1bar}^o]$ is given by:

$$\Delta G_{T,1bar}^o = \Delta G_{T,1bar} - RT\ln\chi_{T,1bar} \qquad (2.62)$$

and where $[\chi_{T,1bar}]$ is the fugacity coefficient of water at a pressure of 1 bar (Fletcher, 1993). The $[\Delta G_{T,P}]$ in equation (2.61) was derived from the HGK equation of state for water (Haar, et al., 1984) and the fugacity coefficient in equation (2.62) was calculated from the equations of Hass (1970). Although the latter equations are only strictly applicable to 350°C, the comparison of the fugacity calculated in this manner to the method of Helgeson and Kirkham (1974) to 1000°C shows excellent agreement (Figure 2.11). Once the fugacity was known at any particular pressure and temperature, the first and second derivatives were obtained using a five-point numerical estimation (Burden and Faires, 1989).

According to Figure 2.12 the apparent partial molal volumes can be predicted reasonably well with equation (2.20), but Figure 2.13 suggests that the heat capacity cannot. This figure depicts a fit of equation (2.60) with and without including the fugacity terms (the dashed and solid lines, respectively). Although neither fit is satisfactory, incorporation of the fugacity term makes the solution strongly divergent at low temperatures. Inspection of the partial derivatives of the fugacity of water with respect to pressure and temperature reveals that the problem at low temperatures is that the first and second derivatives asymptote towards positive and negative infinity, respectively, with the first derivative dominating equation (2.60) (Figure 2.14). Consequently, this equation of state is not an acceptable alternative.

2.4.4 Recommendations

Additional attempts were made to combine elements of the HKF equation of state with the equations in *Section 2.4.3*, but no satisfactory equation of state was derived which accurately reflected the apparent molal volumes and heat capacities of NH_3(aq), H_2S(aq), CO_2(aq), and CH_4(aq) reported by Hnedkovsky, et al. (1996) and Hnedkovsky and Wood (1997). Because the most important partial molal thermodynamic property to this study was $[\Delta\overline{G}^o]$, and based on the accurate prediction of this property using the underestimated partial derivative function $[\overline{C}_P^o]$ and $[\overline{V}^o]$ for NH_3(aq) (Figure 2.15), the remaining sections of this

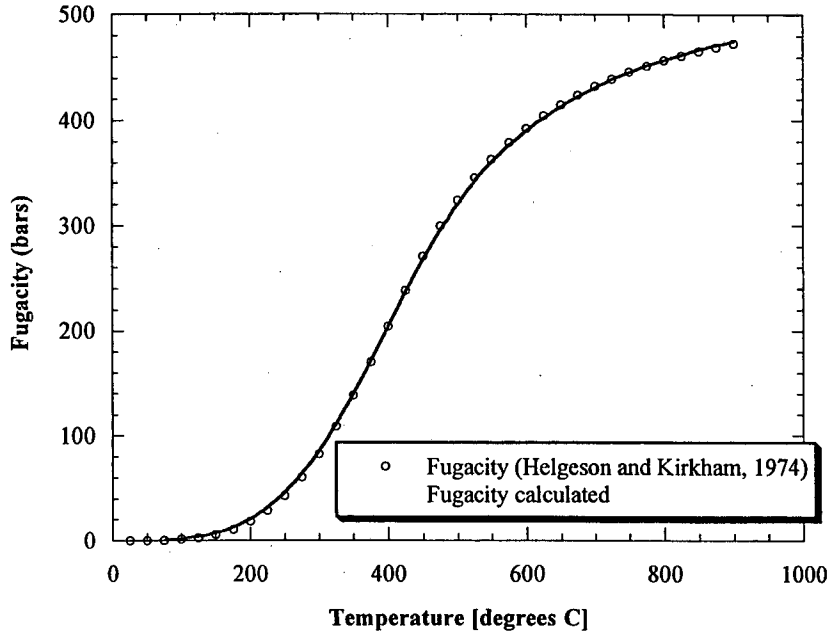

Figure 2.11 Comparison of the fugacity of water calculated from the equations of Hass (1970) to the predictions of Helgeson and Kirkham (1974) at 500 bars pressure.

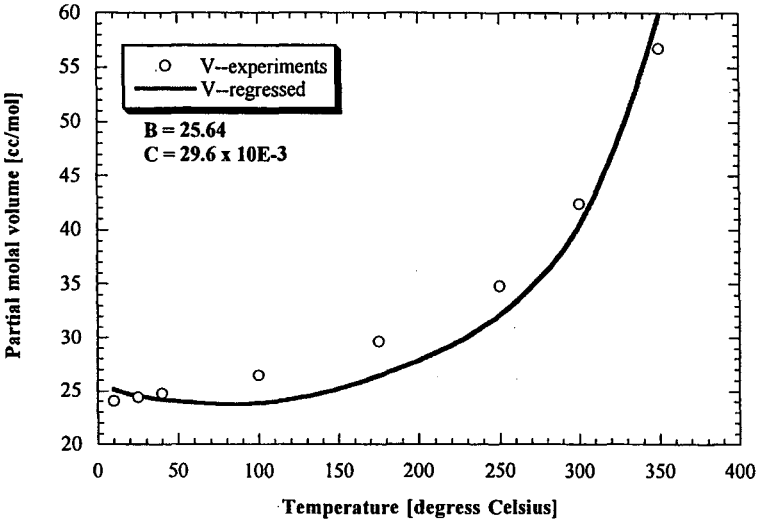

Figure 2.12 Comparison of the experimentally-derived partial molal volume of NH_3(aq) to predictions using the equation of state of Harvey, et al. (1991).

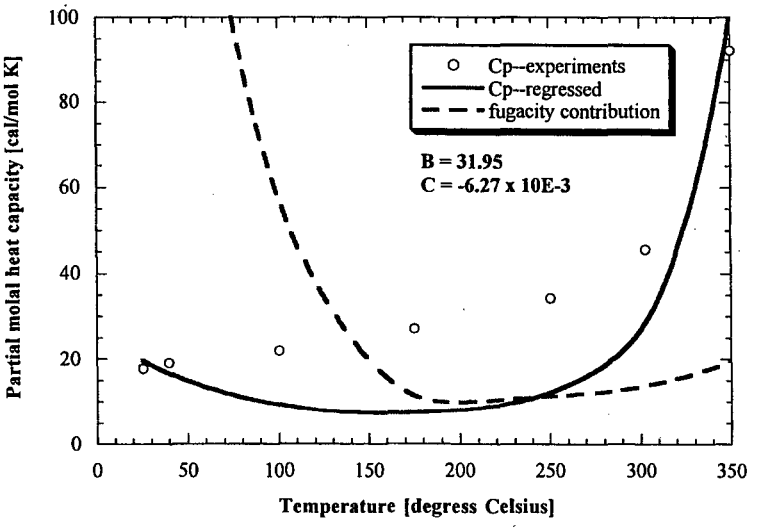

Figure 2.13 Comparison of the experimentally-derived partial molal heat capacity of NH_3(aq) to predictions using the equation of state of Harvey, et al. (1991). The solid line is the least squares fit without incorporating the fugacity term. The dashed line represents the fugacity term's strong deviation at low temperatures.

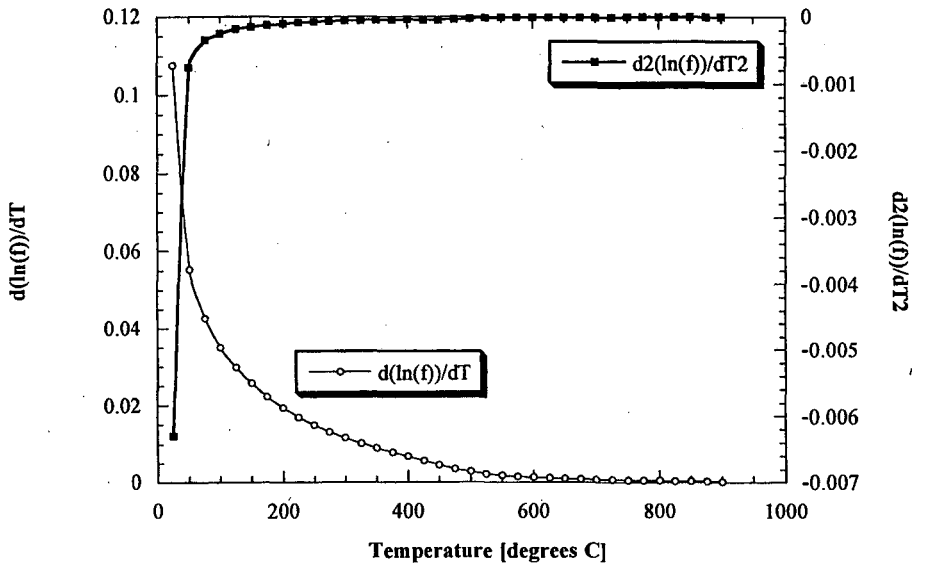

Figure 2.14 Comparison of the first and second derivative of the fugacity of water with respect to temperature.

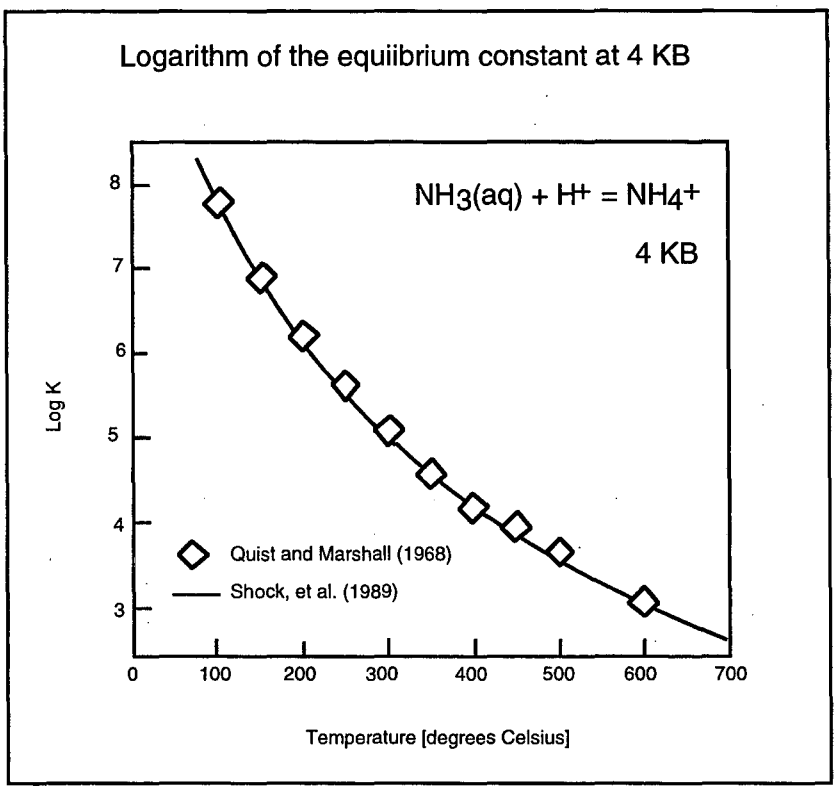

Figure 2.15 Comparison of the predictions of Shock, et al. (1989) to the experimental results of Quist and Marshall (1968) at a pressure of 4 kbars. The predictions are independent of the measurements shown in the figure, and were instead derived along the vapor saturation curve of water.

dissertation utilized the HKF equation of state for neutral species, recognizing future modifications are warranted. To minimize uncertainty in the estimated $[\Delta\overline{G}^o]$ for volatile neutral species, the data of Hnedkovsky, et al. (1996) and Hnedkovsky and Wood (1997) were omitted, and the approach taken to derive their thermodynamic properties was identical to that adopted by Shock, et al. (1989).

CHAPTER 3. Thermodynamic properties of gold, arsenic, and antimony minerals and aqueous species

3.1 Introduction

Considering the reducing conditions and low salinity (≈5 wt. % NaCl from Table 1.1) observed in ore stage fluid inclusions, sulfide and hydroxide complexes were the most likely transporting agents for Au, As, and Sb in the Carlin-type gold deposits. Hayashi and Ohmoto (1991) showed that chloride complexing of gold at 300°C is favored only above the $H_2S(aq)$-SO_4^{2-} isoactivity boundary for $\Sigma S = 0.01$ *m* and $\Sigma Cl = 1.0$ *m*. Also, Nagakawa (1971) and Ovchinnikov, et al. (1982) showed that chloride complexes of arsenic and antimony are unimportant under similar conditions.

In this chapter the available thermodynamic data for the Au, As, and Sb minerals are reviewed and the HKF equation of state parameters for the hydroxide and sulfide complexes calculated. *Sections 3.1* and *3.2* describe the revised HKF of state parameters for $H_2S(aq)$ and HS^-. *Sections 3.3-3.5* subsequently review the updated parameters for Sb, As, and Au hydroxide and sulfide complexes. Finally, estimates of the importance of Au heteropolynuclear complexes are estimated in *Section 3.6*.

3.2 HKF parameters for $H_2S(aq)$

$H_2S(aq)$ was an extremely important aqueous component in the Carlin-type gold deposits as indicated by the nearly perfect correlation between Au solubility and aqueous H_2S concentration in Figure 1.10. Although the HKF equation of state parameters for this species were previously derived by Shock, et al. (1989), the limitations of the HKF equation of state discussed in the preceding chapter and new high temperature $H_2S(g)$ solubility data reported by Suleimenov and Krupp (1994) necessitated a re-evaluation.

Figure 3.1 displays the Henry constant data for H_2S as a function of temperature from the studies of Winkler (1906), Selleck, et al. (1952), Kozintseva (1964), Clarke and

Glew(1970), Lee and Mather (1977), Drummond (1981), Barrett, et al. (1988), and Suleimenov and Krupp (1994). Shock, et al. (1989) restricted their regression calculations to the equilibrium constant data of Drummond (1981) and Kozintseva (1964) for the reaction:

$$H_2S(g) = H_2S(aq) \qquad (3.1)$$

and the heat capacity and volumetric measurements of Barbero, et al. (1982). Using equations (2.29), (2.31), and (2.35), they obtained the $[c_1]$, $[c_2]$, and $[\omega]$ parameters listed in Table 3.1 by regression after first setting $[a_1] = [a_2] = [a_3] = [a_4] = 0$, assuming that the $[a]$-terms are negligible along the water vapor saturation curve. $[a_1]$ through $[a_4]$ were then obtained from equations (2.24), (2.42), and (2.43) after calculating $[\Delta\overline{V}_n^o]$ from equations (2.23) and (2.45).

Because both Drummond (1981) and Kozintseva (1964) utilized stainless steel autoclaves in their experiments, with the former reporting the formation of iron sulfide and hydrogen gas due to corrosion of the vessel, it is likely that the Henry constants used by Shock, et al. (1989) were overestimated. Consequently, the HKF equation of state parameters were re-computed in this study utilizing the Henry constant data of Suleimenov and Krupp (1994) (who employed a titanium autoclave with gold coated seals and gaskets).

The first step in the calculations of this study was to obtain $[c_2]$ and $[\omega]$ from equations (2.29) and (2.35) using the values of Shock, et al. (1989) for all of the other equation of state parameters (these two parameters were selected because they were found to be the most sensitive at the highest temperatures where a modification was required). Next, $[a_1]$ through $[a_4]$ were re-computed in a manner analogous to Shock, et al. (1989) utilizing the updated value of $[\omega]$.

Predictions of $[\Delta\overline{G}_f^o]$, $[\overline{V}^o]$, and $[\overline{C}_{\mathrm{Pr}}^o]$ based on the revised equation of state parameters are compared to those of Shock, et al. (1989) in Table 3.1. Figure 3.2.a shows a difference of 0.1 log units between the predictions of this study and Shock, et al. (1989) for the log K_r of reaction (3.1) at 350°C and P_{sat}. Figure 3.2.b also illustrates a slight improvement in the

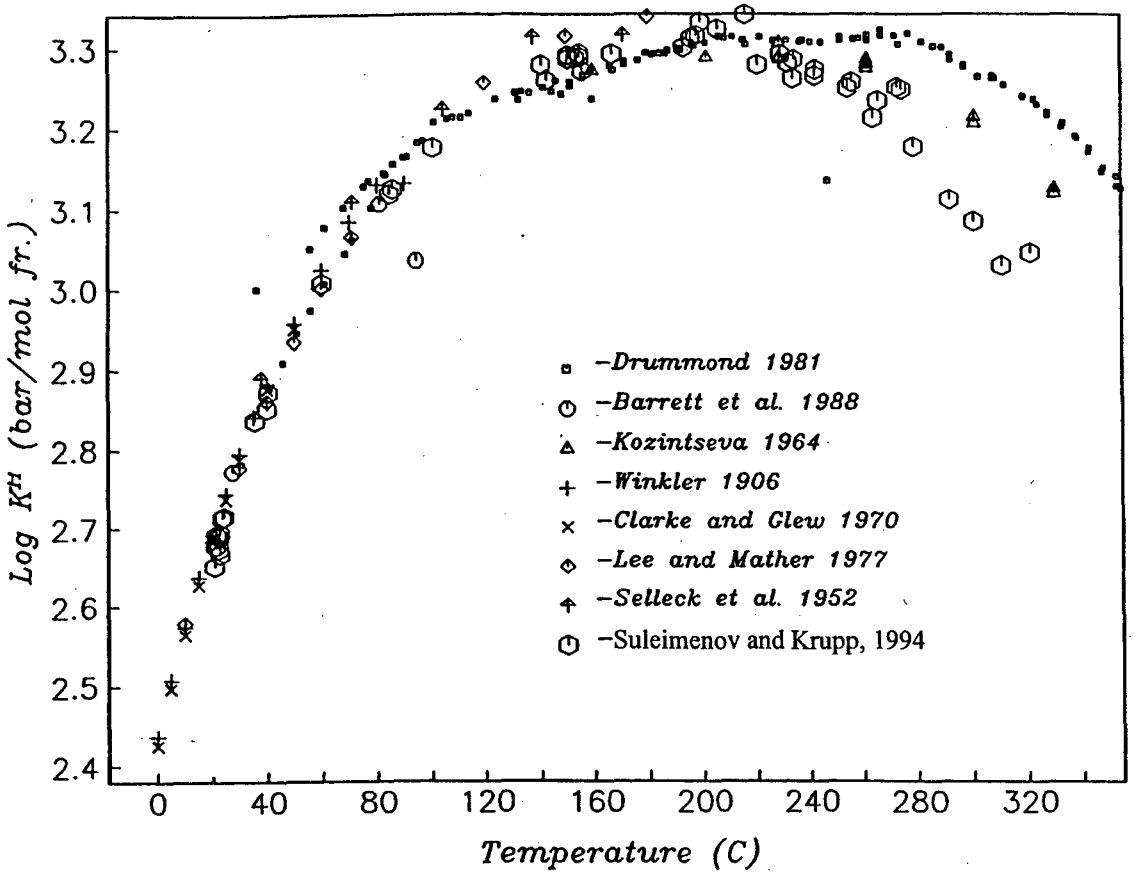

Figure 3.1 Experimental values of the Henry constants for H_2S (Suleimenov and Krupp, 1994).

Study	ΔG°_f[a]	ΔH°_f[a]	S°[b]	C_{pr}°[b]	V°[c]	σ[c]	ξ[d]
Shock, et al. (1989)	-6673[h]	-9001[i]	30.0[j]	42.7[k]	34.92[k]	38.13	-2.37
This study	-6673[h]	-9001[i]	30.0[j]	42.7[k]	34.92[k]	37.68 ±0.26	-2.32 ±0.16

Study	a_1[e] x 10	a_2[a] x 10^{-2}	a_3[f]	a_4[g] x 10^{-4}	c_1[b]	c_2[g] x 10^{-4}	ω[a] x 10^{-5}
Shock, et al. (1989)	6.5097	6.7724	5.9646	-3.0590	32.3[l]	4.73	-0.10
This study	6.4685	6.5969	6.1947	-3.0517	32.3[l]	4.1035 ±1.5152	-0.1774 ±0.0648

Table 3.1 Comparison of equations of state parameters and standard partial molal properties at 25° C and 1 bar for H_2S(aq) a. cal mol^{-1} b. cal mol^{-1} K^{-1} c. cm^3 mol^{-1} d. cm^3 K mol^{-1} e. cal mol^{-1} bar^{-1} f. cal K mol^{-1} bar^{-1} g. cal K mol^{-1} h. Calculated from values of log K at 25°C and 1 bar using standard partial molal Gibbs free energy of formation of the gas species taken from Wagman , et al. (1982) i. Calculated from values of the standard partial molal Gibbs free energy and entropy of formation using the standard entropy of the elements taken from Wagman, et al. (1982) j. Calculated from the temperature dependence of log K for reaction (7.1) using the standard entropy of the elements taken from Wagman, et al. (1982) k. Barbero, et al. (1982) l. Shock, et al. (1989)

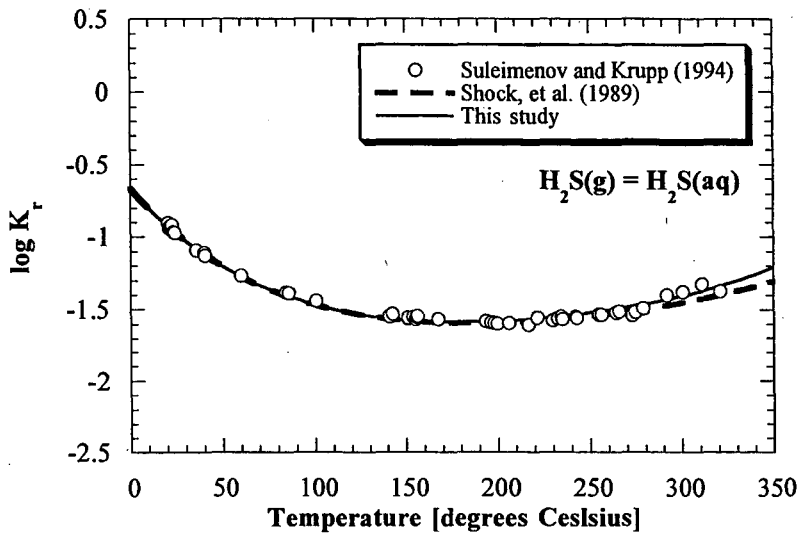

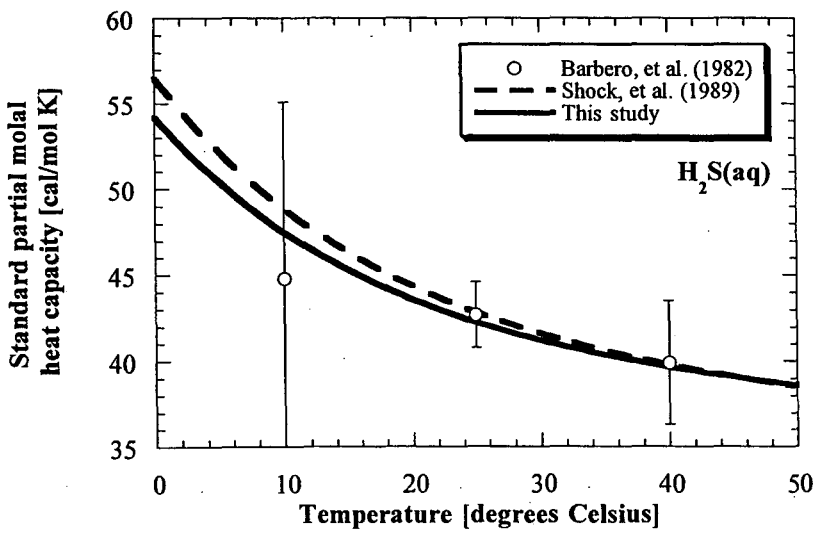

Figure 3.2 Comparison between predicted a) equilibrium constants for reaction (3.1) and b) standard partial molal heat capacities for H_2S(aq) derived in this study and by Shock, et al. (1989).

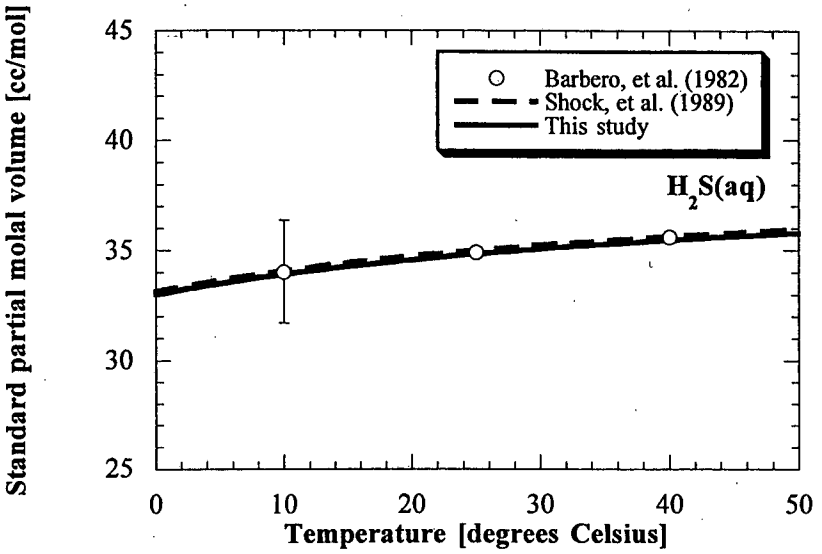

Figure 3.2 Comparison between predicted c) standard partial molal volumes for $H_2S(aq)$ derived in this study and by Shock, et al. (1989).

predicted values for [$\overline{C}^{o}_{Pr}$] at the lowest temperature. Finally, Figure 3.2.c shows that the predicted standard partial molal volume is relatively unchanged.

3.3 HKF parameters for HS-

The HKF equation of state parameters for the HS^- were originally derived by Shock and Helgeson (1988) using the heat capacity and volumetric measurements of Barbero, et al. (1982) and the volumetric measurements of Ellis and McFadden (1972). Their method was first to assume that the crystallographic radius of the HS^- ion [r_x] is approximately equal to that of S^{2-} taken from Pauling (1927). By making this assumption, they were then able to calculate [ω] via equation (2.28), the nonsolvation parameters [σ], [ξ], [c_1], and [c_2] from regression on equations (2.23) and (2.27), respectively, and [a_1], [a_2], [a_3], and [a_4] from the correlations in equations (2.42) and (2.43), making use of the relationship in equation (2.46).

Figure 3.3 compares the subsequent predictions of Barbero, et al. (1982) and Shock and Helgeson (1988) for the following reaction:

$$H_2S(aq) = H^+ + HS^- \qquad (3.2)$$

to the measurements of Kryukov and Starostina (1978), Tsonopoulos, et al. (1976), Ellis and Giggenbach (1971), Sretenskaya (1977), and Suleimenov and Seward (1997). Two important points are evident from this figure. First, the results of Ellis and Giggenbach (1971) differ from all other data, exhibiting an inversion of curvature inconsistent with an increasing degree of association observed for most ions at higher temperatures. Secondly, below 150°C the predictions of Shock and Helgeson (1988) match the remaining data well, but deviate by 0.4 log units from the study of Suleimenov and Seward (1997) at 350°C.

Because the predictions of Shock and Helgeson (1988) were based on low temperature heat capacity and volumetric measurements, a re-evaluation of the HKF equation of state parameters for HS^- was undertaken in this study by constraining the high temperature

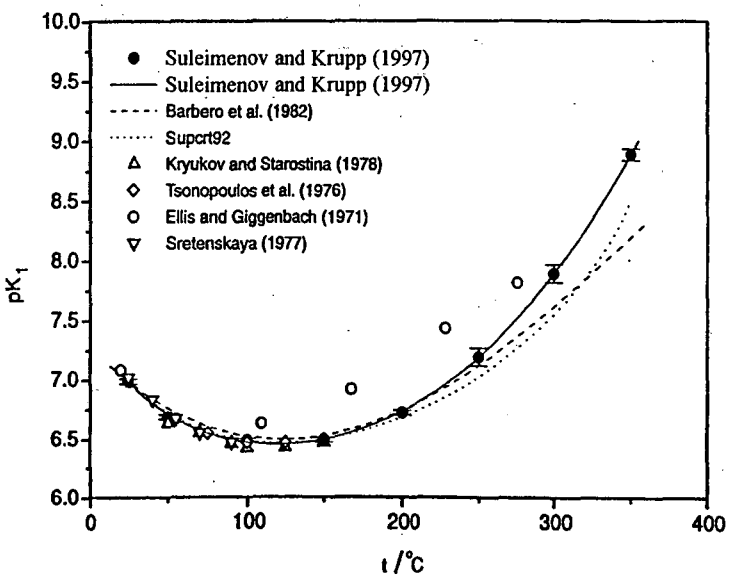

Figure 3.3 Experimental values for the dissociation constant of $H_2S(aq)$ (reaction (3.2)) (Suleimenov and Seward, 1997).

equilibrium constant of equation (3.2) with the data of Suleimenov and Seward (1997). The first step in this study was reconciling possible corrections with the HKF equation of state because it was found that the positions of $[c_2]$ and $[\omega]$ for HS^- had to be shifted from their original positions in the correlations of Figure 3.4. Because these two correlations are an integral part of the HKF equation of state, the maximum deviation in $[\omega]$ from the correlation line was restricted by the deviation of the La^{3+} species from the $[\overline{S}^o]$-$[\omega]$ correlation for trivalent cations, which was considered by Shock, et al. (1988) to still be within the margin of error of the HKF equation of state. Although this is not an ideal situation, given the uncertainties in the HKF model it was assumed reasonable. $[c_2]$ was initially obtained by regression against the new equilibrium constant data using the updated $[\omega]$ value and the HKF equation of state parameters of Shock, et al. (1988). $[a_1]$ through $[a_4]$ were obtained from volumetric data, $[c_1]$ from the heat capacity data, and $[c_2]$ updated until convergence was obtained. Table 3.2 reports these updated values.

Figure 3.5.a through 3.5.c show the new predictions for equilibrium constant, partial molal heat capacity, and partial molal volume, respectively. Although prediction of the equilibrium constant and standard partial molal volume have been improved, prediction of the standard partial molal heat capacity is worse, suggesting a fundamental incompatibility between the measurements of Barbero, et al. (1982), Suleimenov and Seward (1997), and the HKF equation of state model for ions (Tanger and Helgeson, 1988).

Although the experimental techniques of Barbero, et al. (1982) were relatively standard, Suleimenov and Seward (1997) admitted great difficulty in dealing with their dilute H_2S(aq) solutions, with any hydrogen sulfide loss due to volatility or corrosion leading to erroneous results. Similarly, recent molecular dynamics studies of Driesner, et al. (1998) suggest that the HKF correction for dielectric saturation and solvent compressibility may be species dependent, resulting in an underestimated solvation contribution to $[\Delta\overline{G}^o]$ when the universal g-correction factor described in *Section 2.3.4* is applied to HS^-. This latter possibility is particularly intriguing because it implies that the HKF equation of state is only

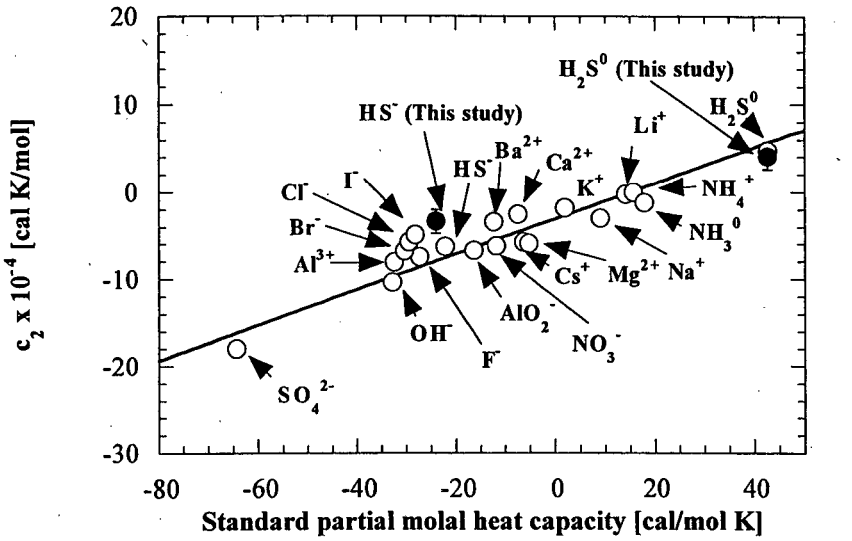

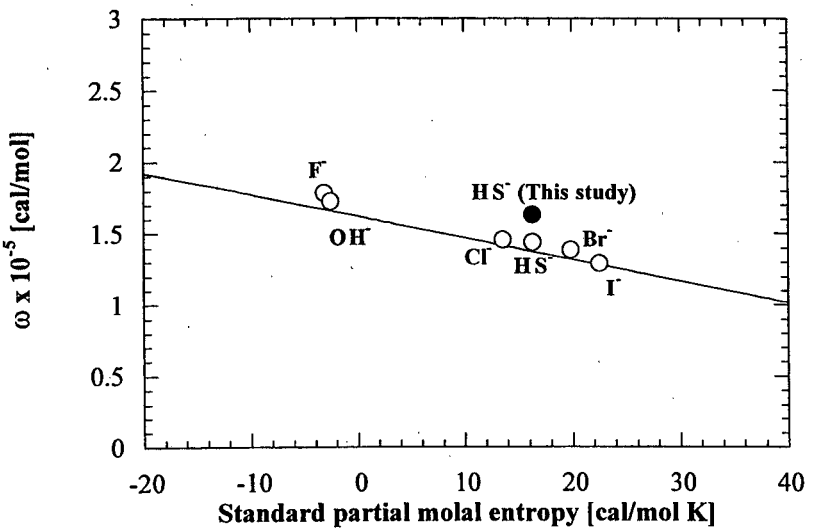

Figure 3.4 Correlations developed by Shock and Helgeson (1988) and Shock, et al. (1989) relating different standard partial molal thermodynamic properties. a) c_2-C_{Pr} for ions and neutral aqueous species. b) S-ω for ions.

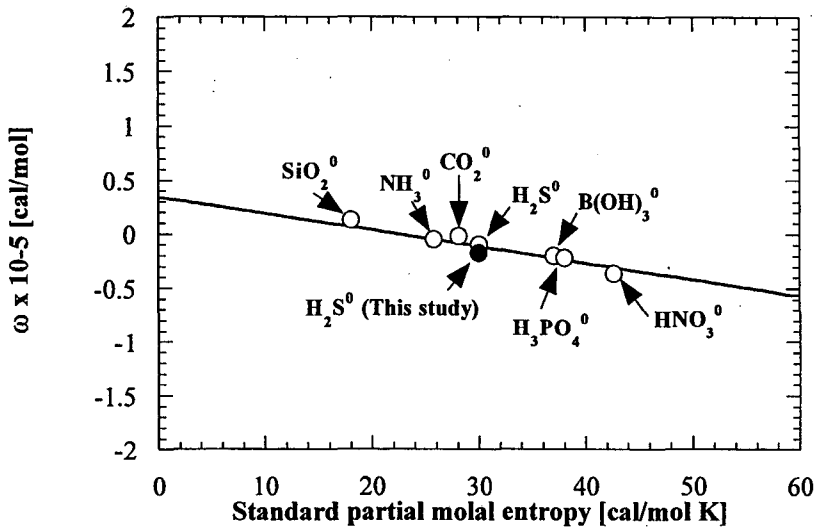

Figure 3.4 Correlations developed by Shock and Helgeson (1988) and Shock, et al. (1989) relating different standard partial molal thermodynamic properties. c) S-ω for neutral aqueous species.

Study	$\Delta G°_f$[a]	$\Delta H°_f$[a]	$S°$[b]	$C_{pr}°$[b]	$V°$[c]	σ[c]	ξ[d]
Shock and Helgeson (1988)	2860[h]	-3850[h]	16.3[h]	-22.17[i]	20.65[i]	38.13	-2.37
This study	2860[h]	-3850[h]	16.3[h]	-23.90	20.65[i]	29.26 ±1.44	-3.07 ±1.38

Study	a_1[f] x 10	a_2[a] x 10^{-2}	a_3[g]	a_4[h] x 10^{-4}	c_1[b]	c_2[h] x 10^{-4}	ω[a] x 10^{-5}
Shock and Helgeson (1988)	5.0119	4.9799	3.4765	-2.9849	3.42	-6.27	1.4410
This study	5.1700	4.7433	4.0980	-2.9750	-1.9779 ±2.3704	-3.3952 ±1.4078	1.63

TABLE 3.2 Comparison of equations of state parameters and standard partial molal properties at 25° C and 1 bar for HS^- a. cal mol^{-1} b. cal mol^{-1} K^{-1} c. cm^3 mol^{-1} d. cm^3 K mol^{-1} e. cal mol^{-1} bar^{-1} f. cal K mol^{-1} bar^{-1} g. cal K mol^{-1} h. Barbero, et al. (1982) i. Tanger and Helgeson (1988)

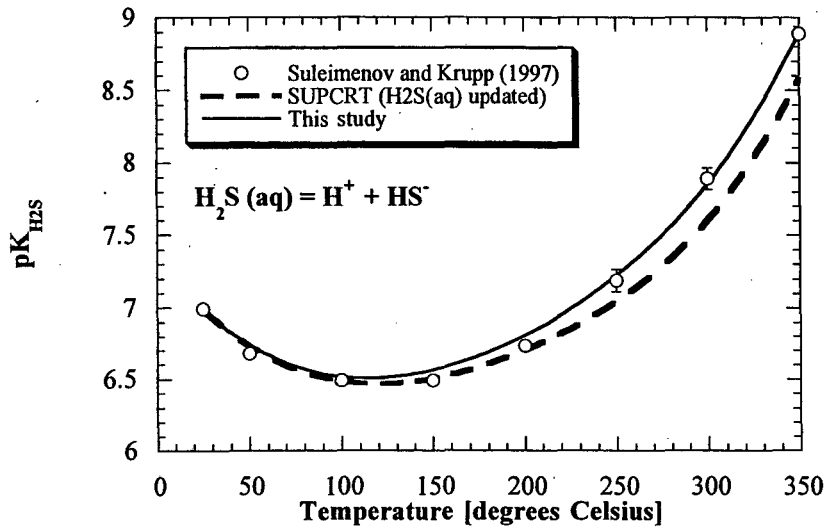

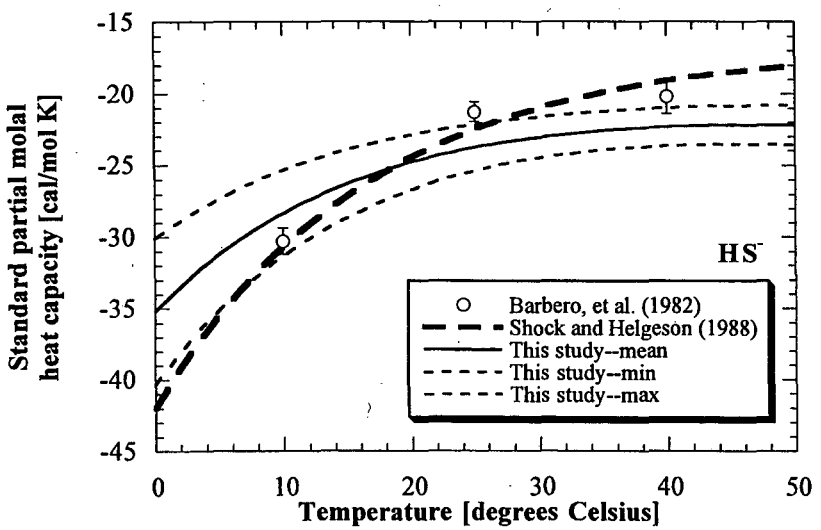

Figure 3.5 Comparison between the predicted a) equilibrium constants for reaction (3.2) and b) standard partial molal heat capacities, and c) standard partial molal volumes for HS^- derived in this study and by Shock and Helgeson (1988).

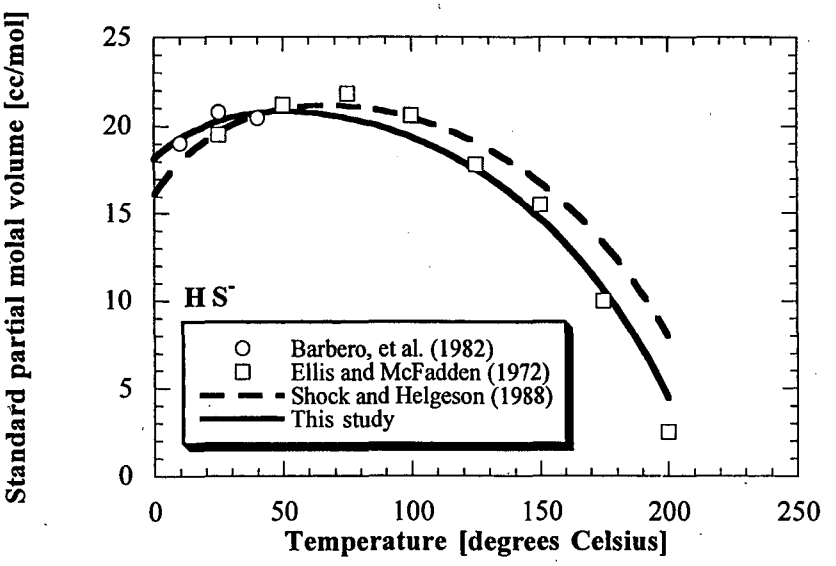

Figure 3.5 Comparison between the predicted c) standard partial molal volumes for HS^- derived in this study and by Shock and Helgeson (1988).

predictive at the highest temperatures for species whose equation of state parameters were derived from high temperature heat capacity or log K_r data. Moreover, those ionic species whose parameters were derived from log K_r data and the correlations of Figure 3.4 would necessarily produce fictive values for $[\overline{C}^o_{Pr}]$ because the error associated with applying a universal g-function correction would be incorporated into the $[c_1]$ and $[c_2]$ heat capacity parameters.

Corroborating evidence for errors in the experimental data of Suleimenov and Seward (1997) could be provided if there were independent solubility experiments on such mineral phases as galena (PbS) or sphalerite (ZnS) in pure water to elevated temperatures. For example, the solubility of galena is governed by the dissolution reaction:

$$PbS\ (gal) + H_2O = Pb^{2+} + HS^- + OH^-, \qquad (3.3)$$

which provides the following equilibrium constant:

$$K = a_{Pb^{2+}} \bullet a_{HS^-} \bullet a_{OH^-}. \qquad (3.4)$$

Because the activity of HS^- $[a_{HS^-}]$ is also controlled by the first dissociation constant of H_2S(aq):

$$H_2S\ (aq) = HS^- + H^+ \qquad (3.5)$$

the solubility of galena depends on the value of this equilibrium constant. Consequently, the dissociation constant of Suleimenov and Seward (1997) could be used to predict the solubility of galena and the result compared to actual solubility measurements. Unfortunately, no reliable data of this type exists.

An equally unsatisfactory dataset is available to examine the possibility that the HKF equation of state g-function is species dependent. Ideally, low temperature heat capacity *and* high temperature $[\Delta\overline{G}^o]$ data would need to be available, from which the $[\Delta\overline{G}^o]$ for all of the other species or phases in the reaction would be known *not* predicted. The only other species in the SUPCRT database (Johnson, et al., 1992) which meets all three of these criteria is OH^-, which is entirely compatible with the HKF equation of state as demonstrated

by the independent prediction of the dissociation constant of water by Tanger and Helgeson (1988).

Based on the close match between Suleimenov and Seward (1997) and other studies where experimental data is available, it was decided in this investigation to accept the HKF equation of state derived by the method outlined above, pending future investigations.

3.4 Sb minerals and aqueous species

The HKF equation of state parameters for Sb aqueous complexes were previously derived by Akinfiev, et al. (1994); however several elements of their study required that the parameters be re-derived in this investigation. First of all, they used the stibnite solubility study of Krupp (1988) to derive the parameters for the sulfide complexes of Sb without correcting for the fact that Krupp (1988) used the dissociation constant for H_2S(aq) of Ellis and Giggenbach (1971), which was previously shown to be inconsistent with all other investigations (Figure 3.3). Secondly, they made several assumptions about the speciation which required additional scrutiny. Finally, several of their HKF parameters were inconsistent with the correlations given in Shock, et al. (1997) and shown in Figure 3.6.

3.4.1 $Sb(OH)_3^0$

As stated above, the equation of state parameters for this species were previously derived by Akinfiev, et al. (1994) using the solubility of senarmontite (Sb_2O_3) in pure water from 25-200°C (Popova, et al., 1975), 210-300°C (Shikina and Zotov, 1991). and 350°C (Akinfiev, et al., 1994):

$$0.5\ Sb_2O_3\ (sen) + 1.5\ H_2O = Sb(OH)_3^0. \qquad (3.6)$$

They also used the solubility of Sb(cr) in an H_2 atmosphere at 450°C and 500 bars (Shikina and Zotov, 1991) to constrain the Born parameter [ω]. Because they found that the regressed heat capacity was too high ($\overline{C}^o_{Pr}$ > 80 cal/mol) and the solubility of Sb (cr) was poorly described, they invoked the dimer species $Sb_2(OH)_6^0$ to help explain solubility under

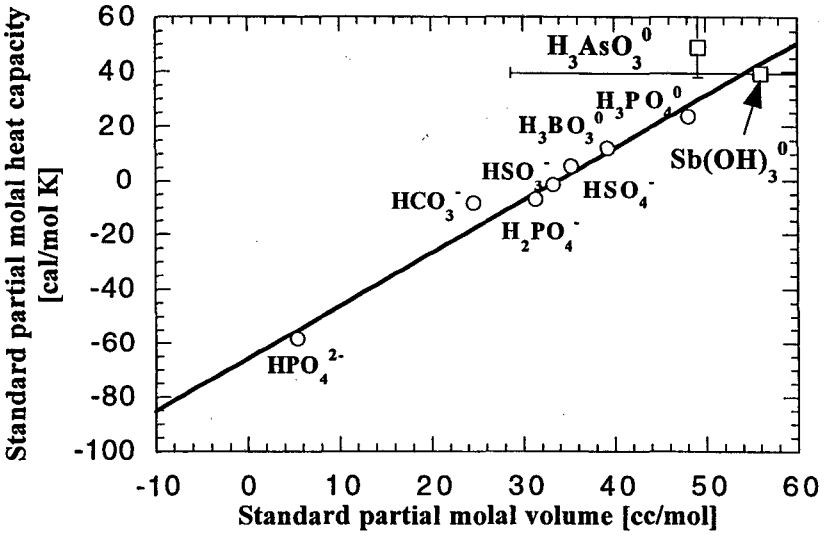

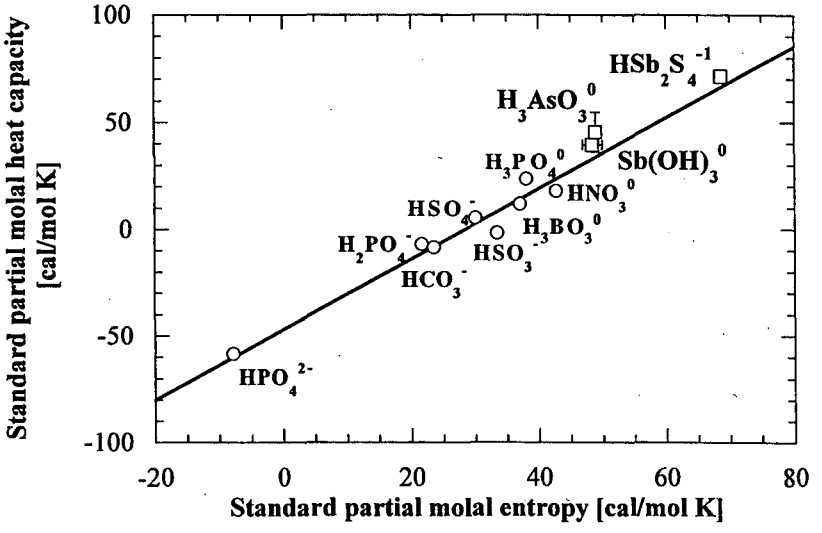

Figure 3.6 Comparison between the predicted standard partial molal thermodynamic properties for the As and Sb species in this study and the correlations for hydrogen-bearing nonmetal acids and oxyanions (Shock, et al., 1997).

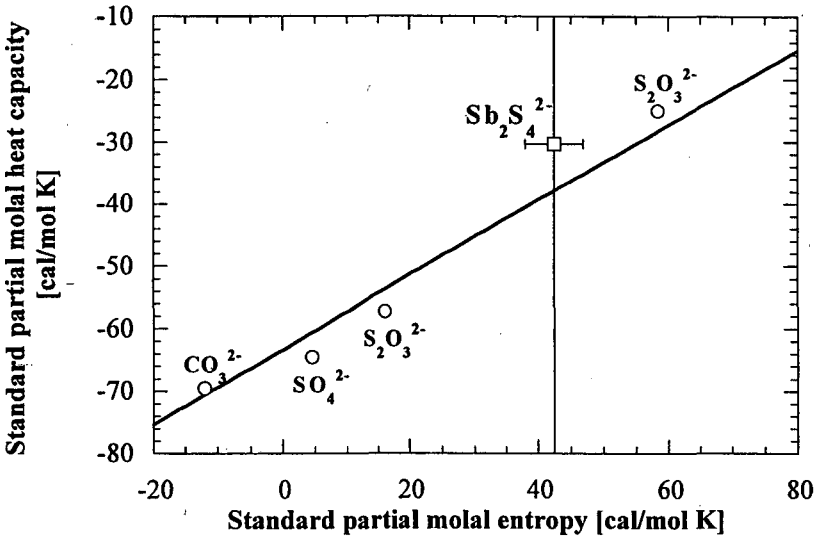

Figure 3.6 Comparison between the predicted standard partial molal thermodynamic properties for the As and Sb species in this study and the correlations for hydrogen-bearing nonmetal acids and oxyanions (Shock, et al., 1997).

conditions where the concentration of Sb in solution exceeded 10^{-3} mol/kg (i.e. the senarmontite solubility experiments above 200°C).

Support for their hypothesis has recently been provided by the spectroscopic study of Gout, et al. (1997), who confirmed the bridging of two $H_3AsO_3^0$ molecules to form $H_6As_2O_6^0$. Although the concentration of As in the solutions was an order of magnitude higher than the concentration of Sb in the senarmontite buffered solutions of Akinfiev, et al. (1994), the regression calculations of this study confirmed the conclusion that the experimental data could only be reconciled by including this additional species.

The HKF parameter for $Sb(OH)_3^0$ was re-derived in this study analogously to Akinfiev, et al. (1994), with the exception that the stibnite solubility measurements of Krupp (1988), Zotov, et al. (1995), and Shikina and Zotov (1999) at temperatures equal to and greater than 200°C were also included in the regression calculations (the latter investigation showed that the dominant species under these conditions was $Sb(OH)_3^0$ rather than $Sb_2S_2(OH)_2$ hypothesized by Krupp (1988)).

The first step in the regression calculations was to select the thermodynamic properties of the Sb-bearing mineral phases in equilibrium with the solutions. Excluding stibnite, the values shown in Table 3.3 were taken from Akinfiev, et al. (1994) who retrieved values from the IVTANTERMO tables for the thermodynamic values of pure substances (Glushko, et al., 1982). Because Seal, et al. (1992) provided updated heat capacity data for stibnite, and additionally supplied independent evidence for the validity of their predicted $[\Delta G_f^o]$, the subsequent thermodynamic values for this mineral phase were deemed to be more reliable. In order to convert the four term heat capacity data provided by Akinfiev, et al. (1994) and Seal, et al. (1992) to the three parameter Maier-Kelly (1932) equation utilized by the SUPCRT database (Johnson, et al., 1992), the heat capacity values obtained from their functions were expressed at five degree intervals and then regressed against equation (2.9).

Following calculation of the thermodynamic properties of the solid phases, the activities of all aqueous species in the study of Krupp (1988) were updated to reflect both the

Solid phase	$\Delta_f G°_{290}$[a]	$S_{298}°$[b]	$C_{p298}°$[b]	$V_{298}°$[c]	a[b]	b[d] x 10^{-3}	c[e] x 10^{5}	T [°C] for C_p
native antimony[f] (orthorhombic Sb)	0	10.773	6.05	18.178	2.49	5.93	1.88	(25-903)
senarmontite[f] (Sb_2O_3)	-149967	30.091	25.00	52.21	21.16	13.30	0.36	(25-879)
valentite[f] (Sb_2O_3)	-148193	32.118	26.74	50.01	22.50	13.76	0.67	(25-928)
stibnite[g] (Sb_2S_3)	-35846	43.499	28.60	73.41	28.76	3.92	-1.27	(25-556)

Table 3.3 Thermodynamic properties of antimony solid phases a. cal mol^{-1} b. cal mol^{-1} K^{-1} c. cm^3 mol^{-1} d. cal mol^{-1} K^{-2} e. cal K mol^{-1} f. Akinfiev, et al. (1994) g. Seal, et al. (1992)

dissociation constant for H_2S (aq) reported by Suleimenov and Seward (1997) and the effect of the aqueous species $NaHS^0$. Although this correction was found to have little affect in the acidic conditions where $Sb(OH)_3^0$ predominates (i.e. pH < pK_{H2S}), the procedure outlined in this section was also used in the calculations for the sulfur-bearing species described below.

Krupp (1988) originally buffered several solution runs to determine the dominant antimony species in solution and then calculated the pH for unbuffered solutions from the following relation:

$$pH = pK_{H2S} - \log (a_{H2S}/a_{HS-}) \quad (3.7)$$

where

$$m_{HS-} = m_{NaOH} - S_{Sb}*D1, \quad (3.8)$$

m_{NaOH} was a known concentration added to solution, S_{Sb} was the total concentration of antimony in solution, D1 was the slope ($\partial \log (S_{Sb})/ \partial(pH)$) for the dominant antimony species in solution,

$$a_{H2S} = m_{H2S} = (TFS - m_{HS-}), \quad (3.9)$$

$$a_{HS-} = m_{HS-}*\gamma_{HS-}, \quad (3.10)$$

TFS was the total free reduced sulfur (excluding ligand sulfur), and the activity coefficients were calculated from the first term in equation (2.37). Because the ligand sulfur concentration was in most cases several orders of magnitude smaller than the "free" sulfur, they calculated it from the initial plots of log (S_{Sb}) versus the log (Total Sulfur) determined analytically.

The equations for [m_{HS-}] and [m_{H2S}] utilized in this study were:

$$m_{HS-} = (m_{NaOH} - S_{Sb}*D1) \ / \ (1 + \gamma_{HS-} m_{Na+} \gamma_{Na+} / K_{NaHS}) \quad (3.11)$$

$$m_{H2S} = TFS - m_{HS-} - (m_{HS-} \gamma_{HS-} m_{Na+} \gamma_{Na+} / K_{NaHS}) \quad (3.12)$$

where the value for the dissociation constant for $NaHS^0$ (K_{NaHS}) was assumed to be analogous to $NaCl^0$ taken from Shock, et al. (1992), the activity coefficents for all charged species were obtained from the same form of equation (2.37) utilized by Krupp, the [å] parameter in the denominator was taken from Helgeson, et al. (1981), and the ionic strength was assumed to

be unchanged due to the slight alteration in pH and log m_{HS^-} (this latter assumption was based on the speciation calculations for Au described below, where differences in ionic strength from reported values had no noticeable effect on the magnitude of the solubility constants).

Once the stibnite solubility experiments had been re-speciated, the hypothesis of Krupp (1988) that two species were present in acidic conditions at 200°C was verified, and the contribution due to the sulfide complex $H_2Sb_2S_4^0$ was subtracted from the total Sb concentration of Krupp (1988) and Shikina and Zotov (1999). The subsequent $[\Delta\overline{G}^o]$ obtained from equation (2.35) was then included in the regression calculations. $[\Delta G_f^o]$ was fixed by the solubility of senarmontite at 25°C (Popova, et al. (1975)), $[\overline{C}_{Pr}^o]$ was calculated from reaction (3.6) after assuming $[\Delta C_{Pr,R}^o] = 0$ for this isocoulombic reaction, and $[\overline{S}^o]$, $[\overline{V}^o]$, and $[\omega]$ were regressed using equation (2.47).

Table 3.4 reports the resulting values for the HKF equation of state parameters for $Sb(OH)_3^0$ and Figure 3.6.a and 3.6.b shows how these relate to the correlations for nonmetal hydrogen-bearing acids and oxyanions. The corresponding equations are:

$$\overline{C}_{Pr}^o = 1.94\overline{V}^o - 65.8 \qquad (3.13)$$

$$\overline{C}_{Pr}^o = 1.65\overline{S}^o - 46.8 \qquad (3.14)$$

for the two plots, respectively. The regressed values in Table 3.4 represent a slight improvement over the predictions of Akinfiev, et al. (1994); however, the large errors for $[\overline{V}_{Sb(OH)3}^o]$ highlight the possibility that the correlations defined by Shock, et al. (1997) contain large uncertainties.

The solubility of stibnite, senarmontite, and Sb(cr) is shown in Figure 3.7.a-c, respectively. A slight overestimation is predicted for Sb solubility with respect to stibnite. For the senarmontite plot, $Sb(OH)_3^0$ is the dominant species throughout the entire temperature range, but solubility becomes increasingly controlled by $Sb_2(OH)_6^0$ (*Section 3.4.2*) near 350°C. The error bars associated with the regression calculations are well-constrained to

Species	$\Delta G°_f$[a]	$S°$[b]	$C_{pr}°$[b]	$V°$[c]	a_1[d] x 10	a_2[a] x 10^{-2}	a_3[e]	a_4[f] x 10^{-4}	c_1[b]	c_2[f] x 10^{-4}	ω[a] x 10^{-5}
$Sb(OH)_3^0$	-153903	48.47 ± 1.55	39.5	56.05 ± 27.33	9.3564	15.0646	-0.1427	-3.4012	27.1291	5.0116	-0.2326 ± 0.0946
$Sb_2(OH)_6^0$	-307806	109.52 ± 2.53	79	112.10	17.1578	34.1133	-7.6071	-4.1892	53.7862	13.0577	-0.46
$H_2Sb_2S_4^0$	-35493	68.56 ± 0.03	71.3	65.08	10.4345	17.6969	-1.1742	-3.5106	41.4204	11.4892	-0.6982
$HSb_2S_4^{-1}$	-28274	48.38 ± 4.45	33.02	49.33	8.8161	13.7451	0.3743	-3.3472	33.6782	3.6916	0.8892
$Sb_2S_4^{-2}$	-15622	42.35 ± 19.81	-30.30 ± 90.31	44.63	8.7514	13.5872	0.4363	-3.3407	12.4638	-9.2062	2.6022

Table 3.4 HKF equation of state parameters and standard molal properties referring to 25° C and 1 bar of aqueous antimony complexes
a. cal mol^{-1} b. cal mol^{-1} K^{-1} c. cm^3 mol^{-1} d. cal mol^{-1} bar^{-1} e. cal K mol^{-1} bar^{-1} f. cal K mol^{-1}

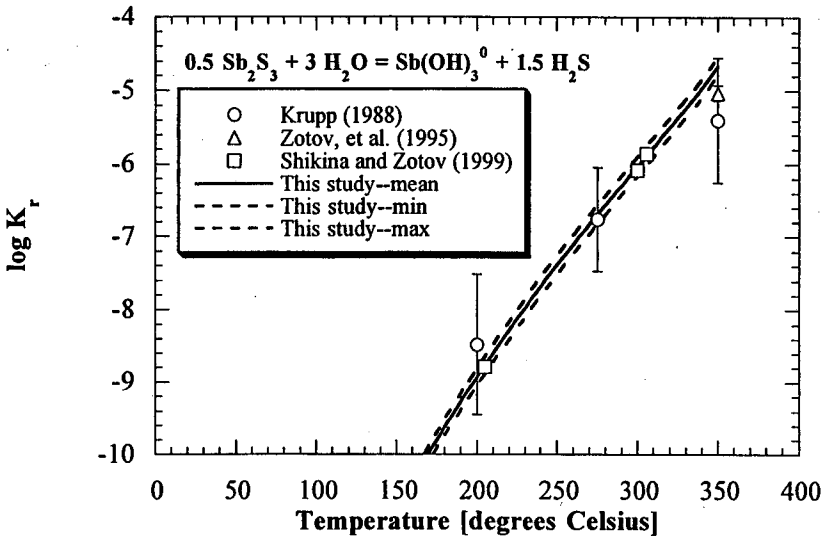

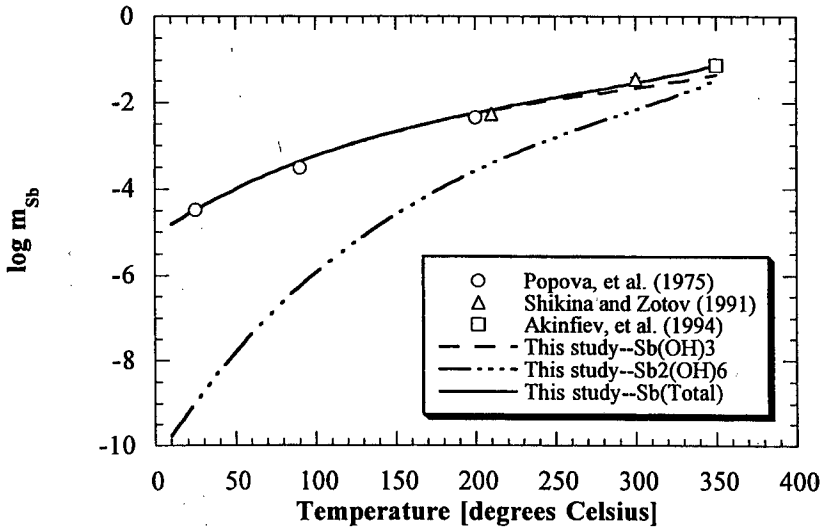

Figure 3.7 Comparison between the predicted equilibrium constants and experimental data for Sb hydroxide complexes. a) Stibnite solubility. b) Senarmontite solubility (Total log m_{Sb}).

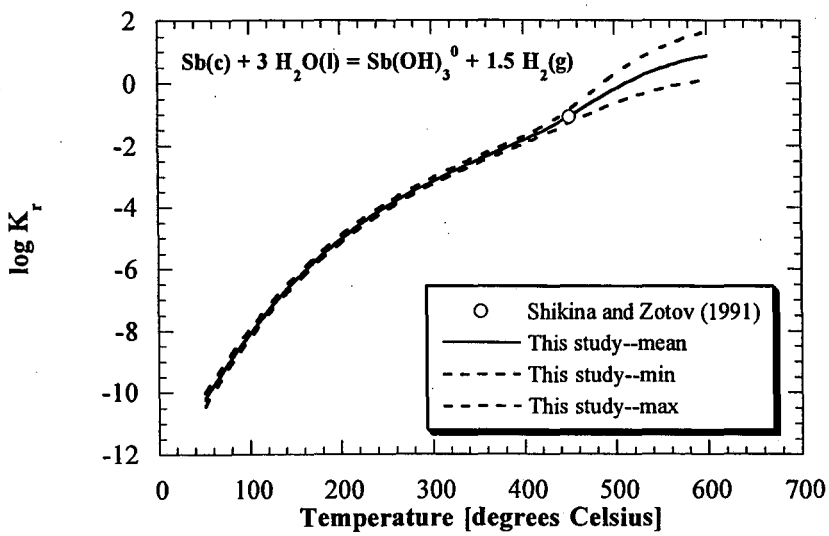

Figure 3.7 Comparison between the predicted equilibrium constants and experimental data for Sb hydroxide complexes. c) Native antimony solubility.

450°C and 500 bars, but become very large outside of the range of experimental data. Consequently, although the HKF equation of state has been made valid for the reaction NaCl = $NaCl^0$ to 1000°C, extrapolation of other equilibrium constants is tenuous.

3.4.2 $Sb_2(OH)_6^0$

The HKF equation of state parameters were derived identically to the study of Akinfiev, et al. (1994). The contribution due to $Sb(OH)_3^0$ was first subtracted from the total senarmontite solubility. [$\overline{S}^o$] was then obtained by regression after assuming that the thermodynamic properties of dimerization were equal to zero for all other parameters. The resulting HKF parameters for $Sb_2(OH)_6^0$ are shown in Table 3.4. The fit to the experimental senarmontite solubility at 350°C in Figure 3.7.a is excellent.

3.4.3 $Sb(OH)_4^-$

The HKF equation of state parameters for this species were derived by Akinfiev, et al. (1994) from the data of Popova (1980) at 25 and 200°C; however, it has recently been suggested that in strongly alkaline solutions (i.e. pH > 12), SbS_2^- is the more important species (Belevantsev, et al. (1998)). Raman spectroscopic measurements of Wood (1989) additionally identified the species SbS_2^- (or SbS_3^{3-}) as being more likely at 25°C, whereas Tossell (1994) identified $HSbS_3^{-2}$. Because strongly alkaline solutions are rarely encountered geologically, and are unimportant for the formation of the Carlin-type gold deposits, no attempt was made in this study to reconcile the contrasting hypotheses. The HKF equation of state parameters for $Sb(OH)_4^-$, as derived by Akinfiev, et al. (1994), are not listed.

3.4.4 $H_2Sb_2S_4^0$

There is now general consensus that antimony sulfide species predominantly form as dimers under geologically realistic conditions. Spycher and Reed (1989) used least squares regression and multicomponent equilibrium calculations of existing stibnite solubility studies

to show that least squares regression errors were minimized for the species $HSb_2S_4^{-1}$ and $Sb_2S_4^{-2}$. Tossell (1994) additionally used ab initio quantum mechanical calculations to demonstrate that $H_2Sb_2S_4^0$ is thermodynamically stable relative to its monomeric or trimeric forms. Finally, Krupp (1988) demonstrated the existence of $H_2Sb_2S_4^0$ under neutral to acidic conditions from plots of log m_{Sb} versus pH and log TFS.

The HKF equation of state parameters for $H_2Sb_2S_4^0$ were derived in this study as follows: First, $[\Delta\overline{G}_f^o]$ was fixed by the solubility reaction of stibnite at 25°C:

$$Sb_2S_3 + H_2S(aq) = H_2Sb_2S_4^0 \qquad (3.15)$$

Next, this reaction was assumed to be isocoulombic, allowing $[\overline{C}_{Pr}^o]$ to be calculated from the heat capacities of stibnite and $H_2S(aq)$. Finally, $[\overline{S}^o]$ was regressed from the experimental data at 25 and 200°C, with $[\overline{V}^o]$ and $[\omega]$ obtained from the correlations for nonmetal hydrogen-bearing acids and oxyanions (Figure 3.6.a) (Shock, et al., 1997) and neutral aqueous species (Figure 3.4.c) (Shock, et al., 1989), respectively. The justification for excluding the datum at 90°C in Figure 3.8 was that it represented only one experimental measurement and additionally resulted in a poor fit to the results at 200°C. The justification for using the correlation of Figure 3.6.a was that S and O in their -2 oxidation states exhibit similar chemical characteristics, and the fact that $H_2Sb_2S_4^0$ is well represented by the hydrogen-bearing acids and oxyanions correlation in Figure 3.6.b.

3.4.5 $HSb_2S_4^{-1}$

The importance of $HSb_2S_4^{-1}$ relative to $Sb_2S_4^{2-}$ at temperature exceeding 200°C and pH > 6 is subject to debate. Krupp (1988) assumed $HSb_2S_4^{-1}$ controls stibnite solubility, but Akinfiev, et al. (1994) hypothesized that $Sb_2S_4^{2-}$ is more important due to their regression calculations which showed that retrieving $[\overline{S}^o]$ and $[\overline{C}_{Pr}^o]$ for $HSb_2S_4^{-1}$ from experiments at 275 and 350°C led to conflicting values at high and low temperatures.

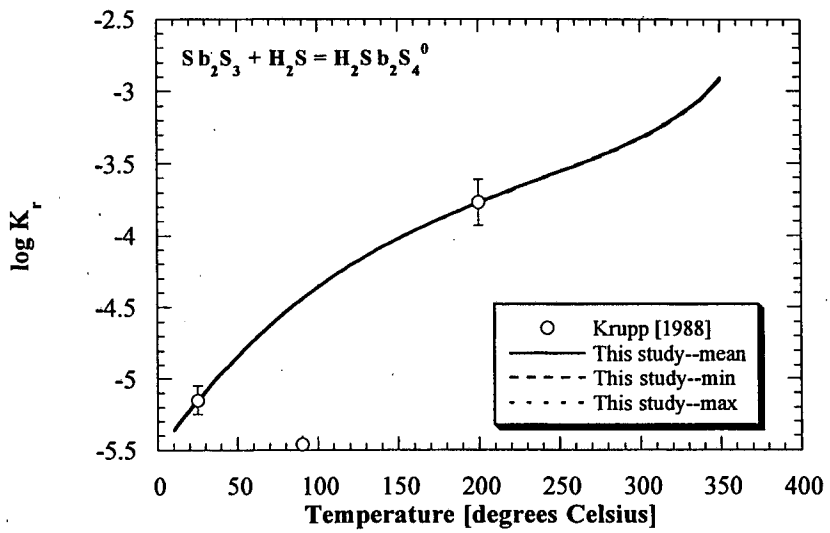

Figure 3.8 Comparison between the predicted and experimental equilibrium constants for reaction (3.15)) based on the HKF equation of state parameters for $H_2Sb_2S_4^0$ derived in this study.

To better resolve this issue, the contribution due to the three neutral species described above was subtracted from the total solubility. Next, possible speciation scenarios were evaluated by plotting log m_{Sb} reported by Krupp (1988) as a function of pH along restricted ranges of log TFS (+/- 0.10 mol/kg at 200°C and +/- 0.30 mol/kg at 275°C). Figure 3.9.a shows that at 200°C, two species are definitely present; however, at 275°C (Figure 3.9.b), the presence of $Sb_2S_4^{2-}$ could replicate all three data points, but $HSb_2S_4^{-1}$ could only explain the low pH datum. Although this method was also extended to 350°C, only one experimental data point remained, making its assignment to either of the sulfide complexes conjecture.

Based on the uncertainty at 275°C, the HKF equation of state parameters for $HSb_2S_4^{-1}$ were derived from the experimental data reported by Krupp at 25, 90, and 200°C. $[\Delta\overline{G}_f^o]$ was constrained by the following reaction at 25°C:

$$Sb_2S_3 + H_2S = HSb_2S_4^{-1} + H^+ \qquad (3.16)$$

$[\overline{S}^o]$ was then obtained from regression, and $[\overline{C}_{Pr}^o]$, $[\overline{V}^o]$, and $[\omega]$ from the same correlations used for $H_2Sb_2S_4^0$. Although $[\overline{C}_{Pr}^o]$ could also have been obtained from regression, the resulting $[\overline{C}_{Pr}^o]$ was inconsistent with the correlation of Figure 3.6.b (a consequence of over-fitting the three regression parameters to only three data points).

Table 3.4 reports the parameters calculated in this study. The parameters both for this species and $H_2Sb_2S_4^0$ described above represent significant improvement over the study of Akinfiev, et al. (1994) relative to the correlations of Shock, et al. (1997). Figure 3.10 shows the resulting equilibrium constant predictions for reaction (3.16). The first important feature of this plot is the large uncertainties associated with the re-computed experiments of Krupp (1988). Although the error between prediction and experiment at 90°C is approximately +/- 0.5 log units, the data is represented within the uncertainty envelopes provided by the dashed lines. Figure 3.12 (described in greater detail below) confirms that the HKF equation of state parameters derived in this study are valid within the uncertainties of HKF model and the experimental data of Krupp (1988).

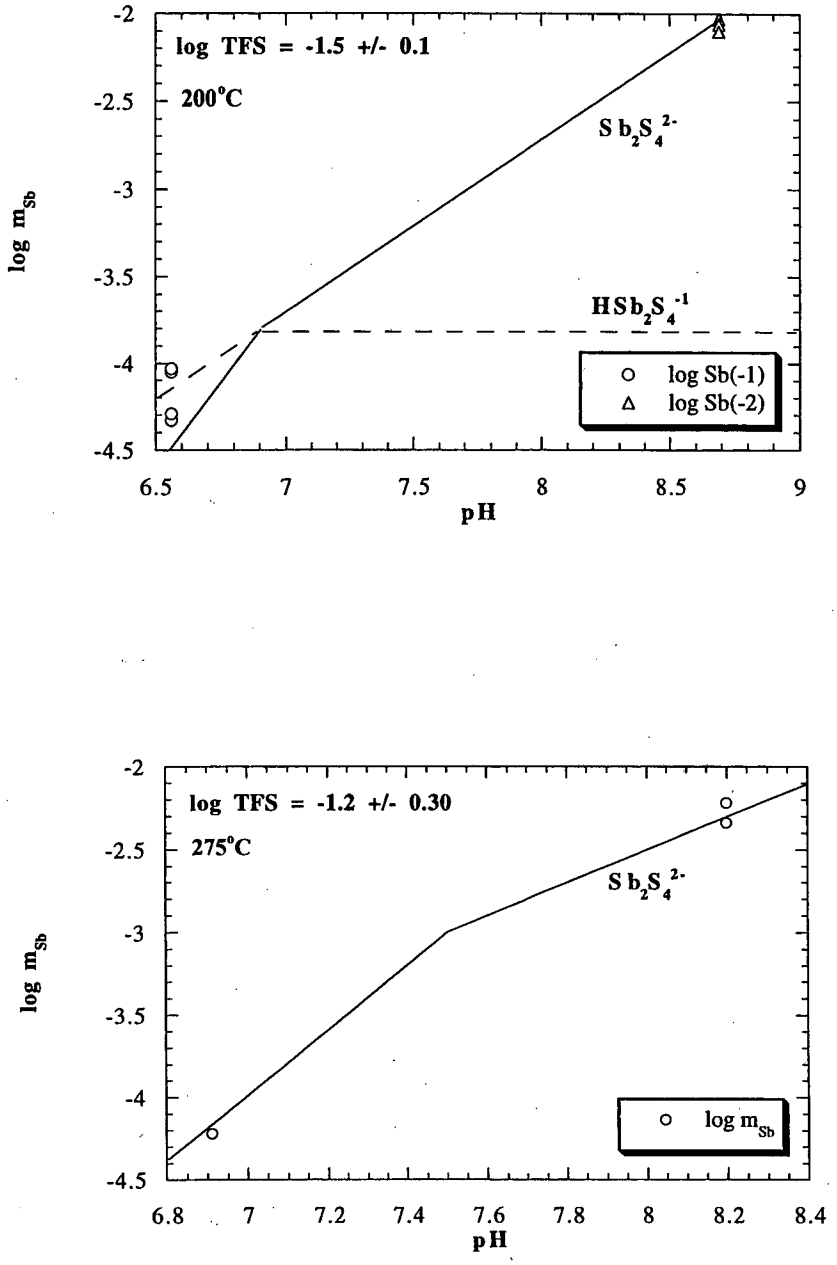

Figure 3.9 Speciation plots for the solubility of stibnite at a) 200 and b) 275°C. The open circles represent experimental data. The solid lines represent the solubility predicted by the species $Sb_2S_4^{-2}$. The dashed lines represent $HSb_2S_4^{-1}$.

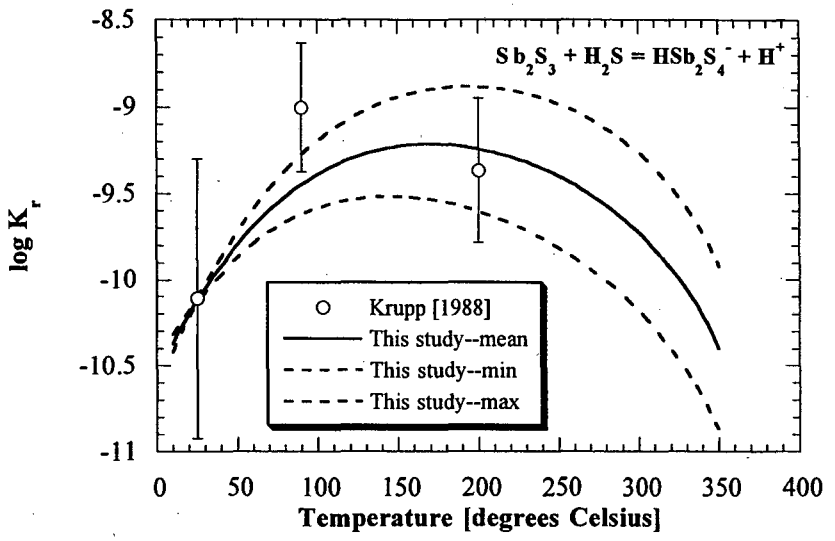

Figure 3.10 Predicted equilibrium constants for reaction (3.16) based on the HKF equation of state parameters for $HSb_2S_4^{-1}$ derived in this study.

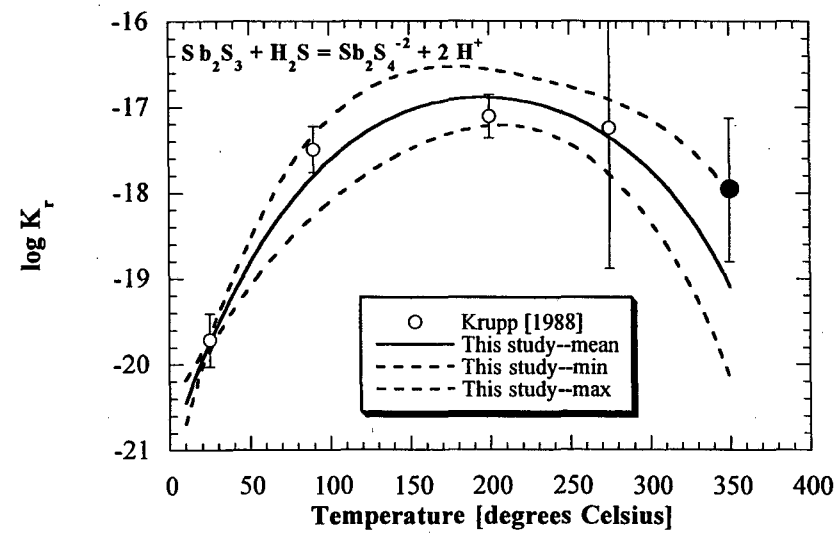

Figure 3.11 Predicted equilibrium constants for reaction (3.17) based on the HKF equation of state parameters for $Sb_2S_4^{-2}$ derived in this study. The filled circle was not used in the regression because it could not be undeniably assigned to $Sb_2S_4^{-2}$.

3.4.6 $Sb_2S_4^{-2}$

Based on the results of Figure 3.9, the solubility of this species was obtained from experiments to 275°C. [$\Delta\overline{G}_f^o$] was obtained from the equilibrium constant at 25°C for the reaction:

$$Sb_2S_3 + H_2S = Sb_2S_4^{-2} + 2\ H^+. \qquad (3.17)$$

[$\overline{S}^o$] and [$\overline{C}_{Pr}^o$] were then obtained from regression on the experimental data of Krupp (1988). Finally, [$\overline{V}^o$] and [ω] were retrieved from the correlations for nonmetal hydrogen-bearing acids and oxyanions (Shock, et al., 1997) and divalent anions (Shock and Helgeson, 1988), respectively. Although the position of $Sb_2S_4^{2-}$ in the correlation of Figure 3.6.c represents further justification for using the correlations of Shock, et al. (1997) to describe nonmetal sulfur-bearing species, the error bars represented in this figure exceed +/- 90 cal/mol K. This implies that similar errors may exist in the other species represented in the figure 3.6, calling into question the validity of the correlations themselves.

The predicted equilibrium constants for reaction (3.17) are shown in Figure 3.11. Assuming that the data at 350°C corresponds to this aqueous species, the predictions of this study at the highest temperature are underestimated.

3.4.7 Summary of Sb complexes

In addition to the study of Krupp (1988), earlier experimental data for the solubility of stibnite in sulfur-bearing solutions include: Learned (1966); Norton (1964); Wei and Saukov (1961); Kolpakova (1982); Akeret (1953); Babko and Lisetskaya (1956); Arnston, et al. (1966); and Dubey and Ghosh (1962). Because only Learned (1966) and Arnston, et al. (1966) explored solubility above 100°C, Akinfiev, et al. (1994) restricted comparison of their predicted solubilities to these two studies, finding agreement within 0.2 logarithmic units (see Figure 4, Akinfiev, et al. (1994)).

Based on the fact that Akinfiev, et al. (1994) additionally found general consistency between their measurements and Krupp (1988), justification for the HKF parameters adopted in this study was sought by comparing the solubility predicted from Table 3.4 by Krupp (1988) at temperatures from 25 to 350°C along the saturated water vapor pressure curve. In order to perform these calculations, two simplifying assumptions were made: 1) a constant ionic strength of 0.01 was selected to represent the average ionic strength of the solutions in the Krupp (1988) study; and 2) experimental data points were projected onto the log TFS = -1.67 ± 0.50 mol/kg plane.

Figure 3.12.a-e illustrates that the resulting predictions match the measured solubilities well. Where discrepancies do exist, (e.g. the acidic regions at 25 and 275°C), the source was found to be the TFS value selected for the projection. Despite the differences in the predicted and observed equilibrium constants at 90°C in Figures 3.8 and 3.10, the overall solubility is well described in Figure 3.12. $Sb_2S_4^{-2}$ is the dominant sulfide species at 350°C; however stibnite solubility is predominantly controlled by $Sb(OH)_3^0$ at this temperature.

3.5 As minerals and aqueous species

Several experimental and theoretical studies have now identified the predominant hydroxide complex of As in equilibrium with orpiment (As_2S_3), claudetite (As_2O_3), and arsenolite (As_2O_3) as $H_3AsO_3^0$. Pokrovski, et al. (1996) identified the species using plots of m_{As} versus m_{H2S} obtained from experimental solubility measurements. They also used Raman spectroscopy to verify their results. In a companion paper, Gout, et al. (1997) demonstrated that additional spectroscopic peaks associated with polymerized forms of $H_3AsO_3^0$ occurred at higher concentrations of As. Finally, Tossell (1997) performed ab initio molecular orbital calculations on $H_3AsO_3^0$ and found that its energetics were consistent with the spectral assignments of Pokrovski, et al. (1996).

The sulfide species of As have also been extensively studied; however, several key issues remain. Spycher and Reed (1989) subjected the available experimental data on the solubility

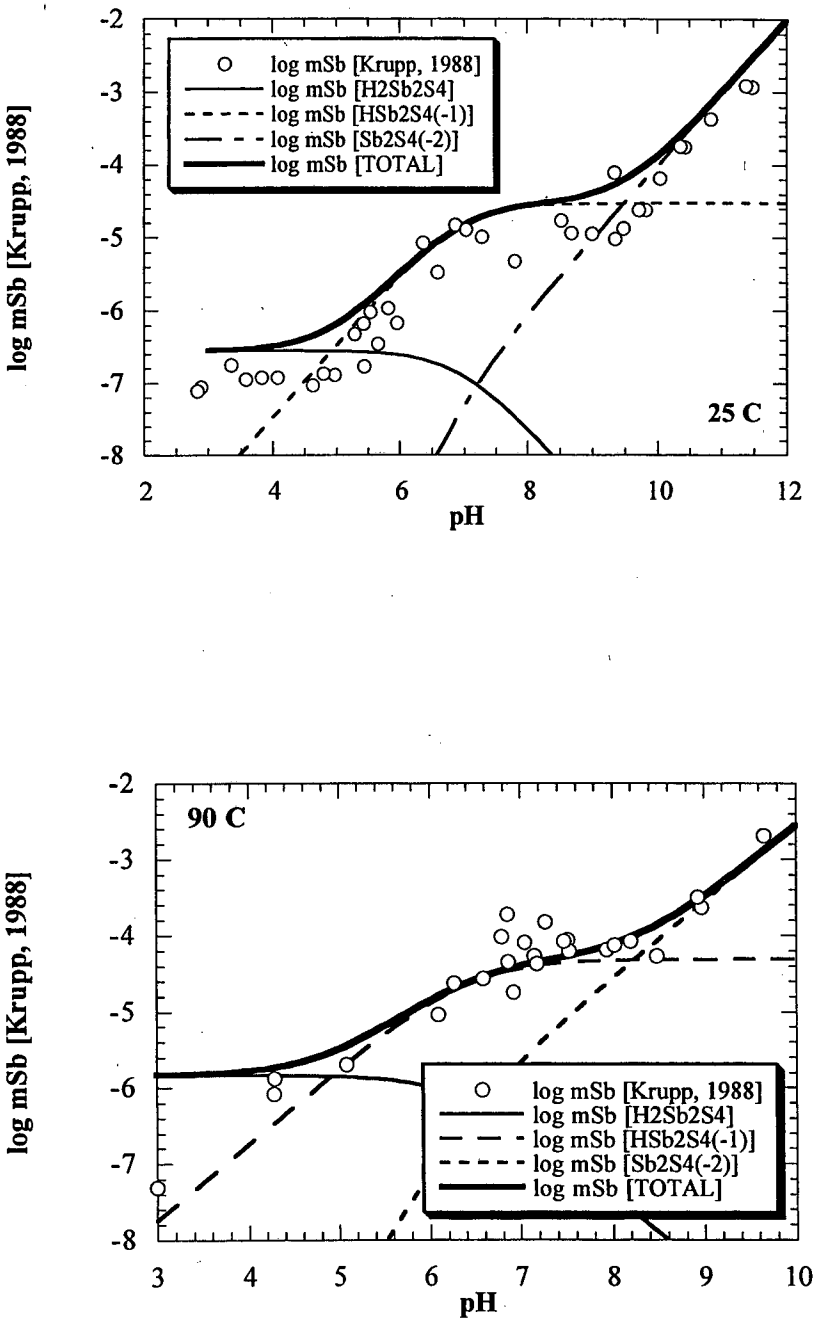

Figure 3.12 Comparison between the solubility and speciation and solubility of stibnite predicted in this study and experimental data at a) 25°C and b) 90°C.

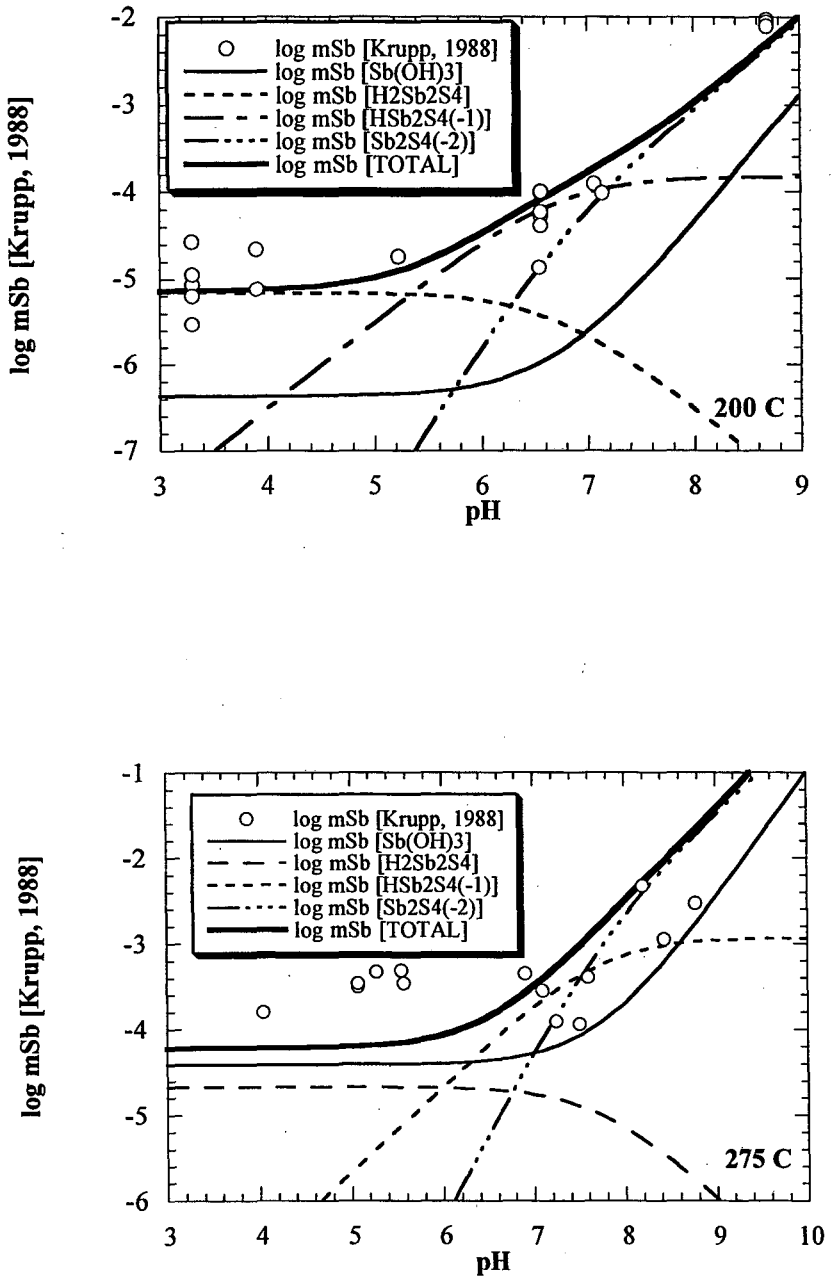

Figure 3.12 Comparison between the solubility and speciation and solubility of stibnite predicted in this study and experimental data at c) 200°C and d) 275°C.

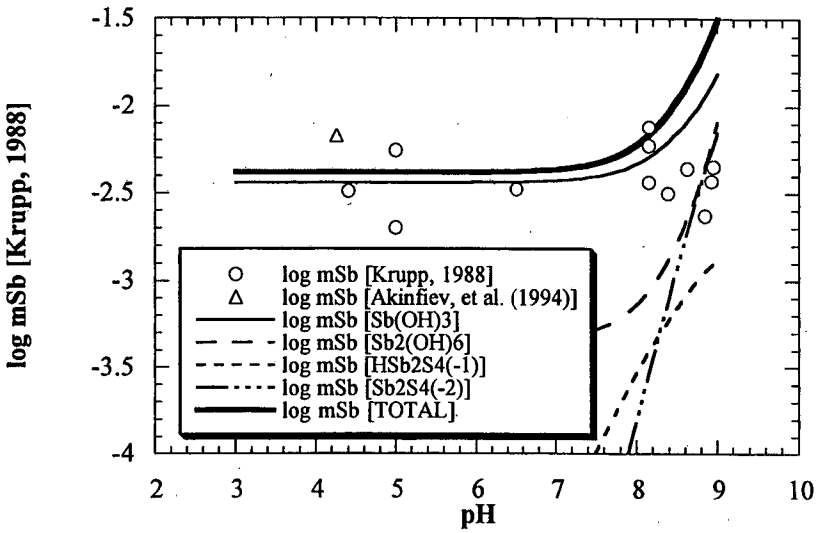

Figure 3.12 Comparison between the solubility and speciation and solubility of stibnite predicted in this study and experimental data at e) 350°C.

of orpiment in sulfide solutions to least squares regression and multicomponent equilibrium calculations and identified trimeric As sulfide species as the most likely oligomerization number. This assertion has since been corroborated by the solubility study of Webster (1990) and Eary (1992). Also, Helz, et al. (1995) employed ab initio quantum mechanical predictions and spectroscopic data to confirm the stability of As-S trimers relative to the dimers advocated by Akinfiev, et al. (1992) in their calculation of HKF equation of state parameters of As sulfide species. In contrast to these findings, Helz, et al. (1995) showed that in solutions undersaturated with respect to orpiment, monomeric species are stable. Also, the stoichiometry of As species in acidic, saturated sulfide solutions remains elusive.

3.5.1 $H_3AsO_3^0$

The HKF equation of state parameters for this species were previously derived by Pokrovski, et al. (1996). Although their method was perfectly valid, the parameters were re-derived in this study in order to obtain the error envelope for reaction (3.18) below. In this study, $[\Delta\overline{G}_f^o]$ was obtained from the following two reactions:

$$0.5\ As_2S_3(orp) + 3\ H_2O = H_3AsO_3^0 + 1.5\ H_2S^0(aq); \qquad (3.18)$$

$$As_2O_3(ars) + 3\ H_2O = 2\ H_3AsO_3^0; \qquad (3.19)$$

using the mean value of $[\Delta\overline{G}_f^o]$ from the equilibrium constant of Mironova, et al. (1984) (reaction (3.18)), Webster (1990) (reaction (3.18)) and Baes and Mesmer (1976) (reaction (3.19)), and also by invoking the thermodynamic properties for the solid phases tabulated in Table 4 of Pokrovski, et al. (1996) (Table 3.5 of this study). $[\overline{S}^o]$ was then calculated from the temperature dependence of the equilibrium constant of reaction (3.19) and the entropies of As_2O_3 (ars) (Table 3.5) and H_2O (Johnson, et al. (1992)). $[\omega]$ was obtained using the $[\overline{S}^o]$-$[\omega]$ correlation for nonvolatile, neutral aqueous species corrected in this study by removing round-off errors:

$$\omega = -1514.2\overline{S}^o + 340000 \qquad (3.20)$$

Solid phase	$\Delta_f G°_{290}$ [a]	$\Delta_f H°_{298}$ [a]	$S_{298}°$ [b]	$C_{p298}°$ [b]	$V_{298}°$ [c]	a [b]	b [d] x 10^{-3}	c [e] x 10^{5}	T [°C] for C_p
arsenolite (As_2O_3)	-137640	-156930	25.67	23.15	51.12	20.98	17.73	-2.70	(25-275)
claudetite (As_2O_3)	-137730	-156600	27.09	23.19	47.26	23.86	10.74	-3.44	(25-315)
orpiment (As_2S_3)	-20550	-20700	39.10	27.53	70.50	22.73	13.82	0.605	(25-307)
arsenic (As)	0	0	8.39	5.89	12.96	5.23	2.22	0	(25-727)
realgar (AsS)	-7930	-8380	12.96	11.37	29.8	12.94	-0.0133	1.396	(25-267)
[f]arsenopyrite (FeAsS)	-26200	-25200	25.9	17.6	26.42	15.03	9.7	0.34	(25-727)
[f]loellingite ($FeAs_2$)	-12450	-10400	30.4	11.05	27.51	5.4	7.3	0	(25-977)

Table 3.5 Thermodynamic properties of arsenic solid phases from Pokrovski, et al. (1996) unless otherwise indicated. a. cal mol^{-1} b. cal mol^{-1} K^{-1} c. cm^3 mol^{-1} d. cal mol^{-1} K^{-2} e. cal K mol^{-1} f. Naumov, et al. (1974)

(Figure 3.4.c) (Shock, et al., 1989). [$\overline{V}^o$] was calculated from the density measurements of As_2O_3-H_2O solutions (Anderson and Story, 1923). Finally, based on the spectroscopic measurements which identified the region where $H_3AsO_3^0$(aq) predominates (Pokrovski, et al., 1996), [$\overline{C}^o_{Pr}$] was determined from regression of the experimental data of arsenolite and claudetite to 90°C (Anderson and Story (1923); Linke (1958); Stranski, et al. (1958); Baes and Mesmer (1976); Pokrovski, et al. (1996)), and orpiment to 300°C (Stranski, et al. (1958); Mironova, et al. (1984); Webster (1990); Pokrovski, et al. (1996)).

Table 3.6 reports the resulting HKF equation of state parameters for this species, and Figure 3.6 shows that the species is consistent with the correlations of equations (3.13) and (3.14). Figure 3.13 additionally depicts the fact that the solubility is well-described by the predictions.

3.5.2 $H_6As_2O_6^0$

Because Gout, et al. (1997) identified $H_6As_2O_6^0$ in solutions with As concentrations between 0.5 and 2.0 molal, an attempt was made in this study to extract HKF equation of state parameters from the three claudetite solubility experiments points which produced solubilities in this range. [$\overline{S}^o$] was obtained by regression after subtracting the contribution from $H_3AsO_3^0$ and assuming that the thermodynamic properties of dimerization were equal to zero for all other parameters (see *Section 3.4.2*). The resulting HKF parameters for $H_6As_2O_6^0$ are shown in Table 3.6. Although regression calculations were only performed between 98 and 150°C, Figure 3.14 shows that the solubility of claudetite is *predicted* at all temperatures. This may at first appear to be a "good" result; however, Gout, et al. (1997) further demonstrated that additional polymeric species become important above 150°C. The importance of $H_6As_2O_6^0$ above 150°C remains an unresolved issue and the HKF equation of state parameters should not be used at higher temperatures until the relative importance of this species has been demonstrated.

Species	$\Delta G°_f$ [a]	$S°$ [b]	$C_{pr}°$ [b]	$V°$ [c]	a_1 [d] x 10	a_2 [a] x 10^{-2}	a_3 [e]	a_4 [f] x 10^{-4}	c_1 [b]	c_2 [f] x 10^{-4}	ω [a] x 10^{-5}
$H_3AsO_3°$	-152906	48.9	45.43 ± 9.32	49	8.3349	12.5701	0.8348	-3.2986	29.0490	6.2199	-0.4004
$H_6As_2O_6°$	-305812	74.73 ± 10.82	90.86	98	14.9051	28.6128	-5.4517	-3.9619	51.9132	15.4744	-0.8
$H_2AsO_3^-$	-140330	26.4	-3.24	25.97	5.7312	6.2127	3.3260	-3.0358	15.5577	-3.6946	1.2220
$^gHAsO_3^{2-}$	-123782	-3.6	-52.78	-0.13	2.8610	-0.7958	6.0724	-2.7461	5.7400	-13.7851	3.2979
$^gAsO_3^{3-}$	-105500	-44.60	-113.50	-17.8	1.199	-4.8540	7.6580	-2.5779	-9.3841	-26.154	5.5349
$H_3As_3S_6^0$	-35184	114.26 ± 0.14	141.73	83.37	12.7043	23.2392	-3.3460	-3.7397	76.1989	25.8367	-1.3902
$H_2As_3S_6^{-1}$	-30825	96.61	112.61	74.37	11.9959	21.5093	-2.6681	-3.6682	73.4542	19.9048	0.15877
$HAs_3S_6^{-2}$	-20057	82.66 ± 0.20	89.58	67.25	11.6409	20.6426	-2.3285	-3.6324	76.8852	15.2133	1.9918

Table 3.6 HKF equations of state parameters and standard molal properties referring to 25° C and 1 bar of aqueous arsenic complexes a. cal mol^{-1} b. cal mol^{-1} K^{-1} c. cm^3 mol^{-1} d. cal mol^{-1} bar^{-1} e. cal K mol^{-1} bar^{-1} f. cal K mol^{-1} g. Akinfiev, et al. (1992)

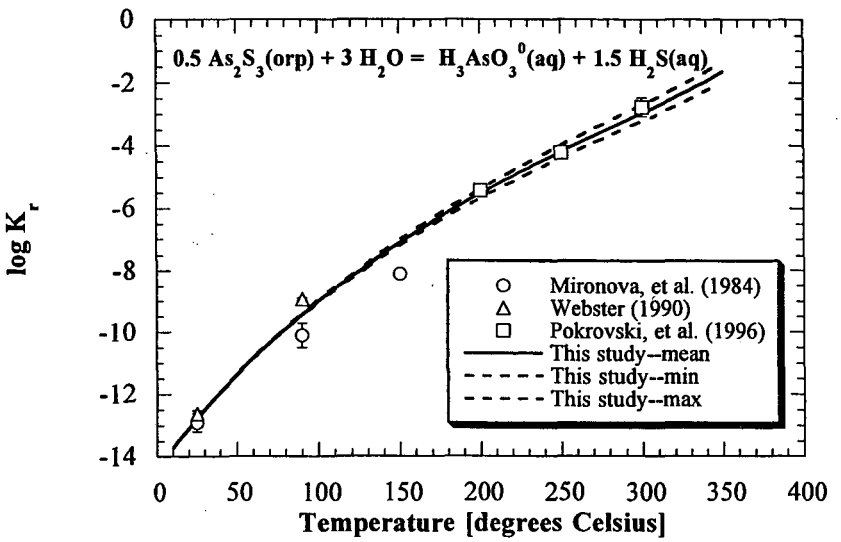

Figure 3.13 Predicted equilibrium constants for reaction (3.18) based on the HKF equation of state parameters for $H_3AsO_3^0$ derived in this study.

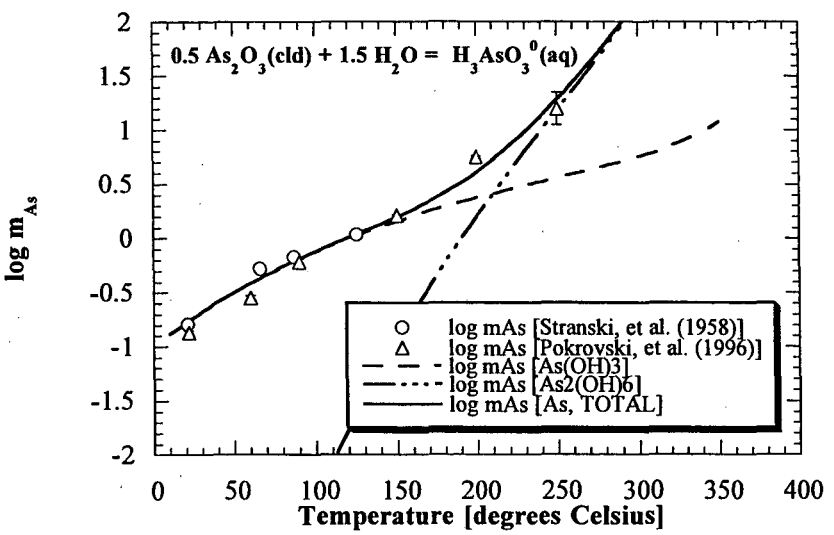

Figure 3.14 Predicted solubility of claudetite based on the HKF equation of state parameters derived in this study.

3.5.3 $H_2AsO_3^{-1}$

The thermodynamic properties of this species were originally derived by Shock and Helgeson (1988) using values of $[\Delta\overline{G}_f^o]$ and $[\overline{S}^o]$ obtained from Wagman, et al. (1982), and $[\overline{C}_{Pr}^o]$, $[\overline{V}^o]$, and $[\omega]$ from their correlations for oxyanions. Table 3.6 reports the values updated in this study to reflect the correlations for nonmetal hydrogen-bearing acids and oxyanions (Shock, et al. (1997)).

3.5.4 $HAsO_3^{-2}$

The HKF equation of state parameters for this species as well as the fully deprotonated AsO_3^{-2} were derived by Akinfiev, et al. (1992) and no further refinements were made in this study (see Table 3.6).

3.5.5 $H_3As_3S_6^0$

The occurrence of this species has been the subject of considerable debate. Mironova and Zotov (1980) originally reported the presence of a neutral sulfide complex of the form $H_2As_2S_4^0$ in their experiments at 90°C and pH of 1.19. Spycher and Reed (1989) re-interpreted this data point to be $H_3As_3S_6^0$ based on their calculations which showed that trimers are favored over dimers. Mironova, et al. (1991) later revised their earlier hypothesis based on the fact that the solubility of As was not found to change with total reduced sulfide concentration at 25°C and 90°C in acidic solutions as would be predicted from the following reaction:

$$3\ As_2S_3\ (orp) + 3\ H_2S\ (aq) = 2\ H_3As_3S_6^0 \qquad (3.21)$$

(Figure 3.15). They instead proposed that the species $As_2S_3 \bullet H_2O$ is important in acidic, sulfide solutions. Finally, Helz, et al. (1995) suggested the experiments of Mironova, et al. (1991) with the highest m_{H2S} suffered from experimental contamination or colloid formation

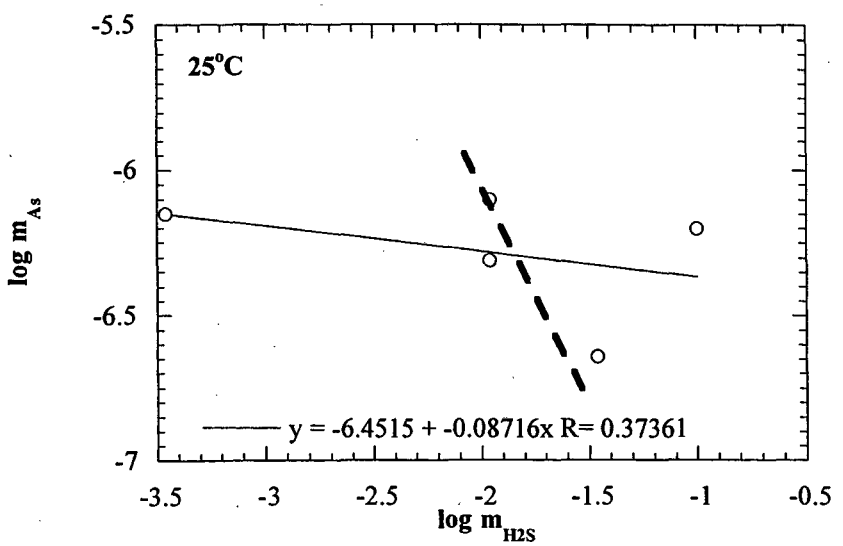

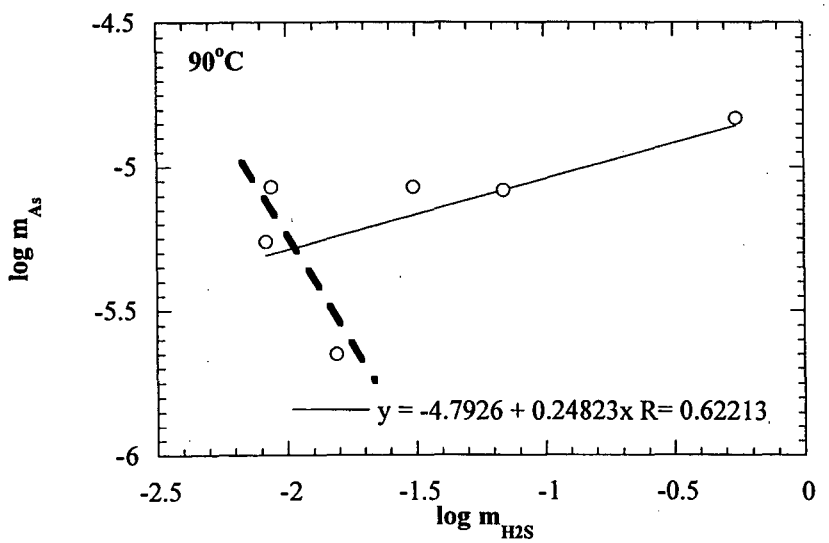

Figure 3.15 Speciation plots for orpiment in acidic solutions (Mironova, et al., 1991) at a) 25°C and b) 90°C. A slope of zero for the plotted experimental data (open circles) was used by these authors to advocate the species $As_2S_3 \bullet H_2O$. The three data points at each temperature which corresponded to a slope of -1.5 (given by the heavy dashed line) were used to calculate the HKF equation of state parameters for $H_3As_3S_6^0$ (see text for discussion).

because if $As_2S_3 \bullet H_2O$ were an important species then the solubility of amorphous orpiment would have been significantly greater than that reported by Eary (1992).

There is currently not enough information to resolve this issue. Because evidence exists for the species $H_2As_3S_6^{-1}$ and $HAs_3S_6^{-2}$, and because the Sb sulfide series described in the previous section had a neutral complex, it was assumed in this study that $H_3As_3S_6^0$ also exists. To reconcile this tentative assumption with the results of Mironova, et al. (1991), only those data points which conformed to the predicted slope of -1.5 in Figure 3.15 were included in the regression calculations (the heavy dashed lines in the figure). The removed points at 90°C incidentally coincided with those points described as erroneous by Helz, et al. (1995). Despite the assertions of Mironova, et al. (1991) that a sulfide complex was present at 150°C, no evidence was found in this study after the contribution due to $H_3As_3S_6^0$ was subtracted. Consequently, regression calculations were limited to the log K_r data for reaction (3.21) at 25 and 90°C.

Figure 3.16 shows the resulting predictions for the case where $[\Delta\overline{G}_f^o]$ was calculated from the equilibrium constant for equation (3.21), $[\overline{S}^o]$ was regressed, and $[\overline{C}_{Pr}^o]$, $[\overline{V}^o]$, and $[\omega]$ were obtained from the same correlations used for the Sb sulfide species. To confirm the validity of this approach, the isoactivity line for the reaction:

$$3\ H_3AsO_3^0 + 6\ H_2S(aq) = H_3As_3S_6^0 + 9\ H_2O \qquad (3.22)$$

was drawn at a constant log m_{As} of -5. Because predictions based on the contribution of $H_3AsO_3^0$ to the total solubility of As at 150°C demonstrated that the species $H_3As_3S_6^0$ was completely masked in the data of Mironova, et al. (1991), the data points in Figure 3.17 should lie below the curve in the $H_3AsO_3^0$ field. This is the case for all but one point in Figure 3.17, indicating that the database derived for this study is at least internally consistent. Although the methodology adopted for this species limits its validity to temperatures below 150°C, it was included in the higher temperature calculations which follow. This is obviously

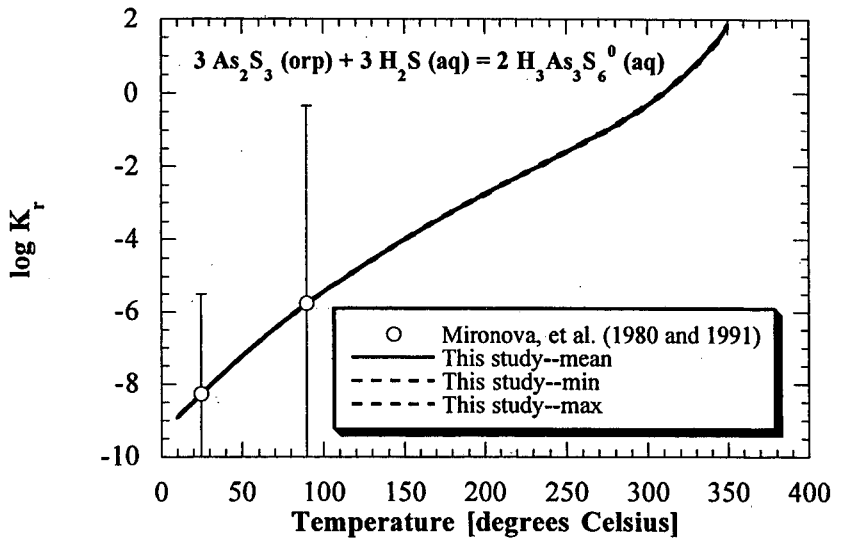

Figure 3.16 Predicted equilibrium constants for reaction (3.22) based on the HKF equation of state parameters for $H_3As_3S_6^0$ derived in this study.

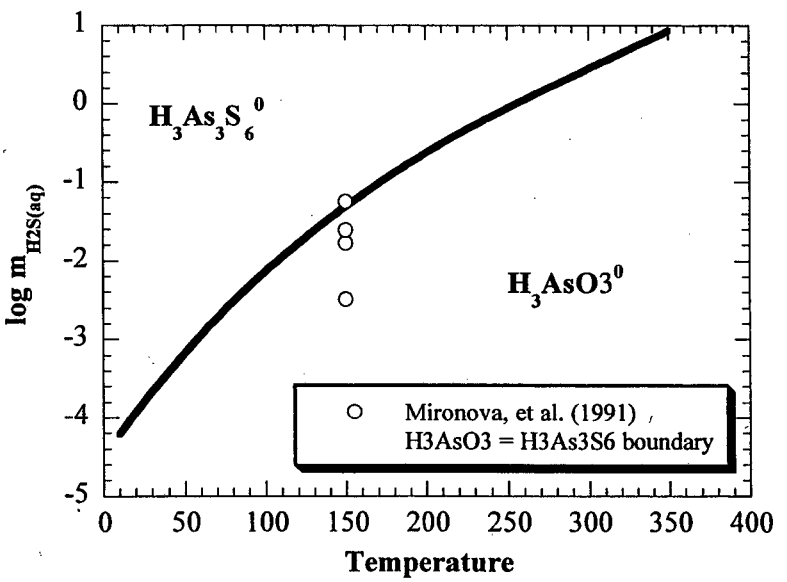

Figure 3.17 Relative stability fields for the two species $H_3AsO_3^0$ and $H_3As_3S_6^0$ predicted in this study. The open circles are experimental data which were found to lie within the $H_3AsO_3^0$ field based on the HKF parameters for $H_3AsO_3^0$. The fact that three of these points continue to fall within this region based on the extrapolation of the equilibrium constant of reaction (3.21) at 90°C was used as justification for the approach adopted in the text.

an unsatisfactory resolution to the problem of As speciation, but is the best that could be done with the limited available experimental data.

3.5.6 $H_2As_3S_6^{-1}$

Many different investigators have obtained information regarding the solubility of As as the complex $H_2As_3S_6^{-1}$. Figure 3.18 shows these various studies written in terms of aqueous species so that the solubility study of Eary (1992) (who measured the solubility of amorphous orpiment) could be included. The reaction shown in the figure is:

$$1/2\ H_2As_3S_6^{-1} + 3\ H_2O + 1/3\ H^+ = H_3AsO_3^0 + 2\ H_2S(aq) \qquad (3.23)$$

which was calculated for the studies of Mironova and Zotov (1980), Mironova, et al. (1991), and Webster (1992) from the equilibrium constant for the reaction:

$$3/2\ As_2S_3 + 3/2\ H_2O + 1/2\ H^+ = H_2As_3S_6^{-1}, \qquad (3.24)$$

and from the $[\Delta\overline{G}^o]$ of $H_3AsO_3^0$ obtained in this study. Eary (1992) directly measured the solubility of both $H_3AsO_3^0$ and $H_2As_3S_6^{-1}$ in equilibrium with amorphous orpiment and subsequently subtracted out the solid phase, so that no calculation was required. The dashed line refers to the study of Spycher and Reed (1989) recalculated by Eary (1992) in terms of this reaction.

In order to derive the thermodynamic data for this species, it was first necessary to correct the 90°C data of Webster (1992) for the dissociation constant of Suleimenov and Seward (1997) because they used the values reported by Murray and Cubiccioti (1983) which differ from those of Suleimenov and Krupp (1997) by 0.1 logarithmic units at this temperature. Given the pH and the TFS, aqueous sulfur speciation was performed by iterating over the mass action and mass balance equations for sulfur, while updating the ionic strength and activity coefficients at each iteration. The data of Mironova, et al. (1980 and 1991) had to be similarly treated in order to determine the equilibrium constants for reactions (3.23) and (3.24).

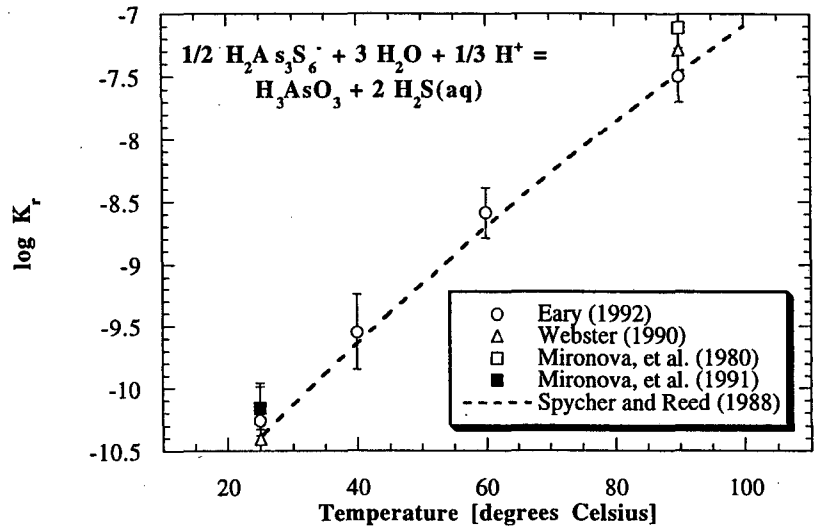

Figure 3.18 Comparison of calculated equilibrium constants for reaction (3.23) using HKF equation of state parameters for $H_3AsO_3^0$ derived in this study to re-compute the experiments of Webster (1990), Mironova, et al. (1980), and Mironova, et al. (1991) in terms of this reaction.

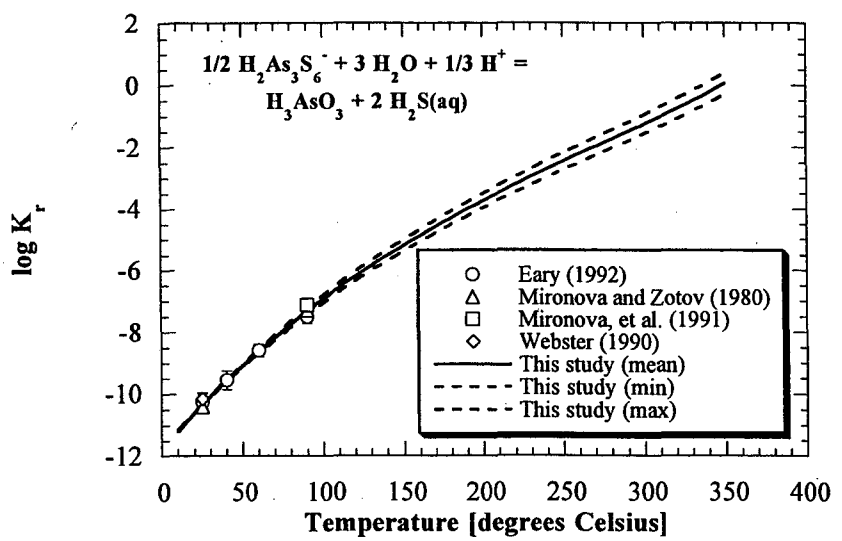

Figure 3.19 Predicted equilibrium constants for reaction (3.23) based on the HKF equation of state parameters for $H_3AsO_3^0$ and $H_2As_3S_6^{-1}$ derived in this study.

Once the aqueous speciation was known for each set of experiments, the HKF equation of state parameters were derived analogously to $H_3As_3S_6^0$. Figure 3.19 shows the resulting predictions to 350°C.

3.5.7 $HAs_3S_6^{-2}$

The data of Mironova, et al. (1980 and 1991) provided the equilibrium constant data necessary to derive the HKF equation of state parameters for $HAs_3S_6^{-2}$. Because Mironova, et al. (1980 and 1991) attributed solubility to a dimer species, their experiments were re-speciated as above and the HKF parameters derived analogously. Figure 3.20 displays the resulting predictions.

3.5.8 Summary of As complexes

Figure 3.21 compares the results of the HKF equation of state parameters derived in this study with the experimental data of Mironova and Zotov (1980). This plot was generated using the same technique as Figure 3.12 above (*Section 3.4.7*). The ionic strength was selected to be 0.25 and the log TFS was chosen as -2.0 to reflect the average value for this suite of experiments. Figure 3.21 displays the deprotonation of the As-sulfide species as the pH increases. The predictions are slightly overestimated for $H_2As_3S_6^{-1}$ as predicted by the relative location of the Mironova and Zotov (1980) data in Figures 3.18 and 3.19. Although $H_3AsO_3^0$ is a secondary species under these experimental conditions, Figure 3.17 demonstrates that it becomes more important at lower m_{H2S} and at higher temperatures.

3.6 Au aqueous species

The hydroxide and sulfide complexes of gold for which experimental solubilities have been derived include: $Au(OH)^0$; $Au(HS)^0$; and $Au(HS)_2^-$. In the discussion which follows, it is shown that Au solubilities predicted from these studies vary by as much as three orders of

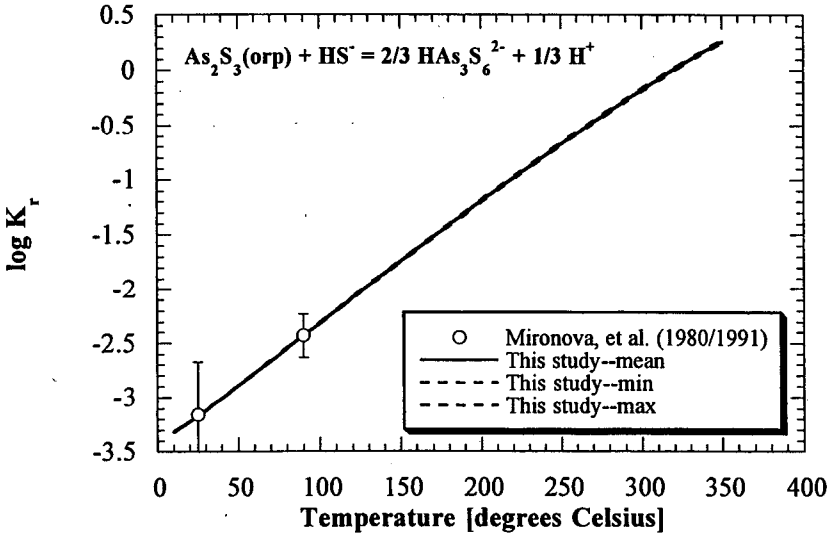

Figure 3.20 Predicted of the equilibrium constants for the dissolution of orpiment based on the HKF equation of state parameters for $HAs_3S_6^{-2}$ derived in this study.

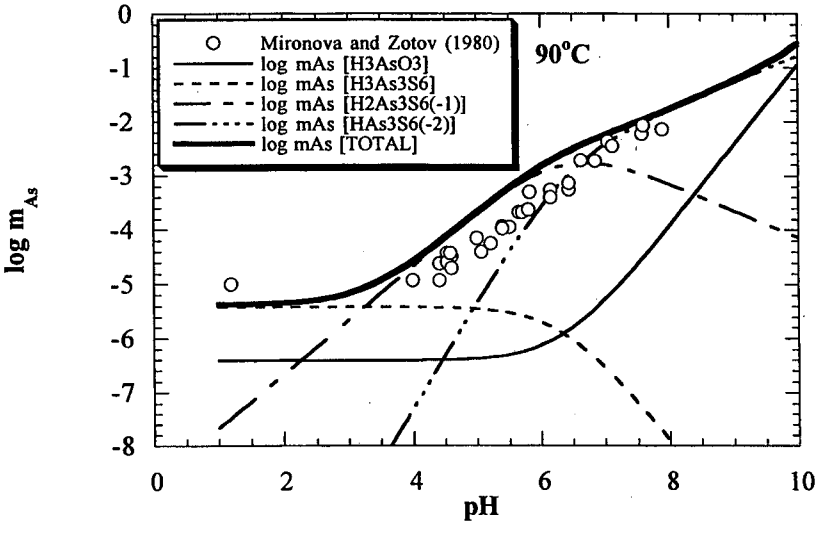

Figure 3.21 Prediction of the solubility of orpiment at 90°C based on the HKF equation of state parameters derived in this study.

magnitude. The HKF equation of state parameters for the sulfide species were derived in this study with error envelopes encompassing these differences. This chapter closes with a discussion of Au heteropolynuclear complexes.

3.6.2 $Au(OH)^0$

The HKF equation of state parameters for this species were derived from the solubility study of Zotov, et al. (1985). Because the high pressure experiments which used different oxidation buffers produced inconsistent equilibrium constants for the reaction:

$$Au\ (c) + 0.5\ H_2O + 0.25\ O_2\ (g) = Au(OH)^0 \qquad (3.25)$$

only the experiments performed at 500 bars and temperatures from 300 to 500°C were included in the regression calculations. $[\Delta\overline{G}_f^o]$ and $[\omega]$ were selected as the regression parameters, and $[\overline{S}^o]$, $[\overline{C}_{Pr}^o]$, and $[\overline{V}^o]$ were obtained from the correlations for the first hydroxylation of a monovalent cation (Shock, et al., 1997).

Table 3.7 reports that the predicted Born parameter $[\omega]$ is consistent the correlation of Figure 3.4.c. Also, Figure 3.22 shows the predictions for the equilibrium constant of reaction (3.25). For comparison, Zotov, et al. (1985) reported an equilibrium constant estimate of Letnikov and Vilor (1981) to be less than -10.0.

3.6.3 $Au(HS)^0$

Gibert, et al. (1998) conducted the most recent series of experiments on the solubility of Au in acidic fluids. After measuring their own solubilities, they recalculated the experiments of Hayashi and Ohmoto (1991) and Benning and Seward (1996) in terms of the thermodynamic properties of H_2S(aq) and HS^- available from the existing SUPCRT database. They subsequently found that their own solubilities were consistent with those of Hayashi and Ohmoto (1991), but advocated the aqueous species $Au(HS)^0$ rather than $HAu(HS)_2^0$ to

Species	ΔG°_{f} [a]	S° [b]	C_{pr}° [b]	V° [c]	a_1 [d] x 10	a_2 [a] x 10^{-2}	a_3 [e]	a_4 [f] x 10^{-4}	c_1 [b]	c_2 [f] x 10^{-4}	ω [a] x 10^{-5}
$Au(OH)^0$	-27441 ± 1032	26.34	-21.03	17.13	4.1579	2.3709	4.8315	-2.8770	-4.7666	-7.3184	0.1441 ± 0.0967
$Au(HS)^0$	8527	63.93 ± 6.26	-63.88	41.96	7.5067	10.5479	1.6272	-3.2151	-31.1409	-16.0480	-0.0008 ± 0.3219
$Au(HS)_2^-$	3821	85.18 ± 23.97	-105.11 ± 98.86	83	13.2348	24.5345	-3.8536	-3.7933	-52.1638	-24.4456	0.3319
$H_2AuSbS_3^0$	*-41263*[g]	*11.25*	*-28.23*	*74.74*	*12.0497*	*21.6408*	*-2.7196*	*-3.6736*	*-8.7414*	*-8.7860*	*0.1696*

Table 3.7 HKF equation of state parameters and standard molal properties referring to 25° C and 1 bar of aqueous gold complexes a. cal mol^{-1} b. cal mol^{-1} K^{-1} c. cm^3 mol^{-1} d. cal mol^{-1} bar^{-1} e. cal K mol^{-1} bar^{-1} f. cal K mol^{-1} g. Italics indicate that the parameters were found to be inconsistent with field observations (see **Chapter 4**).

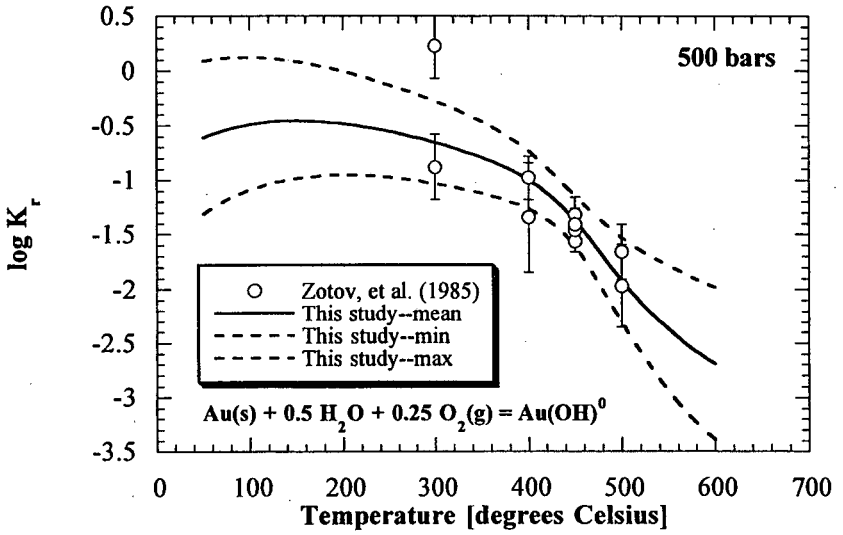

Figure 3.22 Predicted equilibrium constants for reaction (3.25) based on the HKF equation of state parameters for $Au(OH)^0$ derived in this study.

explain the experimental results. They additionally found a discrepancy in Au solubility of up to 3 orders of magnitude between their study and Benning and Seward (1996).

In order to resolve these differences, the first step in this investigation was to speciate the three sets of experiments in terms of the SUPCRT database (updated for $H_2S(aq)$, $NaHS^0$ (aq), and HS^-). The method adopted to calculate aqueous speciation for these experiments and all gold sulfide solutions which follow was the use of the computer speciation software Selektor-A (Kulik, et al., 1997), which incorporates the SUPCRT database, uses a convex programming technique to minimize the Gibbs function, and calculates activity coefficients in a manner analogous to Helgeson, et al. (1981). This particular code was selected because it encompasses the full range of conditions available to the HKF equation of state (1000°C and 5000 bars), and thus allowed calculation of the experiments of Gibert, et al. (1998) at 500 bars. In all experiments, only the average parameters for any reported experimental run were used.

In the study of Gibert, et al. (1998) metallic Au was reacted in a rocking flexible cell hydrothermal apparatus with a solution containing 0.5 *m* KCl solution and buffered with respect to Quartz-K-feldspar-Muscovite and either Pyrite-Pyrrhotite-Magnetite or Pyrite-Hematite-Magnetite. To simplify the modeling of these experiments, the contribution of gold to the overall speciation was neglected. Also, to account for solid solution in pyrhhotite, the corresponding activity coefficient was set to 0.5 in agreement with the findings of Barker and Parks (1986). Convergence was achieved in this study by titrating the various mineral phases into solution using the speciation from the previous iteration as an initial approximation. This procedure was terminated after precipitation of all reported mineral phases occurred.

The experimental data of Hayashi and Ohmoto (1991) had to be treated slightly differently to account for their experimental design. Hayashi and Ohmoto (1991) carried out their experiments in sealed, silica glass capsules containing $S^0 + H_2O +$ Au wire $\pm$ NaCl $\pm$

Na_2SO_4. Because $H_2S(g)$ was allowed to exist in equilibrium with the solution, they had to calculate the $m_{H2S(aq)}$ from the total measured sulfide from quenched solutions using the relative vapor [V_V] to liquid volumes [V_L] of the capsules and the Henry constant for H_2S [K_H]. They then calculated the remaining speciation from the laws of mass action, mass balance, and charge balance, given the total sodium, chloride, and sulfate in their runs.

In order to perform speciation calculations in this study, the relative vapor [V_V] to solution [V_L] volumes first had to be determined because this information was not reported. The following equation was used for this calculation:

$$V_V = \left[\left(\frac{n_{H_2S,T}}{P_{H2S}}\right)1000K_H RT - V_T RT\right]\left(\frac{1}{1000K_H - RT}\right) \qquad (3.26)$$

where [$n_{H_2S,T}$] was the total number of moles of measured reduced sulfide, [P_{H2S}] was their reported vapor pressure of $H_2S(g)$, and [K_H] was the Henry constant for H_2S taken from Drummond (1981) for solutions of similar NaCl concentrations. Once [V_V] was estimated, $m_{H2S(aq)}$ was determined from:

$$m_{H_2S(aq)} = n_{H_2S,T} \Big/ \left(\frac{V_V K_H}{RT} + \frac{V_L}{1000}\right) \qquad (3.27)$$

where [K_H] is the Henry constant from Suleimenov and Krupp (1994) used to fix the HKF equation of state parameters for $H_2S(aq)$ described in *Section 3.2*. Due to the fact that Suleimenov and Krupp (1994) found that K_H was strongly dependent on salt concentration, and given that they restricted their measurements of the salting coefficient to temperatures below 320°C, only the dilute runs of Hayashi and Ohmoto (1991) were included in the Selektor-A calculations which followed. The molality of S, Na, O was used as input parameters, and $H_2(g)$ was titrated into the solution until convergence was reached with the calculated activity of $H_2S(aq)$. An additional iterative loop was performed by updating the ionic strength and recalculating [K_H]; however, it was found that the shift in ionic strength

was minor and did not alter the equilibrium constants within the accuracy of the measurements.

The final set of experiments which were re-speciated for $Au(HS)^0$ were from the study of Benning and Seward (1996), who measured the solubility of a flexible gold reaction cell containing a solution of $H_2S + H_2O + H_2(g) \pm H_3PO_4$. During their experimental runs, solutions were drained from the cell and separated into a vapor and aqueous phase. A gas chromatograph then measured the $H_2(g)$ concentration of the vapor phase, and total sulfide was determined iodometrically. The re-calculation of this study used the initial solution sulfur and H_3PO_4 content as input, and titrated for $f_{H2(g)}$.

In interpreting the preceding recalculated solubility experiments, the assumption was made that the dominant species in the experiments of Gibert, et al. (1998) and Hayashi and Ohmoto (1991) was $Au(HS)^0$ rather than $HAu(HS)_2^0$. Evidence for $Au(HS)^0$ was provided by Renders and Seward (1989) at 25°C, who plotted log $m_{Au,T}$ versus log $m_{S,T}$ and obtained a slope of 0.5 ($HAu(HS)_2^0$ would have produced a slope of 1.5). Also, the molecular orbital calculations of Tossell (1996) demonstrated that $Au(HS)^0$ is more thermodynamically stable than HAu(HS)2^0. Finally, Gibert, et al. (1998) suggested that interpretations of Hayashi and Ohmoto (1989) were tainted by the uncertainty of measuring the volume of silica tubes and large experimental scatter. Because Gibert, et al. (1998) also found that the solubilities of Benning and Seward (1996) were pH dependent even below a pH of 4.0, and because these results were corroborated in this study, the charged species $Au(HS)_2^{-1}$ likely controlled solubility in their experiments. Consequently, this data was omitted from the regression calculations for $Au(HS)^0$.

Before regression calculations were performed, the contribution of $Au(HS)_2^-$ (based on the HKF equation of state parameters described below) was subtracted from the experimentally observed values (assuming an activity coefficient for the complex equal to γ_{HS^-}). This

contribution was never greater than 3.5%. [$\Delta\overline{G}_f^o$] was then calculated from the solubility measurements of Renders and Seward (1989) at 25°C from the equilibrium constant for:

$$Au(s) + H_2S(aq) = AuHS^0 + 0.5\ H_2\ (g) \qquad (3.28)$$

after correcting for their measured solubilities in terms of $Au_2S(s)$ (see the discussion in the following section). [$\overline{V}^o$] was determined from the correlation for the standard partial molal volume of association of a monovalent ligand to a monovalent cation (Sverjensky, et al., 1997), and [$\overline{C}_{Pr}^o$] from the correlation for the hydroxylation monovalent cations (Shock, et al., 1997). Although this latter correlation has *no* experimental basis, any attempt to retrieve [$\overline{C}_{Pr}^o$] from regression overfit the data and resulted in an equilibrium constant with two inflection points between 400 and 600°C. Finally, [$\overline{S}^o$] and [ω] were calculated from regression.

Table 3.7 reports the subsequent equation of state parameters for this species. The Born parameter is inconsistent with the correlation of equation (2.50); however, all attempts to retrieve this parameter from this correlation poorly described the data. Figure 3.23 shows the predicted equilibrium constants for reaction (3.28). Although the data is well-described within the temperature range of the experiments, extrapolation of the equilibrium constant outside of this region is wrought with uncertainty. Comparison between Figure 3.23.a and 3.23.b demonstrates that this error is exacerbated at higher pressures.

3.6.4 $Au(HS)_2^{-1}$

The solubility of Au at 25°C in neutral to mildly alkaline solutions has been investigated by Renders and Seward (1989), Wood, et al. (1994), and Zotov and Baranova (1995). Renders and Seward (1989) and Zotov and Baranova (1995) both performed their experiments on the solid phase $Au_2S(cr)$ and calculated equilibrium constants for the reaction:

$$0.5\ Au_2S(cr) + 1.5\ H_2S(aq) = Au(HS)_2^- + H^+. \qquad (3.29)$$

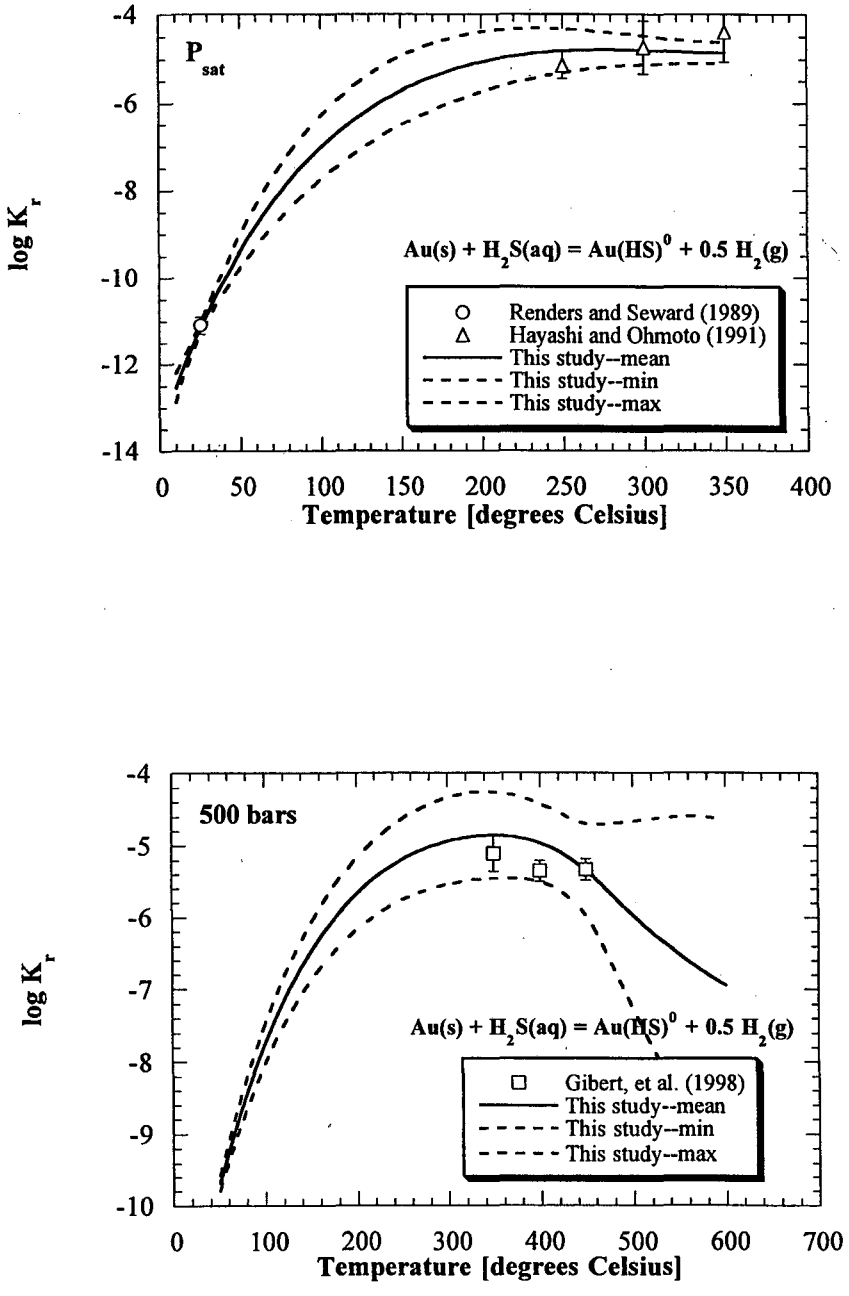

Figure 3.23 Predicted equilibrium constants for reaction (3.28) at a) water vapor saturation pressure and b) 500 bars based on the HKF equation of state parameters for $Au(HS)^0$ derived in this study.

In order to compare the results of these two studies to the high temperature experiments, it was first necessary in this study to recalculate Au solubility in terms of the reaction:

$$Au(s) + H_2S(aq) + HS^- = Au(HS)_2^- + 0.5\ H_2(aq). \qquad (3.30)$$

Because this necessitated a knowledge of $[\Delta G^o]$ for the solid phase in reaction (3.29), a choice also had to be made between the thermodynamic information for $Au_2S(cr)$ provided by the stability product of De Cugnac-Pailliotet and Pouradier (1972) and the high temperature solid solution model of Barton (1980). Because the latter exhibited considerable scatter in the data and also consisted of an extrapolation from 170°C to 25°C, it was deemed less reliable and excluded from this study. Corroborating evidence for this selection is found from the experiments of Wood, et al. (1994), who directly investigated Au(s) at 25°C, and whose calculated solubility closely matches the results of the recalculation in this study (Figure 3.24).

The high temperature solubility studies which were re-speciated in this investigation included: Shenberger and Barnes (1989); Pan and Wood (1994); and Benning and Seward (1996). The first of these workers conducted their experiments in a chromium-lined, stainless steel rocking autoclave to which weighed amounts of gold foil, NaOH(s), and $Na_2SO_4(s)$ were added. The solution composition for each run varied depending upon the pH range which was desired (e.g. H_3PO_4 and KH_2PO_4 as dissolved components in solution were introduced into the cells in the more acidic runs). H_2S was a common component in all experiments and was added as a weighed amount of $H_2S(g)$. Samples were taken to measure Au and total sulfide content.

As an example of how this experimental data had to be treated before speciation calculations were performed, those experiments with the oxidation state buffered by excess $H_2(g)$ required knowledge of the partial pressures of $H_2O(g)$, $H_2S(g)$ and $H_2(g)$. m_{H2S} was first calculated from:

$$m_{H2S} = m_{T,S} - m_{NaHS} \qquad (3.31)$$

where m_{NaHS} is given by the reaction:

$$NaOH(s) + H_2S(g) = NaHS(aq) + H_2O \qquad (3.32)$$

because in the presence of excess $H_2S(g)$, all NaOH converts quantitatively to the electrolyte NaHS. P_{H2S} was then calculated from the Henry's constant data of Suleimenov and Krupp (1994), using the salting coefficient corresponding to the quantity of NaOH added, and the fugacity for $H_2S(g)$ derived from the corresponding states equation of Lee and Kesler (1975). After the vapor pressure of water was determined from the equations of Hass (1976) for the vapor pressure over equivalent NaCl solutions, $P_{H2}(g)$ was derived from:

$$P_{H2}(g) = P_{Total} - P_{H2O(g)} - P_{H2S(g)}. \qquad (3.33)$$

This subsequently allowed determination of $f_{H2(g)}$ from the fugacity coefficients in Shaw and Wones (1964). Given the final composition of the fluid, $H_2(g)$ titration was performed in Selektor-A until the outputted fugacity matched the calculated $f_{H2(g)}$. An additional iteration was also performed using the new ionic strength to adjust $[K_H]$; however, this effect was again found to be unimportant.

The data for Wood, et al. (1994) was treated analogously to Shenberger and Barnes (1989) because they employed a similar experimental set-up. The major exception was that they did not buffer the oxidation state of the solution with $H_2(g)$. Finally, the data of Benning and Seward (1996) was treated the same as the acid runs described above, except that NaOH was added to the solutions rather than H_3PO_4.

Figure 3.24 shows the resulting equilibrium constants as a function of 1/T. An extensive discussion of possible differences between these values can be found in Gibert, et al. (1998); however, the only compelling evidence these authors found to select one dataset over another was that reaction (3.30) should be isocoulombic (i.e. $\Delta C^o_{P,R} = 0$, ΔH^o_R constant, and a plot of log K vs. 1/T a straight line). Although the high temperature data of Shenberger and Barnes (1989) are consistent with the low temperature data in this regard, Seward (1973) measured the solubility of Au(s) in a different experimental set-up as Benning and Seward

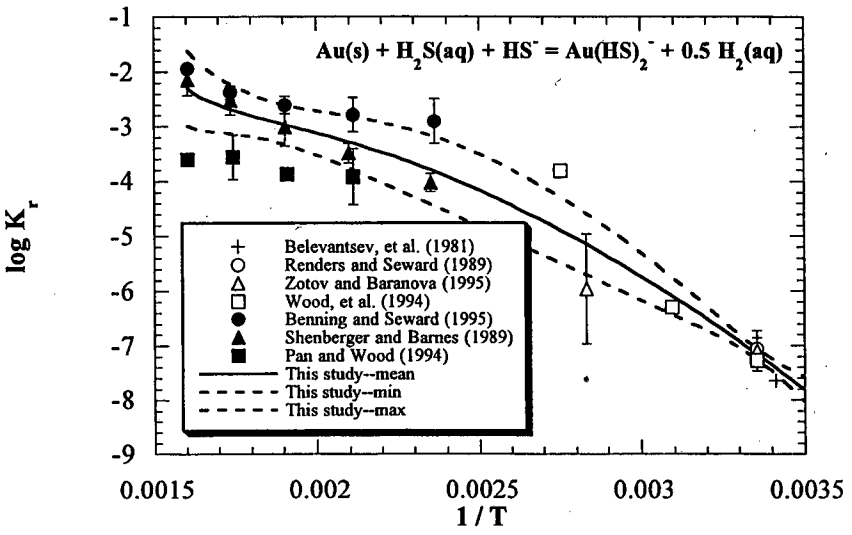

Figure 3.24 Predicted equilibrium constants for reaction (3.30) based on the HKF equation of state parameters for $Au(HS)_2^-$ derived in this study. The data has been plotted as a function of 1/T to compare the data to a pseudo-isocoulombic reaction which should plot as a straight line in the figure.

(1996) and found consistent results. Consequently, it was decided in this study to include all of the data from experiments at or below 500 bars discussed above in the regression analysis until further experimental evidence resolves these inconsistencies.

$[\Delta\overline{G}_f^o]$ for $Au(HS)_2^-$ was constrained by the mean value of the three equilibrium constants at 25°C. $[\overline{V}^o]$ was taken from $\left(\partial\Delta\overline{G}_f^o/\partial P\right)_{T=25^\circ C}$ measured by Zotov and Baranova (1995). Finally, $[\overline{S}^o]$, $[\overline{C}_{Pr}^o]$, and $[\omega]$ were calculated from regression on the experimental data in Figure 3.24. The predicted log K_r values are closest to the experiments of Shenberger and Barnes (1989), but the errors span one logarithmic unit.

3.6.5 $H_2AuSbS_3^0$

In the experiments of Nekrasov, et al. (1982), synthetic gold flakes and stibnite powder were suspended above a solution of 0.1 *n* HCl, saturated with 0.08-0.10 moles of H_2S at 25°C. The solution was then heated, bringing it into contact with the solid phases until equilibration was deduced from the charge stabilization of the autoclave. After determining the quantity of Sb and Au in solution, a one-to-one correlation between Au and Sb concentration in undersaturated stibnite solutions was found. Also, the solubility of Au was an order of magnitude higher in acidic, stibnite saturated solutions than in the Sb-free run.

In order to determine the solubility of Au as a heteropolynuclear complex in these experiments, Au and Sb speciation were determined from the reported solution chemistry using the method described in *Section 3.4.7*. It was subsequently found that the fO_2(g) buffer assemblage reported by Nekrasov, et al. (1982) was inconsistent with their reported Au solubility in their stibnite-free run. Their supposed Ti/TiO_2 buffer would have produced a log m_{Au} concentration of ≈-15, whereas Au solubility was instead found to lie between -5.5 and -6.0 logarithmic units. It was also found that the re-calculated Sb solubilities were two orders of magnitude lower than reported (Figure 3.25).

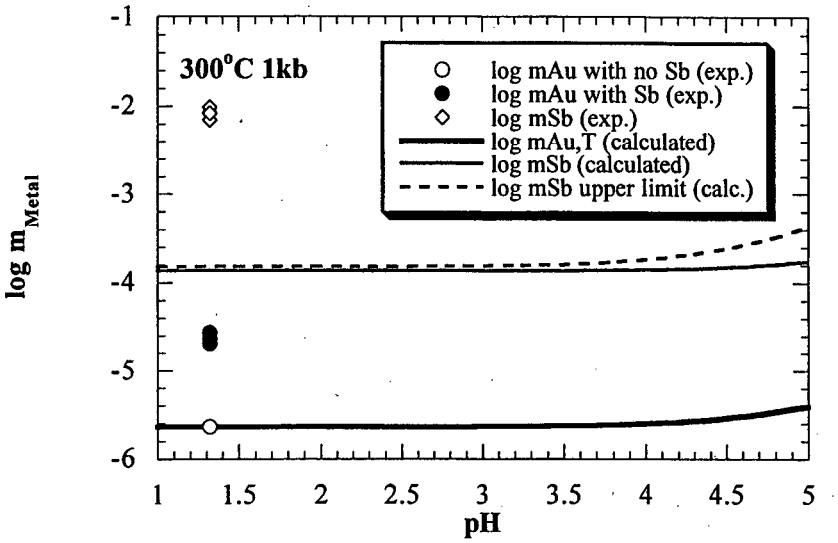

Figure 3.25 Comparison between the predicted and experimental solubility of Sb and Au in the aqueous solutions of Nekrasov, et al. (1982). The symbols represent experimental data, but the curves were drawn based on speciation calculations for a $fO_2(g)$ buffer dictated by reaction (3.30). The dissolution of stibnite is $fO_2(g)$ independent for a specified log $a_{H2S(aq)}$.

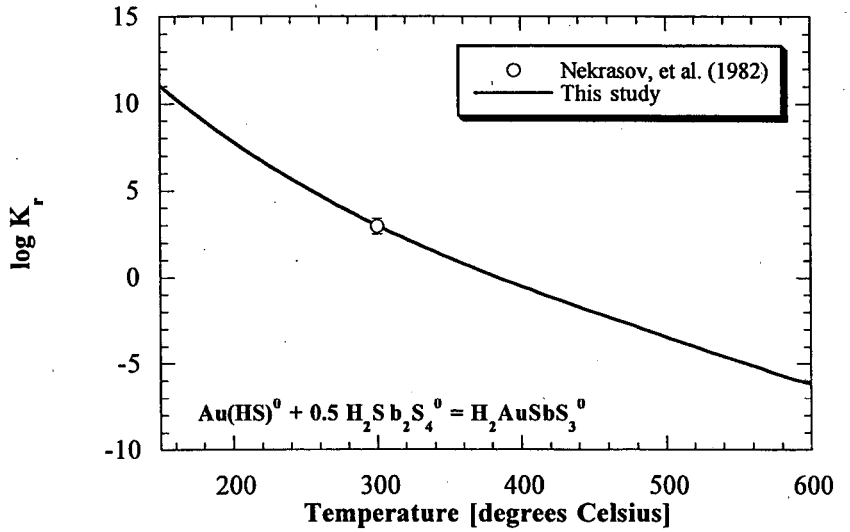

Figure 3.26 Predicted equilibrium constants for reaction (3.34) based on the HKF equation of state parameters for $Au(HS)_2^-$ and $H_2AuSbS_3^0$ derived in this study.

This first issue was resolved by assuming that the buffer assemblage controlling the redox state of the experiments was reaction (3.28). Because no $H_2(g)$ was added to the autoclave, this was the only possible reaction producing it. Secondly, because the solubility of stibnite is well constrained in this temperature range by the multiple experimental studies discussed above, the reported Sb solubility results of Nekrasov, et al. (1982) were presumed to be in error. Their high solubilities are not surprising given the inaccuracies of measuring solubility from the weight loss of stibnite powder suspended from the lid of the autoclave.

According to the re-speciated experiments of this study the dominant Au and Sb species in solution were $Au(HS)^0$ and $H_2Sb_2S_4^0$, respectively (Figure 3.25), and the simplest reaction equating these two species to a Au heteropolynuclear complex of 1:1 stoichiometry is:

$$Au(HS)^0 + 0.5\ H_2Sb_2S_4^0 = H_2AuSbS_3^0 \qquad (3.34)$$

which is exactly the same complex proposed by Nekrasov, et al. (1982) from chemical arguments for likely bonding between Au, Sb, and S. Ideally, confirmation of this species could be attained from measurements of Au in Sb-bearing solutions of varying pH and total reduced sulfide concentrations, or from spectroscopic measurements. Without this further validation, however, the HKF equation of state parameters for this species were derived in this study to investigate its effect on Au migration in the Carlin-type gold deposits. Due to the limited experimental evidence, these results should be viewed skeptically.

$[\overline{C}^o_{\mathrm{Pr}}]$ and $[\overline{V}^o]$ were acquired after assuming $\Delta C^o_{P,R} = 0$ and $\Delta V^o_R = 0$. $[\overline{S}^o]$ and $[\omega]$ were then estimated from the correlations represented by equations (3.14) and (3.20), respectively. Finally, $[\Delta\overline{G}^o_f]$ was derived from regression of the log K_r of reaction (3.34) at 300°C and 1013 bars. Table 3.7 reports the resulting HKF equation of state parameters, and Figure 3.26 displays the predicted equilibrium constant for reaction (3.34). The error bars are not shown in this figure, but are infinite for this one parameter, one equation regression. According to the figure, the importance of $H_2AuSbS_3^0$ increases at lower temperatures.

Additional experimental studies of Au-Sb complexing were performed by Nekrasov and Konyushok (1982) and Grigor'eva and Sukneva (1981), in neutral and moderately alkaline solutions, respectively. In the former investigation, no difference was found between Au solubility in experimental runs containing Sb at a pH of approximately 7.0. Although Grigor'eva and Sukneva (1981) demonstrated increased Au solubility with the addition of Sb, their results were not further explored in this study because their alkaline conditions (pH≈10.85) were extremely unlikely in the Carlin-type gold deposits.

3.6.5 Au/As heteropolynuclear complexes

The solubility of Au in As-bearing solutions was investigated by Akhmedzhanova, et al. (1989) at 200 and 300°C and approximately 1000 bars using a similar experimental procedure as Nekrasov, et al. (1982), with As_2S_3(orp) replacing Sb_2S_3(stb) as the solid phase and Au determined from spectrochemical analysis.

After speciating the fluid as before, an inconsistency between the reported fO_2(g) buffer assemblage and solution speciation was again found. Akhmedzhanova, et al. (1989) purported to have their experimental solutions buffered by the phases Fe/Fe_3O_4; however, Fe/Fe_3O_4 is not a buffer assemblage because there is an intermediate Fe oxidation state represented by the compound FeO. Also, given the concentration of H_2S(aq) in solution and the [ΔG^o] of the mineral phases Fe, FeO, Fe_3O_4, Fe_2O_3, FeS_2, and FeS from the SUPCRT database (using an activity coefficient of 0.5 for this latter mineral), the thermodynamically stable assemblage was calculated to be Fe, FeS, and FeS_2. According to Figure 3.27.a, if redox was controlled by Fe/FeS then the solubility of gold as $Au(HS)^0$ shown in the figure would have been greatly underestimated in the As-free run. In contrast, at the FeS/FeS_2 phase boundary, solubilities would have been higher than predicted and would also imply that the Fe phases in the autoclave were sulfidized.

The only way the experimental data for the As-free solution composition could be reconciled was to assume the fO_2(g) was again buffered by Au/Au(HS)^0; however, if this same buffer was operative in the Au-As experiments, As_2S_3(orp) would have been entirely converted into FeAsS(asp) (Figure 3.27.a). This is inconsistent with Akhmedzhanova, et al. (1989), who instead reported the formation of native As on the walls of the autoclave. Also, the solubility of As would have been lower than reported. It is more probable that after As precipitated, the solution became buffered by As(s)/FeAsS, As(s)/$H_3AsO_3^0$, or As(s)/$H_3As_3S_6^0$. Figure 3.27 shows that any of these assemblages produce As and Au solubilities within the scatter of the experimental results, *without* having to invoke a Au-As heteropolynuclear species.

Without knowing the exact mineral phases present in the solution at equilibrium, it is impossible to perform accurate speciation calculations to determine the importance of Au-As heteropolynuclear complexes. Consequently, no attempt was made in this study to retrieve the HKF equation of state parameters from these experiments. A careful investigation employing a H_2(g) buffer may better resolve the solubility and speciation of possible Au/As heteropolynuclear complexes. Nevertheless, because Akhmedzhanova, et al. (1989) found no change in Au solubility with As concentration in neutral solutions, the geologic importance of a Au-As complexing, if any, is likely restricted to acidic conditions. Consequently, its effect was estimated in this dissertation by examining a potentially analogous species $H_2AuSbS_3^0$ (**Chapter 4**).

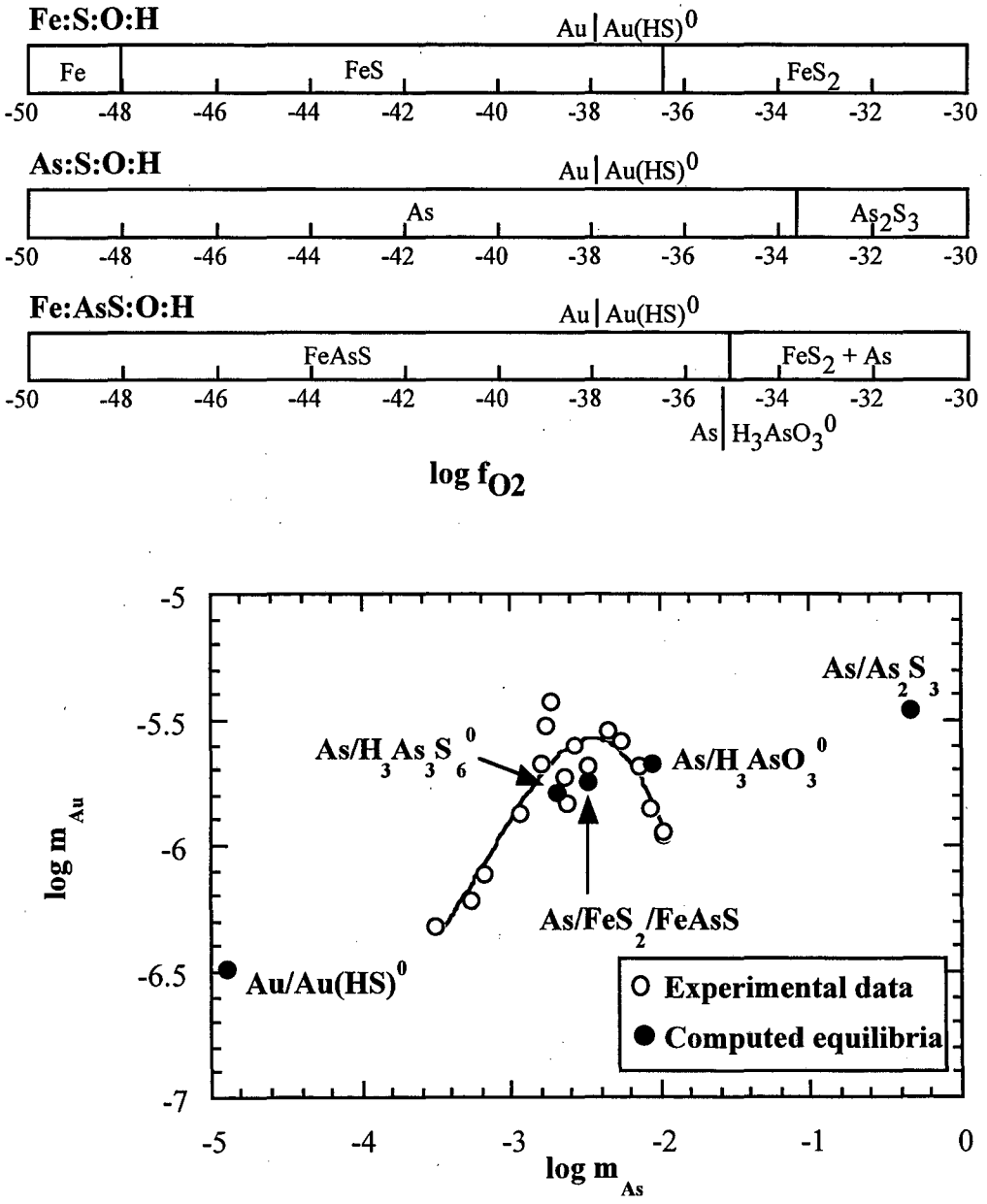

Figure 3.27 a) Potential oxidation state buffer assemblages in the systems Fe-S-O-H, As-S-O-H, and Fe-As-S-O-H. b) Comparison of buffers to the solubility of Au and As measured in the lab.

4.1 Introduction

This chapter utilizes the thermodynamic data calculated in the preceding chapter to examine some of the conditions leading to mineralization in Carlin-type gold deposits. In *Sections 4.2* through *4.4* the stability of antimony, arsenic, and gold-bearing mineral and aqueous phases are discussed. Also, chemical factors such as temperature, pH, oxidation potential, and total free sulfide content (TFS) which control solubility are explored. In *Section 4.5* this information is utilized to evaluate potential geologic processes leading to the observed paragenetic sequence. Finally, in *Section 4.6* additional research which would better illuminate the conditions present during metal deposition is discussed.

4.2 Antimony geochemistry

4.2.1 Antimony mineral phases

In addition to the mineral phases listed in Table 3.3, antimony also occurs in minerals for which the thermodynamic data necessary for determining the $[\Delta G^o]$ is incomplete (where $[\Delta G^o]$ refers to the apparent standard Gibbs free energy of formation using the nomenclature of Johnson, et al., (1992)). These phases include: gudmundite (FeSbS); kermesite (Sb_2S_2O); bertheirite ($FeSb_2S_4$); and seinäjoikite ($FeSb_2$). Based on the comprehensive study of Williams-Jones and Gammons (1997), who reviewed the available data and made slight modifications in the log K_r of certain phase boundaries to represent their field observations, $[\Delta G^o]$ for each mineral along the water vapor saturation curve was derived analogously in this dissertation. To correct $[\Delta G^o]$ for the 800 bars of pressure employed in the phase diagrams discussed below, the $[V^o]$ for each mineral phase was derived as follows: gudmundite was obtained from the Naumov, et al. (1974) database; kermesite (Sb_2S_2O) and seinäjoikite ($FeSb_2$) were estimated from the $[V^o]$ of stibnite (Sb_2S_3) and loellingite ($FeAs_2$), respectively,

using the differences between the molar volumes of antimony and sulfur and arsenic; finally, bertheirite ($FeSb_2S_4$) was estimated by assuming that the $[\Delta V_R^o]$ for the following reaction is zero:

$$Sb_2S_3 + FeS = FeSb_2S_4 \qquad (4.1)$$

utilizing the $[V^o]$ for FeS from the SUPCRT database (Johnson, et al., 1992) and Sb_2S_3 from **Chapter 3**. A more quantitative technique, recommended for future investigations, is to calculate $[V^o]$ from crystallographic properties.

Figures 4.1.a through 4.1.d show the stability of phases in the H-O-S-Fe-Sb system from 300 to 200°C, 800 bars of pressure, TFS from 0.05 to 0.005 *m*, ΣCl = 1.0 *m*, and an ionic strength of 1.0. The temperature and pressure range of these figures was selected to represent the range in temperatures in the main gold ore stage inferred from fluid inclusions (Table 1.1), and the average pressure of the Carlin deposit as calculated by Kuehn and Rose (1995). The TFS range was similarly selected to reflect the estimated H_2S(aq) content of Carlin deposit fluid inclusions (Table 4, Ilchik and Barton (1997)), and a fluid which has sulfidized host rock iron. Finally, a salinity of 5 wt. % NaCl was chosen to reflect the average of the fluid inclusions in Table 1.1. Although the figures only represent reducing conditions (note that the stability of several phases were not extended above the sulfide-sulfate isoactivity line), the stability of pyrite in the deposits and the high concentrations of reduced sulfide justified this simplification.

The first result of this study is that for a TFS of 0.05 *m*, the dominant Fe-bearing phases are pyrite and pyrrhotite, with the presence of magnetite only occurring at lower sulfide contents and a pH between 7.0 and 8.0. The fact that neither magnetite nor hematite are not reported in any of the investigations cited in this study is consistent with the parameters selected above. Also, the bend in the phase boundary for pyrite and pyrrhotite at higher pH is a consequence of the reduced activity of H_2S(aq) relative to HS^- as the isoactivity boundary is approached. For example, for the native antimony (Sb)-seinäjoikite ($FeSb_2$) phase boundary:

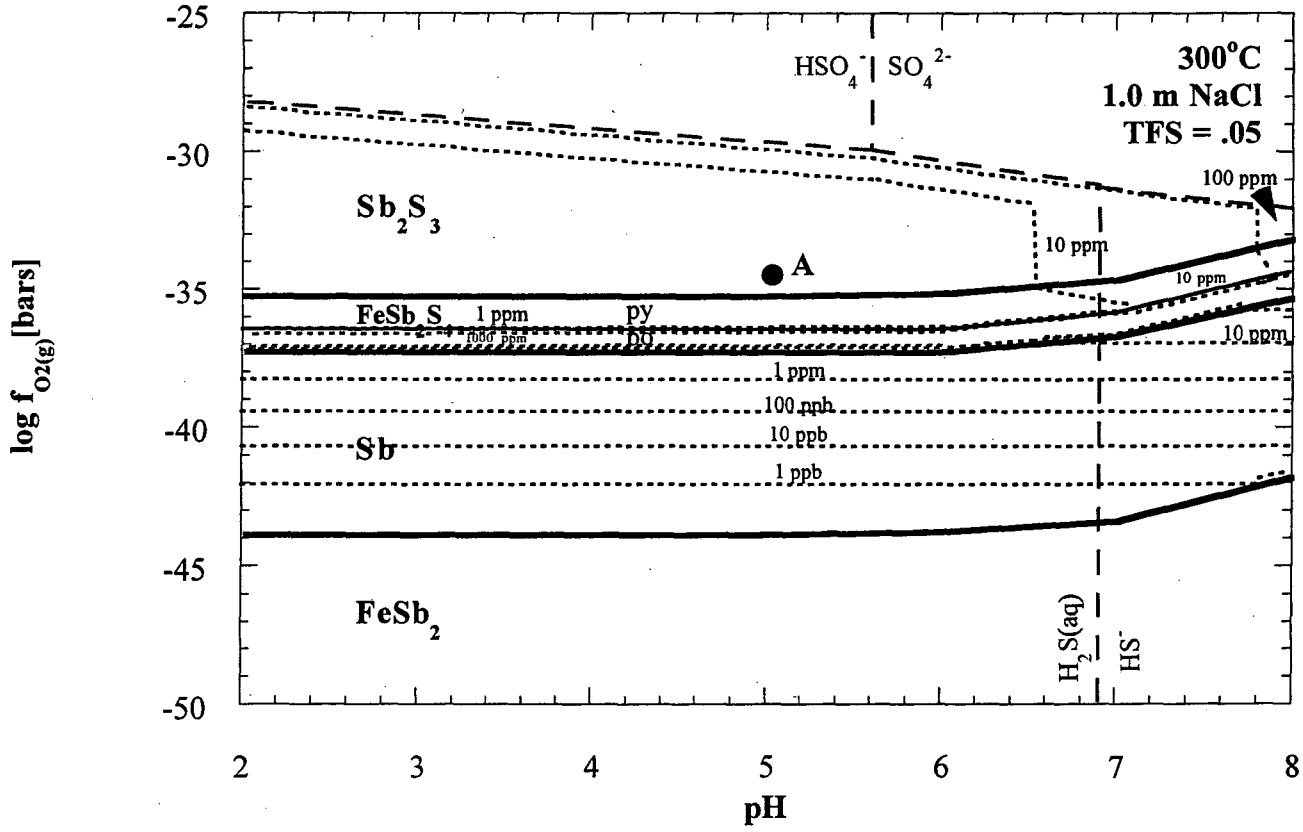

Figure 4.1 Phase diagram for the system Fe-Sb-H-O-S at a) 300°C and 800 bars and a TFS = 0.05. The solubility of antimony is shown by the short, stippled lines. Relationships are drawn only below the sulfide-sulfate boundary.

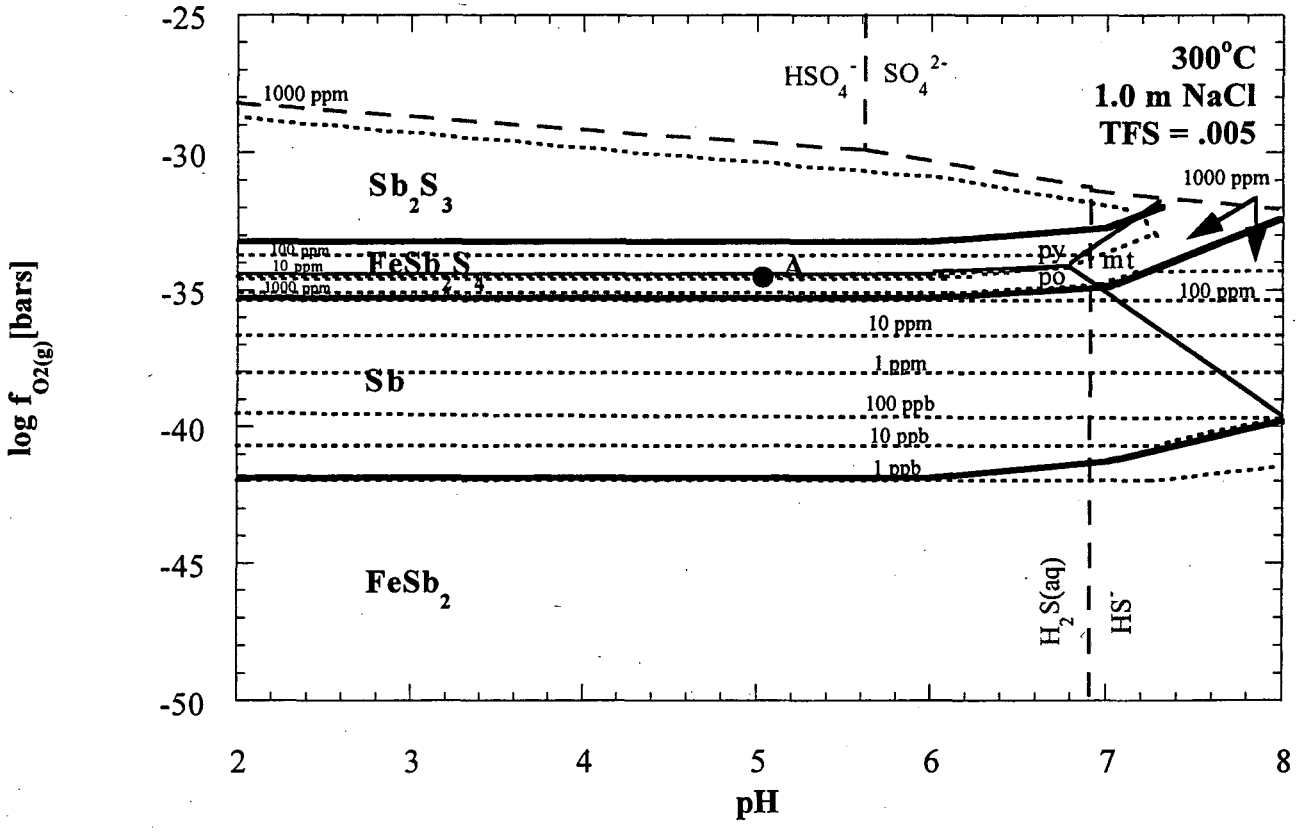

Figure 4.1 Phase diagram for the system Fe-Sb-H-O-S at b) 300°C and 800 bars and a TFS = 0.005. The solubility of antimony is shown by the short, stippled lines. Relationships are drawn only below the sulfide-sulfate boundary.

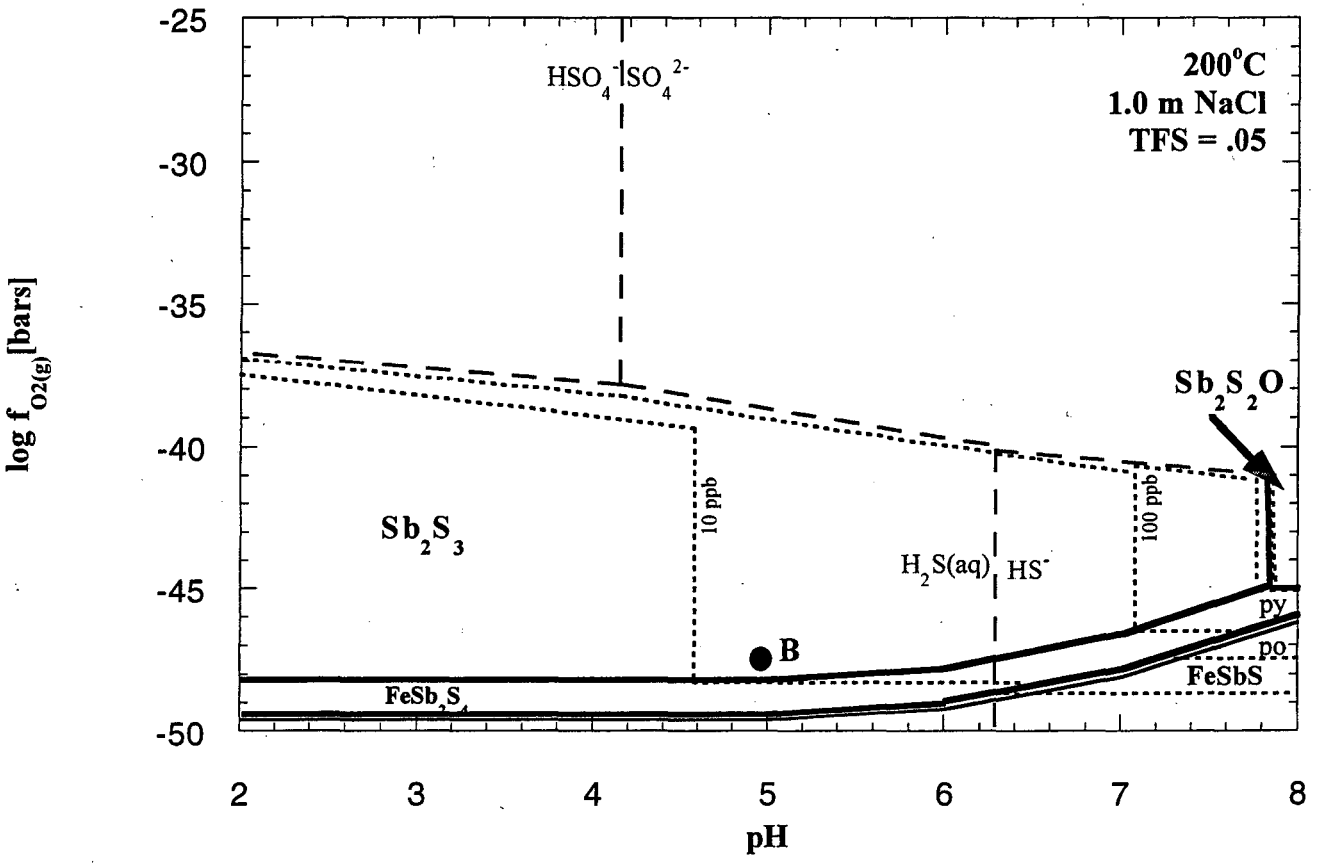

Figure 4.1 Phase diagram for the system Fe-Sb-H-O-S at c) 200°C and 800 bars and a TFS = 0.05. The solubility of antimony is shown by the short, stippled lines. Relationships are drawn only below the sulfide-sulfate boundary.

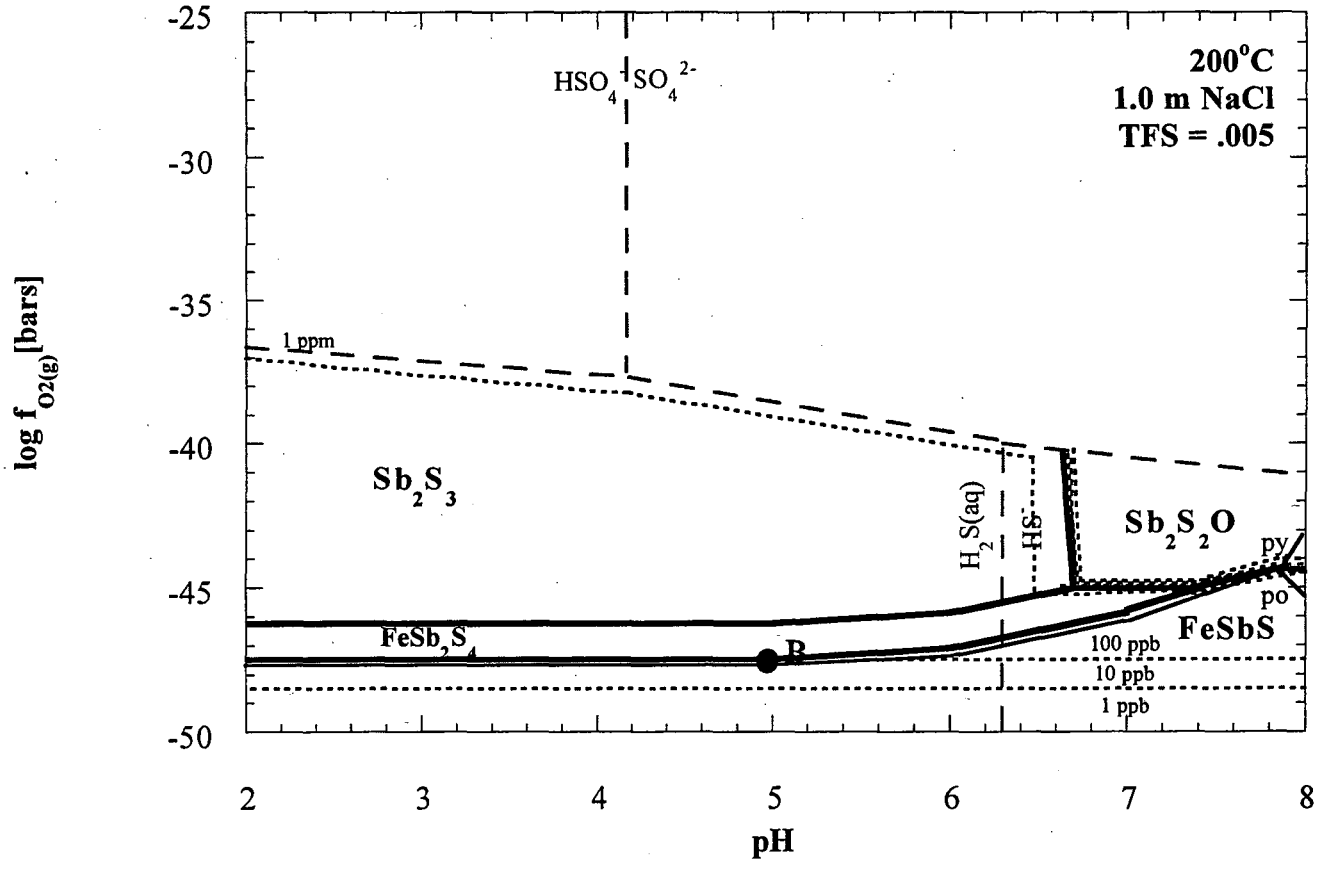

Figure 4.1 Phase diagram for the system Fe-Sb-H-O-S at d) 200°C and 800 bars and a TFS = 0.005. The solubility of antimony is shown by the short, stippled lines. Relationships are drawn only below the sulfide-sulfate boundary.

$$2\ Sb + FeS + H_2O = FeSb_2 + H_2S(aq) + 0.5\ O_2(g) \qquad (4.1)$$

every 1.0 logarithmic unit drop in the $H_2S(aq)$ concentration requires a 2.0 logarithmic unit increase in the $fO_2(g)$ at equilibrium.

The antimony mineral phase stability fields superimposed on this diagram are represented by the heavy solid lines. At any one temperature, the oxidation state of antimony diminishes with the $fO_2(g)$. At 300°C, the stable assemblage within the pH-redox boundaries of the plots is stibnite (Sb_2S_3), berthierite ($FeSb_2S_4$), native antimony (Sb), and seinäjoikite ($FeSb_2$). At 200°C the assemblage consists of stibnite (Sb_2S_3), berthierite ($FeSb_2S_4$), kermesite (Sb_2S_2O), and gudmundite (FeSbS). At this lower temperature, kermesite (Sb_2S_2O) encroaches where the pH > pK_{H2S} (Figures 4.1.c and d), and gudmundite (FeSbS) replaces native antimony (Sb) in the zero oxidation state.

In addition to the phases shown in the figure, William-Jones and Normand (1997) showed that the hematite (Fe_2O_3)-pyrite(FeS_2) and stibnite(Sb_2S_3)-senarmontite(Sb_2O_3) phase boundaries lie slightly above the sulfide-sulfate isoactivity boundary. The high solubility of antimony in the senarmontite field and the lack of this mineral phase in the Carlin-type gold deposits is further justification for only calculating phase relationships in the sulfide region.

A comparison of Figures 4.1.a and 4.1.c reveals that all of the stability boundaries shift to more reducing conditions as a consequence of cooling, with the stability field of stibnite (Sb_2S_3) becoming dominant at 200°C. The extremely reducing conditions required to stabilize gudmundite (FeSbS) at 200°C may explain the lack of correlation between gold and antimony on pyrite surfaces (i.e. it forms a potential solid solution with pyrite, but the required conditions for its existence are never met).

4.2.2 Antimony aqueous species

Calculations performed in this study indicate that the species $Sb(OH)_3^0$ predominates at all conditions considered in this study, except in the acid region at 200°C, TFS of 0.05 *m*, and

a antimony concentration of approximately 10 ppm. Figure 4.2 compares the relative stability of $Sb(OH)_3^0$ to the dominant antimony sulfide complexes at three pH intervals chosen to reflect the stability region of each of the three antimony-sulfide aqueous species. The thick, solid horizontal line in the figure represents the critical concentration of $H_2S(aq)$ required for an equal activity of the sulfide and hydroxide complexes. According to the figure, in very acidic conditions, $H_2Sb_2S_4^0$ is possible at antimony concentrations exceeding 10 ppm; however, because antimony concentrations in most hydrothermal fluids are believed to be less than 1 ppm and rarely exceed 10 ppm (White, 1981), all solubility contours drawn in Figure 4.1 were calculated with respect to $Sb(OH)_3^0$.

4.2.3 Antimony solubility

The solubility of antimony in Figure 4.1 is relatively insensitive to pH except near the $H_2S(aq)/HS^-$ isoactivity line. In contrast, there are strong solubility gradients as a function of oxidation potential, with a solubility maximum occurring in the berthierite ($FeSb_2S_4$) field. Although native antimony (Sb) and seinäjoikite ($FeSb_2$) are relatively insoluble, their absence is indicative that the oxidation state of the Carlin-type gold deposits is higher than that required for their stability (i.e. they are both stable below the pyrite-pyrrhotite phase boundary). The effect of temperature on solubility in Figure 4.1 is strong. Comparison between Figure 4.1.a and 4.1.c demonstrates that stibnite, which is found in the Carlin-type gold deposits, becomes the dominant phase at 200°C and has a relative solubility two orders of magnitude lower at this temperature.

The effect of sulfidation of host rock iron at 300°C is represented by the change in the position of Point A between Figures 4.1.a and Figures 4.1.b, which is constrained by the occurrence of arsenopyrite and pyrite in the deposits (see *Section 4.3.3* below). Not only does the stable antimony mineral change from stibnite (Sb_2S_3) to berthierite ($FeSb_2S_4$), but the solubility for both phases at a constant $fO_2(g)$ actually *increases* from 7 ppm to 104 ppm due

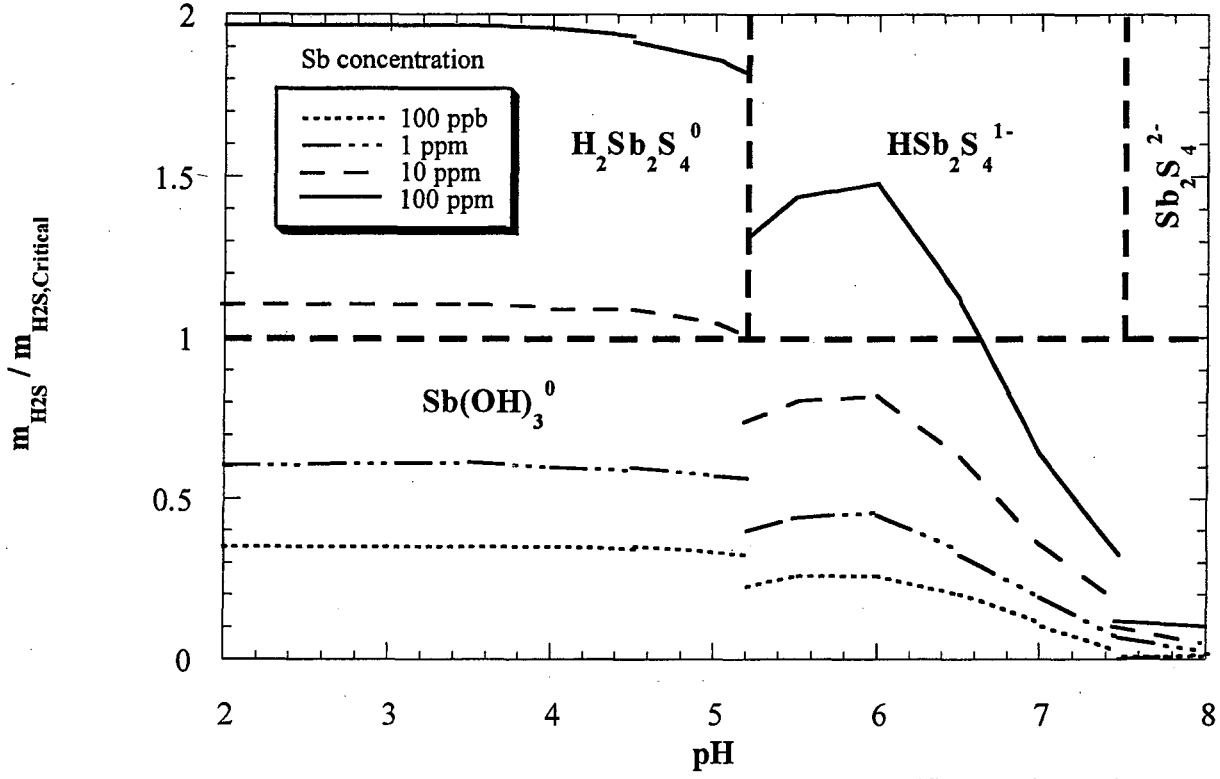

Figure 4.2 The critical concentration of $H_2S(aq)$ for antimony sulfide species to become stable relative to $Sb(OH)_3^0$. The three different plots refer to stability relative to: a) $H_2Sb_2S_4^0$; b) $HSb_2S_4^{1-}$; and c) $Sb_2S_4^{2-}$.

to the fact that $H_2S(aq)$ is a reaction product of mineral dissolution. In fact, according to Table 4.1, sulfidation only *decreases* the solubility of arsenopyrite (FeAsS) (in the pyrite field), and native Au and the rarer phases of loellingite ($FeAs_2$) and seinäjoikite ($FeSb_2$) in either the pyrite or pyrrhotite stability fields. According to Figures 4.1.c and 4.1.d, sulfidation at 200°C produces a similar result (Point B in the figures), with solubility increasing from 10 ppb to 143 ppb. This result can be explained by the relative position of $H_2S(aq)$ in the particular dissolution reaction. For example the dissolution of arsenopyrite proceeds by:

$$FeAsS + H_2S(aq) + 0.5\ H_2O + (5/4)O_2(g) = H_3AsO_3^0 + FeS_2. \qquad (4.2)$$

4.2.4 Implications

The only antimony-bearing mineral in the Carlin-type gold deposit recorded in the generalized paragenetic sequence of Figure 1.4 is stibnite. Based on the phase diagrams represented by Figure 4.1, stibnite saturation is unlikely to occur as a result of sulfidation (although seinäjoikite ($FeSb_2$) could, it would take extremely reducing conditions). By contrast, cooling of the fluid, oxidation from the berthierite ($FeSb_2S_4$) field, or acidification from the kermesite (Sb_2S_2O) field could deposit stibnite. Support for this first possibility is provided by the relatively late position of stibnite in the paragenetic sequence of Figure 1.4. Evidence for the second mechanism is possibly provided by evidence for mixing of two different fluids at Carlin (Kuehn and Rose, 1995); however, the oxidation state of these fluids is unknown. Finally, acidification is unlikely based on numerical calculations suggesting that the observed alteration assemblages were produced instead by acid neutralization (Ilchik and Barton, 1997).

METAL	INCREASE SOLUBILITY	DECREASE SOLUBILITY	NO EFFECT
Sb	Sb_2S_3 Sb_2S_2O $FeSb_2S_4$	$FeSb_2$	Sb(s)
As	As_2S_3 AsS	FeAsS $FeAs_2$	As(s)
Au		Au(s)	

Table 4.1 The effect of host rock sulfidation on the solubility of several minerals considered in this study.

4.3 Arsenic geochemistry

4.3.1 Arsenic mineral phases

The phase diagrams for arsenic minerals at 300°C and 200°C and 800 bars are displayed in Figure 4.3. The mineral assemblage is the same at both 200 and 300°C, except that loellingite ($FeAs_2$) plots outside of the stability field represented by the plots at 200°C. The other mineral phases shown in the figure include: orpiment (As_2S_3); realgar (AsS); native arsenic (As); and arsenopyrite (FeAsS). Consistent with the antimony minerals discussed above, cooling results in a shift of all stability boundaries to lower oxidation potentials, although the pyrite-pyrrhotite phase boundary remains within the arsenopyrite (FeAsS) field. Like stibnite (Sb_2S_3), the relative importance of orpiment (As_2S_3) is larger at 200°C compared to 300°C.

4.3.2 Arsenic aqueous species

Arsenic speciation at 200 and 300°C is entirely controlled by $H_3AsO_3^0$. To illustrate the dominance of this species, the concentration of H_2S(aq) required for equal activities of $H_3AsO_3^0$ and $H_3As_3S_6^0$ is greater than two orders of magnitude at 200°C and up to three orders of magnitude at 300°C. This implies that the H_2S(aq) concentration of approximately 1620 ppm used in this study would need to be at least 162,000 ppm at 200°C for this sulfide species to predominate.

4.3.3 Arsenic solubility

The solubility of arsenic in Figures 4.3.a through 4.3.d is relatively insensitive to pH, but is a strong function of the oxidation state. Although solubility maximum occurs in the realgar (AsS) stability field (this effect is not discernible from Figures 4.3.a and 4.3. b because the maximum solubility contour was drawn at 1000 ppm), solubilities otherwise decline when the system is reduced. Based on the review of Ballyntyne and Moore (1988) of arsenic

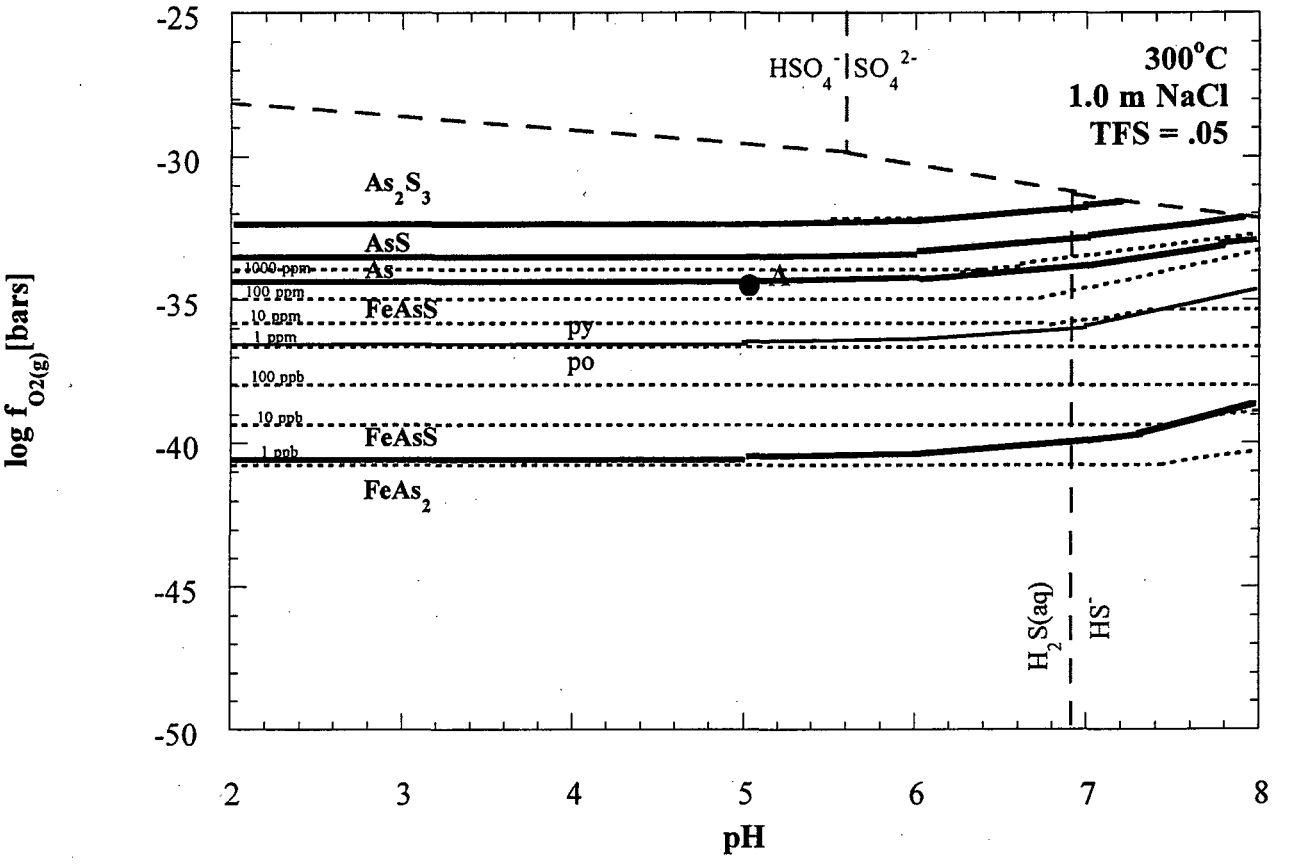

Figure 4.3 Phase diagram for the system Fe-As-H-O-S at a) 300°C and 800 bars and a TFS = 0.05. The solubility of arsenic is shown by the short, stippled lines. Relationships are drawn only below the sulfide-sulfate boundary.

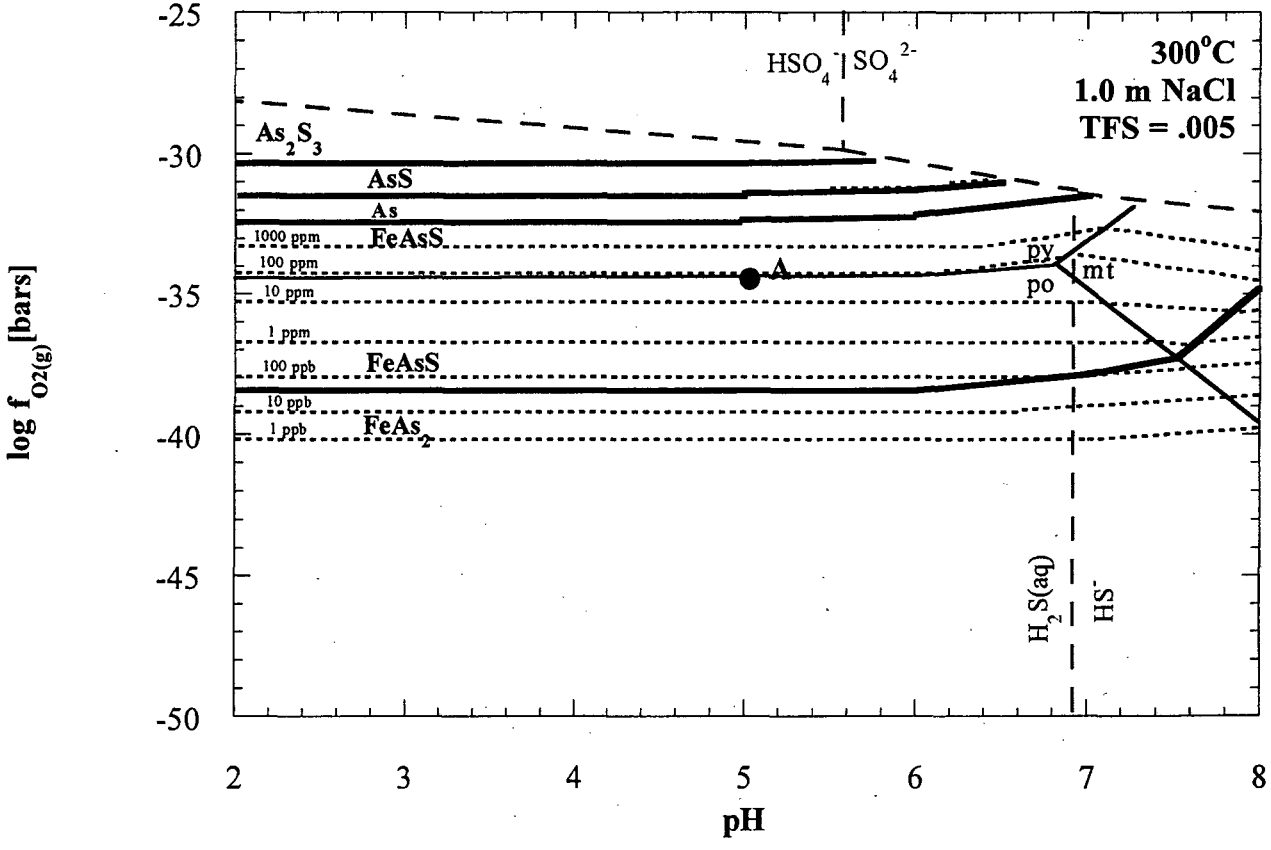

Figure 4.3 Phase diagram for the system Fe-As-H-O-S at b) 300°C and 800 bars and a TFS = 0.005. The solubility of arsenic is shown by the short, stippled lines. Relationships are drawn only below the sulfide-sulfate boundary.

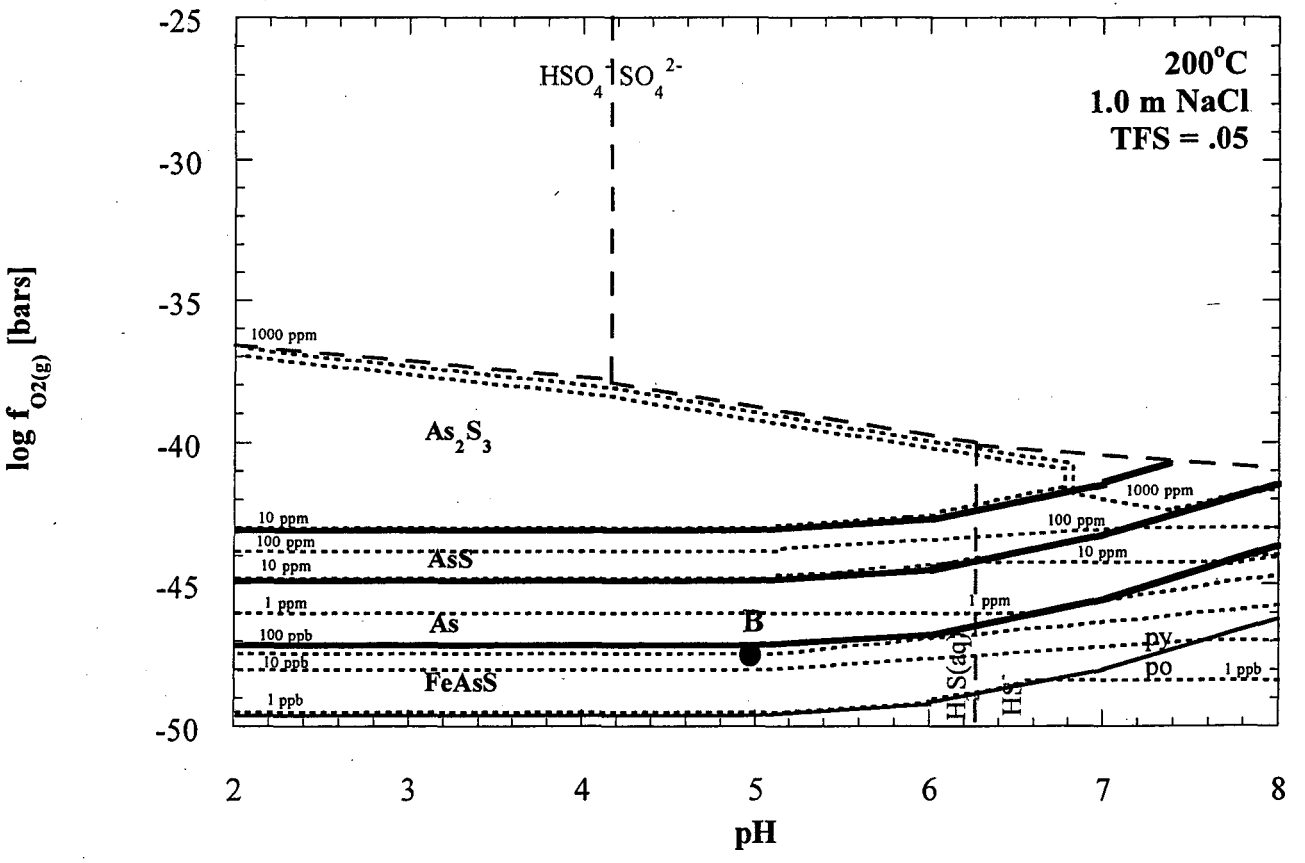

Figure 4.3 Phase diagram for the system Fe-As-H-O-S at c) 200°C and 800 bars and a TFS = 0.05. The solubility of arsenic is shown by the short, stippled lines. Relationships are drawn only below the sulfide-sulfate boundary.

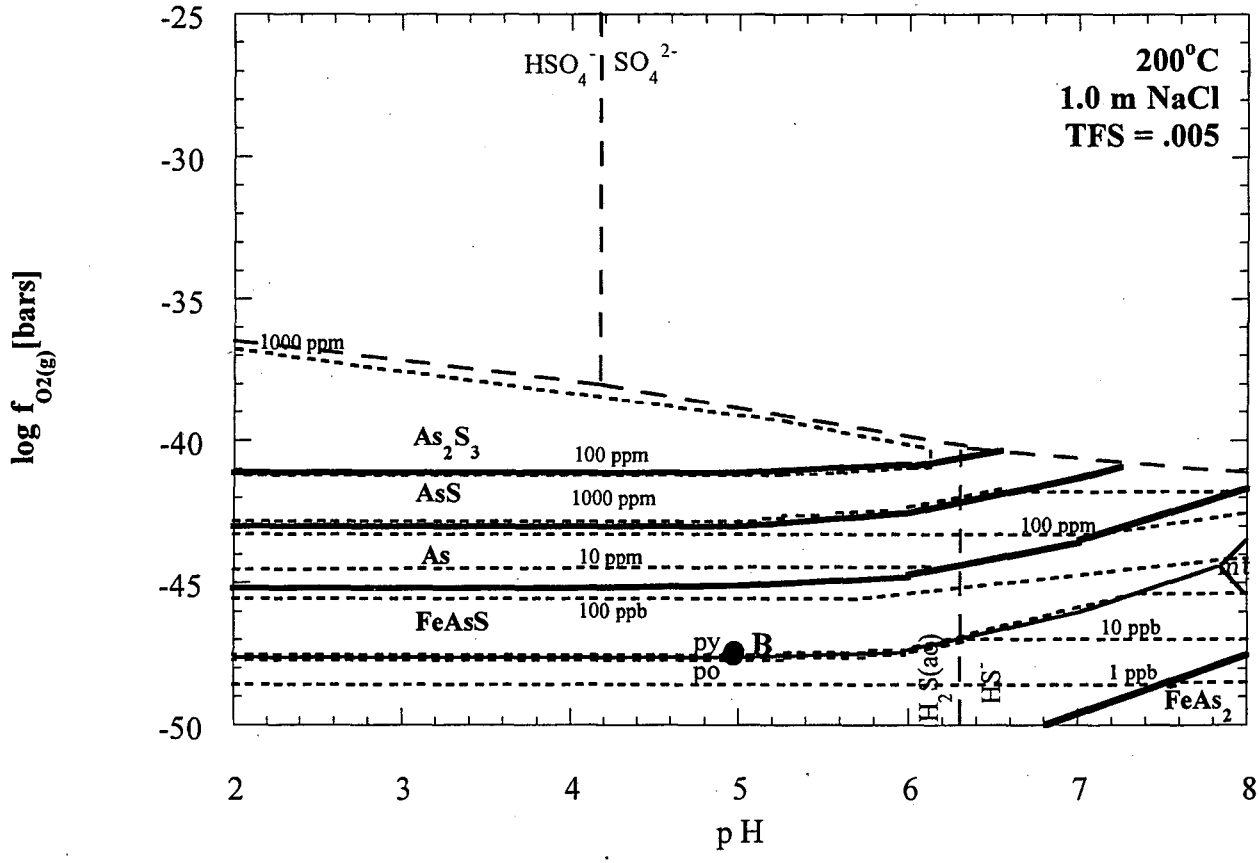

Figure 4.3 Phase diagram for the system Fe-As-H-O-S at d) 200°C and 800 bars and a TFS = 0.005. The solubility of arsenic is shown by the short, stippled lines. Relationships are drawn only below the sulfide-sulfate boundary.

concentrations in several hydrothermal systems, the concentration predicted for the Carlin deposit is approximately 1 ppm. This implies that at 300°C the only insoluble phases in Figure 4.3.a and 4.3.b are arsenopyrite (FeAsS) (below the pyrite-pyrrhotite boundary) and loellingite ($FeAs_2$). By contrast, native arsenic (As) and arsenopyrite (FeAsS) are insoluble at 200°C under all conditions of pH < pK_{H2S}. Also, saturation with respect to orpiment and realgar is being approached at this temperature.

The effect of sulfidation on each mineral phase is tabulated in Table 4.1. The solubilities of orpiment (As_2S_3) and realgar (AsS) increase, loellingite ($FeAs_2$) and arsenopyrite (FeAsS) (in equilibrium with either pyrite or pyrrhotite) decrease, and native As remains unchanged at a fixed fO_2(g). This effect is illustrated by Point A in Figure 4.3, which was constrained to lie within the arsenopyrite and pyrite fields both before *and* after precipitation based on field evidence that they were precipitated synchronously. Solubility at this point decreases from 300 ppm to 30 ppm. Because this solubility is higher than the likely 1 ppm responsible for arsenic transport, sulfidation is also examined in Figures 4.3.b and 4.3.c at 200°C. Here the solubility of Point B declines from 40 ppb to 4 ppb. The actual temperature of deposition of arsenopyrite (FeAsS) by this mechanism would have to lie at some intermediate temperature.

4.4.4 Implications

Like its antimony, changes in pH have very little effect on solubility; however, cooling or changes in oxidation potential do. Cooling can explain the precipitation of any of the arsenic minerals. Similarly, reduction of the fluid can explain the precipitation of all the arsenic minerals except orpiment (As_2S_3), which precipitates by fluid oxidation from the realgar (AsS) solubility maximum. Because there is strong evidence that sulfidation of the host rock occurred (Stenger, et al., 1998), and based on the correlation between arsenopyrite (FeAsS), arsenian pyrite ($FeAs_xS_{1-x}$), and pyrite (FeS_2) it is possible that arsenopyrite was precipitated by this latter mechanism. Orpiment (As_2S_3) may have then precipitated due to

cooling or oxidation, and realgar (AsS) from cooling later in the paragenetic sequence (consistent with Figure 1.4).

4.4 Gold geochemistry

4.4.1 Au mineral phases

Simon, et al. (1999) showed that gold exists as Au(I) on the surface of arsenian pyrite grains, and less frequently as Au(s). Without knowing the thermodynamic properties of a (Fe,Au)(As,S)S solid solution, this study can only model gold relative to its zero oxidation state. [ΔG^o] for native gold was subsequently calculated from the parameters given in the existing SUPCRT database (Johnson, et al., 1992).

4.4.2 Gold aqueous species

The aqueous species considered in the reducing conditions of the Carlin-type gold deposits were $Au(HS)^0$, $Au(HS)_2^-$ and $Au(OH)^0$; however, this latter species was found to be unimportant. In addition to these aqueous species, the HKF equation of state parameters for $H_2AuSbS_3^0$ were also calculated in *Section 3.6.5* of this dissertation. According to Figure 3.26, this species should become extremely important at lower temperatures.

Before discussing the solubility of gold relative to its native state it is important to note that the HKF equation of state parameters calculated in this study for $H_2AuSbS_3^0$ are inconsistent with the field conditions in the Carlin-type gold deposits. The predicted solubility of Au(s) as $H_2AuSbS_3^0$ at 200°C and a TFS = 0.05 *m* based on the extrapolation of the 300°C experiments using the HKF equation of state ranges from 1 ppm to greater than 1000 ppm near the sulfide-sulfate boundary. These high solubilities suggest that any gold previously precipitated in the deposit would be leached and removed from the system. This result is inconsistent with the existence of Carlin-type gold deposits. Until either additional experimentation is undertaken, or HKF equation of state correlations are developed for this

type of complex, the importance of Au heteropolynuclear complexing remains unresolved. These complexes are not considered further in this dissertation. Given the fact that As and Sb form as hydroxide complexes, their relative importance may have been less than the solubility studies purporting them in **Chapter 3**.

4.4.3 Gold solubility

Like arsenic and antimony, the solubility of gold is only weakly dependent on pH, but strongly dependent on temperature and oxidation potential (Figure 4.4). Although both reduction and oxidation (above the sulfide-sulfate boundary) could lead to precipitation, considering the oxidation potentials represented by Points A and B at 300 and 200°C, only the former mechanism was likely important in the Carlin-type gold deposits. Also, assuming that the concentration of Au in solution was between 1 and 10 ppb (estimated in Table 4 of Ilchik and Barton (1997) from Jerritt Canyon fluid inclusions), sulfidation would not have precipitated gold at 300°C, but may have at 200°C.

4.4.4 Implications

The geochemistry of gold is complicated by the fact that it precipitates in both the 0 and +1 oxidation states (the latter in conjunction with arsenian pyrite ($FeAs_xS_{1-x}$)). Consequently, two different depositional processes could have been operative in the Carlin-type gold deposits. Based on the co-precipitation of Au with As, the oxidation state of the system was fixed far enough below the sulfide-sulfate activity boundary that oxidation would not have been important process leading to mineralization. Also, the relative insensitivity to pH implies that this process was unlikely to have produced a chemical gradient strong enough to precipitate gold. Cooling, reduction, and sulfidation, by contrast, are all potential depositional mechanisms.

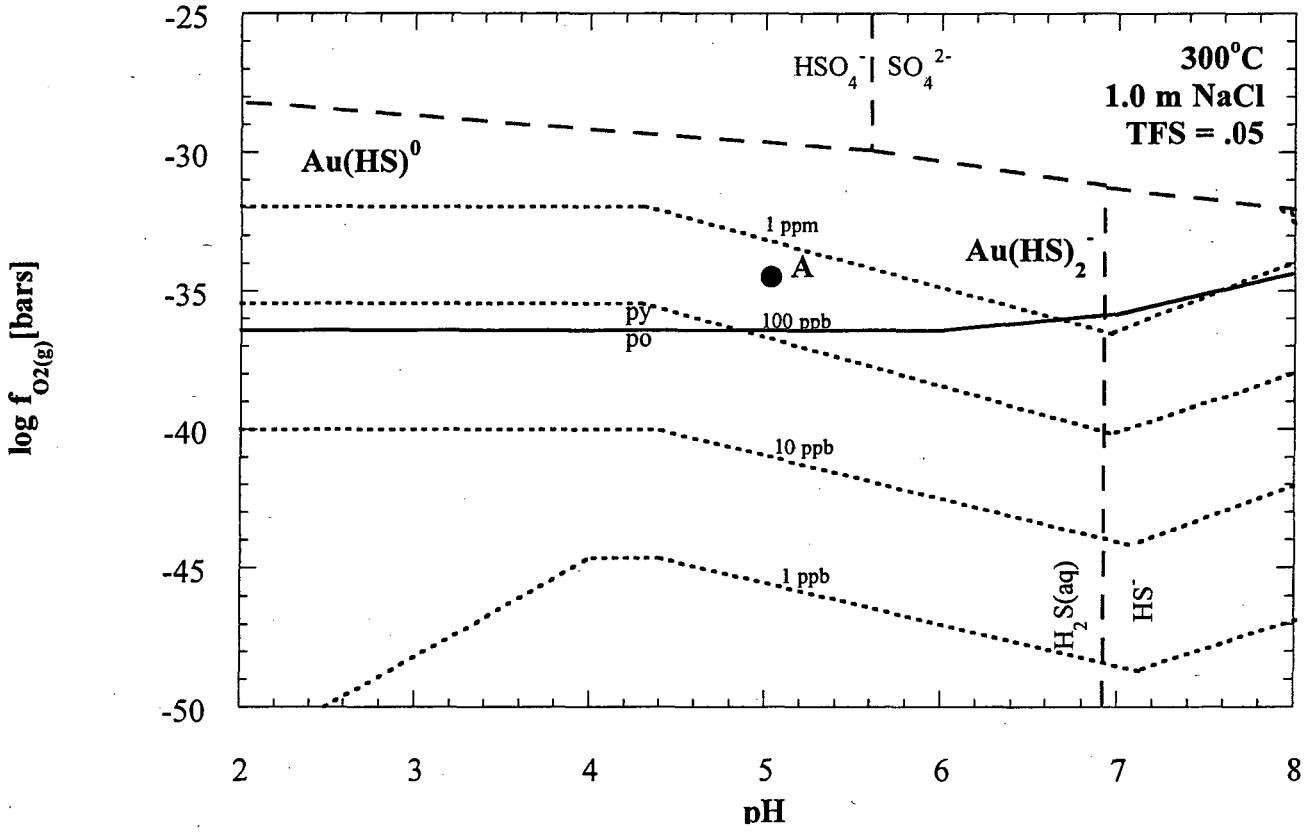

Figure 4.4 Phase diagram for the system Au-H-O-S at a) 300°C and 800 bars and a TFS = 0.05. The solubility of gold is shown by the short, stippled lines. Relationships are drawn only below the sulfide-sulfate boundary.

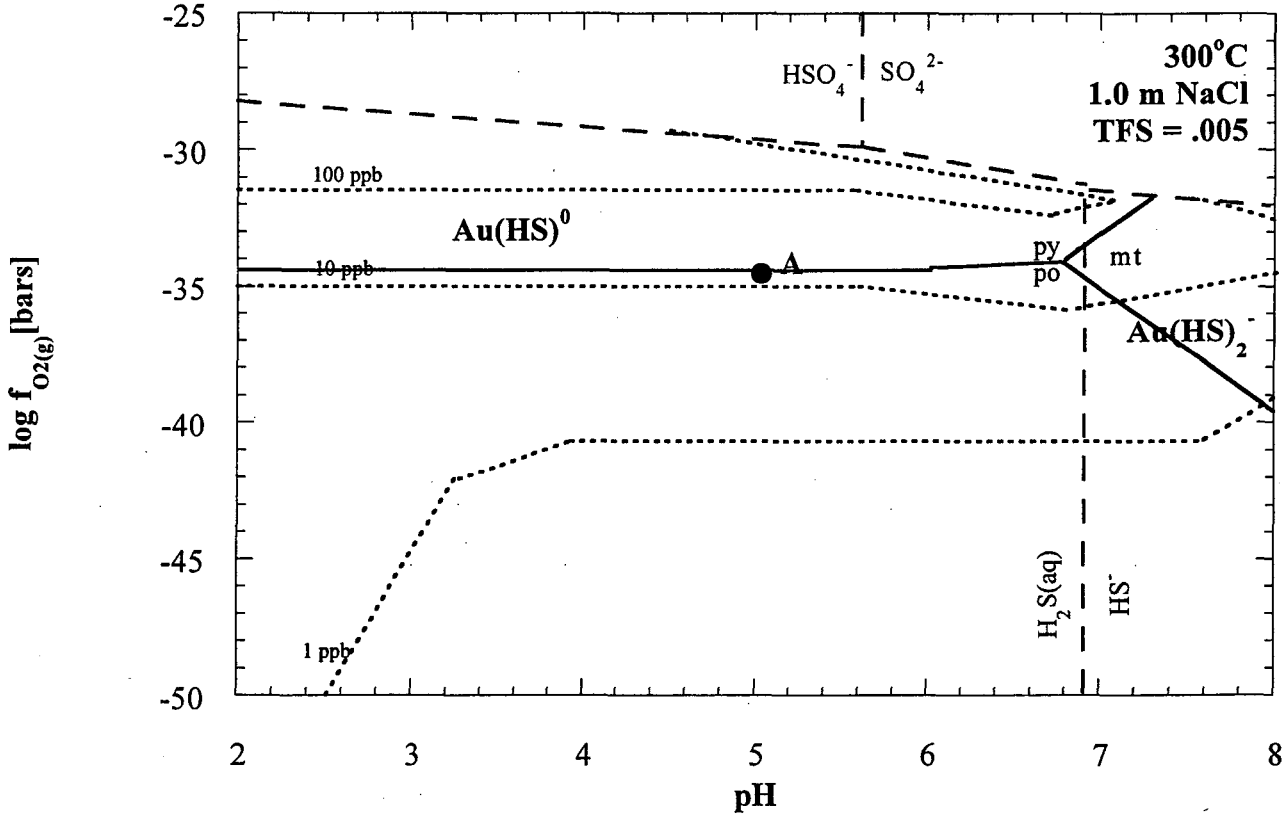

Figure 4.4 Phase diagram for the system Au-H-O-S at b) 300°C and 800 bars and a TFS = 0.005. The solubility of gold is shown by the short, stippled lines. Relationships are drawn only below the sulfide-sulfate boundary.

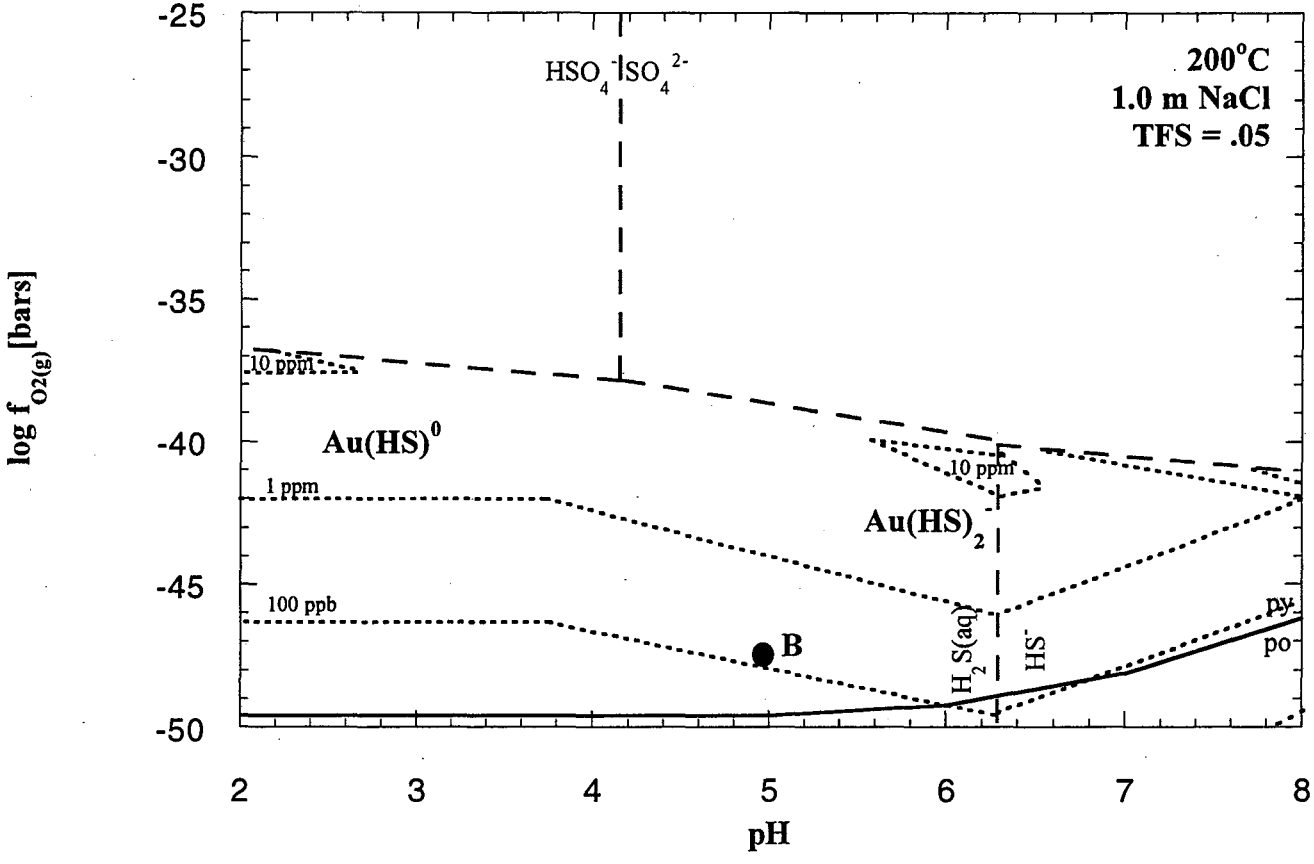

Figure 4.4 Phase diagram for the system Au-H-O-S at c) 200°C and 800 bars and a TFS = 0.05. The solubility of gold is shown by the short, stippled lines. Relationships are drawn only below the sulfide-sulfate boundary.

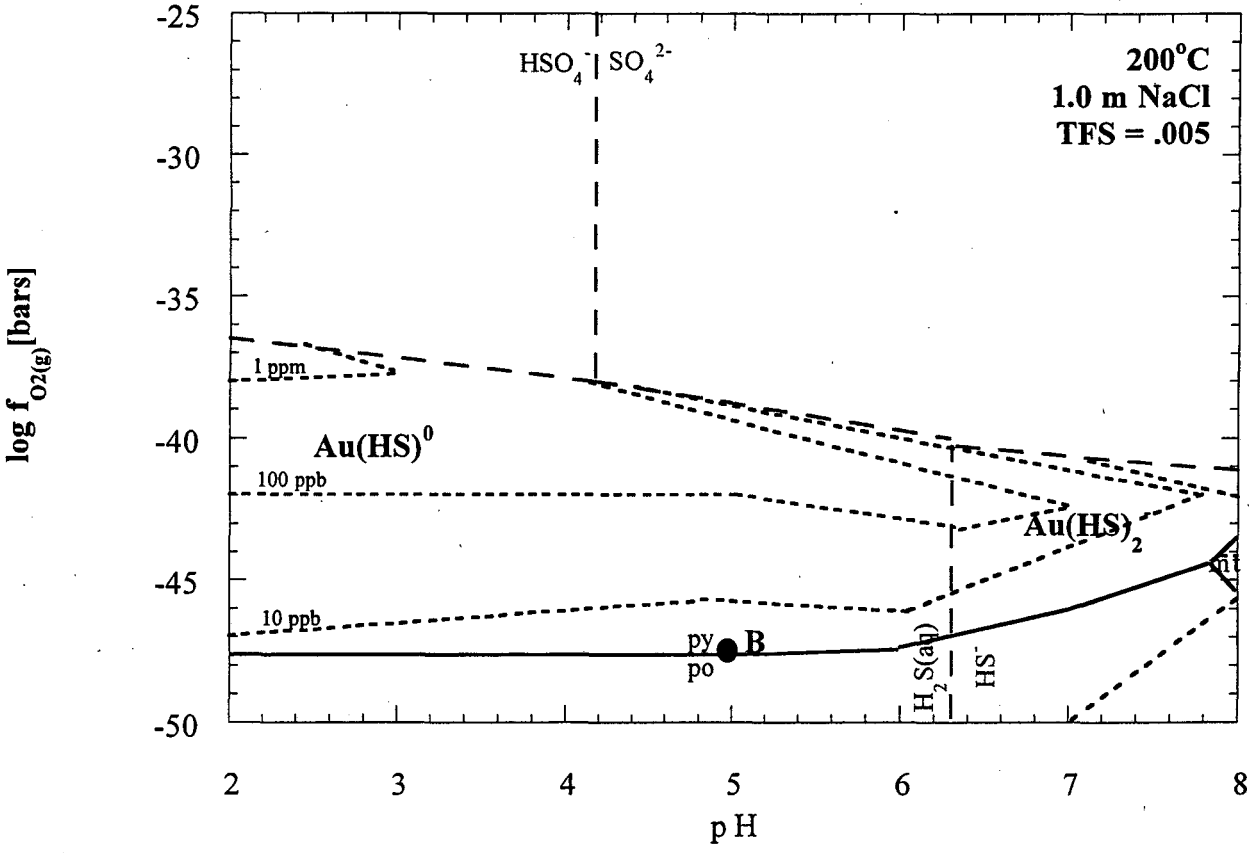

Figure 4.4 Phase diagram for the system Au-H-O-S at d) 200°C and 800 bars and a TFS = 0.005. The solubility of gold is shown by the short, stippled lines. Relationships are drawn only below the sulfide-sulfate boundary.

4.5 Implications for mineralization

The first important result of this study is that sulfidation was a selective method to preferentially precipitate the main gold stage minerals: arsenopyrite (FeAsS); arsenian pyrite ($FeAs_xS_{1-x}$); and Au(s) (Table 4.1). Adsorption reactions involving Au(I) on arsenian pyrite surfaces would also be favored. This result is consistent with the general paragenesis of the deposit, where these arsenic and gold phases preceded stibnite (Sb_2S_3) and orpiment (As_2S_3). It is also consistent with the measurements of Stenger, et al., (1998) which suggested that the dissolution of the host rock generated Fe^{2+} in solution, which immediately reacted with H_2S(aq) to produce pyrite (FeS_2), arsenopyrite (FeAsS), and arsenian pyrite ($FeAs_xS_{1-x}$).

The second important finding of this study is that the oxidation state of the fluid is a key variable in the system, controlling phase boundaries, as well as overall mineral solubilities. Reduction was found to be a particularly effective method to precipitate Sb, As, or Au, with the exception of stibnite (Sb_2S_3) and orpiment (As_2S_3) as discussed above; however, geologic circumstances leading to reduction are unclear without a better understanding of the source rock buffer assemblage and, consequently, the initial fluid composition. The deposition of stibnite (Sb_2S_3) and orpiment (As_2S_3) at later paragenetic stages are, by contrast, consistent with an increasing degree of oxidation of the fluid with time, and with cooling contributing to precipitation.

An important unresolved issue in these deposits is the localization mechanism. Sulfidation of favorable host rocks can explain ore localization during the main gold stage; however, cooling as a mechanism to precipitate stibnite (Sb_2S_3) and orpiment (As_2S_3) as the system became more oxidized is more difficult to reconcile because thermal gradients are gradual. One explanation provided by Kuehn and Rose (1995) was that an impermeable geologic seal separated the ore-bearing solutions from cooler, dilute fluids. Episodic throttling would not only lead to a sharp thermal gradient, but dilution and/or pressure drop with the expulsion of CO_2(g) and H_2S(g). This model awaits confirmation from numerical calculations, because if this same seal was present during the main gold stage, stibnite (Sb_2S_3) might also be

precipitated (see Points A and B in Figure 4.1), a result inconsistent with the mineral paragenesis.

4.6 Conclusions

Sulfidation during the main gold stage, and cooling during later mineral precipitation, are both consistent with the ore deposit descriptions of **Chapter 1**; however, much additional analysis is required. For example, there are depositional mechanisms which were not explored in this study but *were possible* in the Carlin-type systems. One such mechanism is the throttling of overpressured fluids and the exsolution of $CO_2(g)$ and $H_2S(g)$ (Kuehn and Rose, 1995). Incorporation of the full suite of metals in the deposit (including silver and mercury) would better constrain the oxidation states at various stages of paragenesis, making it possible to more quantitatively know the oxidation conditions present during precipitation. Also, reaction path simulations at various temperatures and pressures could be used to generate source fluids similar to those observed in fluid inclusions, thus better constraining the water-rock reactions which occurred during deposition. Finally, detailed field and microscopic analysis of phase relations would be a vast improvement over the "fish" diagrams of Figure 1.4, providing more accurate observations by which to assess predictive models.

CHAPTER 5. Prologue to Part II

The three studies described below are a tribute to the late Dr. Neville G. W. Cook (1938-1998), who was responsible for their inception, but was unfortunately unable to see their completion. Dr. Cook's research interests were vast and he made significant contributions to the fields of experimental and theoretical rock mechanics, geophysics, and seismology. The following three chapters consist of a field-scale rock mechanics study, a laboratory seismic study, and an experimental fracture mechanics investigation.

The first of the three studies presented in the following chapters attempts to discern the relative contribution of far field tensile to compressive driving stresses in jointing at a field site on Vancouver Island, British Columbia. The particular site was selected because it contained embedded calcareous concretions with fractures in precisely the same orientation as one or more joint sets in the surrounding matrix. This observation implied that the fractures in the concretions likely formed in the same stress field as the joint sets, thereby constraining the most probable jointing scenarios to those which could explain their occurrence. In **Chapter 6** observations made at the field site of the concretion fractures and joint sets are first described. Next, field and laboratory measurements aimed at determining their mechanical properties are discussed. Finally, the results of numerical modeling calculations validating compression-driven extensile fracturing as a viable geologic process are presented.

In **Chapter 7** of this dissertation, the application of seismic methods to the detection of fractures in three limestone cores is subsequently examined. In these experiments, P-wave amplitude anisotropy measurements were taken at various angles to bedding. Next, the differences in amplitude were interpreted in terms of the presence of cracks from: 1) the structure observed in thin section; and 2) an analysis in the frequency domain using a displacement discontinuity model. The potential of applying these techniques to field-scale fractures is discussed.

Finally, in **Chapter 8** of this dissertation a new fracturing mechanism which can occur in granular media in the vicinity of underground wells is described. In order to understand the characteristics and importance of this new mechanism, a series of borehole breakout experiments were performed on sintered glass bead bricks of various degrees of cementation. The first result of this investigation was that opening mode fractures were found to form perpendicular to the applied compressive stress in weakly cemented bricks. SEM microscopy and numerical modeling verified that fracturing proceeded by a process of grain debonding and expulsion from the samples. It is concluded that this failure is most likely the process generating in sand during oil and natural gas recovery.

CHAPTER 6. The role of compressive stresses in jointing on Vancouver Island

6.1 Introduction

Joints are a distinct *mode* of geologic fracture, distinguished from faults in that the displacement that occurs across the fracture interface is a dilation. Because joints do not form in isolation, but as parallel trending sets of closely-spaced fractures, they often control the mechanical and hydraulic properties of the enclosing rock mass. Consequently, they affect erosion and structural lineaments in continents (Nur, 1982), the productivity of oil and natural gas reservoirs (Huang and Angelier, 1989), the generation of hydrothermal ore deposits (Wilkinson and Johnson, 1997), and the stability of underground excavations (Goodman, 1993).

Currently, the dominant explanation for joint sets in the geologic community is that tensile driving stresses, applied either as a far field (i.e. field-*scale*) tensile stress perpendicular to a crack face or as a fluid pressure acting on it, can create a stress concentration at the tip of a crack which exceeds the fracture toughness of the rock (Pollard and Aydin, 1988). Despite the fact that the stresses in the Earth are predominantly compressive, several different scenarios have been devised to account for the occurrence of tensile effective stresses. For example, tension can develop in a sedimentary basin during burial below the chord of the earth, or renewed uplift, where plate flexure occurs (Price and Cosgrove, 1990). Tensile stresses may also develop along the crest of folds (Nur, 1982; Kemeny and Cook, 1985), or where thermal or mechanical strains are applied to a layered sequence of differing elastic properties (Suppe, 1985; Wu and Pollard, 1995). Finally, tensile effective stresses are believed to develop in a buried rock mass due to very high pore pressures (Secor, 1965).

Although tensile joint driving mechanisms have been used to describe many small scale features associated with joint sets (e.g. Cruikshank, et al., 1991), there are two fundamental problems with asserting that all joints are driven by a far field tensile stress or high pore fluid pressure. The first is that tensile driving stresses cannot explain one of the most important joint properties from a geological and engineering perspective--the clustering of joints into zones of

closely-spaced fractures (Huang and Angelier, 1989; Olson, 1993). Pollard and Segall (1987) demonstrated that the dilation of an opening mode crack disrupts the surrounding stress field so that the tensile crack driving stress is only 72% of its remote value at one crack length away. This stress shadow not only makes it improbable for incipient joints to form closer than the length of a pre-existing joint in bedded rock in which joints are confined to a single layer, but also makes joint zones even more unlikely if either bedding planes are not completely welded or joints in adjoining layers contribute to it.

The second fundamental problem with considering only tensile stresses in joint propagation is that hydraulic fracturing, which is used to explain the observations of joint sets in the absence of obvious deformation, may be less important than previously held because the last term in equation (6.1) below is often wrongly neglected (Lorenz, et al., 1991a). Assuming uniaxial strain boundary conditions during burial of a sedimentary basin, the confining stress [σ_3] is given by:

$$\sigma_3 = \left(\frac{\nu}{1-\nu}\right)(\sigma_1 - \alpha p) + \alpha p \qquad (6.1)$$

where [σ_1] is the gravitational loading stress, [ν] is the Poisson's value, [α] is a constant relating the loading stress to hydrostatic stress, and the compressive stress and fluid pressure are positive. Although an increase in [αp] reduces the effective stress, it also contributes to the confining stress [σ_3], such that the effective confining stress [σ_3'] is given by:

$$\sigma_3' = \sigma_3 - \alpha p \qquad (6.2)$$

and

$$\sigma_3' = \left(\frac{\nu}{1-\nu}\right)(\sigma_1 - \alpha p) \qquad (6.3)$$

Assuming [α] is equal to one, for the effective confining stress to become tensile (i.e. negative) to propagate a joint, the fluid pressure must exceed the overburden stress. This is inconsistent with observations in deep basins (Lorenz, et al., 1991a), and is counterintuitive because a typical

hydrostatic stress profile shows that the hydrostatic stress is less than the lithostatic stress (Engelder, 1993).

An alternative to these tensile mechanisms is that in an environment of high deviatoric stress, where either tensile strains or high pore pressures have significantly reduced the compressive confining stress acting perpendicular to a joint face, a far field compressive stress acting parallel to it can generate microscale tensile stresses at the tip of a joint in excess of the rock's fracture toughness. Compression-driven extensile fracturing is well documented from decades of rock mechanics research into the failure of rock under compressive stresses (see Jaeger and Cook, 1979). Important examples include Jaeger and Cook (1963), who showed that extensile fractures were formed under a biaxial compressive loading stress in cylindrical rock cores, and Kemeny and Cook (1987) and Costin (1987), who developed mathematical models to explain the interaction and coalescence of microcracks into macroscopic extensile fractures.

Although evidence for compression-driven extensile fracturing has been predominantly absent from the geologic literature, there are two notable exceptions. First of all, Lorenz, et al. (1991b) suggested that joints in the Piceance Basin, Colorado were formed by large compressive thrust faulting stresses because their timing and orientation coincided. Secondly, Engelder and Fischer (1996) asserted that exfoliation fractures in granite formed in an environment of low vertical confining stress, and in response to a high horizontal compressive stress. In contrast to this latter study, Suppe (1985) argued that exfoliation fractures are best developed in domes rather than valleys, exactly the opposite as would be expected from a compressive stress concentration. Also, Price and Cosgrove (1990) hypothesized that residual tensile stresses, which develop in granite due to different thermal expansitivities of the various mineral grains, is a more likely mechanism.

If compression-driven extensile fracturing is an important geologic process then many of our predictions on the occurrence, orientation, and spacing of joints in rock may be inaccurate and require revision because geologists predominantly employ the "tensile" theories described above. Consequently, the objective of this study was to determine the relative

importance of far field tensile to far field compressive stresses at a field site on Vancouver Island, British Columbia. The approach was to first make field observations and measurements of the jointed site and then compare these with model predictions for the failure of rock under both tensile and compressive loads to determine which driving stresses were most compatible with the field data.

6.2 Geologic background

6.2.1 Geologic setting

The field site selected for this study was located along a beach on southeastern Vancouver Island, British Columbia, within the circled region of Figure 6.1 (England, et al., 1997). The rock exposures at the site consisted of a sandstone and conglomerate sedimentary succession known as the DeCourcy Formation, which was a subset of the larger Nanaimo Group illustrated in the figure. Also present in the vicinity of the field site was the Wrangellia terrane basement complex which formed the core of Vancouver Island. This terrane was older than the Nanaimo Group and may have provided detritus to the younger sediments (Mustard, 1994).

The dominant structural feature of the region was the Cowichan Fold and Thrust System (CFTS), which covered an approximate area of 140 by 60 kilometers, and completely encompassed the field site (England and Calon, 1991). The CFTS was bounded to the south by the San Juan and Leech River Faults, and extended twenty kilometers to the northeast of the field site into the Strait of Georgia. England (1990) interpreted the thrust faults depicted in Figure 6.1 to be listric, connecting to the San Juan/Survey Mountain Fault at depth and resulting in an estimated 12 kilometers of crustal shortening in the CFTS.

The observations and measurements of this study were made in a region of homoclinal folding, approximately one kilometer northeast of an anticlinal hinge. Although no thrust faults were observed in the study area, right lateral strike-slip faults were identified by England and

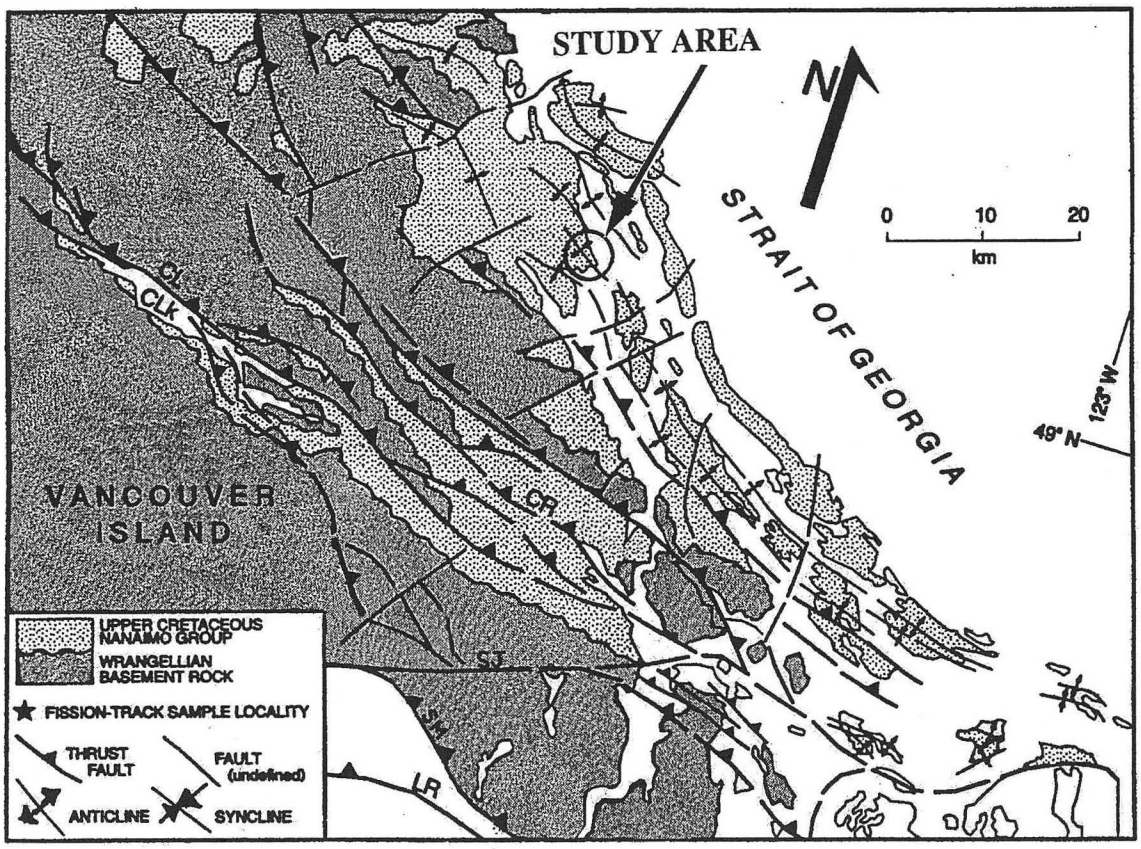

Figure 6.1 Simplified geologic map of southern Vancouver Island, British Columbia as envisaged by England, et al. (1997). The study area was located within the circled region of the figure on a 400 meter stretch of coastline. The stippled regions in the figure identify the Nanaimo Group sedimentary sequence of which the field sit e was a member. The structural features represented in this figure include anticlines, synclines, thrust, and strike-slip faults. The Survey Mountain and San Juan faults are indicated by the symbols SM and SJ, respectively.

Calon (1991) within a 10 kilometer radius. The fact that these faults cut across the CFTS suggested that they post-dated this deformation.

6.2.2 Geologic history

The DeCourcy Formation was originally deposited between 77.5 Ma to 76.5 Ma, in either a forearc (England, 1990) or foreland basin (Mustard, 1994) along the western edge of North America. This basin remained active until 66.5 Ma, resulting in an additional three kilometers of sedimentation (Mustard, 1994) and a total tectonic subsidence of 2.7 kilometers (England, et al., 1997). Although little information is available on the fate of the DeCourcy Formation during the Paleocene (65-54 Ma), development of the CFTS occurred at the close of the Eocene (42-38 Ma), subsequently folding and faulting all of the sedimentary units in the Nanaimo Group and initiating the uplift of sedimentary strata which continues today.

The current tectonic configuration of Vancouver Island was attained in the Miocene (26-7 Ma), with the Juan de Fuca Plate being subducted to the west, and the Georgia Basin resulting from consequent lithospheric flexure to the east. Present uplift and eastward tilt of Vancouver Island is caused by overthrusting and isostatic rebound from the last Ice Age (Monger and Journeay, 1994).

6.3 Field observations

6.3.1. Sandstone lithology

Field observations were made on a 400 by 10 meter outcrop of DeCourcy Formation sandstone on a gently-dipping coastline. The strike of the jointed sandstone unit ranged from S40E to S50E, and was subparallel to the strike of a nearby anticline (Figure 6.1). Because bedding did not plunge significantly over the interval of the study area, a single stratigraphic horizon was exposed over the entire length of the beach. Figure 6.2 shows the general appearance of this medium to coarse-grained sandstone pavement. Although there were locally small lenses of siltstone, bedding was generally thick and massive.

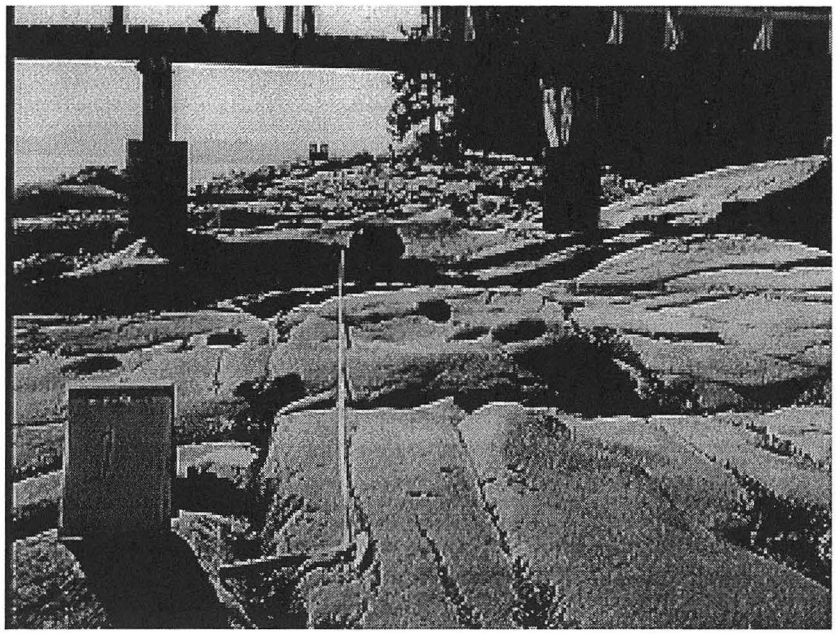

Figure 6.2 Photograph of the sandstone pavement in Area 1 of Figure 6.4. The picture was shot looking down the strike of the beach. The dock at the far end of the picture coincided with Area 8. The sandstone was not smooth, owing in large measure to the preferential erosion in the various fracture zones and a lack of erosion near embedded calcareous concretions. The fractures observed in the figure were members of fracture set #1, which were classified as joints. A more orthogonal fracture set can be seen just below the tape measure cutting across joint set #1.

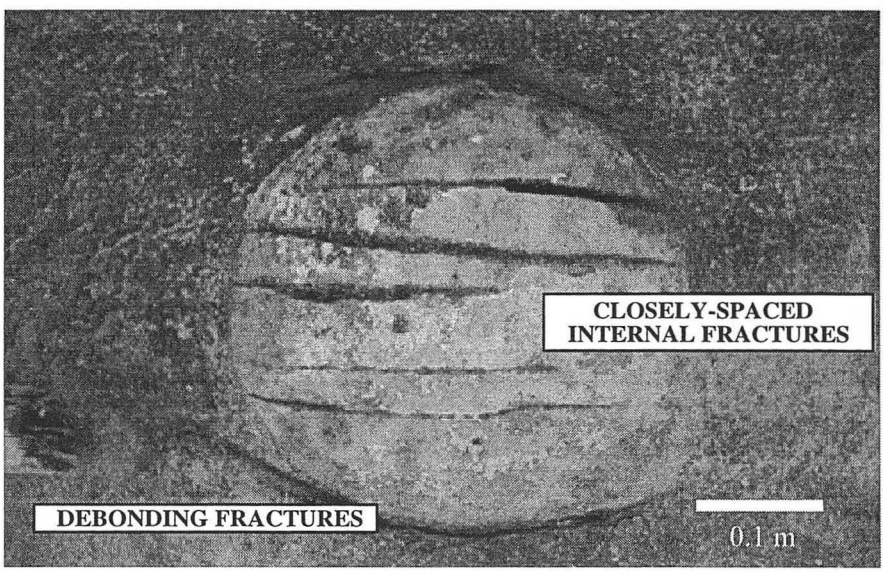

Figure 6.3 An example of the morphology of a concretion and its fractures. This photograph represents concretion #9 of Area 9 (see Figure 6.18). The concretion was nearly spherical and protruded from the surrounding sandstone. There were multiple fractures in the concretion, all in the direction of joint set #1. In addition to the internal fractures, the concretion was also partially debonded from the sandstone matrix. This particular concretion was classified as the "ideal" situation on which modeling calculations were performed.

To determine the mineralogy of the sandstone a petrographic microscope was used on three different thin sections obtained from 0.5" diameter drill cores. A hundred random counts were taken for each thin section, with the mean and standard deviations for the three cores reported in Table 6.1.a. According to the results of the thin sections the sandstone was predominately composed of quartz and feldspar, and had the composition of an immature arkosic wacke. This classification was consistent with the results of Rinne (1973) who performed a petrographic evaluation of a larger, but inclusive, study area, but the relative amount of feldspar to quartz was greater than that reported by Mustard (1994) for the DeCourcy Formation as a whole. These differences may have been real, or the product of interpretation due to the fact that the only distinguishing characteristic between the potassium feldspar and quartz was the biaxial verses uniaxial indicatrix of the two minerals, respectively.

6.3.2 Concretion lithology

A key difference between the sandstone unit at the field site and most other sandstone facies within the Nanaimo sedimentary sequence was the presence of spherical to elliptical concretions, which ranged in size from 0.1 to 3 meters and often protruded from the surrounding matrix because they better resisted erosion. An example of one of these concretions is shown in Figure 6.3. To determine the mineralogy of this second lithologic feature, a series of thin section from concretion cores taken adjacent to the sandstone drill cores of Table 6.1.a was analyzed. A comparison between the concretions and sandstone showed that the mineralogy of the concretions differed from the surrounding sandstone in that the pore spaces were filled with calcite cement. Table 6.1.b reports a great variability in calcite content between concretions, with Concretion #1 not only containing less calcite, but small quantities of the chlorite/illite cement observed in the sandstone samples.

In addition to mineralogical differences, thin section analyses also revealed that the microstructure of the concretions was very distinct. First of all, calcite cement not only filled the pore spaces of the concretions, but actually completely separated pre-existing mineral grains.

Mineral	Sandstone 1	Sandstone 3	Sandstone 4	Mean
Quartz	21	31	21	24.3 ± 4.7
Plagioclase/ K-Feldspar	45	46	63	51.3 ± 8.3
Biotite/ Muscovite	12	7	6	8.3 ± 2.6
Chlorite	1	4	1	2.0 ± 1.4
Sphene	0	2	0	0.7 ± 0.9
Chert	3	2	0	1.7 ± 1.2
Lithic	3	0	0	1.0 ± 1.4
Chlorite/ Illite Cement	14	8	9	10.3 ± 2.6
Unknown Cement	1	0	0	0.3 ± 0.5

Table 6.1 a) Summary of the thin section analyses on the sandstone cores taken from the field site. The sandstone was an arkosic wacke with some lithic fragments and clay cementation.

Mineral	Concretion 1	Concretion 2	Concretion 3	Concretion 4	Mean
Quartz	23	14	12	15	16.0 ± 4.1
Plagioclase/ K-Feldspar	49	38	40	37	41.0 ± 4.5
Calcite	13	36	35	40	31.0 ± 10.3
Biotite/ Muscovite	4	7	8	4	5.8 ± 1.7
Hornblende	0	0	2	1	0.8 ± 0.7
Chlorite	1	0	2	2	1.3 ± 0.5
Fe-oxides	0	0	1	0	0.3 ± 0.4
Chert	5	4	0	0	2.3 ± 2.1
Lithic	1	1	0	0	0.5 ± 0.4
Pore	0	0	0	1	0.3 ± 0.4
Chlorite/ Illite Cement	2	0	0	0	0.5 ± 0.8
Unknown Cement	2	0	0	0	0.5 ± 0.8

Table 6.1 b) The concretions of the study area also contained a high percentage of quartz and feldspar, but were distinguished from the sandstone by the occurrence of calcite cement. This cementation accounted for approximately 35-40% of the observed mineralogy, but was significantly less for Concretion core #1. This sample also had some of the clay cement which characterized the sandstone.

Secondly, the mineral grains in the concretion were less weathered and deformed than the sandstone thin sections. Plagioclase grains were cloudier, biotite grains bent, and oxidation of the Fe-bearing minerals more prevalent in the sandstone, indicating that both deformation and weathering had advanced further in the sandstone.

The preservation of the biotite mineral grains and the quantity of calcite cement in the concretions suggested that the concretions formed during the early stages of sandstone burial. Raiswell (1971) hypothesized that the amount of calcite cement in a concretion is directly proportional to the amount of pore space at the time of lithification. The concretions of his study were 80 to 90% calcite, a fact he attributed to diagenesis within the upper few meters of the seafloor. Based on the quantity of cement in the concretions at the field site, this reasoning suggested a depth of formation for the concretions at Vancouver Island between 100 and 1000 meters (Maltman, 1994). Concretion formation at this depth could have occurred if fermentation of organic matter produced sufficient carbonate ions to react with pore fluid Ca^{2+} to precipitate calcite (Raiswell, 1987).

6.3.3 Halo lithology

One important observation from the field site was that many of the concretions exhibited rings of discolored sandstone adjacent to them. The lithology of this additional feature is reported in Table 6.1.c for the "halo" surrounding Concretion #2. It has been proposed that concretions initiate from decaying organic matter, and grow outward as carbonate is produced and Ca^{2+} and other nutrients diffuse to the surface (Raiswell, 1976). Consequently, directional permeability is thought to control the rate at which a concretion can grow in any particular direction and thus influence the shape of the concretion itself. The fact that this halo zones had a calcite cement content intermediate between the sandstone and concretion supported the hypothesis that a chemical gradient existed. It additionally implied that the outermost shell of the concretions may have possessed different mechanical properties than the core at the time of fracturing.

Mineral	Halo for Concretion 4
Quartz	19
Plagioclase/ K-Feldspar	55
Calcite	21
Biotite/ Muscovite	5

Table 6.1 c) In some cases, there was a transition zone of partially-calcified sandstone surrounding the concretions of which this core is an example. This sample was taken adjacent to Concretion core #2 (note that there was no sandstone sample for this concretion). The "halo" zone contained as much as 21% calcite.

6.3.4 Observations of sandstone fractures

The field site was mapped along an eighteen foot wide scan line for 850 feet of its length (Figure 6.4). Because the strike of the beach in which the joints were located shifted slightly (from S40E to S50E), the strike for any particular 100 foot section is shown at the top of each interval in the figure. The most notable exception to the sectioned mapping is the missing area between 45 and 100 feet, which was partially infilled by water even during low tide, and which was also previously disturbed by blasting when an inlet was created (this precluded testing the rock properties in this area, which was the purpose of the scanline).

Figure 6.4 shows both the fractures along the scanline, as well as the distribution of concretions along the beach (the latter can be identified by their circular to elliptical shapes). Where either a slight discoloration of the sandstone or an erosional ring was observed surrounding the concretions, a halo was drawn in with dashed lines. In cases where fractures were obscured, dashed lines were also used to indicate inferred fracture orientations. This is most evident within the fracture zone at 180 feet. According to this figure, the fractures in the sandstone matrix were relatively diffuse, but intense fracture zones were present in some locations (especially in Areas 1 and 2). Concretions, by contrast, were generally more heavily fractured than the sandstone, with fracture zones especially pronounced in Area 4.

Three dominant fracture sets were identified for both the concretions and sandstone by taking a random sampling of 200 sandstone and 100 concretion fracture orientations (Figure 6.5). The most dominant fracture set roughly paralleled the strike of the beach and the anticlinal axis, while the two other fracture directions were more oblique. The most interesting result of Figure 6.5 is that the fractures in the concretions coincided with one or more fracture sets in the sandstone. This suggested that they may have formed in the same stress field.

The morphology of fracture set #1 is shown along the Area 1 scanline in Figure 6.2. The fractures were very linear and parallel, and, in a few cases, a slight increase in erosion was observed in the immediate vicinity of the fractures, resulting in ponding of water during low-tide,

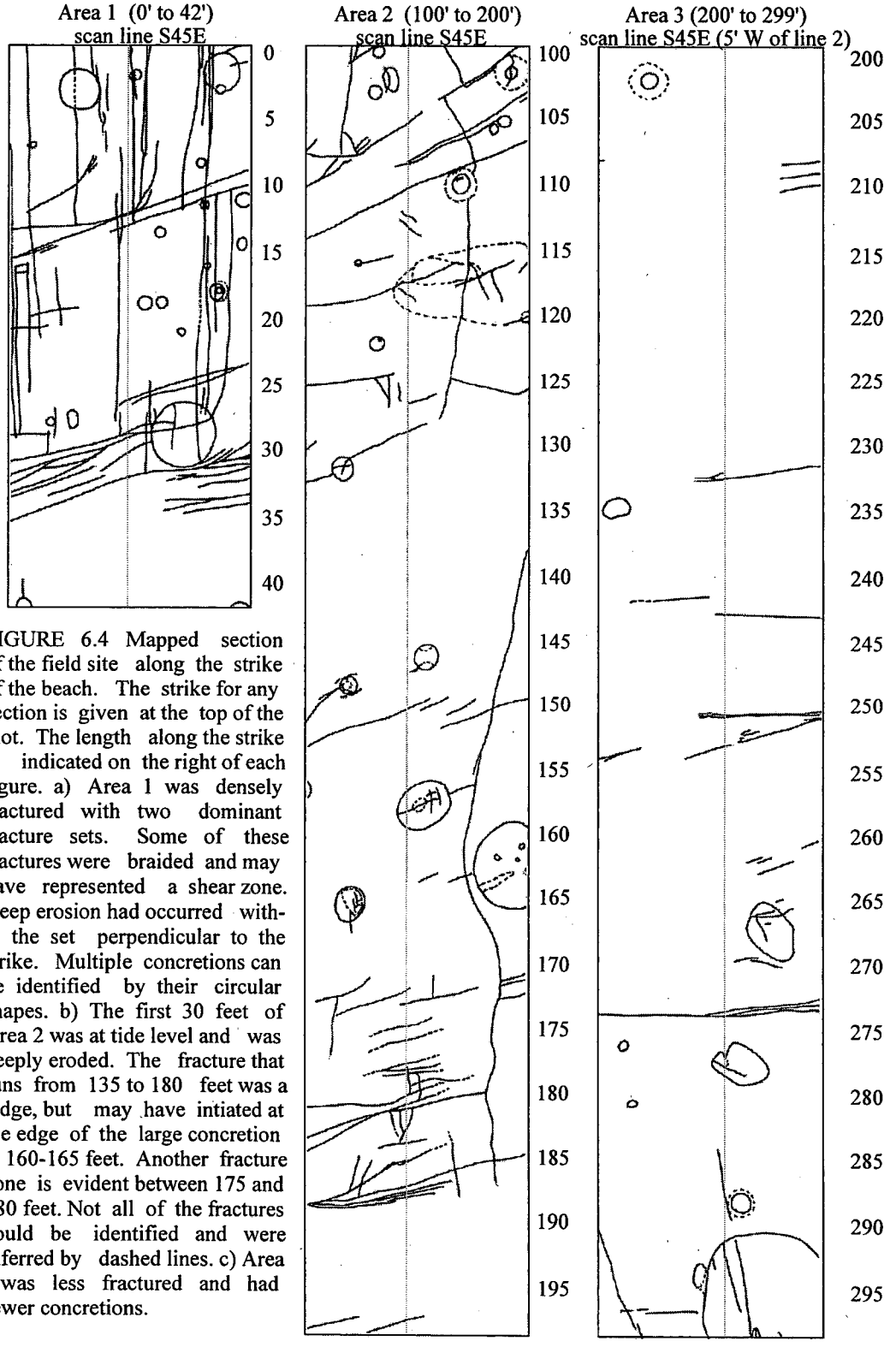

FIGURE 6.4 Mapped section of the field site along the strike of the beach. The strike for any section is given at the top of the plot. The length along the strike is indicated on the right of each figure. a) Area 1 was densely fractured with two dominant fracture sets. Some of these fractures were braided and may have represented a shear zone. Deep erosion had occurred within the set perpendicular to the strike. Multiple concretions can be identified by their circular shapes. b) The first 30 feet of Area 2 was at tide level and was deeply eroded. The fracture that runs from 135 to 180 feet was a ledge, but may have intiated at the edge of the large concretion at 160-165 feet. Another fracture zone is evident between 175 and 180 feet. Not all of the fractures could be identified and were inferred by dashed lines. c) Area 3 was less fractured and had fewer concretions.

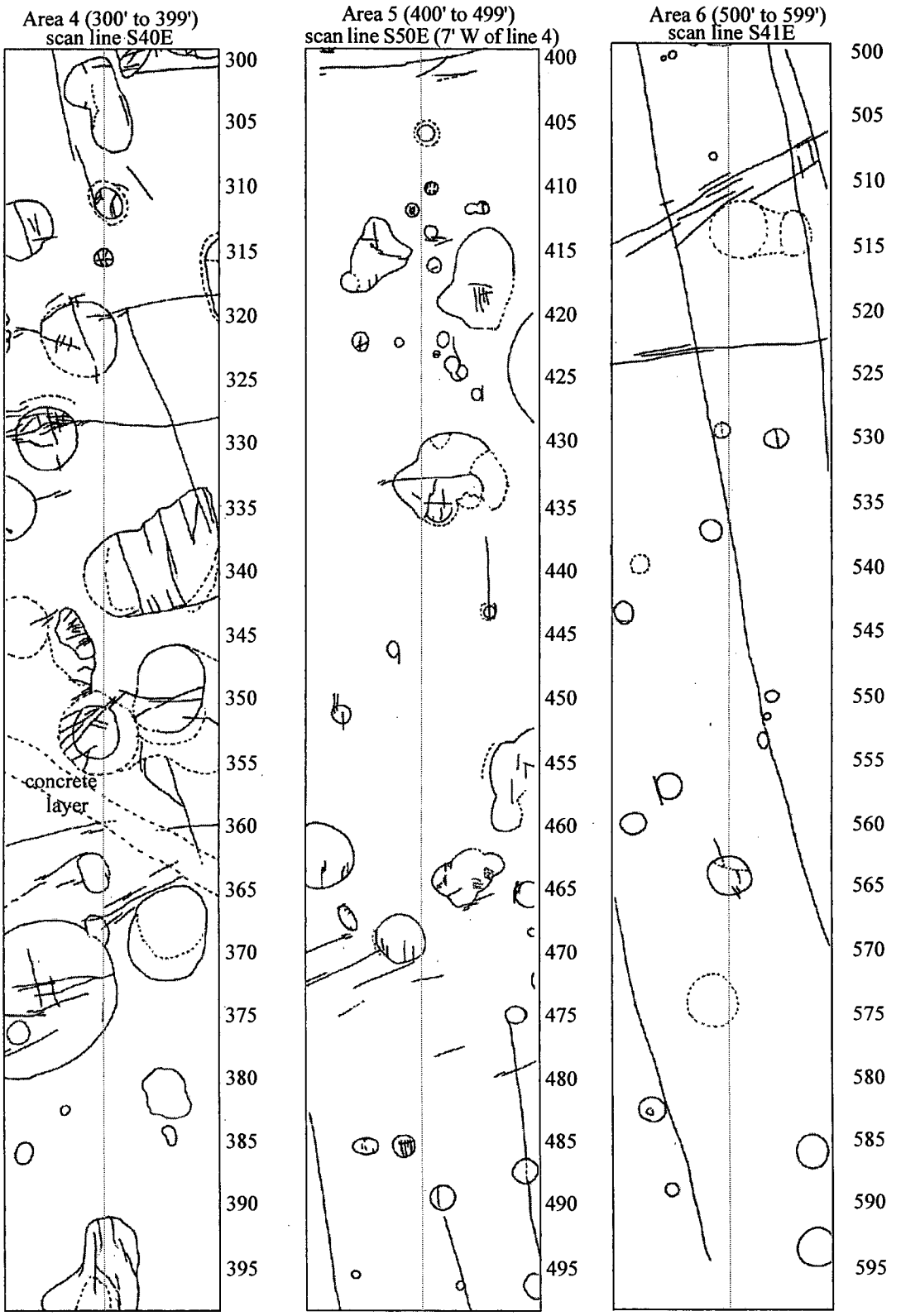

Figure 6.4 d) Area 4 contained many large concretionswhich were also heavily fractured. By contrast the sandstone was not heavily jointed. Halos were drawn with dashed lines surrounding concretions. e) Many of the concretions were fractured. f) Fracture zone at 505-515 feet. Several long joints of set #1.

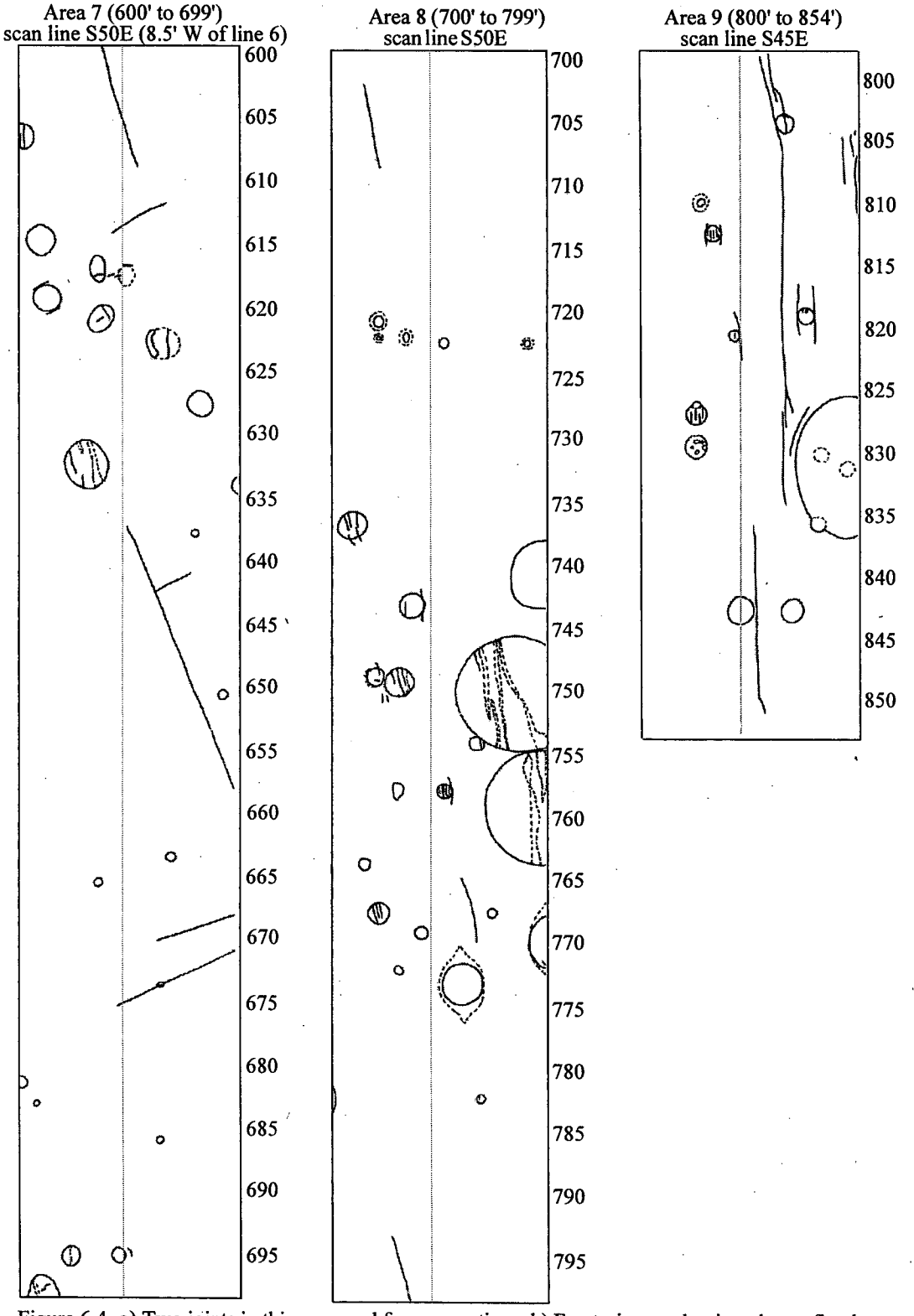

Figure 6.4. g) Two joints in this area, and few concretions. h) Fracturing predominantly confined to the concretions in this area. Some debonding. i) Area 9 contained the concretion in Figure 6.3. Several long debonding fractures had become joints.

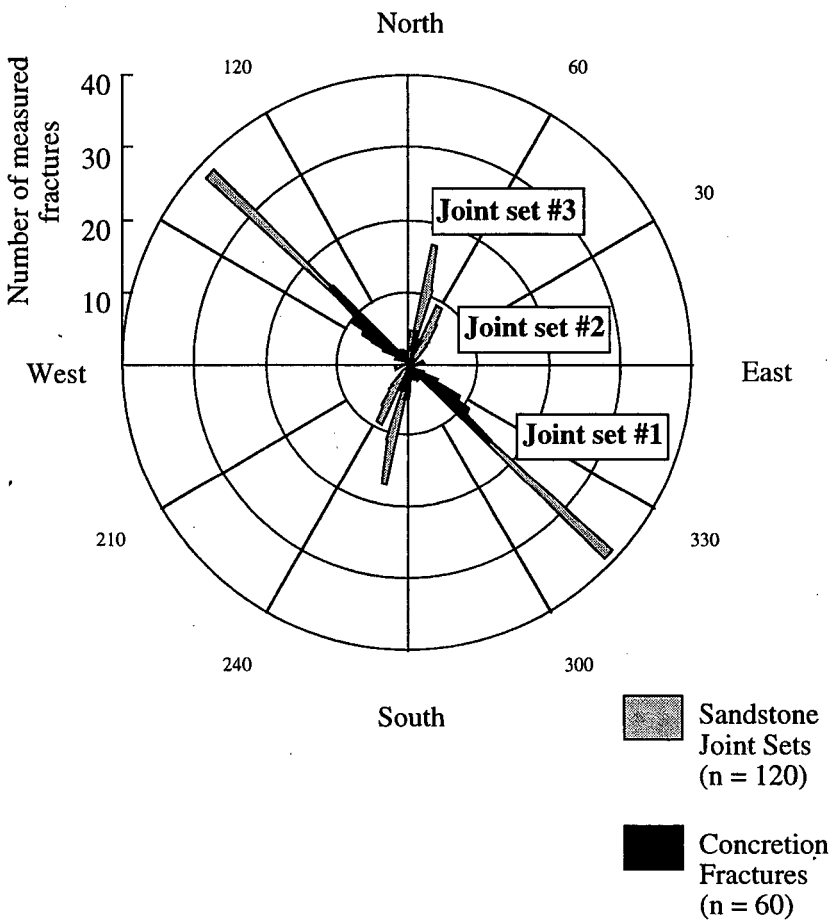

Figure 6.5 The orientation of a random sampling of 120 joints and 60 concretion fractures. The joint sets and concretion fractures had precisely the same orientation. Joint set #1 was roughly parallel to the anticlinal hinge of Figure 6.1.

and preferential vegetation. The dilation of the fractures generally occurred on the microscale. Because no mode II displacement was discerned, the fractures in set #1 were likely *joints* .

To measure the ratio of joint height to spacing of joint set #1, additional mapping was performed in two locations where vertical cross sections were available. Figure 6.6.a is a more extensive map of the Area 1 scanline with joint spacing measured along the line A-A' versus 4.5 feet of exposed bedding. Joint spacing was also measured in Area 10, slightly offset from the scanline of Figure 6.4, across the B-B' scanline of Figure 6.6.b. Figure 6.7 illustrates that joint spacing was considerably closer than the height of exposed bedding, which raised some preliminary concerns about the relative importance of tensile driving stresses at the field site. Pollard and Segall (1987) showed that at one length away from an open crack in a far field tensile stress field only 72% of the remote driving stress is recovered. A hypothetical "tensile" jointing distribution may resemble the curved line in Figure 6.7, which is exactly the opposite of the observed distribution.

Fracture sets #2 and #3 most commonly displayed the same linearity and lack of discernible dilation as joint set #1. In some cases, however, they were also characterized by measurable mode II offset and had served as zones of deep erosion. Shear displacement was most noticeable in the region along the scanline between 45 and 100 feet where right-lateral horsetail features and left-lateral en echelon jointing were observed. It is possible that fracture sets #2 and #3 were originally joints that were later sheared (much the same as the faulted joints described by Segall and Pollard (1983)). The fact that there were many unsheared fractures belonging to sets #2 and #3, and the morphology of these unsheared fractures were nearly-identical to joint set #1, supported this hypothesis.

The relative ages of the *joint* sets could not be determined based on the field observations because no systematic cross-cutting relationships were identified. Renshaw and Pollard (1995) showed that for the case where pre-existing joints are closed, younger joints may intersect rather than terminate against older joints.

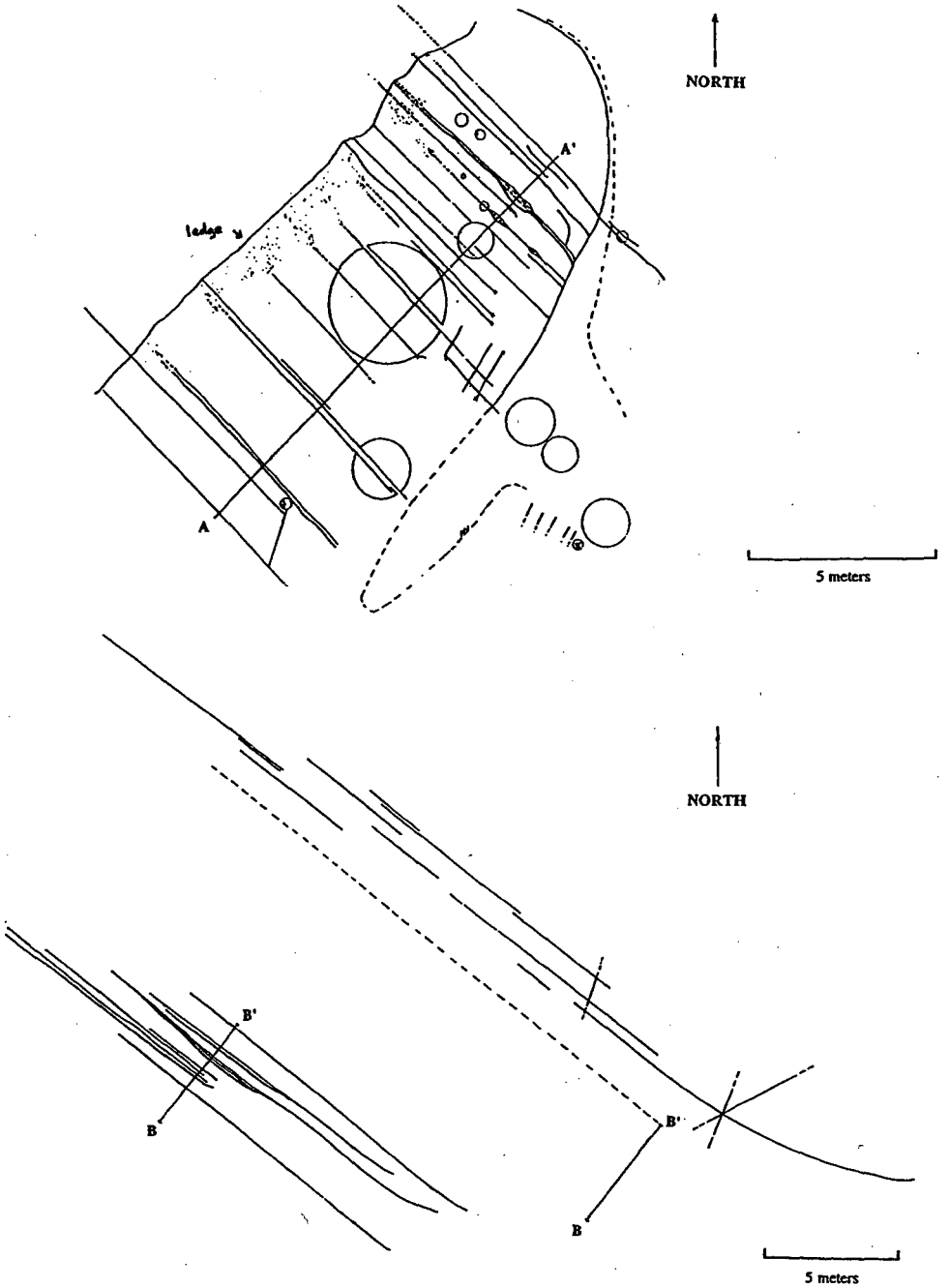

Figure 6.6 a) An extended map of Area 1, with portions not shown in Figure 6.4. The scanline A to A' was used to measure fracture spacing versus the exposed bedding depth of 4 feet. Because bedding was massive, the depth of this particular bedding may be thicker than can be observed. b) Map of Area 10 slightly offset from Area 9. The joints in this figure are very closely-spaced and linear for most of their lengths. The joints constrained by line B to B' actually lie across B to B' in the joint zone to the right. Fracture spacing measurements were also made along this line. The long dashed line parallel to the joints represents a ledge. The crossed lines at the end of the joint zone on the right represents the other two fracture sets of the region. Past Area 10 along the strike of the beach the fractures become so dense that no attempt was made to map them.

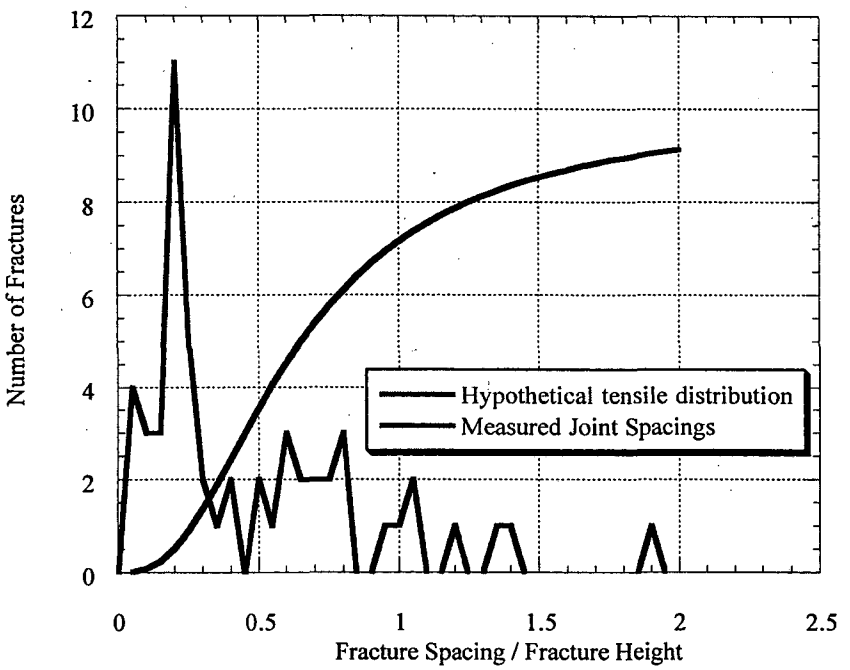

Figure 6.7 The results of the joint spacing measurements versus exposed bedding height. Most joints were spaced much closer than exposed bedding depth. A hypothetical joint distribution formed in a tensile stress field is represented by the solid line. The shape of this curve is based on predictions of Pollard and Segall (1987) described in the text.

6.3.5 Observations of concretion fractures

The fractures in the embedded concretions were more complex than those in the sandstone matrix, and concretions were initially subdivided into five different categories for purposes of this study: 1) unfractured (Type #1); 2) fractured by one or more joints which extended from the sandstone through the concretion (Type #2); 3) unfractured internally, but exhibiting debonding from the matrix (Type #3); 4) fractured internally, without debonding (Type #4); and 5) internally fractured with debonding (Type #5). Examples of the various types of concretion represented by the core samples of Table 6.1 are shown in Figure 6.8. The amount of dilation of the fractures was highly variable, ranging from the microcrack scale to completely open. Some of the dilated fractures likely represented increased erosion.

The fractures in the concretions at the field site should not be confused with fractures in septarian concretions. In the latter case, fractures in horizontal cross-sections show no preferential orientation (Astin, 1986). Fractures in septarian concretions are also generally widest at the center of the concretions and narrowest towards the edges (Hounslow, 1997). Finally, calcite cement often fills these fractures with the same isotopic signature as the outer edges and are thus likely created while the concretions are forming (Marshall, 1982). It has been proposed that the fractures in septarian concretions form early in diagenesis when cementing of pore spaces occlude dewatering, thus localizing excessive pore pressures within the concretions, and causing hydraulic fracturing (Hounslow, 1997). The concretion fractures at Vancouver Island not only exhibited preferential orientations, but because they were in precisely the same orientation as the joint sets in the sandstone, they were paleostress indicators which likely formed in the same stress field as the joint sets, after at least partial sandstone diagenesis had occurred.

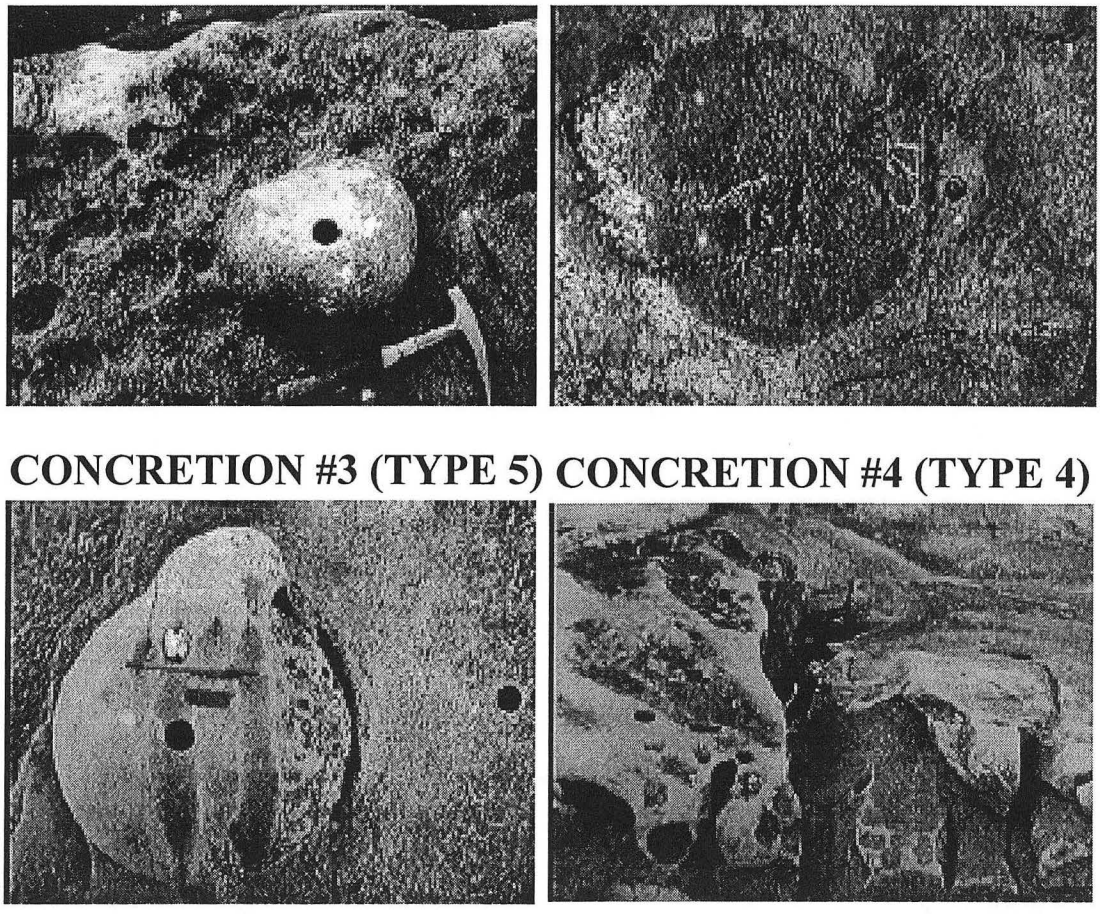

Figure 6.8 The concretions and sandstone from which the cores in Table 6.1 were derived. a) Concretion #1 was unfractured and classified as a Type #1 concretion. b) Concretion #2 had two internal fracture sets internal to the concretion, but no clear debonding (Type #4). A "halo" zone surrounded the concretion. c) Concretion #3 contained multiple, internal fractures which had been filled with eroded sediment. Debonding fractures were evident in the sandstone matrix (Type #5). This concretion also represented the concretion labeled #6 in Figure 6.20. d) Concretion #4 was over a meter in diameter. There were multiple internal fractures, but no debonding (Type #4).

6.4 Field measurements

6.4.1 Field methods

The objective of the field measurements was to record the mechanical properties of the two distinct lithologic units, and the method chosen was a portable nondestructive testing device called a Schmidt hammer, which measures the rebound of the Schmidt hammer plunger mass with the rock. The impact between the Schmidt hammer and rock can be treated as an inelastic collision, and the equation governing the resultant rebound can be derived from the laws of conservation of mechanical energy and conservation of linear momentum to be:

$$k = -\frac{v_2}{v_1} = \sqrt{\frac{h_2}{h_1}} \tag{6.4}$$

where k is the coefficient of restitution, v_1 and h_1 are the impact velocity and height, and v_2 and h_2 are the rebound velocity and height (Hucka, 1965). The coefficient of restitution has also been called the coefficient of dynamic elasticity, and the value for a particular impact has been shown to be governed mostly by the properties of the softer material. Because v_1 and h_1 are functions of the test hammer, the relative rebound height for the N-type hammer is a measure of the surface hardness of the rock being impacted. The maximum rebound value recorded by the Schmidt hammer ranges from 0 to 100, indicating the percent of the forward distance the mass rebounded.

Many different Schmidt hammer measurement techniques have been conceived (e.g. Atkinson, 1978; Poole and Farmer, 1980), but the method selected for this study was to take seven consecutive hits at any one location, discard the first two impacts, and average the middle three. Although this method may have caused some compaction, it was justified on the basis that the first two impacts were highly variable and were lower than the remaining five impacts (Figure 6.9). Impacts were made every three feet along the scanline of Figure 6.4 to measure the variation in sandstone properties, and within and adjacent to each concretion to measure the contrast in properties between the two lithologic units. To account for the ISRM recommendation that no cracks should be present within 6 cm depth, all impacts which produced a low frequency

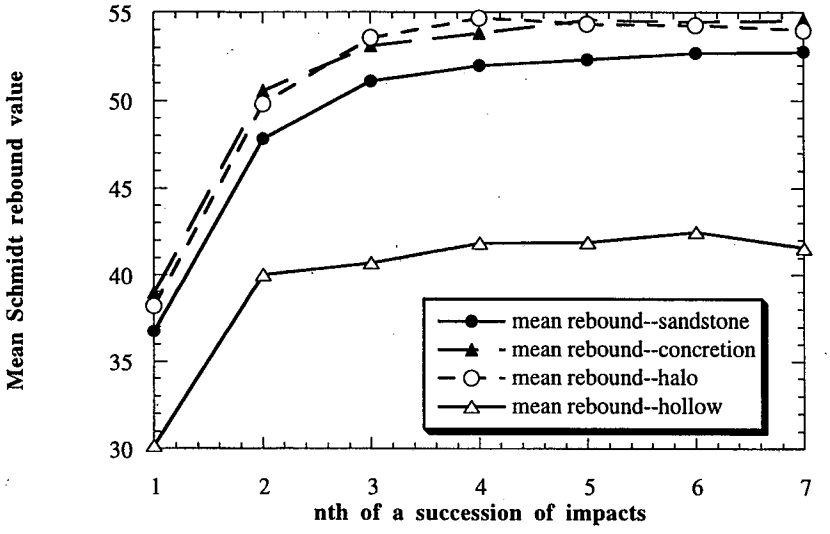
Mean Schmidt rebound value
55
50
45
40
35
30
1
2
3
4
5
6
7
nth of a succession of impacts
mean rebound--sandstone
mean rebound--concretion
mean rebound--halo
mean rebound--hollow

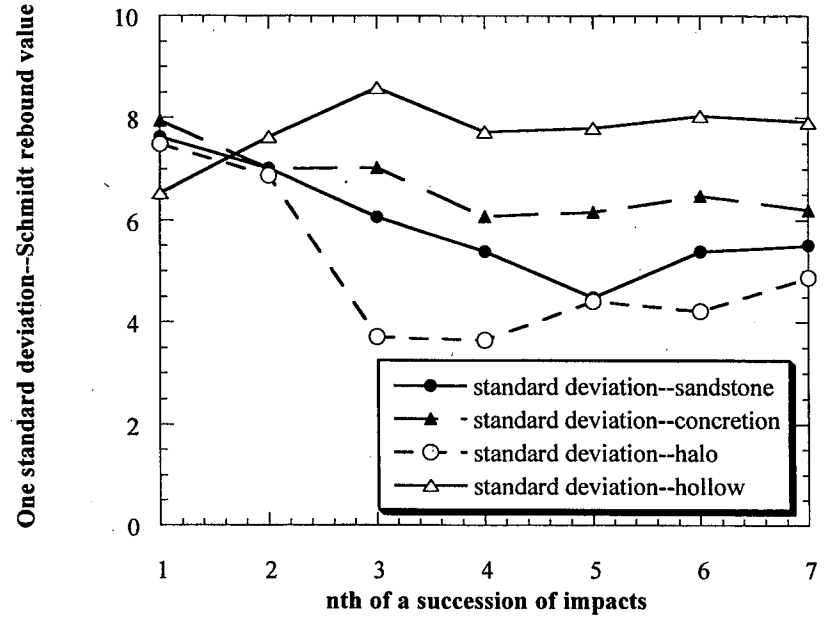
One standard deviation--Schmidt rebound value
10
8
6
4
2
0
1
2
3
4
5
6
7
nth of a succession of impacts
standard deviation--sandstone
standard deviation--concretion
standard deviation--halo
standard deviation--hollow

resonance were considered to have sampled delamination of the sandstone and were removed from further consideration (the bottom curve in Figure 6.9.a shows the justification for this procedure).

One potential source of measurement error which had to be accounted for in the field study was the possibility that Schmidt rebound values would decline with use due to a build-up of metal fillings within the hammer (which increases friction and damping) (McCarroll, 1987). Figure 6.10 shows the distribution of Schmidt hammer rebound values for the sandstone matrix with time (the gaps are due to concretion impacts). The mean sandstone values actually increased slightly with time because Areas 1 and 2 (which had rebounds lower than the mean) were measured first. Consequently, this source of measurement error was unimportant.

6.4.2 Measurement of sandstone rebound values

To try and identify trends in the sandstone Schmidt readings along the scanline, a 6-foot moving average value was assigned to each measurement point based on its rebound value and the value of its two neighboring rebounds. Figure 6.11 shows the moving average of Schmidt rebound values as a curve, with a 6-foot moving average fracture density contour map indicated by the shading underneath the curve. It is immediately clear from this figure that the most densely fractured regions were Areas 1 and 2. Schmidt values below the mean were also indicative of these two areas.

Because Figure 6.11 suggested that lower Schmidt values may have been spatially associated with fracture zones, different Schmidt hammer subpopulations within the field site were identified using an F-statistical test. The theory behind F-statistical tests can be found in Weiss (1993), but the general idea is that if F-values calculated from the means and standard deviations of each population under comparison exceed tabulated F-statistic values, then the null hypothesis holds, and the two data sets are from different subpopulations. The mean values used in these calculations are shown in Table 6.2 for unfractured sandstone, fractured sandstone (i.e. a fracture density > 0.75 ft/ft^2), concretions, halos, and concretions which were surrounded by halos.

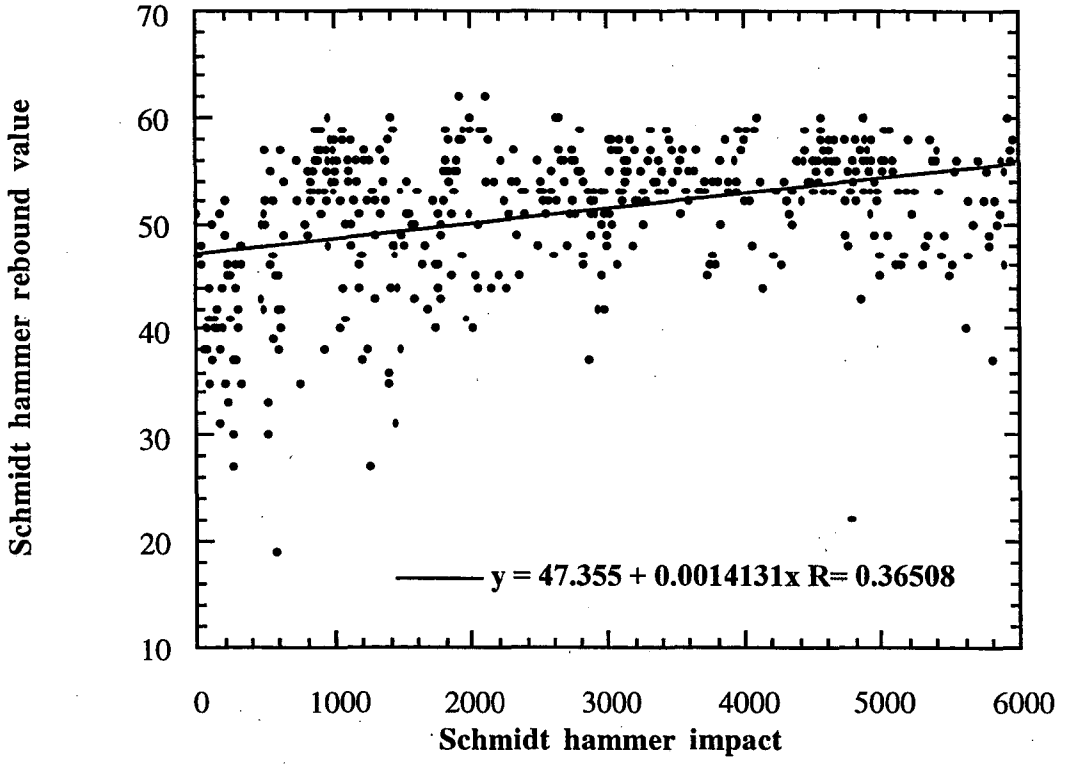

Figure 6..10 Distribution of mean Schmidt rebound values within the sandstone as a function of time. The gaps in measurements in the figure represent concretion impacts. The overall trend of Schmidt values increased with time (see text for explanation).

Figure 6.11 Comparison of Schmidt rebound values to fracture densities along the scanline in the middle of Figure 6.4. Schmidt values were recorded at three foot intervals and the curve represents their moving average. The mean value was 53.7 and is given by the vertical line. The shading represents the relative fracture density measured around a 36 square foot area encompassing each rebound. Fracturing was diffuse except in Areas 1 and 2 and a portion of Area 6. Lower Schmidt readings were also recorded there.

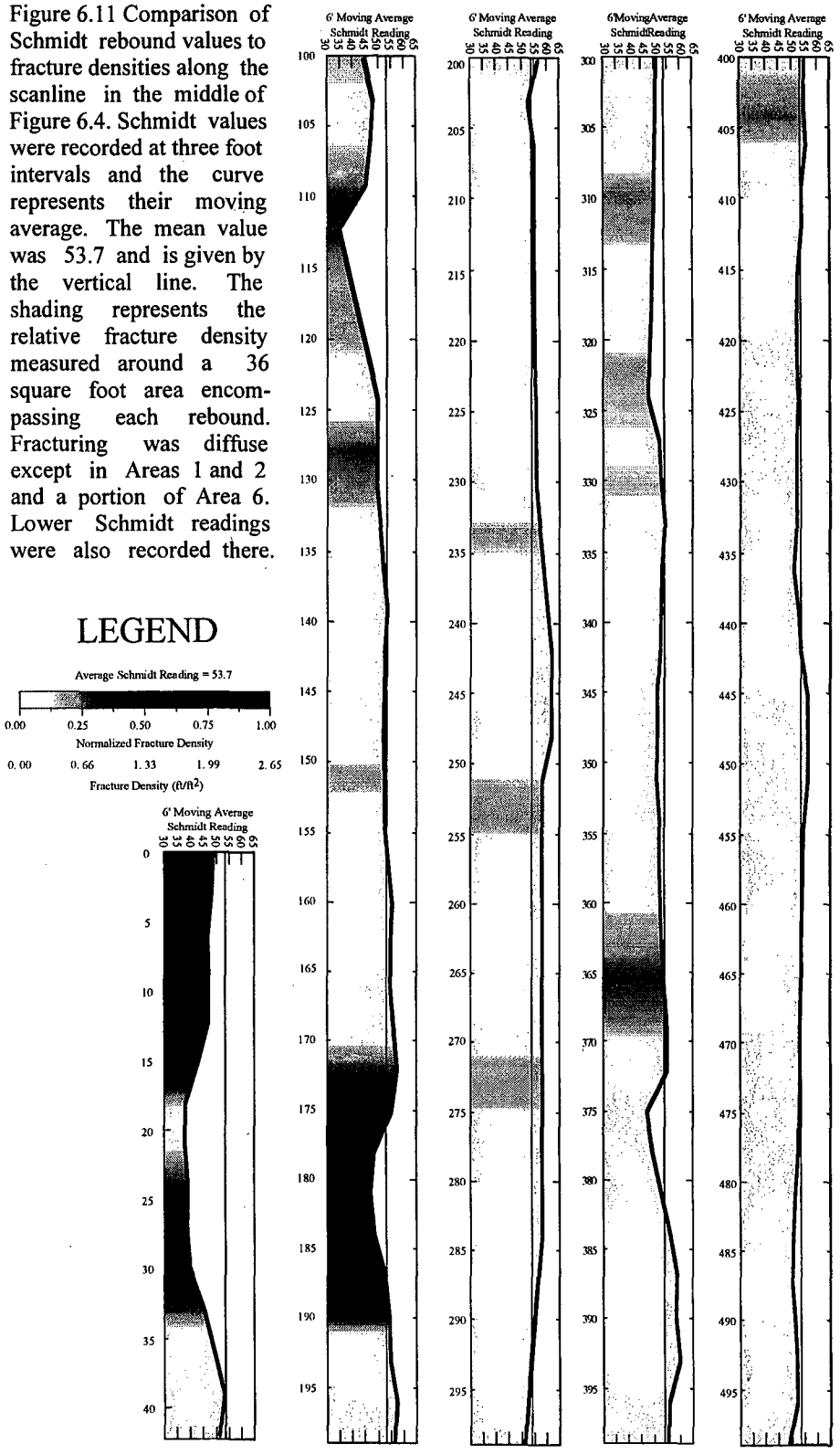

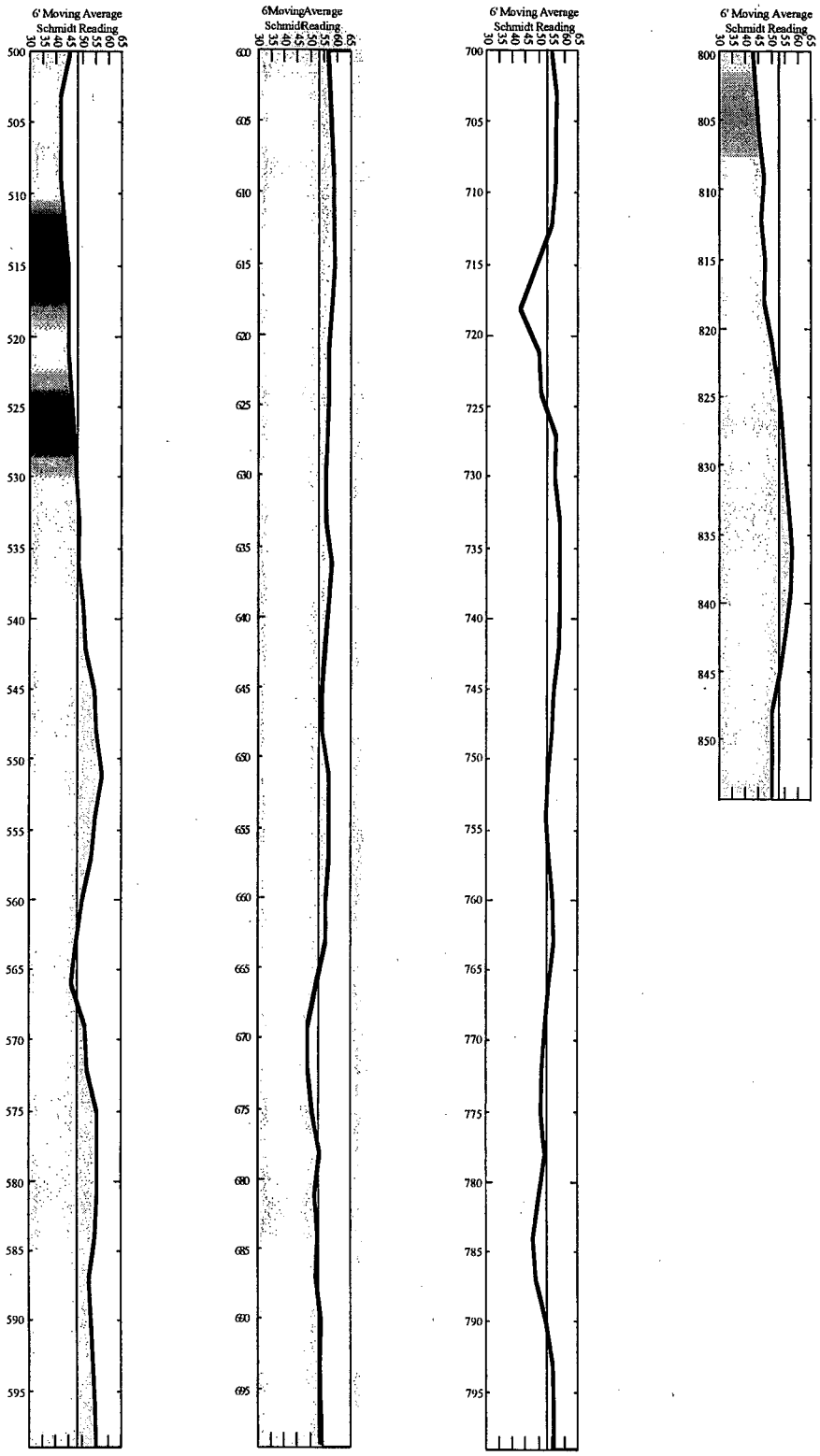
6' Moving Average
Schmidt Reading
30 35 40 45 50 55 60 65
500 505 510 515 520 525 530 535 540 545 550 555 560 565 570 575 580 585 590 595
6'MovingAverage
SchmidtReading
30 35 40 45 50 55 60 65
600 605 610 615 620 625 630 635 640 645 650 655 660 665 670 675 680 685 690 695
6' Moving Average
Schmidt Reading
30 35 40 45 50 55 60 65
700 705 710 715 720 725 730 735 740 745 750 755 760 765 770 775 780 785 790 795
6' Moving Average
Schmidt Reading
30 35 40 45 50 55 60 65
800 805 810 815 820 825 830 835 840 845 850

Population Type	Mean Schmidt Rebound Number [%]
Unfractured Sandstone	52.6
Fractured Sandstone	47.2
Concretion	54.6
Halo	55.6
Concretion with Halo	56.6

Population 1	Population 2	F-value	F-table value	Subpopulations
Unfractured Sandstone	Fractured Sandstone	20.17	<3.92	DIFFERENT
Unfractured Sandstone	Concretion	16.88	<3.92	DIFFERENT
Unfractured Sandstone	Halo	4.81	<3.92	DIFFERENT
Halo	Concretion	0.53	<3.92	SAME
Halo	Concretion with Halo	0.44	4.2	SAME

Table 6.2 a) Mean Schmidt hammer rebound numbers measured along the scanline of Figure 6.4 used to identify regions of the field site with different mechanical properties. Unfractured sandstone was distinguished from fractured sandstone by its fracture density per square foot (i.e. > 0.75 ft/ft^2). The fractured sandstone had the lowest rebound values and concretions the highest. b) F-statistical test results indicated that the mean and standard deviations of the unfractured sandstone, fractured sandstone, and concretions were from different subpopulations. The halos could not be distinguished from the concretions they formed around.

According to the table, the fractured sandstone had the lowest mean Schmidt rebound number, the unfractured sandstone intermediate values, and the concretions and halos the highest. Table 6.2 also indicates that the unfractured sandstone formed a different subpopulation from the fractured sandstone, and Figure 6.12 illustrates this result graphically, by comparing the average rebound value of fracture zones along the scanline to the average rebound values of the relatively unfractured sandstone on either side. Almost all of the unfractured areas had higher Schmidt values than their adjacent fracture zones. The only exception was in Area 1, where the entire area had low Schmidt values. The key question from this analysis is: Were the lower Schmidt readings a product of increased weathering in the vicinity of the fractures, or did locally, weaker sandstone control the location of fracture zones?

6.4.3 Measurement of concretion rebound values

To test if the concretions exhibited a similar relationship to fracture density as the sandstone, concretion subpopulations were also identified using an F-statistical test. The first of these tests is shown in Table 6.2, in which it can be observed that halos cannot be distinguished from either the concretions they formed around, or from any other concretion. A second concretion subdivision was made by testing if the five different categories of concretions described above were mechanically separable. Table 6.3 reports the mean Schmidt rebound values for each concretion type which were used to identify three distinct subpopulations: Type #1; Type #2; and Types #3, #4, and #5. Because the former two types were distinguished only by the fact that the latter happened to be in the path of a sandstone fracture, they were grouped together for remainder of this presentation and renamed Group #1 (Types #3, #4, and #5 were similarly reclassified as Group #2). Figure 6.13 shows both the distribution of concretion Schmidt values, and the ratio between the concretion and adjacent sandstone values. The most highly fractured concretions had the highest Schmidt values and highest Schmidt values relative to the surrounding sandstone. This positive correlation between concretion hardness and fracture density was exactly the *opposite* of the sandstone.

Population Type	Mean Schmidt Rebound Number [%]
Type 1	52.2
Type 2	47.1
Type 3	57.4
Type 4	57.4
Type 5	58.4

Population 1	Population 2	F-value	F-table value	Subpopulations
Type 1	Type 2	4.95	<4.0	DIFFERENT
Type 1	Type 3	30.07	3.92	DIFFERENT
Type 3	Type 4	0.00	<3.92	SAME
Type 3 and 4	Type 5	0.74	<3.92	SAME

Table 6.3 a) Mean concretion rebound numbers used for each of the "types" of concretions discussed in the text. Types 1 and 2 had the lowest rebound numbers. b) F-statistical test results indicated that the mean and standard deviations of concretion types 3, 4, and 5 overlapped. This meant that they could not be mechanically discerned from one another based on Schmidt rebound numbers. Although Types 1 and 2 belonged to different subpopulations, for purposes of this study they were grouped together and labeled Group 1 for the remainder of the paper (see text).

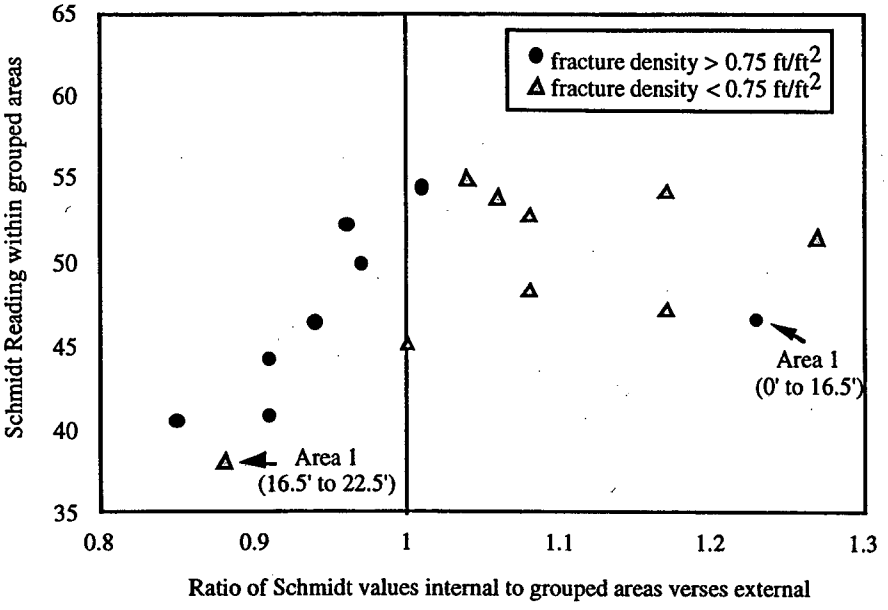

Figure 6.12 Comparison of mean Schmidt rebound numbers for different regions of the study area grouped together by their fracture densities. For example, Area 1 (0' to 16.5') represented a relatively unfractured region (fracture density < 0.75 ft/ft^2) surrounded by two regions with fracture densities greater than 0.75 ft/ft^2. The mean Schmidt value for any region is shown along the vertical axis and the ratio of the mean value to the surrounding two regions along the horizontal axis. Except for two regions in Area 1, the largest Schmidt rebound number and ratios occurred for the unfractured regions.

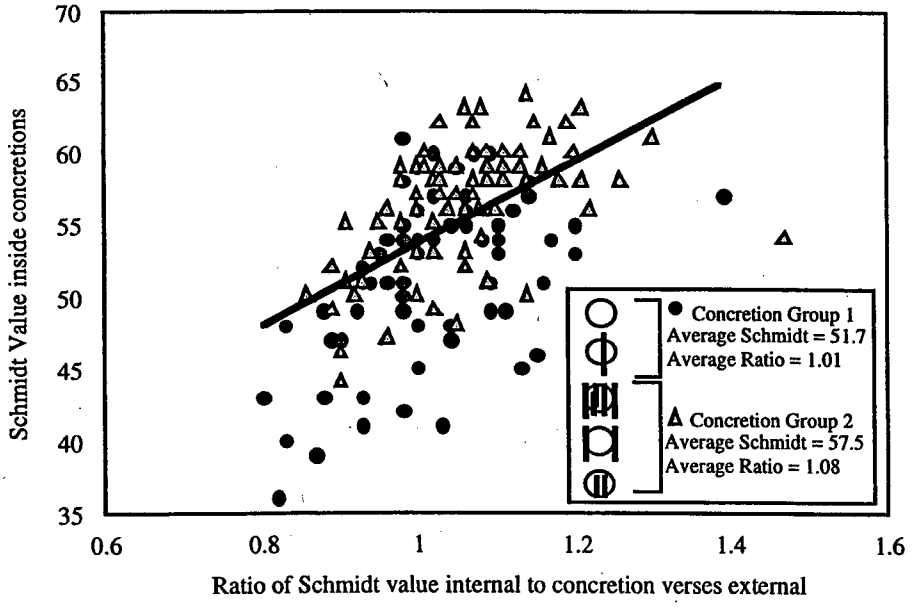

Figure 6.13 Comparison of the mean Schmidt rebound values of "unfractured" (Group 1) and fractured (Group 2) concretions. The vertical axis is the mean value and the horizontal axis the ratio of the mean value measured within and outside of the concretion. The fractured concretions had both the highest Schmidt values and ratios. This result was exactly the *opposite* of the sandstone in Figure 6.12.

6.5 Laboratory measurements

6.5.1 Objective of laboratory experiments

Because field observations suggested that the fractured concretions were paleostress indicators (i.e. clues to the geologic stress at the time of fracturing), the most plausible jointing scenarios consisted of those which conformed to the following additional observations: 1) many concretions were preferentially fractured relative to the surrounding sandstone matrix; 2) debonding occurred along the concretion/sandstone contact; and 3) many concretion fractures were closely-spaced relative to their shortest dimension. Although field measurements indicated that the hardest concretions may have concentrated geologic stresses in excess of their strength, hardness values could not be used as input into analytical and numerical models to test this hypothesis. Consequently, this section describes experimentally-determined elastic moduli and strengths which could.

6.5.2 Uniaxial compression tests

Static moduli were calculated from uniaxial compression tests on the cores described in Table 6.1, after sections of the longer cores had been removed for Brazilian testing. The third column of Table 6.4 shows the height to diameter ratios of the cores used in the uniaxial tests. These ratios were smaller than the 2.5-3.0 recommended by the ISRM (Bieniawski, Z. T., 1979). Consequently, it was likely that the steel end platens interacted strongly with the rock cores, restricting their lateral expansion, and making resulting strength and Young's modulus measurements upper estimates of their *in situ* value. Apart from this discrepancy, measurement methods were in accord with those of the ISRM. The rock specimens were placed between steel end platens on a spherical seat in a testing machine, and LVDT strain gauges measured both axial and diametric displacement. The Young's modulus was calculated from the slope of the linear portion of the resulting stress-strain curve, and the Poisson's ratio was calculated from:

$$\upsilon = -\text{(Young's modulus)} / \text{(slope of diametric stress-strain curve)}; \qquad (6.5)$$

Core	Sample #	height/ diameter	Compressive Strength [MPa]	Youngs Modulus E [GPa]	Youngs Modulus E* [GPa]	Poisson Ratio	E* / E	E/ Strength
Sandstone 1	1	1.44	95.2	15.0	31.1	0.06	2.07	327
Sandstone 2	2	1.42	121.0	20.8	40.0	0.14	1.92	330
Sandstone 4	1	1.44	118.3	17.5	35.0	0.07	2.00	296
Concretion 1	1	1.42	105.4	21.0	45.8	0.18	2.18	435
Concretion 2	1	2.27	191.0	63.3	86.3	0.31	1.36	452
Concretion 3	1	2.24	197.6	58.0	66.7	0.26	1.15	337
Concretion 4	1	1.43	141.3	50.0	68.0	0.23	1.36	354
Halo	1	2.30	142.3	32.5	52.0	0.07	1.60	366

Table 6.4 Results of the uniaxial compression tests. The sandstone had lower moduli and strength than the concretions, except for Concretion #1, which was weaker. These results were consistent with thin section and Schmidt hammer results which suggested that Concretion #1 was both petrologically and mechanically different than the other three concretion cores. The results for a "halo" zone is also included in the final row. Its static moduli were lower than the Type 2 concretions, but its strength was comparable, and higher than the sandstone. Also given in the table were Youngs moduli determined during unloading loops [E*]. The significance of these is discussed in the text.

where the slope of the diametric curve was negative.

Table 6.4 shows that the static moduli of the sandstone was always less than the concretions. The sandstone strengths were also less that the concretions, except for Concretion #1, which had comparable strength. Based on the thin sections discussed above, it was likely that the additional calcite cement stiffened grain contacts while more effectively redistributing the axial loading stress horizontally.

During the linear portion of the stress-strain loading curve, small strain unloading cycles were performed and the average Young's modulus [E*] was calculated from the slope of the unloading loop. The values of E* that was obtained was always greater than the static Young's modulus [E], consistent with the hypothesis that during small strain unloading cycles frictional sliding along microcracks and grain boundaries are immobilized (Hilbert, et al., 1994). With this hypothesis in mind, a frictional indicator is given by the ratio E*/E in Table 6.4. Because frictional sliding of grain contacts can induce microcrack growth, the E*/E ratio should also have given a relative indicator of strength, because microcrack growth is a precursor to extensile failure. With the exception of Concretion #1, the concretions were much stronger than the sandstone, had the lowest E*/E ratio, and the highest static Young's modulus.

6.5.3 Brazilian tensile tests

Tensile strengths were determined indirectly via the Brazilian test. In these experiments a compressive stress applied as a point load induced tensile stresses in an orthogonal direction. In preparation for these experiments, samples were first machined to an approximate thickness to diameter ratio of 0.5:1, as recommended by ISRM (Bieniawski, Z. T., 1978) (Table 6.5). Small pieces of paper were then placed in between the rock samples and steel platens to distribute the load over a small arc and decrease the likelihood of shear failure initiating at the contacts (Jaeger and Cook, 1979). Finally, the tensile strength was calculated from the maximum load using the following equation:

$$\text{Tensile strength} = (\text{Maximum Load}) \,/\, (\text{Thickness} * \text{Diameter}). \qquad (6.6)$$

Table 6.5 shows that the concretions generally had a higher tensile strength than the sandstones, and compressive strengths were generally an order of magnitude larger than the tensile strengths.

6.5.4 Correlation of laboratory to field results

Table 6.6 summarizes the coefficients of correlation between the Schmidt rebound values obtained from the sandstone and concretions represented by Table 6.1 and the rock properties measured in the laboratory. The values for coefficients can theoretically range from -1.00 to 0 to 1.00, indicating a perfect negative correlation, no correlation, and a perfect positive correlation, respectively. This table shows that the coefficients of correlation were relatively strong for all of the properties except the Poisson's ratio. Based on Figure 6.13, this confirmed the Schmidt hammer results that the highest moduli and strongest concretions were also the most likely to be fractured.

6.6 Analysis of concretion fracturing

6.6.1 Selection of input parameters

It was decided to infer the applied stresses leading to the genesis of joint set #1 by testing which combination of stresses could have created the preferential debonding and internal fractures observed in the concretion represented by Figure 6.3 (located in Area 9). The finite element code chosen for this investigation was Ansys 5.4, which was capable of modeling both elastic deformation and which could also solve for the stress and strains in three-dimensions by taking advantage of the symmetry imposed by the spherical concretions. In order to perform the simulation, an isolated concretion was enclosed in a sandstone matrix extending six radii from the concretion center. The error associated with not enclosing the concretion in an infinite medium was always less than 1.5%, as calculated by the analytical solution for an unfractured inclusion (Eshelby, 1957).

Because high pore pressures and/or tectonic tensile stresses are required even for compression-driven jointing (in this case, to create a high deviatoric stress), the first challenge of

Core	Sample #	height/ diameter	brazilian strength [MPa]	comp./ tensile strength
Sandstone 2	1	0.49	10.9	11.1
Sandstone 3	1	0.49	10.2	
Concretion 1	2	0.47	9.4	11.2
Concretion 2	1	0.48	17.7	10.8
Concretion 3	1	0.47	15.1	13.1
Concretion 4	2	0.49	22.5	6.3
Halo	1	0.48	10.7	13.3

Table 6.5 Tensile strengths for the cores represented by the thin sections of Table 6.1. Concretion #1 was found to be weaker than the sandstones, but the other concretions were stronger.

	Calcite	Static Youngs Modulus	Unloading Youngs Modulus	Poisson Ratio [υ]	Compressive Strength [Co]	Tensile Strength [To]	Schmidt Rebound Number
Calcite	1.00						
Static Youngs Modulus	0.93	1.00					
Unloading Youngs Modulus	0.92	0.97	1.00				
Poisson Ratio [υ]	0.80	0.84	0.86	1.00			
Compressive Strength [Co]	0.78	0.93	0.88	0.72	1.00		
Tensile Strength [To]	0.83	0.77	0.77	0.64	0.50	1.00	
Schmidt Rebound Number	0.78	0.81	0.76	0.58	0.77	0.67	1.00

Table 6.6 Coefficients of correlation between the different rock properties measured in the field and in the laboratory. The amount of calcite cement had a strong positive correlation with all of the other rock properties, suggesting it stiffened grain contacts. The Schmidt rebound number also had a positive correlation with the laboratory results. The Schmidt hammer correlations were used to estimate the moduli of the concretions in Figure 6.20.

this study was to select which tensile stress scenarios might have occurred at the field site and estimate what the rock properties were as input parameters to the model. Examples of the conditions leading to tensile stresses in the Earth were reviewed in *Chapter 6.1* and included: burial of a sedimentary basin below the chord of the earth, or renewed uplift, where plate flexure occurs (Price and Cosgrove, 1990); deformation along the crest of folds (Nur, 1982; Kemeny and Cook, 1985); thermal or mechanical strains applied as a result of differing elastic properties within a layered sequence (Suppe, 1985; Wu and Pollard, 1995); and, finally, tensile effective stresses due to very high pore pressures (Secor, 1965).

Based on the observations described above, the only unlikely scenario at the field site was the generation of tensile strains due to interlayers of contrasting material properties (i.e. the rock unit was generally homogenous and massive). By contrast, tensile stresses could have occurred during burial of the sedimentary sequence below the chord of the Earth, or during folding when the anticline in Figure 6.1 was produced. The fact that joint set #1 was parallel to both the anticlinal axis and the long axis of the basin supported either of these scenarios. Elevated pore pressures may have assisted in reducing the gravitational confining stress, although it would also have had the effect of reducing the maximum compressive stress parallel to the joint, which would have inhibited compression- driven extensile fracturing.

The first two cases described below explore the folding scenario where fracturing occurred during anticline development, using the mean rock properties measured in the laboratory and listed in Table 6.7. The properties of the concretions used for this analysis were divided into Group #1 (unfractured) and #2 (fractured), consistent with the Schmidt hammer results above. The rock properties of the sandstone for the case of burial (Case #3) were more speculative because diagenesis may not have been completed when fracturing occurred. This case is discussed in greater detail below.

PROPERTY	CONCRETION GROUP 1 (UNFRACTURED)	CONCRETION GROUP 2 (FRACTURED)	STRONG SANDSTONE	WEAKER SANDSTONE
E [MPa]	21.0	57.1	17.8	10.34
υ	0.20	0.27	0.09	0.32
σ_C [MPa]	105.4	176.6 ± 25.1	112 ± 11.6	91.2
σ_T [MPa]	9.4	18.4 ± 3.1	10.6 ± 0.4	10.2

Table 6.7 Summary of the rock properties used in the numerical simulations. The values for Concretion Type 1, Concretion Type 2, and the Strong Sandstone were based on the mean values determined in the laboratory. The properties for the Weak Sandstone were taken from (Touloukian, et al., 1989) to represent the condition where the sandstone was not completely lithified. The results could actually have been applied to any case where the ratio of rock properties were different than those measured in the field. For example, temperature and stress are known to impact mechanical properties of rock and the weak sandstone case may have occurred during folding instead of burial (Price and Cosgrove, 1990).

6.6.2 CASE #1: Tensile loading

The far field tensile loading stress applied to the concretion and matrix in this case was uniaxial and had a magnitude of 10.6 MPa, or the mean tensile strength of the sandstone. The objective of using this value was to analyze the static case where the stress inside the concretion had already been exceeded before the sandstone had begun to fracture.

Unfortunately, the first result of this analysis was that *unfractured* Concretion Group #1 should have been in a state of stress in excess of its strength (126%), a result which was inconsistent with observations. This incompatibility implied three possibilities: 1) The rock properties represented by the laboratory measurements were not the same as those present when fracturing occurred; 2) Since only one data point was available for analysis, its strength and modulus were not statistically representative; and/or 3) Because this concretion was found in the middle of the joint swarm of Area 2, it may have been partially shielded from the applied stress.

Recognizing that this issue represented a fundamental uncertainty, this analysis was nonetheless continued for the case of Concretion Group #2. Figure 6.14.a shows the subsequent tensile stress within and adjacent to such a concretion under an applied uniaxial tensile stress. Using dashed horizontal lines to delineate the stresses leading to both sandstone and concretion fracture, the three dimensional solution predicted failure both in the concretion and in the sandstone directly adjacent to it. For comparison, the two-dimensional plane strain case did not produce enough stress to preferentially fracture the concretion.

Because the stress in the sandstone just outside of the concretion along the x-axis was the same as the stress within the concretion, it was likely that debonding of the concretion would have preceded concretion fracturing. Figure 6.14.b shows the state of stress along both the x-axis and y-axis for the case where a debonding fractures on either side of the concretions had extended a distance of one diameter from the edge. According to the figure, the stress along the x-axis was very close to zero, and the stress along the y-axis never again exceeded the strength of the concretion.

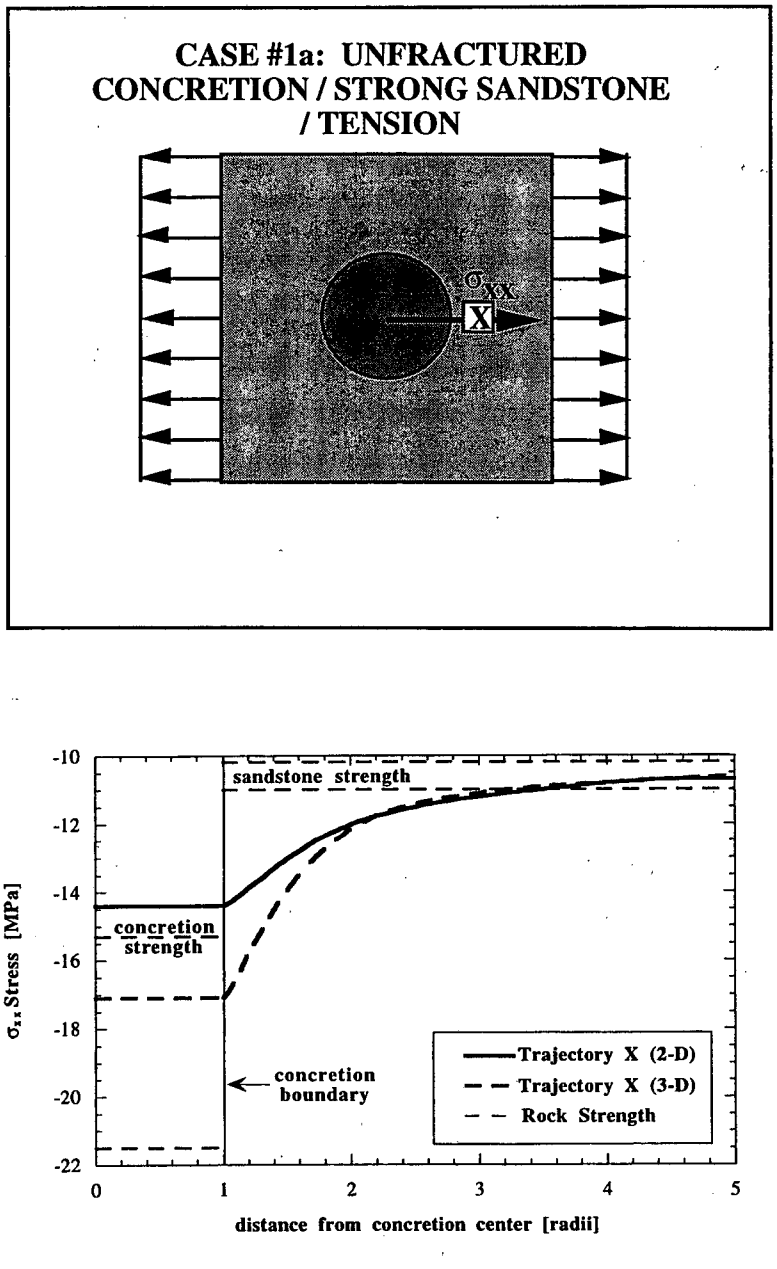

Figure 6.14 Results of the numerical experiments for the case where tensile loading stresses were applied. The top figures depict the loading cases and the location of any fractures within and around the concretions. The lower plots show the σ_{xx} stress versus distance along the x-axis from the concretion center. The upper and lower limits for the strength of the sandstone and concretion were determined from one standard deviation in the measured laboratory values. a) For the unfractured concretion, a stress concentration occurs within the concretion and along the contact with the sandstone.

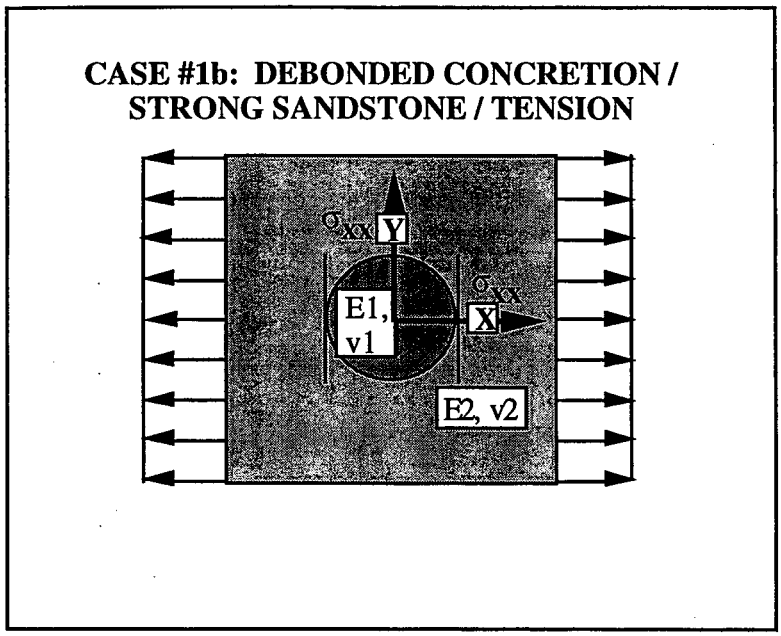

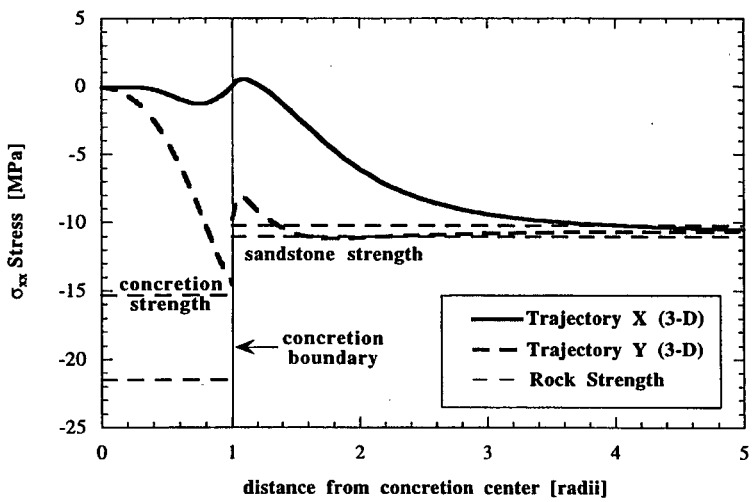

Figure 6.14 b) The stress at the debonding fracture is zero along the x-axis and decreases the stress inside of the concretion to a level significantly below its strength.

Based on these results, the only explanation for concretion fracturing under uniaxial tensile stresses applied perpendicular to the crack face was that fracture growth occurred subcritically. Under these conditions, the sensitivity of crack growth to the stress concentration factor is measured by the stress corrosion exponent [n], which is diminished by adsorption and/or dissolution reactions occurring at the crack tip. Olson (1993) and Renshaw and Pollard (1994) found that one joint cluster began to develop in their numerical experiment for a value of [n] = 12 and multiple joint clusters began to develop for values of [n] < 6. Despite these observations, there are two problems with attributing a similar mechanism to the Vancouver Island field site. First of all, their results relied on constant strain boundary conditions in which a more ductile layer transmitted stress to the brittle, fractured layer. Geologic analogs to this situation include: dolomite beds in phyllites; chert layers in limestone; and sandstone layers embedded in shales (Mandal, et al., 1994). Secondly, their initial joint cluster still created a stress shadow which inhibited cracking within a distance of one layer thickness away. Although they did observe higher joint densities for smaller stress corrosion indexes, they had to invoke values which were several orders of magnitude lower than have been produced experimentally. Crack growth at this small a value for [n] would occur essentially in the absence of any stress concentration at the tip, and is only possible for high temperature, solid state diffusion cracking which has not been verified for rock (Atkinson, 1987).

6.6.3 CASE #2: Compressive loading

Because knowledge of the mechanics of compression-driven jointing were not completely established, a couple of important issues regarding its diagnostic characteristics needed to be resolved in order to determine if compressive stresses could have generated the observed concretion fractures. The first uncertainty was the stresses leading to extensile failure. It has been shown that the failure mode and stress in uniaxial compression tests are greatly affected by the interaction of the rock with the end platens (Jaeger and Cook, 1979); however, because Turner (1999) verified that the mode of failure under true biaxial compression was extensile fracture, and

Jaeger and Cook (1963) found that the strength of the rock under a biaxial compressive stress was very similar to the uniaxial strength, the uniaxial compressive strength measurements of Vancouver Island rock cores were used to represent both the extensile failure mode and stress.

A second issue which needed to be addressed was understanding the spacing of fractures under compressive stresses. The dilation associated with extensile fracture should generate a small confining stress on adjacent grains, inhibiting nearby cracking. To model this effect, a crack with a constant opening displacement was generated using a finite difference code, and the resultant stresses analyzed in the direction perpendicular to the crack face (Figure 6.15.a). Figure 6.15 first illustrates that to achieve a constant opening, the tractions applied along the free surfaces of the crack must be greater at the tip than for a pressurized elliptical crack. Secondly, it reveals that the stress shadow associated with a constant opening for a longer crack is roughly one-half the case of a shorter crack. This result suggests that the compressive confining stress induced by a compression-driven crack becomes less important as the crack grows beyond the microscale. Because this result is consistent with Turner (1999), who found that extensile cracks were often spaced within a few grain diameters of one another, and given the macroscopic nature of concretion fractures, it was decided to ignore this small confining stress contribution.

Figure 6.16.a shows the stress in a concretion and along the concretion/sandstone interface for the case of a two-dimensional and three-dimensional uniaxial compressive load of 112 MPa applied along the y-axis. Also illustrated in the figure are two hypothetical failure envelopes for the concretion and sandstone. These failure envelopes have two fixed points, the uniaxial compressive strength and the tensile strength. The dashed lines in the figure represent one standard deviation in the strength measurements. Without having measured a failure envelope using the biaxial load cell of Jaeger and Cook (1963) and Turner (1999), the shape of a failure envelope is debatable; however, it was made linear in this study based on theoretical and experimental evidence cited in Jaeger and Cook (1979). Figure 6.16.a shows that the concretion in this case encountered confining stresses in the minimum principal stress direction, and would not fracture.

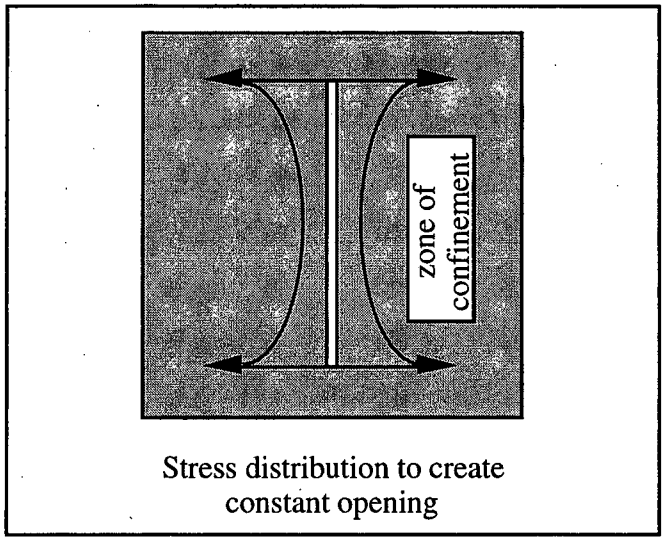

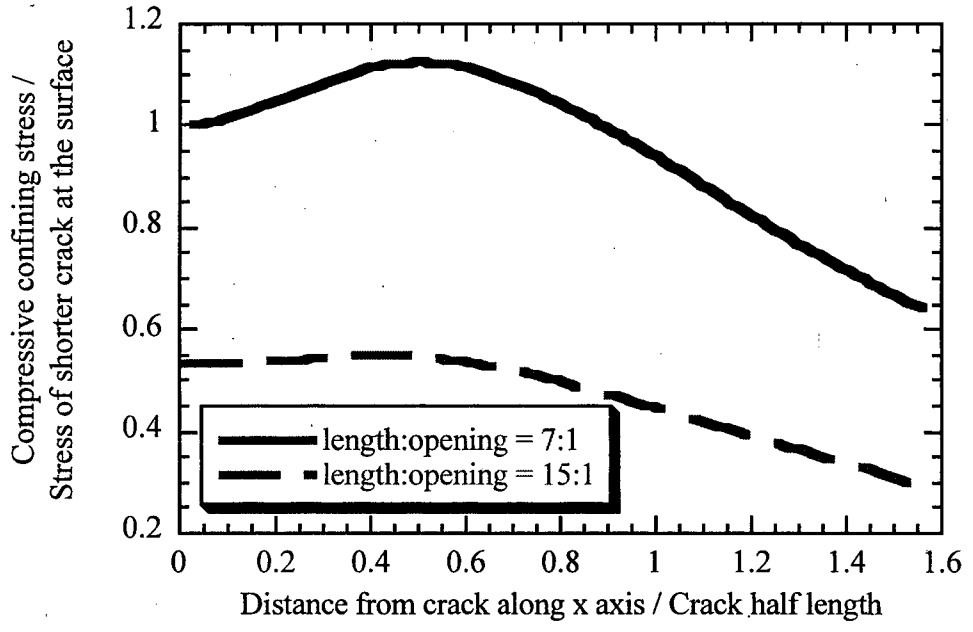

Figure 6.15 Plot of the compressive confining stress acting along the x-axis for the case of a crack with a constant opening displacement shown in the top figure. To achieve a constant opening the stress field was not uniform, but greatest at the tip. The stress for a crack of length to opening dimensions of 15:1 was approximately one-half the case for a crack with a ratio of 7:1, as can be observed by the normalized bottom plot.

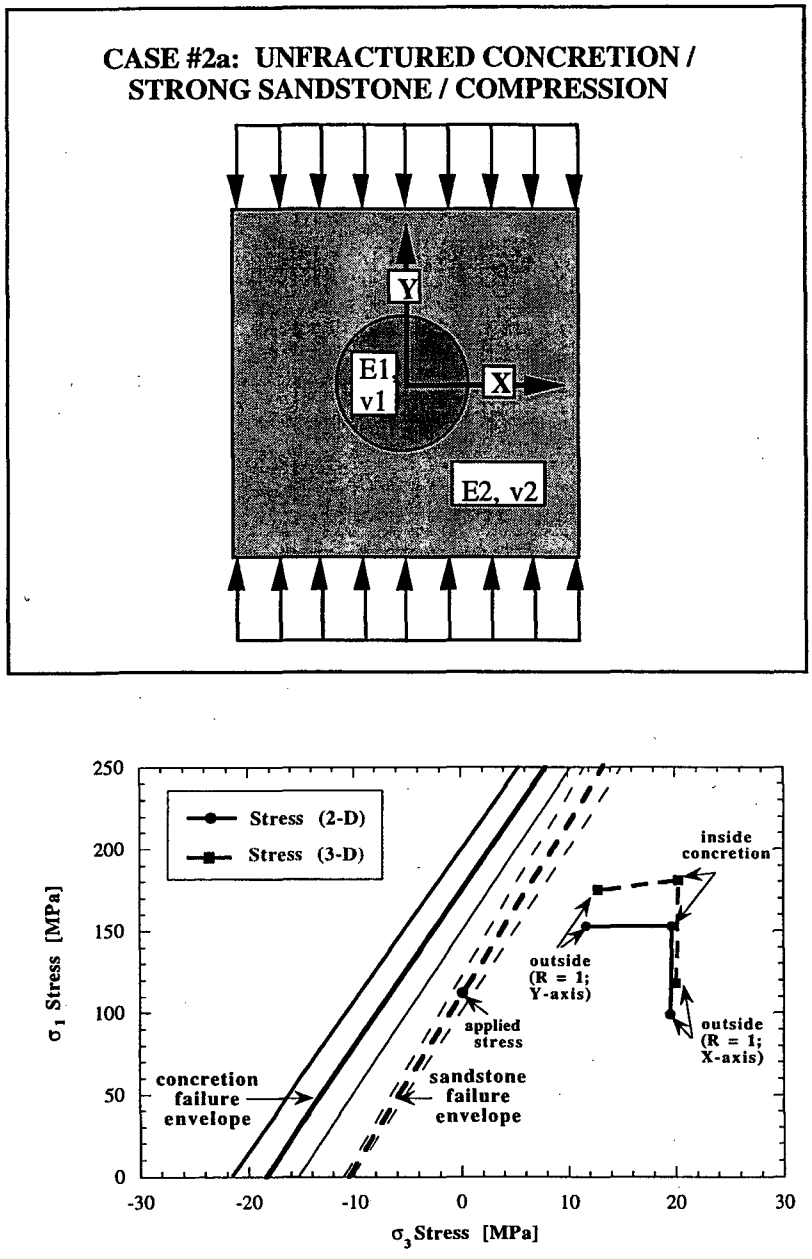

Figure 6.16 Stress field inside of a concretion under uniaxial compressive loading. The depicted scenarios are shown in the top figures. The lower plots show the σ_1 and σ_3 state of stress inside each concretion and at the contact with the sandstone. The stress at any particular point is displayed relative to a linear fracture envelope defined by the tensile and compressive strengths measured in the laboratory. The standard deviations for the concretions are drawn as solid lines and the standard deviations for the sandstone are drawn with dashed lines. a) The two-dimensional plane strain and three-dimensional cases for an unfractured concretion. Because the stress field is uniform, only the stress in the center and at the boundary at the x-axis and y-axis are shown. The stresses lie below the failure envelope and no fracturing is predicted.

The fact that the stress was not great enough to cause failure was due largely to the Poisson's difference between the concretion and sandstone. Because the Poisson's ratio in the concretion exceeded the value in the matrix, the sandstone restricted its lateral expansion and generated a compressive confining stress resisting crack dilation. To test whether the Poisson's ratios measured in the laboratory experiments were correct, the Young's modulus and Poisson's ratio were compared to those obtained from a host of other rocks (Jaeger and Cook, 1979), and a favorable relationship was found (supporting the above conclusion).

Although Figure 6.16.a suggested that a uniaxial compressive stress could not have caused concretion fracturing, the static stress field for the case of debonding was explored because the magnitude of remote stresses change with time, and an episode of debonding may have preceded the application of the uniaxial compressive loading stress. Figure 6.16.b subsequently shows the state of stress within the concretion if debonding *were* possible along the sandstone/concretion contact. Because the introduction of debonding fractures disrupted the symmetry of the model, only a two-dimensional case was investigated. According to this figure, debonding from the matrix allowed both expansion of the concretion and fracturing to occur, particularly near the center of the concretion.

Figures 6.16.c and 6.16.d. show the state of stress along trajectories x1 and x2 within the concretion assuming one fracture and three fractures were allowed to exist, respectively. With one fracture, the stress in the middle of the concretion was beyond the failure envelope. To extend to the edge of the concretion, however, a fracture had to enter a zone of confinement represented by the x2 trajectory. For the case of three fractures, additional fracturing within the center of the concretion became more difficult, but the confining stress along the x2 trajectory was broken up near pre-existing fractures, making extension in this region more probable.

In summary, a uniaxial compressive stress could have generated fractures within a concretion which had been partially debonded from the matrix; however, the results of this study also demonstrated that extension of even one fracture to the end of the concretion would have been inhibited by the confining stress imposed by the Poisson's difference. Although one possible

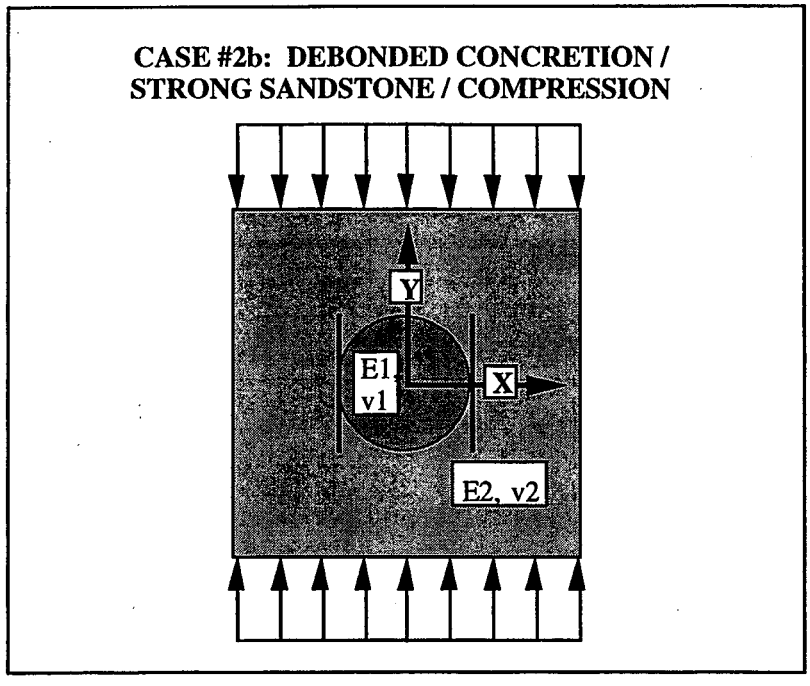

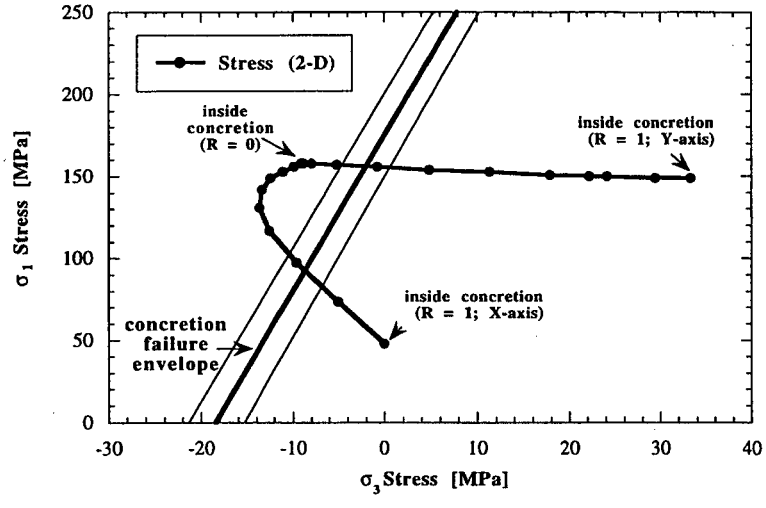

Figure 6.16 b) Stress inside concretion after debonding has occurred. The center of the concretion is identified and points at each 0.1 radii are also illustrated. Fracturing should occur internal to the concretion.

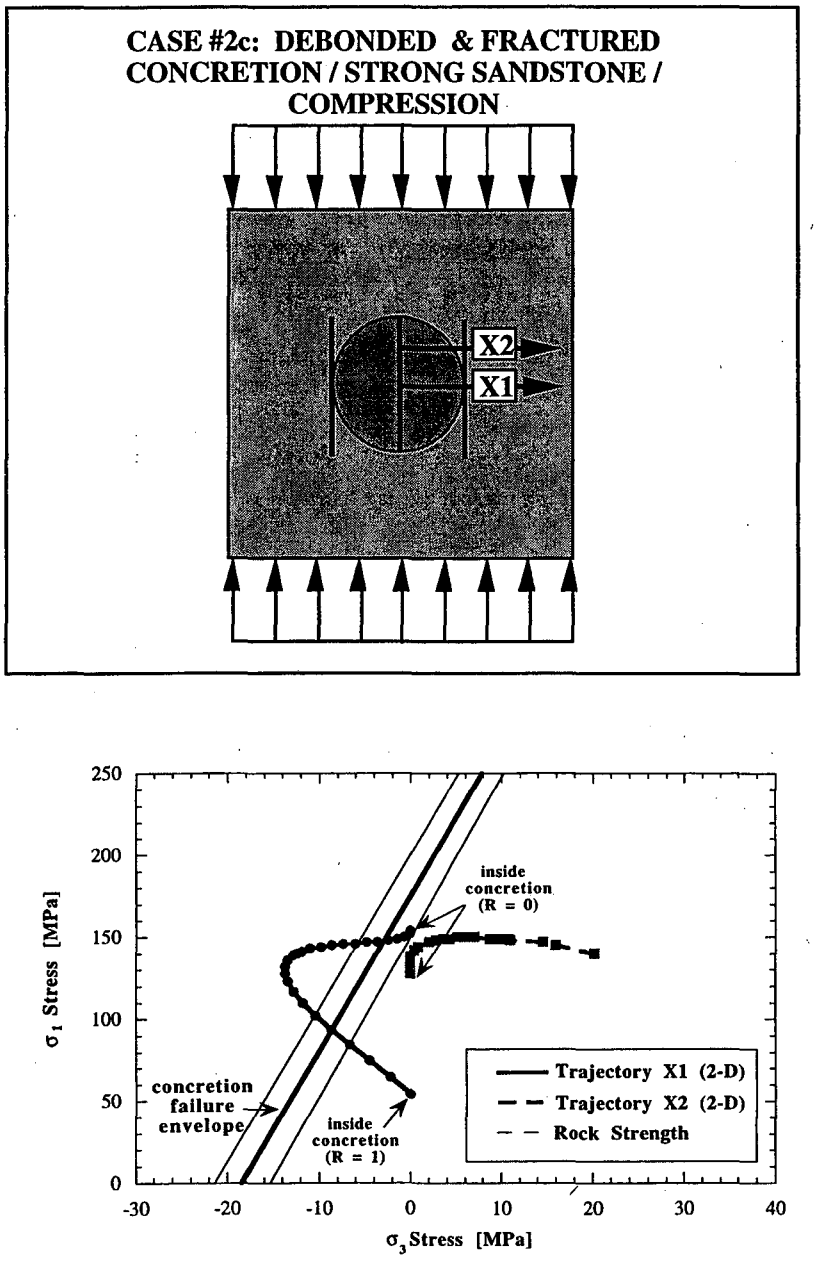

Figure 6.16 c) Stress along trajectories x1 and x2 for the case where debonding and one internal fracture has occurred. Fracturing is favored along trajectory x1 in between the center of the concretion and edge, but not along trajectory x2.

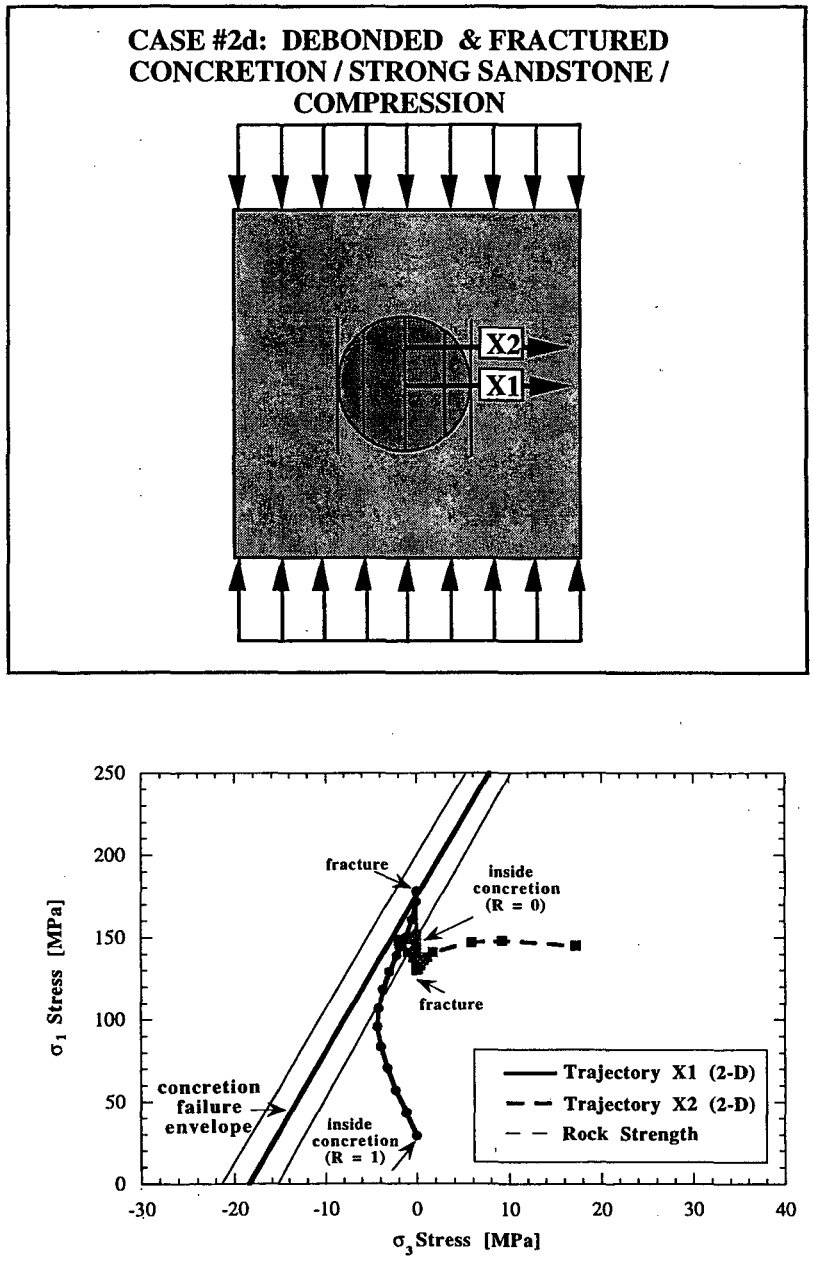

Figure 6.16 d) The stress inside a concretion for the case of multiple fractures along the x1 and x2 trajectories given as a function of distance in radii. The fracture on either side of the middle fracture is indicated in the plot. The stress field is more conducive to fracturing along the x2 trajectory than the Figure 6.16.c result, but less conducive along the x1 trajectory.

explanation for the occurrence of fractures extending to the sandstone interface was that the stress concentration at the crack tip offset the confining stress, the positive stress intensity factor associated with a crack with a constant opening displacement (Tweed, 1971) would have also experienced a negative stress concentration due to the compressive confining stress perpendicular to the crack. An alternative explanation was that the material properties within the concretions were not homogeneous and the outermost shell was more susceptible to failure. This possibility was not investigated further.

6.6.4 CASE #3: Fracturing during burial

A third possible fracturing scenario to the two mentioned above, was that fracturing occurred during burial when the sandstone had different material properties than those measured in the laboratory. Price (1974) used low values of the Young's modulus and high values for the Poisson's ratio to account for the effects of thermal strains and incomplete lithification of the sediments. In this study, this effect was modeled by assigning the Berea sandstone properties reported in Table 6.7 (Touloukian, et al., 1989) to the sandstone matrix. This sandstone had a Young's modulus and strength lower than those measured for sandstone on Vancouver Island, but a higher Poisson's ratio (the concretion values were retained based on their origin early in diagenesis).

Figure 6.17.a shows the state of stress in and adjacent to a concretion for a uniaxial and biaxial applied compressive stress of 91.2 MPa and for both two-dimensional plane strain and three-dimensional boundary conditions. All three cases in this figure led to preferential concretion fracturing because the larger Poisson's ratio of the sandstone generated tensile stresses internal to the concretion. Eidelman and Reches (1992) have previously explained preferential fracturing of included pebbles in a sandstone matrix by this tensile stress concentration, and these results implied that the importance of this mechanism to concretion fracturing could not be discounted.

Because only three dimensional boundary conditions resulted in preferential debonding of the concretion from the matrix, these conditions were simulated after debonding had occurred by

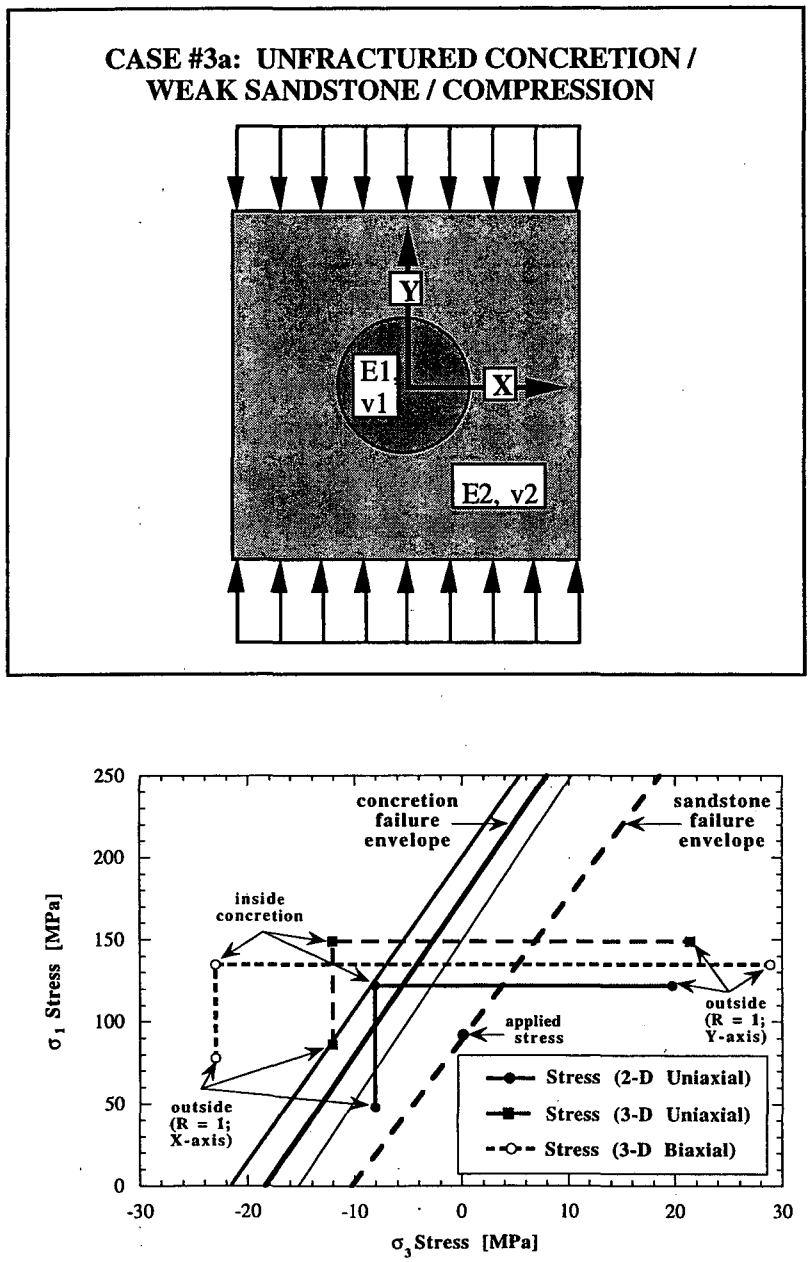

Figure 6.17 Stress field inside of concretions if the sandstone has a higher Poisson ratio and lower Youngs modulus and strength than the sandstone. a) Stress inside an unfractured concretion for three different boundary conditions. The stresses greatly exceed the concretion failure envelope.

shifting the sandstone failure envelope to the right so that the distance between the three dimensional stress inside the concretion and its original envelope was the same as the distance between the two-dimensional stress and the modified envelope. Figure 6.17.b shows the subsequent stresses inside a concretion after a debonding fracture had grown to a length of one concretion diameter on either side of it. According to the figure, the most favorable location for additional fractures to grow would have been along the x-axis, slightly off center.

Assuming that one fracture was able to extend across the concretion, additional fractures would still have been able to form (Figure 6.17.c). The region most favorable to additional fracturing would have been the concretion center along the x1 trajectory. It is important to note that the stress responsible for fracturing would have been predominantly tensile in this case. By contrast, the state of stress for a concretion which had three fractures is shown in Figure 6.17.d. Confining stresses along the x2 axis had been reduced, and additional fractures were possible inside the concretion. The stress distribution within the concretion was very similar to Case #2 in Figure 6.16.d, which was nearly uniaxial and compressive.

6.6.5 Summary of concretion fracturing mechanisms

It was very difficult to explain the origin of the concretion fractures using the rock properties measured in the laboratory. A uniaxial tensile stress would have favored concretion debonding without the generation of any internal fractures. Similarly, a uniaxial compressive stress would have inhibited fracturing in the high modulus concretions because of the Poisson's difference between the concretions and sandstone.

Only after an initial stage of debonding occurred would fractures have been able to develop in the concretions. In this case, they would have been driven by a compressive stress, but would have had to extend into a zone of compressive confining stress near the sandstone contact. If one fracture was able to extend to the sandstone interface then fracturing would have become more favorable because the confining stress would have been broken up, however.

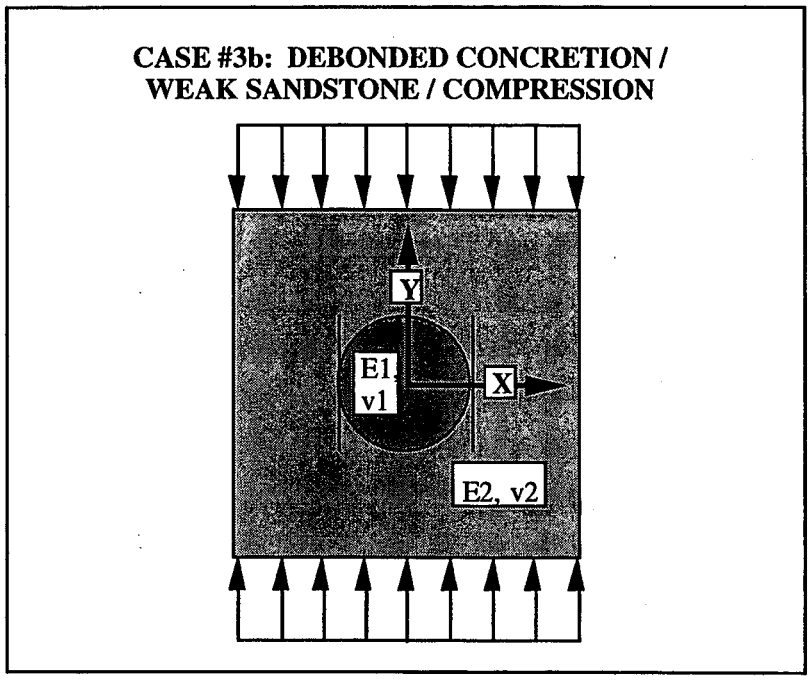

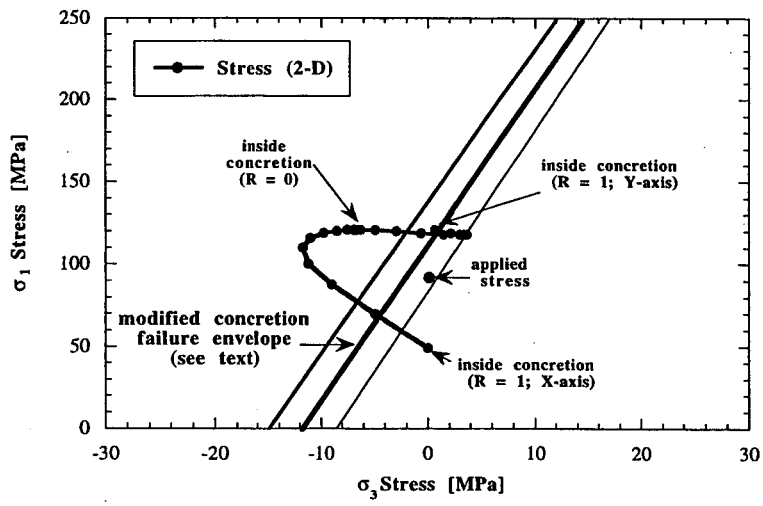

Figure 6.17 b) Case of a debonded concretion. Point A represents the stress along the y-axis at the boundary of the concretion when debonding has initiated but not yet extended into the sandstone matrix as it has in the illustration above the plot.

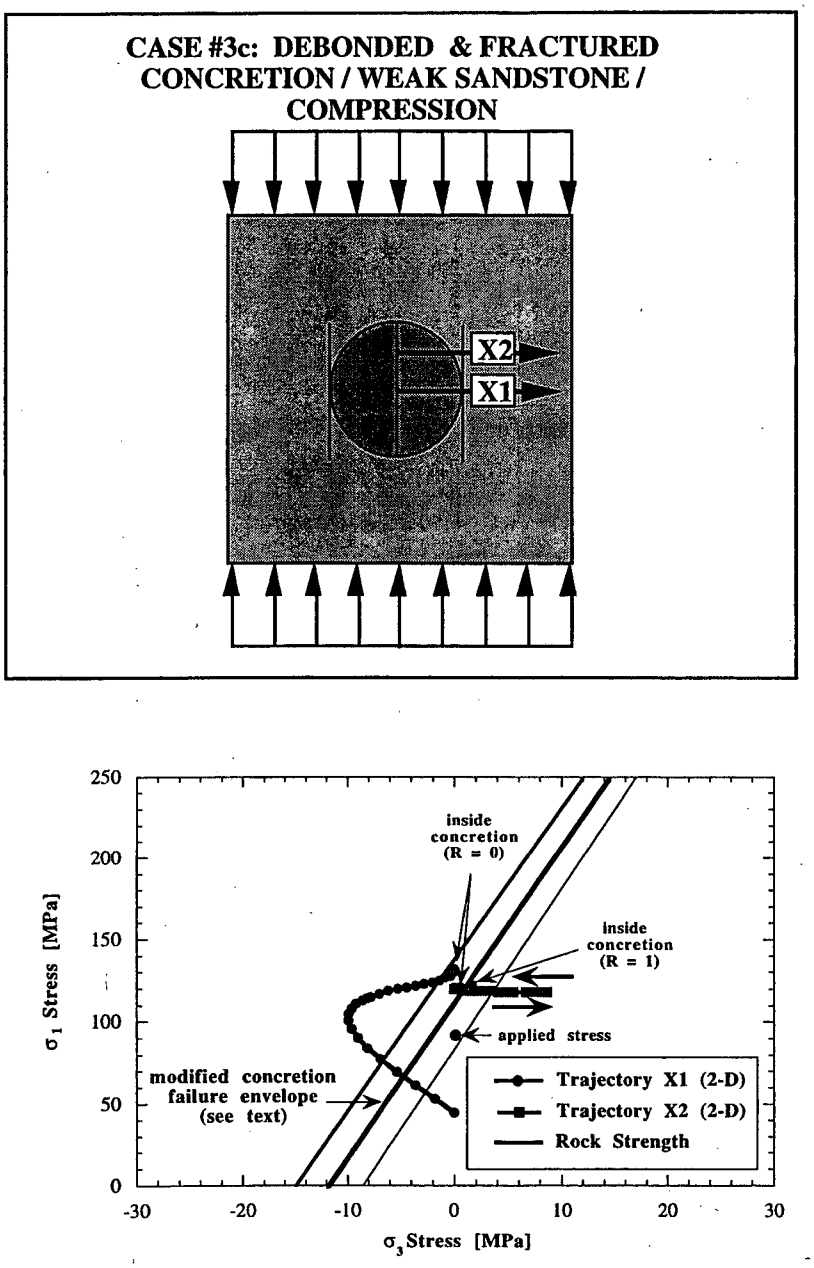

Figure 6.17 c) Stress after an internal fracture is added to the model. Along the x2 trajectory the σ_3 confining stress initially increases and then re-approaches zero as indicated by the arrows.

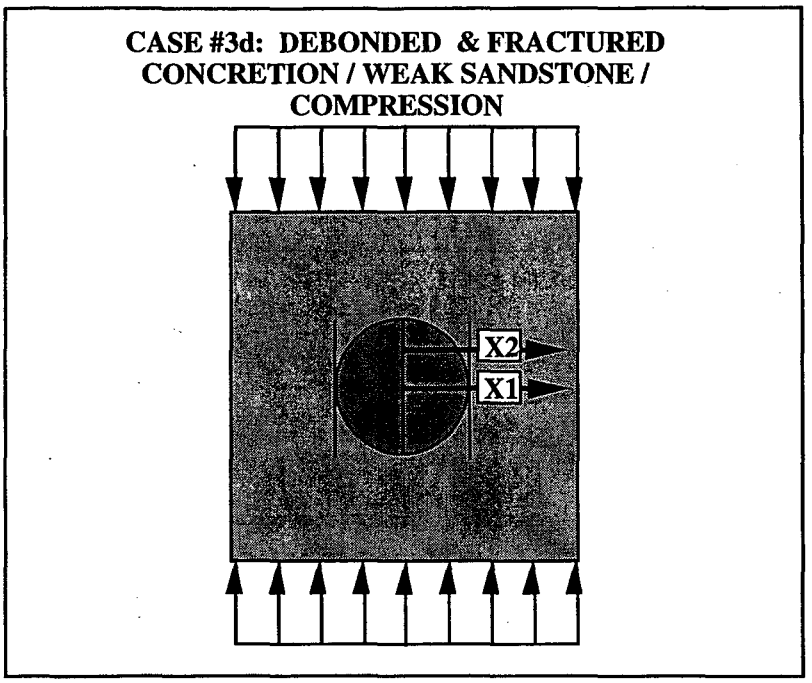

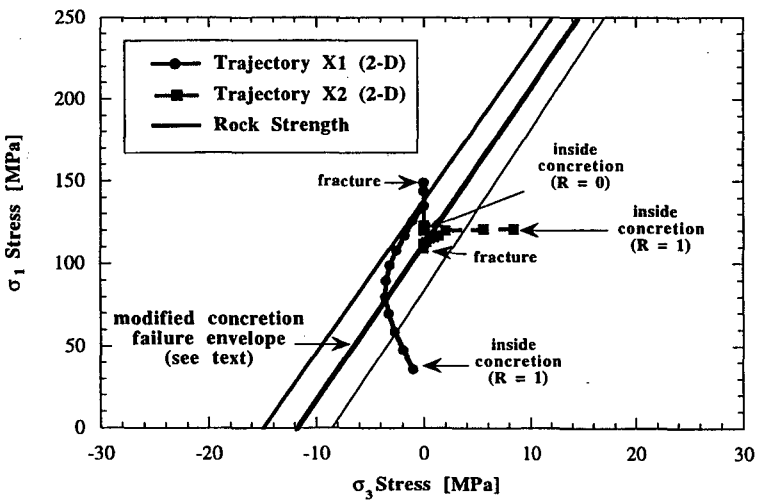

Figure 6.17 d) Three internal fractures and two debonding fractures were used in this case. The additional fractures break up the stress field and make additional fracturing more likely along trajectory x2.

An alternative scenario may have been that fracturing occurred during burial of the sedimentary rock, while the sandstone was still incompletely lithified. Using the rock property values of the "weak" sandstone in Table 6.7, multiple internal fractures were again able to form inside of the concretion. Although the stress inside of a debonded concretion was found to be large enough for tensile fracturing to occur, by the time three internal fracture were present, the stress field had been altered so that any additional fracturing would have been generated under nearly uniaxial compressive stress conditions. Because the concretion represented by Figure 6.3 exhibited more than three fractures, compression-driven fracturing was implied.

6.7 Analysis of jointing scenarios

6.7.1 Relative importance of tensile stresses

The analysis provided in *Section 6.6* demonstrated that the closely-spaced concretion fractures could only have been generated by a compressive driving stress large enough to additionally create joints in the surrounding sandstone; however, in the case where fractures were generated during anticline development, an episode of tensile debonding was required. Also, for the scenario of fracture generation during burial, where a uniaxial compressive stress was applied, tensile stresses were again generated within the sandstone matrix in the vicinity of the concretions. Because field observations suggested that debonding fractures in the vicinity of concretions were often the source of the joints, and the results of this study indicated that these were "tensile" environments, some transition from tension-generated jointing to compression-driven jointing was likely at the field site.

To determine at what point this transition might have occurred, the stress field of Area 9 in the absence and presence of the observed joints was examined using the previous finite element method. This particular area of the field site had several concretions with both debonding and multiple, internal fractures, and three primary joints, all initiating as debonding fractures adjacent to concretions (Figure 6.18). The first joint was adjacent to concretion #9 and extended several diameters on either side of the concretion. The other two joints were associated with concretion

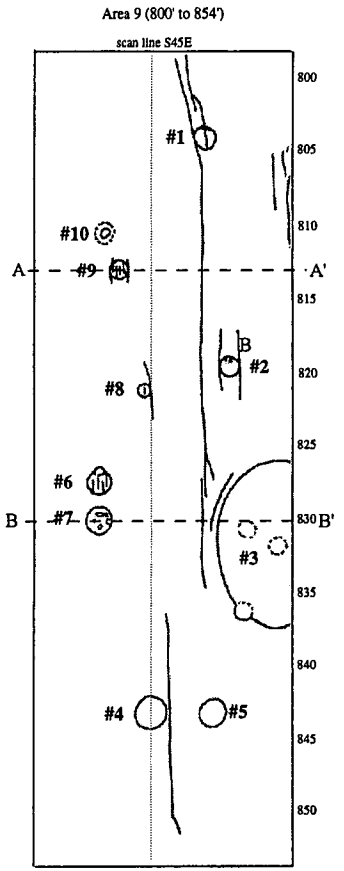

Concretion Number	Schmidt Rebound	Youngs modulus	Poisson ratio
1	59	66	0.30
2	55	34	0.16
3	55	34	0.16
4	56	42	0.20
5	52	10	0.06
6	58	58	0.26
7	51	2	0.02
8	56	42	0.20
9	61	82	0.37
10	54	26	0.13
strong ss		17.8	0.09
weak ss		10.34	0.32

Figure 6.18 Map of Area 9 where numerical simulation of the joint sets were conducted. The table next to the figure reports the Schmidt rebound values and elastic moduli used for each of the concretions numbered in the plot. The values for the strong and weak sandstone are identical to those in Table 6.7.

#7. Figure 6.18 shows that one of these joints extended through the boundary of Area 9. The second joint was subparallel to the first and initiated on the other side of the concretion. A portion of this joint can be observed next to the 810 foot line in the figure.

6.7.2 Tensile stresses during anticline formation

The properties of the concretions used in this analysis were taken from measured Schmidt rebound values and the correlations between these values and laboratory elastic moduli discussed above. Although heterogeneity was also measured in the sandstone only the average sandstone properties were used. Figure 6.18 and its accompanying table demonstrate that most of the concretions had Young's moduli and Poisson's ratios in excess of the sandstone. The exceptions were concretions #10 and #12.

After choosing appropriate material properties, the modeled region was enclosed within a surrounding sandstone medium to isolate it from boundary effects, and a constant stress was applied. These boundary conditions were selected on the basis that no ductile interlayer was observed to justify constant strain boundary conditions. The meshed equivalent of Figure 6.18 was pinned on one corner and isolated from rigid body motion by a roller on another.

The effect of a 10.6 MPa tensile remote stress applied along the x-axis is shown in the A-A' and B-B' cross-sections of Figure 6.19. Instead of modeling every fracture present in Figure 6.18, the situation was idealized with a single joint by noting that the joints extending from concretion #9 and #7 virtually bisected the region into two areas. Figure 6.19.a and 6.19.b show the initial and final σ_{xx} stress field across trajectories A-A' and B-B'. Each point in the figure represents the stress at one node intersected by the scanline.

For line A-A', the tensile stress was initially concentrated in concretion #9; however, once jointing occurred, this stress was transformed into a confining stress. The tensile stress was also significantly reduced after jointing, thus restricting the strain energy available to the joint spaced six feet away in Figure 6.18.

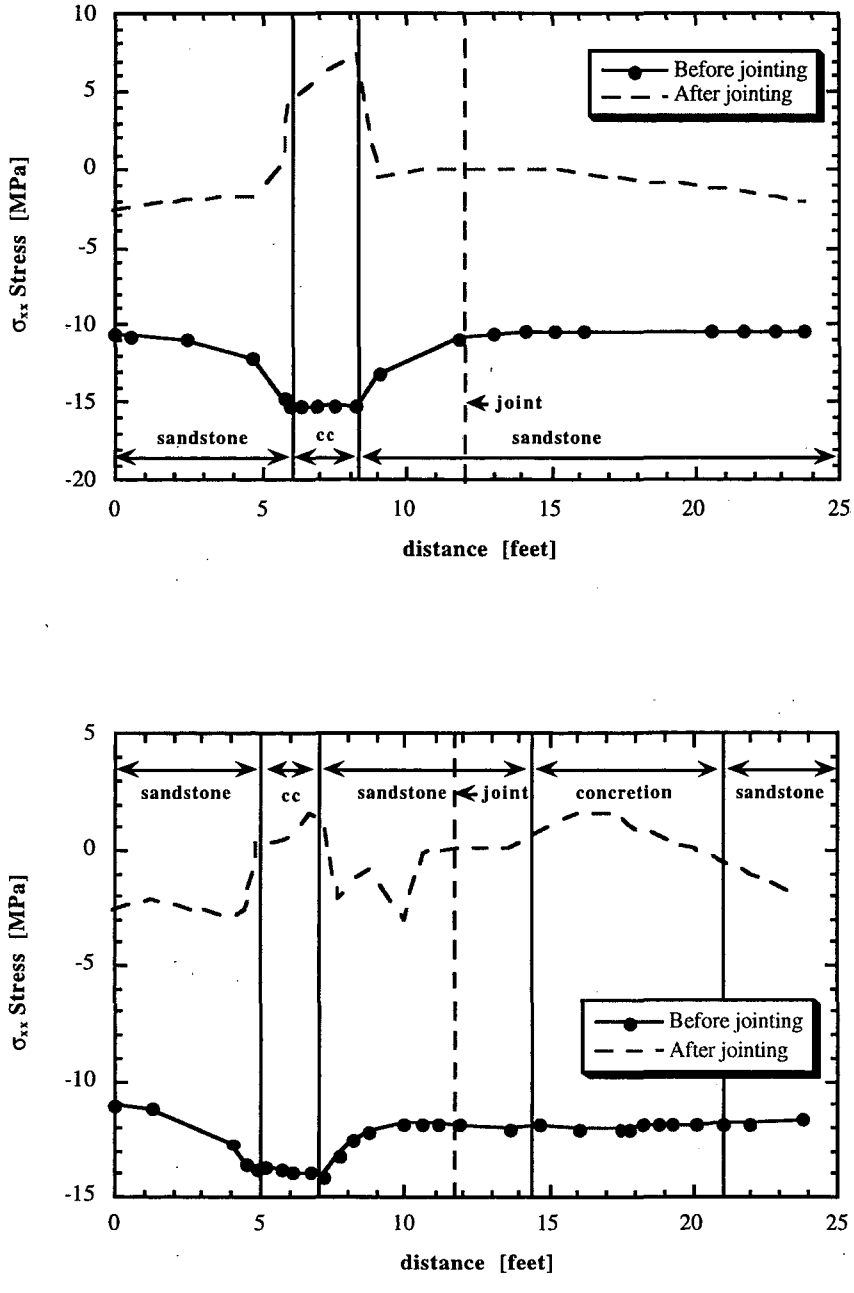

Figure 6.19 The σ_{xx} stress field for the case of the weak sandstone after far field uniaxial tensile stresses have been applied in the horizontal direction along a bordered region surrounding the area of Figure 6.18. The stresses are reported for scanlines A-A' and B-B' of Figure 6.18 before and after one joint is allowed to extend all the way through the middle of the region. The stress is shown on the y-axis and the distance on the x-axis. The boundaries of the concretions are drawn with solid vertical lines and the joint with a dashed line. After jointing, the tensile stresses are nearly extinguished across both scanlines, making the existence of the joint to the right of concretion #7 very difficult to explain.

Scanline B-B' was more complex by virtue of the fact that it crossed two concretions; however, it illustrated the same general results. Before jointing occurred, stresses were concentrated mostly in concretion #7. After jointing, tensile stresses were mostly eliminated in the concretions and sandstone, making it improbable that tension-driven jointing could have created both joints emanating from concretion #3.

The fact that the formation of a single joint greatly diminished the driving stress for either concretion or sandstone fracturing implied that if fracturing occurred during anticline development, and the rock properties were the same as those measured in this study, then after a few tensile joints formed in the sandstone all remaining concretion fractures and joints were compression-driven.

6.7.3 Tensile stresses during downwarp

Figure 6.20.a shows the σ_{xx} stress in Area 9 for the case where jointing occurred during burial, under a uniaxial compressive stress loading stress of 112 MPa applied in the direction of the y-axis and using the properties of the "weak" sandstone in Table 6.7. Along the trajectory A-A' in the figure, tensile stresses were greatest outside of concretion #9, but smaller inside because its Poisson's ratio was higher than the sandstone. The horizontal stress across A-A' was relatively unaffected by the presence of fracturing in the sandstone.

From B-B' in Figure 6.20.b, tensile stresses were greatest outside of concretion #7 because of the large Poisson's ratio mismatch (Figure 6.18). After jointing occurred, tensile stresses were still large enough to generate a joint on the right side of concretion #3, but could not have explained the extension of this joint to the A-A' intersection. Additional compression-driven extension of the joint would have been required.

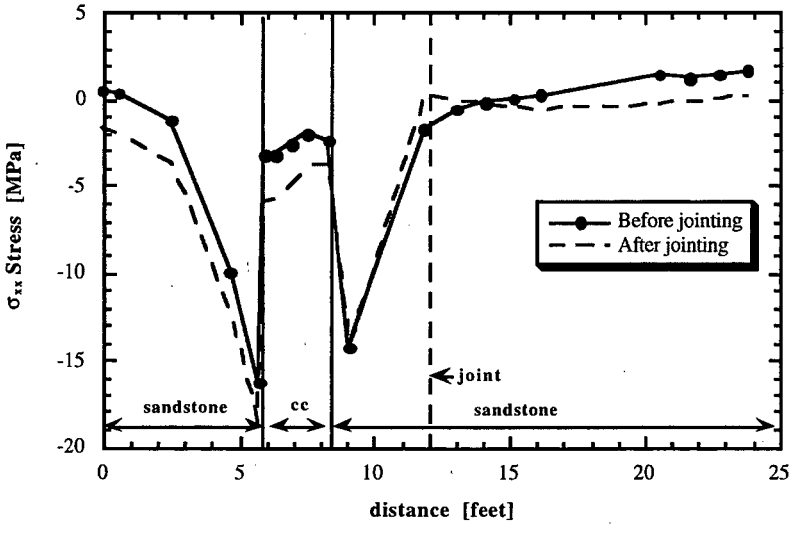

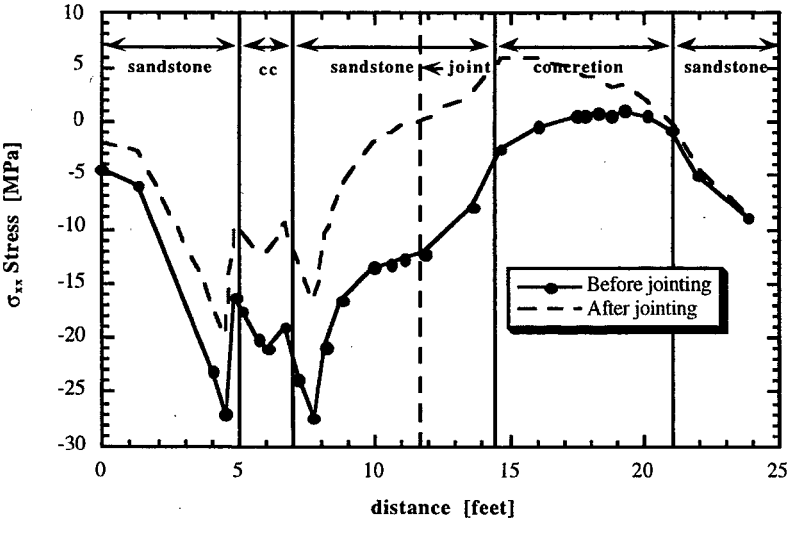

Figure 6.20 The σ_{xx} stress field for the case of the weak sandstone after far field uniaxial compressive stresses have been applied in the vertical direction along a bordered region surrounding the area. a) Tensile stresses are generated in both the concretions and sandstone, but are localized in the vicinity of the concretions. b) After one joint is allowed to extend all the way through the middle of the region of Figure 6.18, the tensile stresses have been only slightly reduced in the vicinity of the concretions.

6.7.4 Probable jointing scenarios

The results for the anticline model, where the rock properties were the same as those measured in the laboratory, suggest that far field tensile stresses may have locally resulted in jointing in the sandstone, particularly nearby high modulus concretions. Extension of even one of these joints, however, would have greatly reduced the tensile driving stresses available to other joints. Furthermore, debonding and fracturing of other concretions would have been unlikely.

Although the downwarp model described was less restrictive, allowing concretions to fracture even after jointing had occurred, additional jointing of the sandstone was suppressed away from the concretions. Consequently, after an initial "tensile" joint episode seeded the sandstone with a small population of joints, compression-driven fracturing would still have become the dominant fracturing mechanism.

Additional support for compression-driven extensile fracturing at the field site was provided by the many concretions which were fractured internally, without having debonded from the matrix. The two scenarios analyzed above produced tensile stresses along the sandstone/concretion interface promoting debonding. The only way this tensile stress concentration could be eliminated while still allowing multiple concretion fractures to exist, is if there was no Poisson's ratio mismatch, and if the fracturing stress was compressive (based on the tensile stress shadow arguments above).

6.7.5 Origin of jointing stresses

During burial, far field tensile stresses necessary to produce stress anisotropy would have developed due to the fact that the surface of the Earth is curved and that for a sedimentary basin of length AC (Figure 6.21), shortening would have occurred during burial to length ABC, but the basin would have extended thereafter (Price, 1974). Figure 6.21 also shows the equations relating basin length [L], Earth radius [R], depth to maximum compression [z], and total strain [e]. Using the estimated basin dimensions of 230 km by 120-130 km (Mustard, 1994), after just 0.28 km of burial, the short axis of the basin would have undergone extension. Assuming the DeCourcy

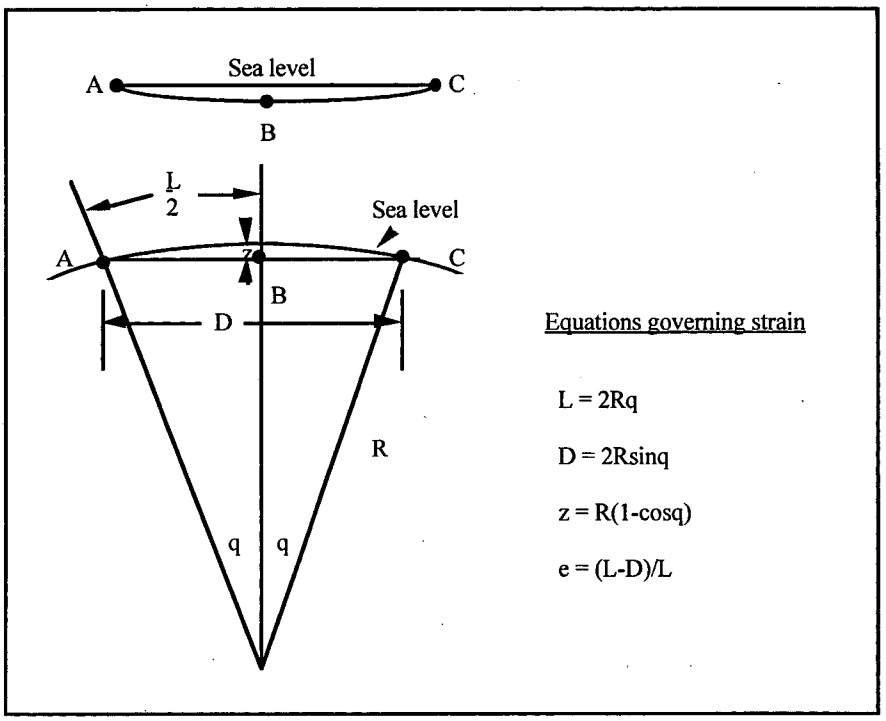

Figure 6.21 Illustration of how tensile strains can be generated in a downwarping basin (after Price, 1974). The basin appears concave, but relative to the dimensions of the Earth it is convex. Consequently, as it is buried to line ABC it is compressed, but thereafter it is in extension. The depth to this confinement zone [z] is only 0.28 kilometers for the short axis of the Nanaimo Basin on Vancouver Island. Thereafter, tensile strains were generated. The equations relating strain to the dimensions of the basin and Earth are shown to the right of the figure.

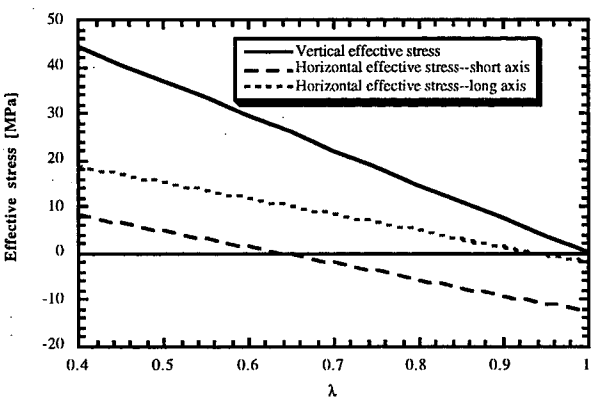

Figure 6.22 Calculated effective stresses in a basin undergoing downwarp as a function of the ratio of pore pressure to loading pressure [l]. All stresses are compressive (i.e. positive) for low values of l, but decrease and can actually become tensile for the short axis of the basin for higher values of l.

Formation was buried approximately 3 km (England, 1990), the total tensile strain would be -1.2 x 10^{-3} and -2.1 x 10^{-4} for the short and long axes, respectively.

The combined equations utilized by Price (1974) to explain the effective horizontal stresses in such a downwarping basin are given by:

$$\sigma_x' = \frac{\upsilon}{(1-\upsilon)}\sigma_z - \varepsilon_x E - p; \tag{6.7}$$

$$\sigma_y' = \frac{\upsilon}{(1-\upsilon)}\sigma_z - \varepsilon_y E - p; \tag{6.8}$$

where cross strain terms were neglected without introducing significant error. Based on the effective stress law as re-stated by Lorenz, et al. (1991a), an increase in pore pressure also contributes to the total stress [s] such that a correct expression of equation (6.7) should instead be:

$$\sigma_x' = \frac{\upsilon}{(1-\upsilon)}(\sigma_z - p) - \varepsilon_x E; \tag{6.9}$$

$$\sigma_y' = \frac{\upsilon}{(1-\upsilon)}(\sigma_z - p) - \varepsilon_y E; \tag{6.10}$$

Figure 6.22 shows the corresponding state of stress for the DeCourcy Formation at Vancouver Island, assuming an average density of 2.5 g/cm^3 for the overlying sediments and using the average rock properties during burial given in Table 6.7. The parameter [λ] in the figure measures the ratio of pore pressure to the vertical gravitational loading stress, and Figure 6.22 demonstrates that for the short axis of the basin to have experienced effective tensile stresses a value of [λ] of 0.65 would have been required (the long axis of the basin would only have experienced tensile effective stresses as the ratio of pore pressure to vertical pressure approached 0.95).

Because the resultant basin stresses were not large enough to preferentially fracture the concretions (Figure 6.23), it was difficult to explain jointing in the absence of a tectonic stress component. Although tectonic stresses might have been generated during CFTS deformation much the same as Lorenz, et al. (1991b), their orientation would not have coincided with joint set

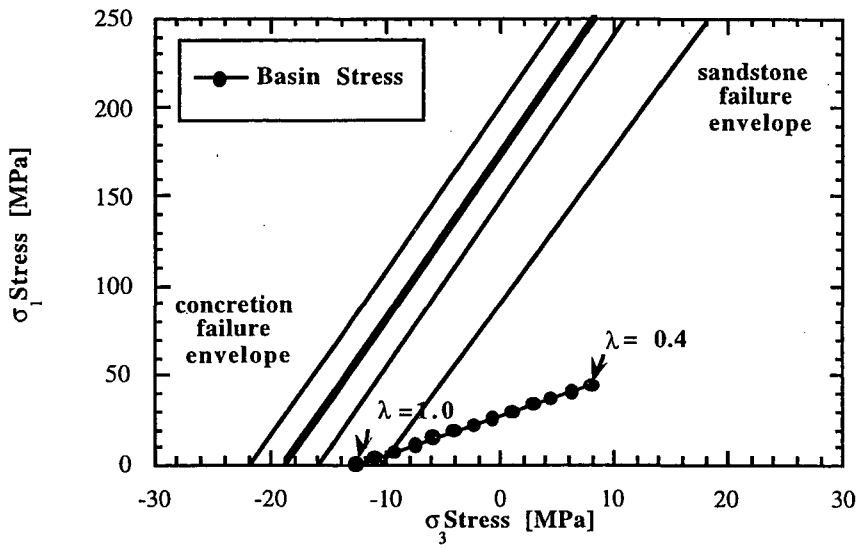

Figure 6.23 Calculated effective stresses in the Nanaimo Basin assuming uniaxial strain conditions and a lambda parameter ranging from 0.4 to 1.0. The stress was only large enough to cause jointing at a high value for lambda. Because Figure 6.22 shows that the compressive loading stress under such a condition is very small, a tectonic component was necessary for jointing.

#1. Based on our incomplete knowledge of the complex geologic history of the field site, the origin of this tectonic stress component remains a mystery.

6.8 Unresolved issues

The primary uncertainty associated with the above analysis was estimating the rock properties at the time of fracturing, particularly the Poisson's ratio, which greatly affected the state of stress within the concretions. Price and Cosgrove (1991) discussed evidence that the Poisson's ratio of rock increases with temperature and stress, but this effect was not incorporated in the analysis of this study. Instead, two scenarios were selected which covered the case where the Poisson's ratio of the concretions were both higher and lower than the surrounding sandstone.

A second unresolved issue was the stresses leading to compression-driven extensile fracturing at the field site. This study used a linear stress-strain envelope, recognizing there is most likely a tension "cut-off" after which the failure mode becomes tensile (Jaeger and Cook, 1979). The strengths used in this study were also probably much higher than were required to break the rock *in-situ*. Subcritical crack growth, higher temperatures, and lower strain rates would all have lowered the strengths measured in the laboratory (Paterson, 1978). Consequently, the results presented above are more qualitative than quantitative. Additional laboratory testing under the biaxial stresses imposed by the load cell of Turner (1999) may yield a "true" extensile failure envelope.

Finally, the factors controlling the spacing of compression-driven joints was uncertain. When an opening mode fracture forms in a rock, the relative displacement that occurs across the face of the fracture must be accommodated within the unfractured rock by a combination of elastic deformation and displacement of external boundary conditions. In the case where the boundaries are fixed such as in a biaxial test cell, dilation must be accommodated entirely by elastic deformation. Given that the compliance of a rock core of axial dimension (l) is:

$$1/K = (\varepsilon_3 * l) / \sigma_3, \qquad (6.11)$$

where [K] is the stiffness, [ε_3] is the axial strain, and [σ_3] is the minimum confining stress, under zero axial displacement, the compliance of the system in the direction of fracture dilation would be zero because [ε_3] would be zero. Consequently, the number of fractures which could possibly grow in this situation would be limited.

6.9 Conclusions

This study explored the relative importance of tensile to compressive joint driving stresses on a field site on Vancouver Island. This field site was unique in that it contained paleostress indicators in the form of fractured calcareous concretions which were used to deduce the combination of stresses responsible for joint set #1 in the surrounding sandstone.

The first scenario used to explain jointing used the sandstone and concretion mechanical properties measured in the laboratory, and replicated concretion fracturing with a far field uniaxial compressive stress after an initial debonding stage had occurred. The second assumed that the Poisson's ratio of the sandstone was higher than the concretion during fracturing, and was able to produce debonding fractures and concretion fractures with the same far field compressive stress. In either case, an initial "tensile" episode likely occurred at the field site, seeding it with a small population of joints. Additional jointing and concretion fracturing, however, would have required a large compressive stress acting parallel to the joint face. Furthermore, the fractured concretions which were not debonded from the sandstone could only have been produced by a far field compressive stress large enough to additionally generate joints in the sandstone.

Despite the many uncertainties in this study, the results were consistent with the hypothesis of Lorenz, et al. (1991a), who suggested that compression-driven jointing is an important jointing mechanism. Further studies must address the timing of the fractures and the material properties of the rock during fracturing. Although there was a large tectonic component to the compressive joint driving stress, its source also could not be identified. Finally, the initiation, propagation,

termination, and spacing of joints formed under realistic geologic compressive stresses is still unknown.

7.1 Introduction

This chapter investigates a method of detecting fractures in three limestone cores using seismic amplitude anisotropy measurements. Previous attempts to discern fractures in rock from seismic measurements include Lo, et al. (1986), who measured velocities in drill core at different orientations and as a function of confining pressure and concluded that the slower velocities at low confinement were due to open microcracks and pores. They further reasoned that the residual anisotropy at higher pressures was due to aligned minerals and bedding. Another study was performed by Remy, et al. (1994), who measured quality factor Q on rocks during freeze-thaw cycles and demonstrated that the decrease in velocity and Q with successive cycles was due to the extension of microcracks.

This chapter contends that P-wave amplitude measurements taken at various orientations to bedding are a more sensitive indicator of structure than velocity measurements, and can be used to effectively identify the presence and orientation of planes of weakness in rocks. A nonwelded interface model (Pyrak-Nolte, et al., 1990a) was used to confirm that the observed amplitude anisotropy was caused by the presence and compliance of fracture planes because it was able to account for both the amplitude changes and dispersion.

7.2 Experimental method

The experimental set-up consisted of a water immersion cell and two 1 MHz piezoelectric P-wave transducers (Figure 7.1). The excitation signal was a broad band pulse and a digital oscilloscope recorded the transmitted signal. To provide effective coupling, the samples were immersed unjacketed into a water bath so that a thin layer of water separated the rock and transducers. A dial underneath the cell allowed the sample to be rotated relative to the two P-wave transducers, changing the orientation of the measured signal from zero to

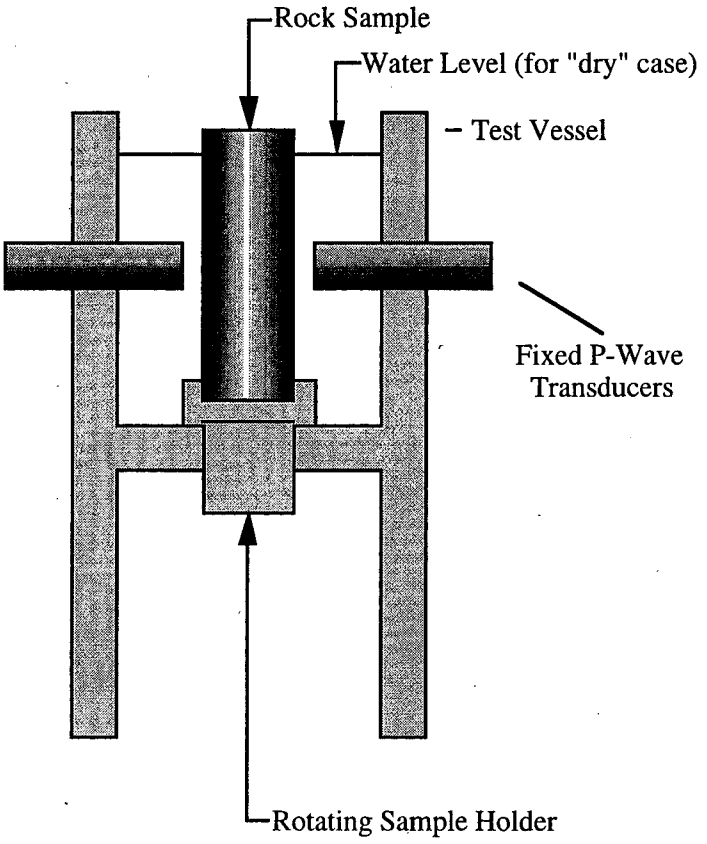

Figure 7.1 Immersion bath for P-wave amplitude anisotropy measurements. The sample could be rotated to any angular orientation to the transducers while preserving acoustic coupling conditions.

ninety degrees to bedding in 10 degree increments. Measurements were performed on both vacuum saturated and vacuum/oven-dried cores.

Figure 7.2 shows two arriving wave pulses. Only the initial, well-defined compressional pulse of energy was used to compare the P-wave amplitudes. This particular case was for the signal arriving perpendicular and parallel to an observable fracture. The signal parallel was both faster and stronger than the corresponding signal perpendicular. Also shown in Figure 7.2 is the ratio of the difference in velocity (or amplitude) divided by the maximum velocity (or amplitude). For the dry and saturated cases, the changes in velocity between parallel and perpendicular orientation were 14% and 8.3%, respectively, but the changes in amplitudes were much larger, at 50% and 66%.

It is important to note that the unjacketed rock in the experiments was never completely dry because fluid began to imbibe immediately upon immersion. To determine the effect of this imbibition, the mass of water imbibed was measured versus time under natural (no vacuum) and forced (vacuum) conditions (Figure 7.3) (Hilbert, et al., 1995). According to Figure 7.3, under natural conditions water filled only a fraction of available void space even after thirty minutes. Because the seismic transmission experiments of the "dry" rock were concluded within five minutes, saturation would have been less than five percent.

Because it was probable that fractures in the rock acted as conduits for fluid, it was still necessary to determine if this small mass of water had a large effect on the amplitude, for example, by changing the stiffness or viscosity of the fracture between the nominally dry and completely dry case. Cadoret, et al. (1995) demonstrated that drying under atmospheric pressures is controlled by preferential paths, and it is therefore likely that fracture imbibition as operative during the experiments. Walsh (1995) additionally demonstrated that for high porosity limestone in the presence of a wetting fluid, an attenuation peak occurred at less than a few percent saturation. The strong correlation between signals which transversed fractures and reduced amplitudes suggested that the fractures of this study were only partially filled.

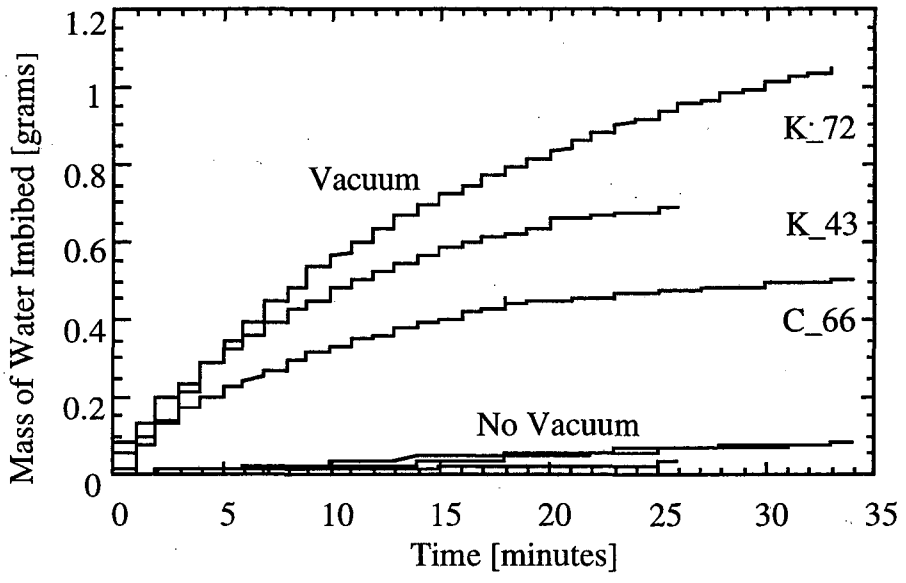

Figure 7.3 Imbibition curves for three specimens (K43, K72 and C66) under atmospheric (no vacuum) and forced (vacuum) conditions (Hilbert, et al., 1995). The mass of water imbibed under vacuum at long times corresponded to full saturation. Saturation was considerably less for non-vacuum imbibition and was negligible during the initial 5 minutes, which was the time required to obtain the initial set of seismic measurements.

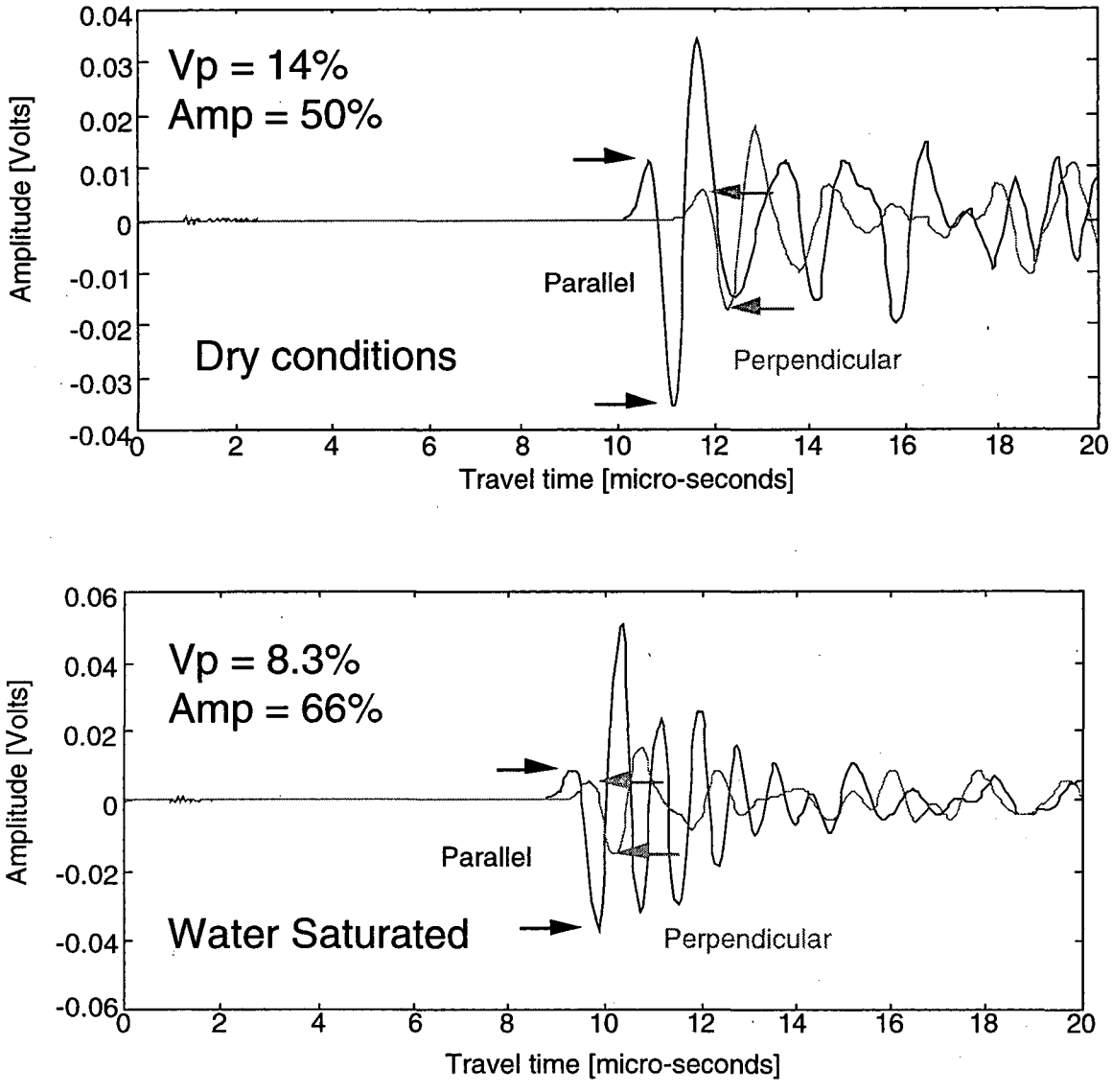

Figure 7.2 Typical examples of the waveforms measured under dry (top) and saturated (bottom) conditions. The two waveforms shown in each plot corresponded to two orthogonal directions (parallel and perpendicular to bedding). The compressional pulses were sharp, well-defined, and easy to characterize. The changes in velocity (14% and 8.3%) were considerably smaller than the changes in amplitude (50% to 66%).

7.3 Description of samples

The seismic measurements were conducted on cylindrical limestone samples (37.8 mm in diameter) cored parallel to bedding so that all angles oblique to bedding could be measured by rotating the samples in the immersion cell. Cross sections along the planes where measurements were taken are shown in Figure 7.4. A blue epoxy was impregnated into the samples following the seismic transmission experiments to highlight the regions of greatest porosity (the epoxy shows as the dark regions in the figures). Three important features were distinguished in sample K43 (Figure 7.4.a): first, there were clear bedding planes and aligned, lenticular amphibole grains; secondly the rock matrix had no porosity except for these partially dissolved amphibole grains; and finally, there were two macroscopic cracks. Fracture #1 was displaced about fifteen degrees from bedding and extended through the core. Fracture #2 was oriented about sixty degrees and narrowed within the core. Figure 7.5.a (50x magnification) illustrates the concentration of blue epoxy in the amphibole grains. Bedding features were not strong but were distinguished by a slight increase in grain size upwards in the photograph. Figure 7.5.b (100x magnification) shows two subparallel fractures (set 1) that were filled with blue epoxy. The upper fracture exhibited some mineral alteration indicating the fracture had served as a pathway for water in the environment over geologic time. No blue epoxy was distinguished in the matrix. Figure 7.8 summarizes the preceding observations.

Sample K72 (Figure 7.4.b) was the most complex of the three cores examined in this study. Bedding planes were again very evident by the large quantities of blue epoxy filling particular layers. In addition to bedding there were two conjugate fracture sets sixty degrees from bedding, a filled fracture orthogonal to bedding, and a set subparallel to bedding. Figure 7.5.c (100x magnification) clearly illustrates the preferential porosity along certain layers. At the top of the photo is a layer of aligned coarse grains with no porosity. Below it are finer dolomite grains with interstitial porosity. Figure 7.5.d (100x magnification) displays

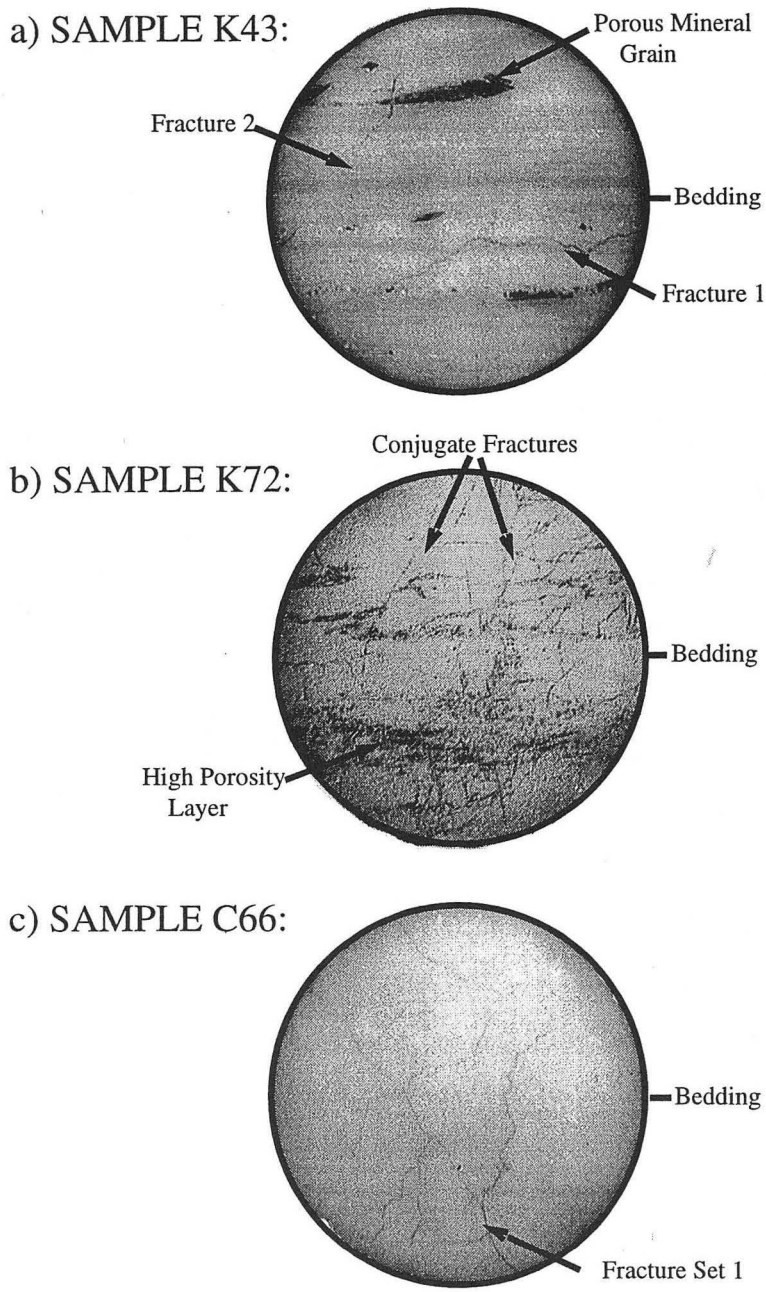

Figure 7.4 Thin sections for the three cores of this study (all of the photographs were taken with bedding parallel to the text). Blue epoxy was imbibed into the samples to distinguish between matrix and fracture porosity. a) Sample K43 had identifiable bedding, high porosity grains and two fractures that were oriented 15 and 60 degrees to bedding, respectively. b) K72 had a pair of conjugate fractures and bedding planes that were distinguished by the coarse-grained lighter-colored minerals and higher porosity (dark) layers. c) C66 had a set of indistinguishable fractures parallel to bedding and a dominant fracture at 75 degrees.

two fracture sets which, unlike the fractures in K43, were discontinuous and had variable thickness.

Sample C66 (Figure 7.4.c) exhibited a bedding structure that was only visible when the surface was wet. The core additionally exhibited two fracture sets: one of the sets had variable orientations to bedding and the other was inclined at approximately 75 degrees. A closer examination of the core (Figure 7.5.e) revealed that the grains were not readily discernible even at a magnification of 100x. The fracture in this photograph is labeled Fracture #1 and is identified by the blue epoxy. Fracture Set #2, in Figure 7.5.f (200x magnification), was only readily observable at higher magnification. The fracture aperture in this second set was also extremely variable.

7.4 Experimental results

The changes in velocity and amplitude as a function of orientation for K43, K72 and C66 are shown in Figure 7. 6 and summarized in Table 7.1. The first two columns of Table 7.1 are the percentage change in velocity and amplitude between the reference direction (taken as the maximum saturated signal) and the orthogonal direction. According to the table, the velocity varied from -0.6% to 12%, whereas the amplitude varied from 30% to 94%, implying that amplitude was a more sensitive indicator of anisotropy for these particular rocks at 1 MHz. This result was confirmed by comparing the uniformity of velocities with orientation in Figure 7.6 to the angular dependence of amplitude.

In Figure 7.6, the solid line corresponds to "dry" conditions, whereas the stippled lines represent saturation, and the ordinate values in all plots correspond to bedding. For K43, the maximum amplitude occurred 15 degrees from bedding for both the dry and saturated cases, and declined considerably at oblique orientations. Figure 7.4.a suggested that bedding, large porous amphibole grains, and fractures all contributed to the observed anisotropy. Because the matrix had low porosity and bedding did not consist of aligned dolomite grains, it was unlikely to have generated large amplitude anisotropy. The coplanar amphiboles, however,

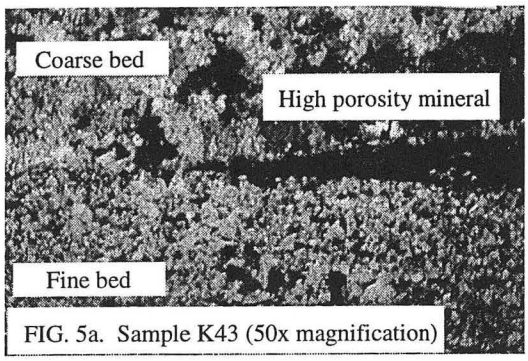

FIG. 5a. Sample K43 (50x magnification)

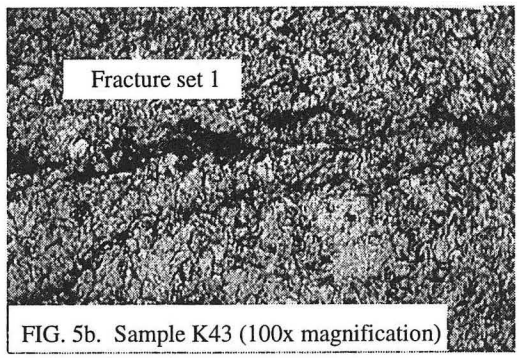

FIG. 5b. Sample K43 (100x magnification)

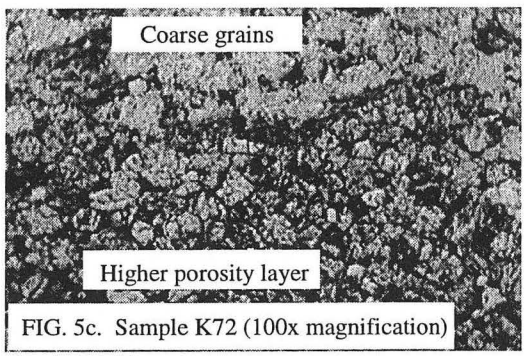

FIG. 5c. Sample K72 (100x magnification)

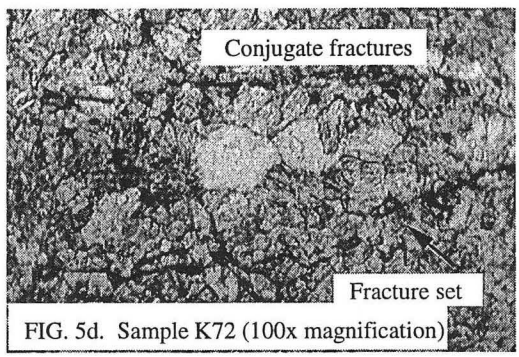

FIG. 5d. Sample K72 (100x magnification)

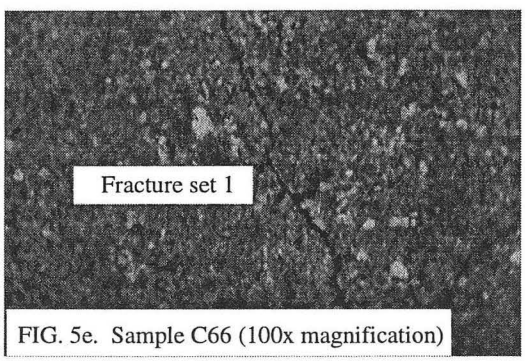

FIG. 5e. Sample C66 (100x magnification)

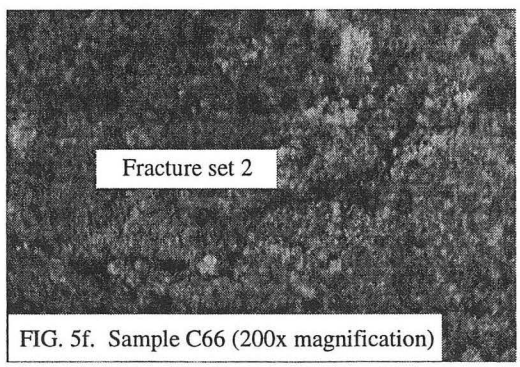

FIG. 5f. Sample C66 (200x magnification)

Figure 7.5 Microscopic examination of the samples K43, K72, and C66 with bedding parallel to text. a) and b) Sample K43 had porosity confined to amphiboles and fractures. c) and d) K72 had high porosity within certain beds and multiple fracture sets. e) and f) C66 had no clear bedding, but a dominant fracture at 75 degrees (100x mag.) and a minor set parallel to bedding (200x mag.).

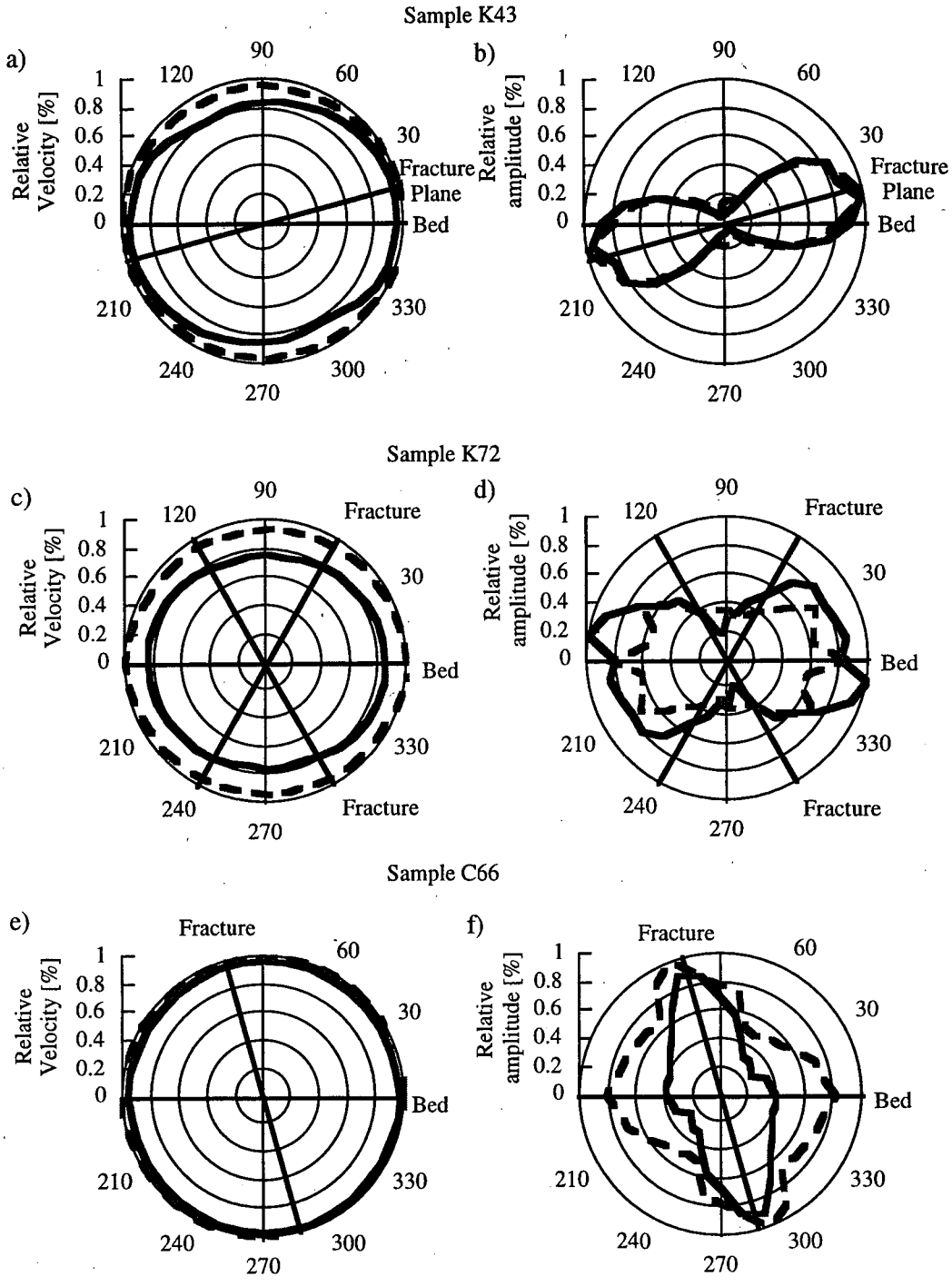

Figure 7.6 Summary of the measurements of velocity and amplitude as a function of orientation, for dry (solid line) and saturated (broken line) conditions. The orientation at zero degrees corresponds to bedding. The ordinate values in all plots were normalized with respect to the values occuring at the maximum saturated amplitude.

Sample	Condition	Velocity Change [%]	Amplitude Change [%]
K43	dry	12.0	93.9
K43	sat	4.5	87.0
K72	dry	10.8	58.7
K72	sat	7.4	58.9
C66	dry	1.3	61.7
C66	sat	-0.6	29.6

Table 7.1 A comparison of anisotropy parameters for K43, K72, and C66. The changes in velocity and amplitude between the orientation of the maximum saturated amplitude and a perpendicular direction ranged from -0.6% to 12%, and 30% to 94%, respectively (K43 had the largest amplitude anisotropy). Saturation conditions diminished amplitude and velocity differences.

Amplitude Ratio	Sample K43	Sample K72	Sample C66
U_{sat} / U_{dry} parallel to maximum saturated amplitude	1.0	1.0	1.1
U_{sat} / U_{dry} perpendicular to maximum saturated amplitude	2.2	1.0	2.1

Table 7.2 A measure of the change in amplitude induced by saturation. Parallel to the maximum saturated amplitude there was no change for any of the three cores. Samples K43 and C66 were preferentially stiffened perpendicular to this orientation, while K72 showed no change in energy transmission. Observations of Figure 3.6 indicated that although the energy at zero degrees was unchanged, the three cores exhibited drastically different behaviors. The amplitude for K43 was unchanged with saturation; whereas, the amplitude for K72 decreased and C66 increased. Possible explanations are discussed in the text.

were extremely porous (as indicated by the blue epoxy that fills them) and were likely more compliant than the matrix. Scattering effects along the contact of the amphibole grains may have contributed to attenuation at these inclusions. The large grain at the top of Figure 7.4 was intersected by the P-wave from approximately 65 degrees to 130 degrees (and also the complimentary angles 245 to 310 degrees)(Figure 7.8), which corresponded to the extremely reduced transmitted signal in this range. Several smaller amphibole grains may have offered compliance in other orientations (e.g. an amphibole grain in the center of the photograph was visible from 25 to 35 degrees; the grains in the lower right were visible from 120 to 140 degrees and 150 to 160 degrees, respectively) though none was as dominant as the former because of its size. The two fractures in the photograph (distinguished by blue epoxy filling) also introduced directional compliance and were visible over the entire range of the core except for a small window near 15 degrees (subparallel to the direction of the maximum compressional wave signal).

K72 (Figure 7.4.b) was difficult to interpret because both the sample and the peak-to-peak amplitude plot were more complex. However, despite the fact that there were several amplitude peaks and their orientations changed with saturation, amplitudes generally decreased with oblique angles to bedding. Bedding in this sample was distinct because coarser grains were aligned and finer layers had higher porosity. The bulk of this porosity was concentrated below the center of the photograph and was visible by the seismic pulse at every angle other than a 20 degree window on both sides of the horizontal bedding, making it likely that the signal at 0 degrees to bedding crossed the most intact rock. There were three porous fracture sets that offered additional compliance, but because they were all oriented differently they may have diminished the overall stiffness of the rock, without introducing clear directionally-dependent amplitudes.

C66, which had indistinguishable bedding and two fracture sets, also had two directional amplitude peaks, one of which was subparallel to the orientation of aligned fractures (compare Figure 7.4.c and Figure 7.6.f). The largest occurred subparallel to fractures set 1,

which can be seen in Figure 7.5.e. The second was subparallel to bedding and fracture set 2. Unlike fracture set 1, fracture set 2 was discontinuous and irregular with respect to orientation (Figure 7.5.f).

The change in seismic amplitude resulting from the imbibition of water was approximated by the difference in area under the amplitude plots for the dry and saturated curves of figure 7.6. Table 7.2 shows the ratio of saturated amplitude to dry amplitude to highlight the effects of water on energy transmission. For K43 the overall transmitted energy was relatively unchanged over most of the range of measured orientations (Figure 7.6.b), except for the 2:1 difference between the directions perpendicular and parallel to the maximum saturated amplitude, respectively. In K72, the transmitted energy actually declined. The porous nature of certain layers indicated that possible squirt-flow mechanisms were operative (Dvorkin and Nur, 1993; Dvorkin, et al., 1995). Finally, C66 exhibited an overall increase in energy with saturation, with the transmission at ninety degrees preferentially enhanced. These results were consistent with water stiffening preferentially-oriented, compliant interfaces for samples K43 and C66.

7.5 Nonwelded interface model

The change in velocity and amplitude as a function of orientation due to the presence of fractures can be interpreted in two different ways. The first approach is a static approximation which sums up the additional compliance of each fracture in a derivation of elastic moduli for the rock mass (e.g. O'Connell and Budiansky, 1974; Crampin, 1981). Hudson (1981) determined the effect of a dilute population of cracks on displacement fields, derived velocities from the calculated elastic moduli, and subsequently applied a scattering formulation to determine fracture-induced attenuation. The drawback of this effective medium approach is that it is a zero frequency approximation and cannot, therefore, account for attenuation and dispersion. This removes a very powerful tool for distinguishing between fracture-induced and intrinsic anisotropy.

The second approach is the nonwelded interface model, which retains the frequency dependence of the wave transmission and reflection coefficients, and the phase velocity (e.g. Schoenberg, 1980; Pyrak-Nolte, et al, 1990 a and b; Schoenberg and Sayers, 1995; Pyrak-Nolte, 1997). For spacing between fracture asperities that are much smaller than the wavelength, this method treats aligned interfaces as displacement discontinuities of zero thickness across which the stresses are continuous but the displacements are not. Schoenberg (1980) and Pyrak-Nolte, et al. (1990a) have calculated elastodynamic equations for plane waves incident upon nonwelded interfaces resulting in reflection and transmission coefficients and group time delays that are a function of angle, frequency, and stiffness/seismic impedance ratios. Pyrak-Nolte, et al. (1990b) have additionally verified model predictions by matching theoretical velocity and amplitude dispersion to measured values across a nonwelded fracture of known stiffness.

In this study, compressional pulses were analyzed in the frequency domain to determine if measured dispersion could be modeled as a single, compliant interface oriented parallel to the direction of maximum amplitude that incorporated the effect of all planar features. Although the transmitted energy in this study sometimes only crossed one or two fractures because of the size of the samples, the nonwelded interface model was used to explain amplitude anisotropy corresponding to a series of parallel fractures that occurred on a larger scale. In order to accentuate the directionality of the measurements the ratio between the maximum saturated amplitude and ninety degrees (i.e. the maximum and minimum velocities and amplitudes in the general case) were examined. Spectral amplitudes were computed by tapering the waveform with a Blackman window and then applying a Fast Fourier Transform. The attenuation, Q^{-1}_{excess}, was calculated from the spectral ratio of the waves traveling in the parallel and perpendicular directions as follows:

First, the particle displacement of a plane wave was expressed as:

$$u_j = A_o G_j \exp\left[i\left(\hat{k}_j j - \omega t\right)\right]; \tag{7.1}$$

where $j = x, y, z$; $\hat{k}_j = k_j + i\alpha_j$ was the complex wave number, and ω was the angular frequency. Defining the direction along the axis of the specimen as z, the parallel and perpendicular particle displacements were calculated:

$$u_x = A_o G_x \exp[-\alpha_x x]\exp[i(k_x x - \omega t)]; \tag{7.2}$$

and

$$u_y = A_o G_y \exp[-\alpha_y y]\exp[i(k_y y - \omega t)]; \tag{7.3}$$

where α_x and α_y were the attenuation coefficients in the x and y directions, respectively. Assuming that the geometric spreading was approximately the same in the two directions, so that $G_x \cong G_y$, the attenuation in the parallel and perpendicular directions was expressed as a sum of their isotropic and direction-dependent components,

$$\alpha_x = (\alpha_{iso} + \alpha_{frac\_x}); \tag{7.4}$$

$$\alpha_y = (\alpha_{iso} + \alpha_{frac\_y}). \tag{7.5}$$

This led to:

$$\left(\frac{u_y}{u_x}\right) = \left(\frac{\exp[-(\alpha_{iso} + \alpha_{frac\_y})y]}{\exp[-(\alpha_{iso} + \alpha_{frac\_x})x]}\right); \tag{7.6}$$

where x = y = d, the diameter of the specimen. Thus, the *excess* attenuation in the x-direction was determined by:

$$Q^{-1}_{excess} = \frac{2\alpha_{excess} c(\omega)}{\omega} \quad ; \tag{7.7}$$

where

$$\alpha_{excess} = (\alpha_{frac\_x} - \alpha_{frac\_y}) = \frac{1}{d}\ln\left(\frac{u_y}{u_x}\right); \tag{7.8}$$

and $c(\omega)$ was the phase velocity. Choosing the x-direction to coincide with the observed maximum saturated amplitude, the excess attenuation α_{excess} was the extra attenuation perpendicular versus parallel to the inferred fracture plane.

The dashed lines in Figure 7.7 show the results of the analysis in the frequency domain. The excess phase velocity and the excess attenuation (Q^{-1}_{excess}) were plotted for both dry and saturated conditions. The frequency dependence of the phase velocity was relatively small. Also, the magnitude was independent of the level of saturation. The attenuation, however, had a strong frequency dependence and, except for sample K72, a larger attenuation dry compared to saturated conditions. On theoretical grounds, it might have been anticipated that the presence of water in a compliant interface would have increased its stiffness, thus reducing P-wave scattering attenuation across the fracture (Pyrak-Nolte, et al., 1990a). Based on the measurements of water imbibition as a function of time (Figure 7.3) and the partially wetting behavior of the specimen surfaces, it was inferred that fractures in the rock were predominantly dry despite the fact that the rock was immersed in a water bath during the "dry" experiment. Consequently, in the vacuum saturated experiment the additional water increased both the global stiffness of the specimen and the stiffness of the compliant interface for K43 and C66. Consequently, Q^{-1}_{excess} plots were consistent with water stiffening a compliant interface and increasing the amplitude of P-waves propagating across the interfaces for samples K43 and C66 (see discussion of Table 7.2).

The exception to this behavior was sample K72, which displayed attenuation that increased when the sample was vacuum saturated with water, which was consistent with the microstructural complexity of the high porosity layers which were only present in sample K72. A possible explanation was that the compliant grain boundaries were serving as sites for squirt-flow dissipation (Dvorkin and Nur, 1995; Dvorkin, et al., 1995).

To determine if the measured attenuation could be accounted for by a nonwelded interface, the phase velocity and attenuation that would have resulted from a nonwelded interface were compared to measured values in the frequency range of interest. First, the transmission coefficient was calculated from the ratio of the measured amplitudes parallel to the compliant interface and a normal direction (see equation (7.6)):

$$T_p(\omega) = A_{perpendicular}(\omega) / A_{parallel}(\omega). \qquad (7.9)$$

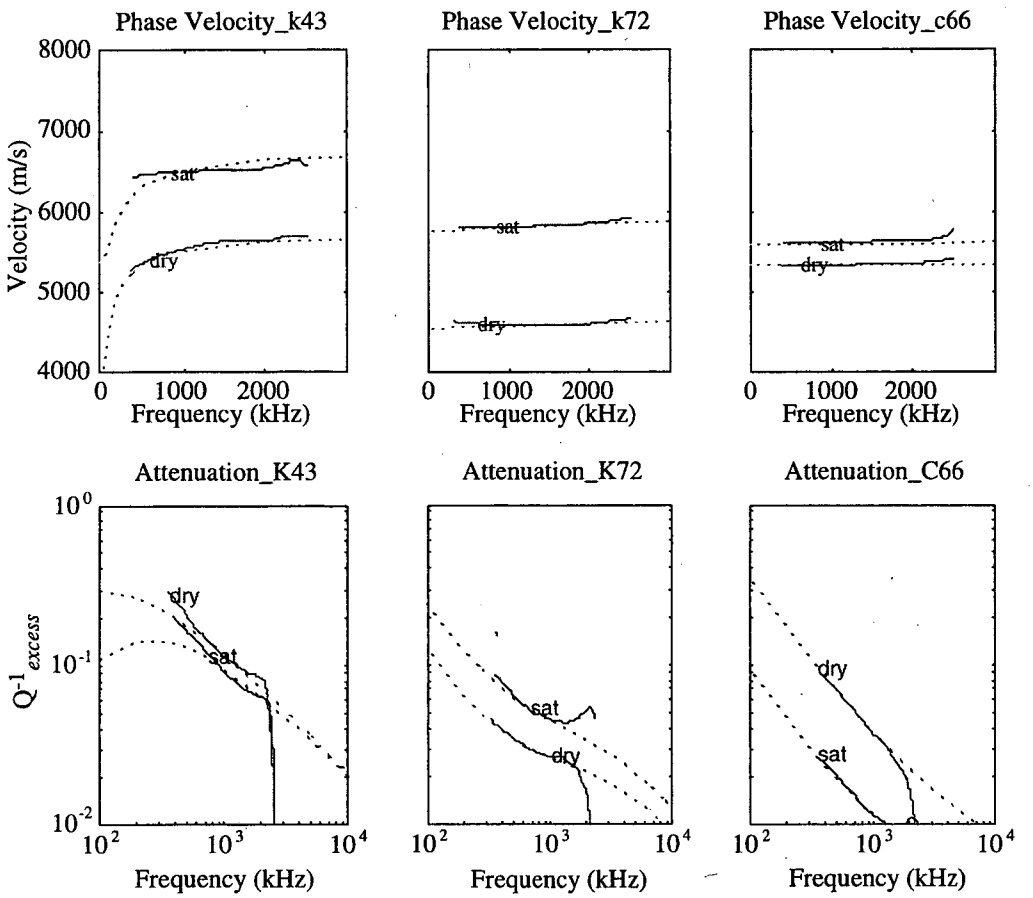

Figure 7.7 Measured (solid lines) and predicted (dotted lines) values of phase velocity (top) and attenuation (bottom) for P-wave propagation across limestone rocks. Modeling was performed using an elasto-plastic, compliant interface. The match was nearly identical. Saturation increased phase velocity in all cases. For samples K43 and C66, saturation also reduced attenuation. Sample K43 was modeled by only specifying a stiffness and time delay term and was therefore the most easily interpreted as being caused by a fracture. K72 and C66 were modeled with a viscosity term that may have reflected only global anisotropic properties. The nonwelded interface model additionally predicted velocities that were too low at zero frequency for K43 because of the low stiffness value.

The orientation of the fracture plane selected from Figure 7.6 aligned with the direction of maximum amplitude for the saturated condition. Secondly, the theoretical transmission coefficient for a plane wave normally incident upon a single nonwelded interface was given as follows (Pyrak-Nolte, et al., 1990a):

$$T_p(\omega) = \left[\frac{1}{1 - i\frac{z\omega}{2}\left(\frac{1}{\kappa} + i\frac{1}{\omega\eta}\right)} \right]. \tag{7.10}$$

where $z = \rho c$ was the acoustic impedance, κ was the interface stiffness [Pa/m], and η was the interface viscosity [Pa•s/m]. An optimization algorithm was then used to determine the best pair, κ and η, that minimized the error between the measured and predicted transmission coefficients for a range of frequencies. The phase velocity was also predicted by the nonwelded interface model as a function of the same κ and η parameters:

$$c(\omega) = L / (t_o + t_\theta); \tag{7.11}$$

$$t_\theta = \frac{\theta}{\omega} = \frac{1}{\omega}\arctan\left[\frac{\frac{\omega z}{2\kappa}}{\left(1 + \frac{z}{2\kappa}\right)} \right]; \tag{7.12}$$

where L was the travel length, t_o the arrival time of the reference signal (parallel to the interface), and t_θ the additional time delay resulting from phase shifts as the wave traveled across the interface (Pyrak-Nolte, et al., 1990a). Finally, the phase velocity was used as input in equation (7.8) to calculate the predicted attenuation Q^{-1}_{excess}.

It was found that although the transmission coefficient could be matched by the nonwelded interface model, the predicted phase velocity was sometimes faster than measured values. It was therefore necessary to add an additional time delay, Δt, corresponding to additional microstructural mechanisms not accounted for by the nonwelded interface model for an isotropic solid:

$$c'(\omega) = L / (t_o + t_\theta + \Delta t). \tag{7.13}$$

With this correction, $c(\omega)$ was calculated and the resulting values matched phase velocity and Q^{-1}_{excess} in the 1 MHz range, which was the peak frequency of the signal (see the dashed lines in Figure 7.7).

Table 7.3 reports the stiffness, viscosity, and time delay parameters used to match predicted and measured dispersion; however, not all three parameters were required to match any of the individual limestones: for K43 a stiffness and time correction factor were required (for the dry core only); for K72, a viscosity and time delay had to be specified (the stiffness term represented an essentially welded interface, κ was on the order of 10^{13}); finally, for C66, a viscosity and stiffness were needed. Sample K43 had the most compliant plane of weakness according to Table 7.3, which was consistent with the strong amplitude anisotropy of figure 7.6.

7.6 Discussion

It was apparent by comparing Figure 7.4 and Figure 7.6 that maximum amplitudes occurred for orientations near-parallel to major structural features in the samples. For the simple case of sample K43, there was a strong amplitude anisotropy that was related to the fracture sets and the highly porous amphibole grains, both of which showed a preferential orientation. The very high amplitude dispersion that occurred in this sample was also consistent with preferentially-oriented planes of weakness, and the decrease in attenuation with saturation was explained by the stiffening of these interfaces (Table 7.2 and Figure 7.7). The nonwelded interface model matched phase velocity and attenuation (Q^{-1}_{excess}) with only a stiffness term (κ) in the saturated state. The time delay correction for the dry core had two sources: the simple assumption of a nonwelded interface in an isotropic media (Schoenberg and Haugen (1995) have derived equations for the nonwelded interface in an anisotropic media); also, there may have been a time delay associated with the first-arriving signal being unable to cross the large, porous amphibole grain of Figure 7.8. The first of these effects was accounted for by measuring the velocities parallel and perpendicular to the maximum

Sample	Condition	Velocity Parallel [m/s]	Velocity Perpendic. [m/s]	Fracture Stiffness κ [Pa/m]	Fracture Viscosity η	Time Delay $\Delta t'$ [μs]
K43	dry	6562	5718	2.3×10^{12}	0.0	0.84
	sat	6812	6620	6.6×10^{12}	0.0	0.02
K72	dry	5146	4572	2.7×10^{13}	1.6×10^{7}	0.80
	sat	6136	5851	2.3×10^{13}	1.1×10^{7}	0.20
C66	dry	5400	5400	2.8×10^{13}	3.0×10^{6}	0.0
	sat	5600	5600	8.2×10^{13}	2.1×10^{7}	-0.06

TABLE 7.3 Nonwelded interface parameters κ, η, and $\Delta t'$ used to match predicted phase velocity and Q^{-1}_{excess} to measurements. No viscosity term is required for sample K43. For K72 and C66, the large stiffness parameter implies that the interface is welded and only a viscosity and time delay term need to be specified to match the curves. The time delay term is a correction factor because the nonwelded interface model only predicts small phase time delays. It physically implies additional anisotropy in velocity not characterized by the nonwelded interface model. Its value is significant for dry cores K43 and K72 and can be explained for K43 (see text).

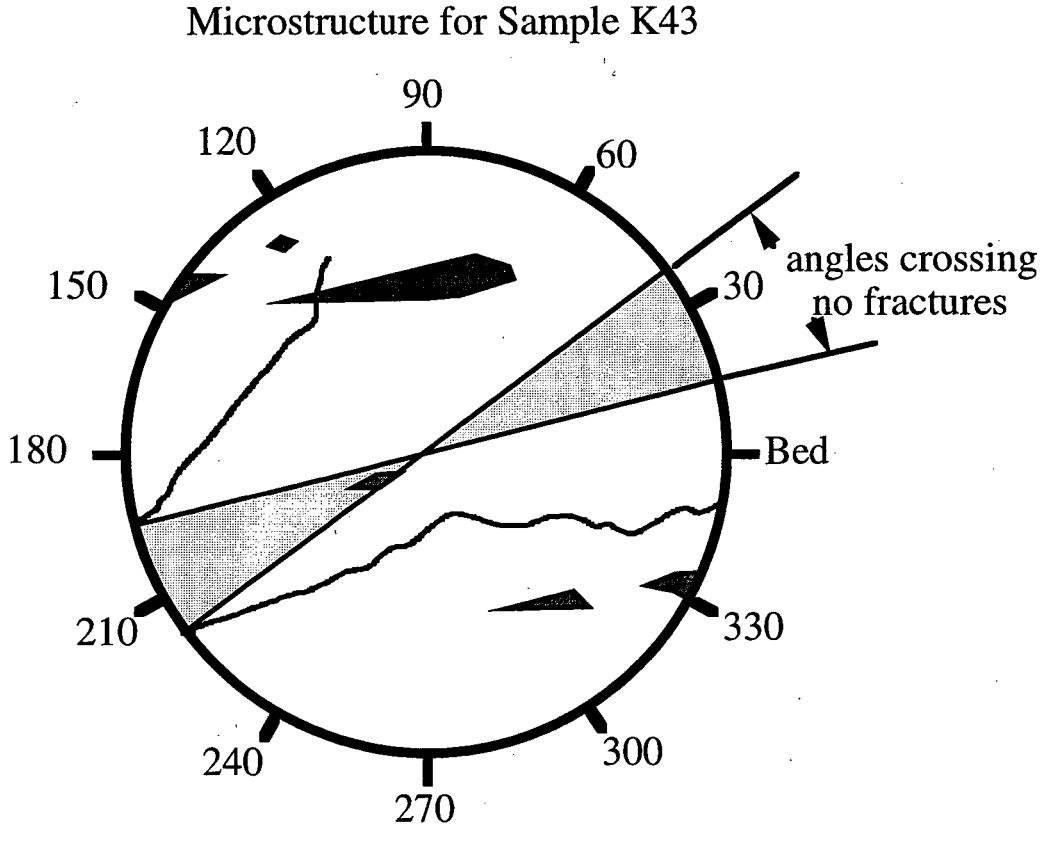

Figure 7.8 Schematic of structure along the plane that measurements were recorded for sample K43. Bedding was at zero degrees. Mineral grains were darkened. Only measurements taken from15 to 35 degrees did not intersect fracture planes.

saturated amplitude (in the completely dry state in a cube of rock containing no fractures or interfaces). This contribution to the 0.84 μs time delay term is 0.17 μs. The additional travel time required for the wave to diffract around the amphibole inclusion was estimated to be 0.57 μs.

Sample K72 was very complex and this is reflected in Figure 7.6.d. Amplitude anisotropy measurements distinguished a major amplitude peak in the dry case that was replaced by three peaks in the saturated case; however, the minimum direction was always perpendicular to bedding and may have been caused by the seismic pulse intersecting the highly porous beds in Figure 7.4.b. An increase in attenuation with saturation might be expected for higher porosity rock due to squirt-flow and other mechanisms (Johnston, et al., 1979), and a decrease in amplitude with saturation in the amplitude polar plots (Figure 7.6) was consistent with increasing attenuation preferentially in a direction that was orthogonal to the compliant interfaces (Figure 7.7). Sample K72 represented the limitations imposed by both the experimental techniques and the nonwelded interface model because it contained both porous bedding planes and multiple fracture sets. As a result, calculated fracture stiffness values only represented an average stiffness in a particular orientation.

For C66, there appeared to be two dominant fracture sets in this sample and amplitude anisotropy measurements identified the most compliant fracture set 1. Photographs of thin sections (Figure 7.5.e and 7.5.f) confirmed that fracture set 1 (Figure 7.4) was more compliant than fracture set 2, and this was also reflected in a positive Q^{-1}_{excess}. Although the experiments identified fracture set 1, the nonwelded interface model may not have been appropriately applied because a viscosity term was required to match theoretical and measured values. Therefore, the attenuation could not simply be modeled as resulting from a single, or multiple but parallel, plane of weakness.

7.7 Conclusions

This chapter has endeavored to ascertain the presence of planes of weakness in three dolomitic limestones by measuring both the velocity and amplitude anisotropy under partially and fully saturated conditions. This study has demonstrated that when fractures are present in a rock sample, the resulting amplitude anisotropy may be large and more revealing than velocity measurements. There was noticeable anisotropy in velocity (from 0.7% to 13%), but a much larger amplitude anisotropy (from 30% to 94%) as determined from the ratio between orthogonal directions. For sample K43 the amplitude anisotropy difference (over a range of frequencies) was larger than the velocity difference (measured at 1 MHz) down to 2.4 kHz and 26 kHz for the dry and saturated samples, respectively.

In none of the experiments did the maximum dry amplitude coincide with bedding. In fact, for K43 and C66 the maximum amplitude was oriented in the same direction as observed compliant interfaces in thin section. Q^{-1}_{excess} plots supported the interpretation that amplitude anisotropy was due to fractures because there was direction-dependent dispersion as would have been predicted by a set of compliant interfaces, and there was a decrease in attenuation with saturation (i.e. a stiffening effect). Because the size of the samples used in this study and the wavelength of the seismic pulse were small, most microstructure was probed and the resulting Q^{-1}_{excess} plots reflected an average stiffness. As evidenced by the complexity imposed by sample K72, laboratory amplitude anisotropy measurements may work best in rocks that have lower porosity and one dominant direction of amplitude anisotropy (e.g., saturated K43).

Weak elastic anisotropy theories describe the effect of anisotropy on velocity (e.g. Thomsen, 1986), but they do not describe the associated change in wave amplitude, nor the observed frequency dependence of measured amplitude. Consequently, in cases where discontinuities are present and the amplitude anisotropy is large, nonwelded interface models may be employed to examine the anisotropy between maximum and minimum signals. The nonwelded interface model matches the presence and effect of preferentially-oriented planes

of weakness on phase velocity and attenuation by specifying one or more amplitude anisotropy parameters (κ, η, Δt). Although this model identified a plane of weakness for sample K43, the attenuation was due to two effects: a fracture and a porous mineral grain (Figure 7.8). A single nonwelded interface was even less able to describe measured amplitude anisotropy for K72 and C66, because the samples were complex and viscous loss mechanisms contributed to the attenuation. Since field conditions are complex (with many sources of attenuation), and in many cases time delay corrections would not be able to be explained because the structure of the rock would not be known, the application of the nonwelded interface model to identify planar fractures in the field must be approached with caution.

CHAPTER 8. A new fracturing mechanism for granular media

8.1 Introduction

The stability of boreholes is a particularly important problem in the oil and natural gas industry, where wells driven to great depths in the Earth must withstand large stress concentrations. The damage that is incurred as the result of these stresses is generally called borehole breakout, and in past experiments fracturing has been observed to proceed through the following sequence of events: extensile fractures separated by many grain diameters form parallel to the borehole wall in the direction of the maximum compressive stress; en echelon shear bands then initiate at an angle to the borehole wall to compensate for the dilation of the extensile fractures; finally, macroscopic shear displacement occurs where these shear bands intersect the borehole wall (i.e. slabs of broken material spall off into the opening incrementally (Ewy and Cook, 1990 a and b)). Stabilization of the breakout has been shown to occur when two-dimensional cone structures form on either side of the borehole, generating a confining stress at the tip of the fracture process zone (Zheng, et al., 1989).

This chapter explores an alternative type of borehole breakout failure which can occur in weakly cemented sedimentary rock. The most diagnostic feature of this new damage mechanism was that it produced a macroscopic fracture plane oriented perpendicular to the applied compressive stress. Although this may at first seem counterintuitive because the loading stress caused a shortening to occur against the opening of the fracture, it was hypothesized that removal of debonded grains compensated for this volume reduction. The objectives of this chapter were to describe the mechanical processes responsible for this unusual result and identify situations where it might occur.

8.2 Experimental Methods

Sintered glass bead bricks were created for this study because glass beads are uniform in size, shape and material properties, making it is possible to model the effects of increasing

the bond strength of the bricks on the type of observed fracture. Bricks with relative height, width, and thickness dimensions of 4.5: 3: 1 were created by pouring 100 μm to 200 μm diameter glass beads into molds and heating them to temperatures above the annealing point of 548 degrees Celsius, but below the softening point of 730 degrees Celsius, to induce grain-to-grain cementation. The degree of sintering in these bricks was controlled by the maximum heating temperature, as well as the duration of exposure. Brick A was sintered at 675 degrees Celsius for 30 minutes; Brick B was sintered at 670 degrees Celsius for 90 minutes; and Brick C was sintered at 680 degrees Celsius for 90 minutes. Following a technique of Berge, et al. (1995), the bricks were allowed to cool slowly through the annealing point to reduce thermal stresses and prevent cracking.

In preparation for the uniaxial compression tests, the bricks were cored through their thickness, so that the breakout could be compared to borehole breakouts obtained from rock samples. To reduce the possibility that uneven loading would result in bending stresses, the ends of the bricks were planed parallel to one another in preparation for the tests. Although no strain measurements were taken in conjunction with loading, the boundary conditions on the bricks appeared to be nearly uniaxial. No bending displacements were visually detected, and because fracturing was localized around the borehole across both the width and thickness of the brick, it was inferred that the fracturing was controlled by the local compressive stress concentration and not by any bending-induced stresses.

8.3 Experimental Results

Figure 8.1 shows the differences in porosity, dynamic Young's modulus and compressive strength between Brick A, Brick B, and Brick C. Under light sintering the beads were fused together over a small region at the point of contact. As sintering increased with time and/or temperature, the cross-sectional area of the fused region grew. This resulted in an accompanying porosity reduction, and an increase in modulus and compressive strength at failure (the vertical scales). The increase in strength and modulus observed in Figure 8.1 was

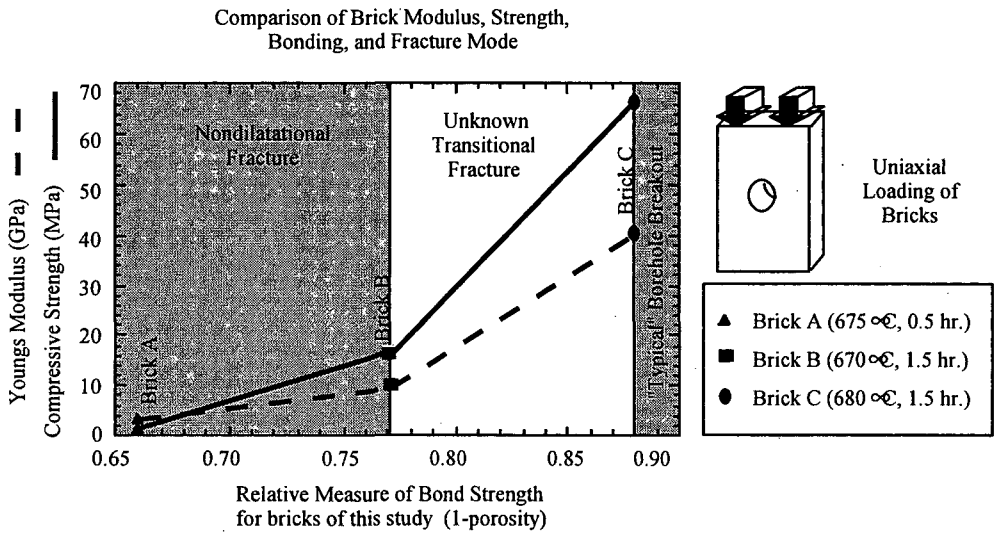

Figure 7.1 Comparison of material properties and fracture behavior for the three bricks of this study. A relative indicator of bond strength was given by (1 - porosity). Brick A had the highest porosity and lowest modulus and strength. Figure C had the lowest porosity and the highest modulus and strength. The grey sections of the figure separate the observed fracture patterns as a function of the degree of cementation. Brick A and Brick B exhibited the "nondilatational" fracturing that is discussed in the text. Brick C failed by grain cracking, extensile fracturing, and shearing. An unknown fracturing mode exists between these extremes.

consistent with Dvorkin, et al., 1991. Brick A had the lowest Young's modulus and compressive strength at failure, Brick B had the intermediate modulus and strength, and Brick C the highest. Because the strength of individual beads was unchanged, the ratio of grain contact/bond strength to grain strength increased from Brick A to Brick C.

In addition to showing the material properties of the bricks, Figure 8.1 delineates two different fracture mechanisms. Brick A and Brick B both exhibited fractures that propagated perpendicular to the applied compressive stress, while Brick C resembled a "typical" borehole breakout. A large transition zone of unknown fracturing behavior (i.e. a large range in bond strengths) separated Brick B from Brick C.

During the fracturing of Brick A (Figure 8.2.a), individual grains were expelled from the sample by the energy released during grain contact rupturing events. Single planar fractures that extended through the entire thickness of the sample subsequently formed on either side of the borehole at 2 MPa, propagating perpendicular to the applied compression until the load was removed. Because the compressive strength of individual beads was 250 MPa, it was unlikely that the strength of individual grains exceeded. SEM inspection along the front fracture surface of Figure 8.2.a revealed that none of the beads were cracked (Figure 8.2.b), but most were chipped along their contacts, indicating grain contacts had broken and beads were removed. Upon inspection of the beads (Figure 8.2.c), it was additionally found that they were removed individually and not as slabs. In Figure 8.2.d the fracture zone was five diameters wide. If this dimension were less, it grains may not have been able to leave the sample because intact grains may block the path of debonded grains.

For Brick C spalling occurred in two planes parallel to each of the free surfaces at 67 MPa (Figure 8.3.a and 8.3.b), which was higher than the compressive strength of Berea sandstone loaded in a similar configuration. In Figure 8.3.c, aligned microcracks had cut through beads parallel and obliquely to the free surface of the borehole wall. Fracture localization is evident in this photograph by the preferential orientation of fracturing through several adjacent beads (the line in the Figure 8.3.c indicates one plane). The results

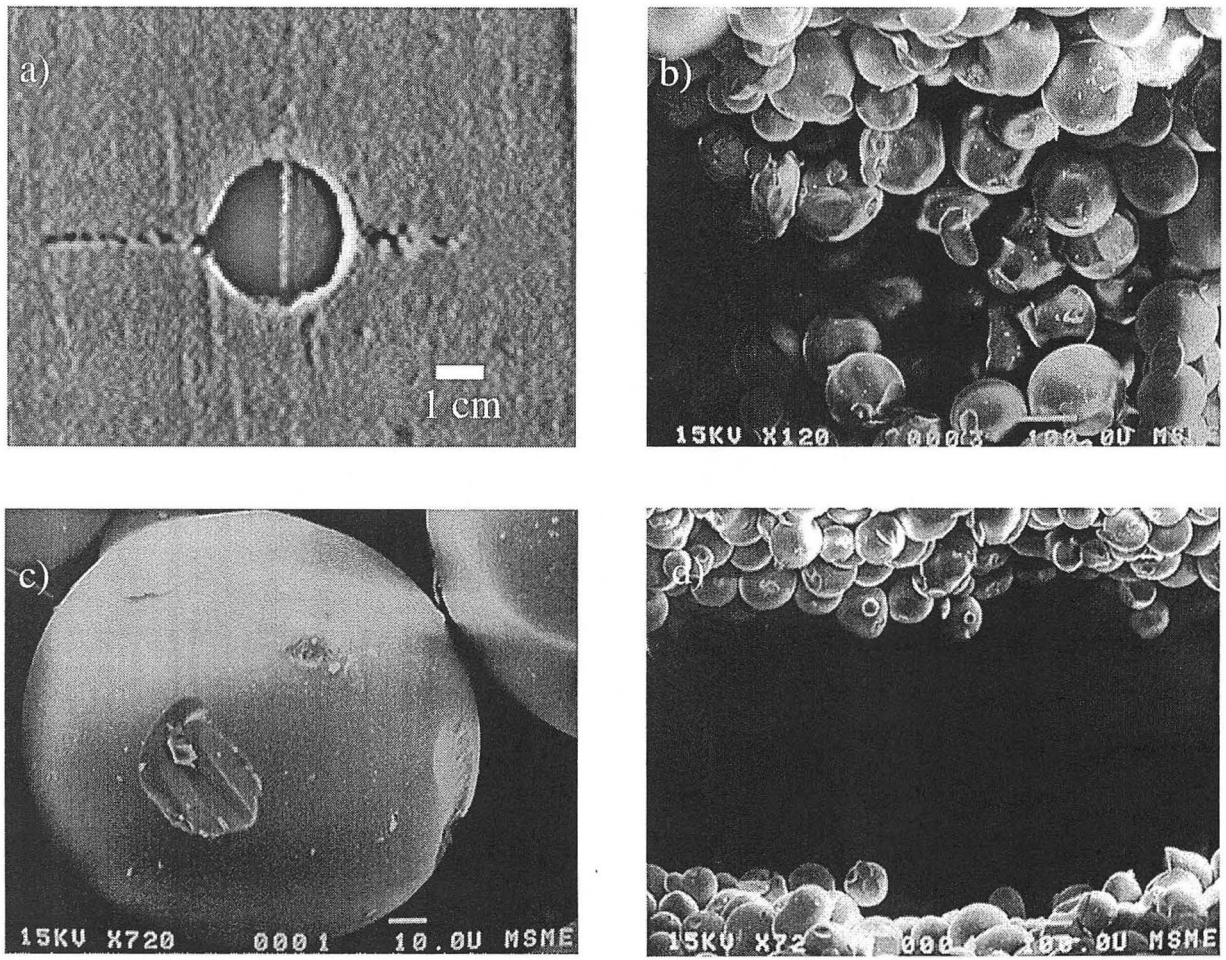

Figure 7.2 Borehole breakout in Brick A (a through d is from left to right). a) Fractures formed linear features from the borehole wall in a direction perpendicular to the applied compressive stress. b) SEM photography revealed that the fracture surface was characterized by beads with broken grain contacts. c) A bead recovered from the removed debris was broken only along its contacts. d) Fracture zone was > 5 bead diameters wide.

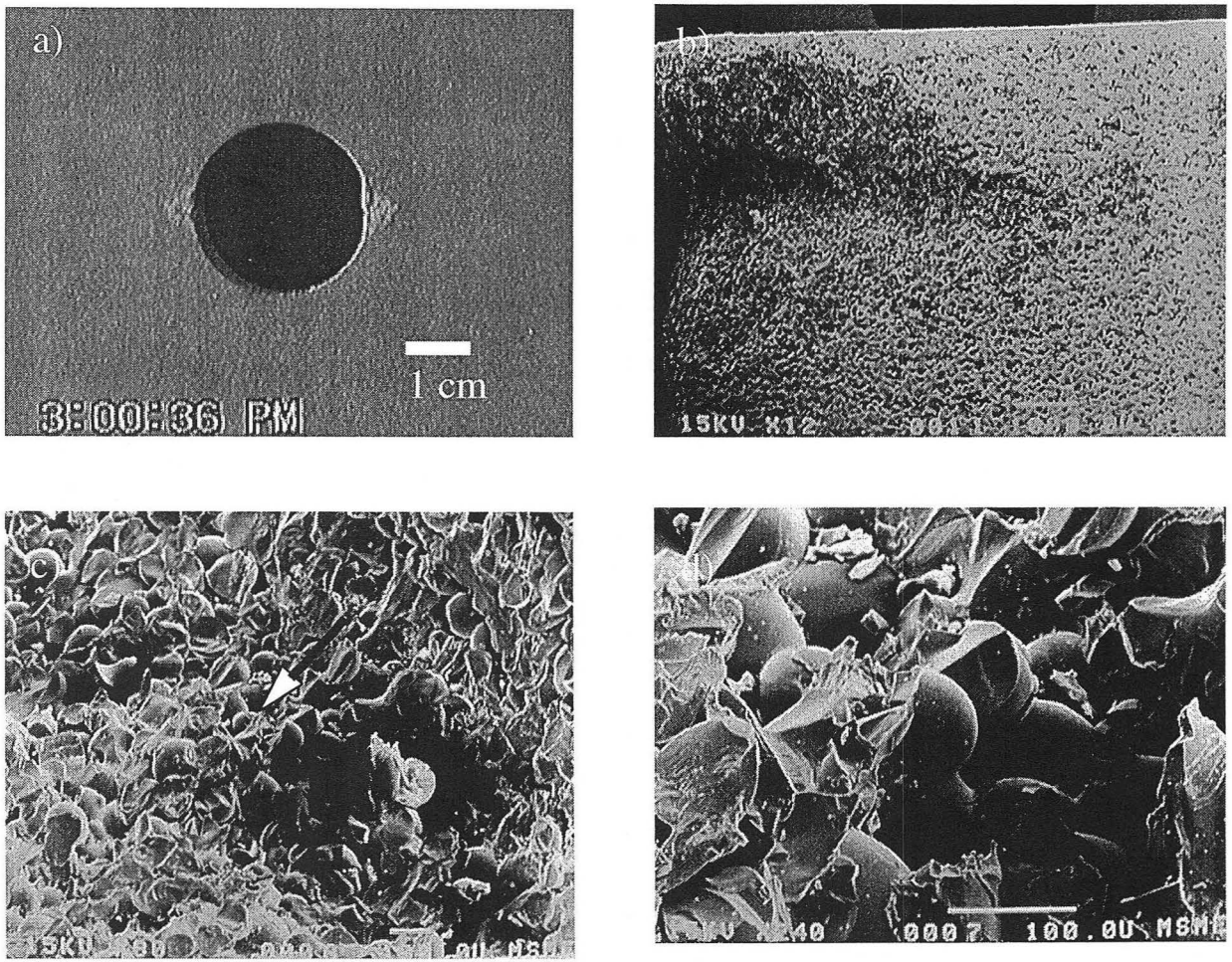

Figure 7.3 Borehole breakout of Brick C. a) Borehole breakout exhibited cone features on either side of the hole. b) SEM photograph of spalled section of brick. c) Aligned planar cracks along the arrow and parallel to the plane of the photograph. d) Fractures propagated through individual beads and not along grain contacts.

of Figure 8.3.d confirmed that the beads were more well sintered than Brick A and fractures had, in fact, cut through individual grains rather than debonding contacts.

Because the new fracturing mechanism reported for Bricks A and B did not result in opening displacements within grains, only grain debonding and removal, it was termed "nondilatational."

8.4 Numerical Simulation

A boundary integral code based on the theory of elasticity had been developed by Liu, et al. (1993), and was used to ascertain the effects of grain contact failure and subsequent grain removal on the direction of fracture propagation. The advantage of this particular code was that it was capable of calculating the stresses within a matrix of randomly packed grains of similar elastic properties, and higher grain strengths to bond strengths loaded in uniaxial compressive. During the calculation, each grain was divided into n segments, the contact stresses and displacements were chosen as variables, and the following matrix equation solved:

$$B_C\{\sigma_{BC}\} = A\{u_{BC}\} \tag{8.1}$$

where $[A_C]$ and $[B_C]$ were the geometrically dependent influence coefficients, $[\sigma_{BC}]$ the contact stress vector, and $[u_{BC}]$ the contact displacement vector. As the uniaxial compressive stress increased, the stress at 400 points in each grain and along grain contacts was calculated, and when the compression-induced tensile stress reached the tensile strength of the grain, the grain was broken and its Young modulus reduced 75% for the next step of the calculation. If the tensile stress exceeded the grain contact strength anywhere within the assemblage, the interface was broken by making the contact elements traction-free. Recontact of two detached grains during loading required that the matrices $[A_C]$ and $[B_C]$ of the grains be recalculated due to the changed contact situation (Myer, et al., 1995).

Because the purpose of the numerical simulation was to determine if failure at the grain scale due to local tensile stresses could lead to the observed macroscopic behavior under far-field compressive stresses, simplifying assumptions were invoked to make the modeling feasible. These included: modeling only the nearly uniaxial loading configuration at the incipient stage of fracturing near the surface of the borehole (Region B, Figure 8.4); and reducing the Young's modulus of grains broken by a tensile criterion to simulate the effect of grain removal. Although additional complexities such as shear fracturing and debonding mechanisms should be included in future investigations, the particular assumptions of this study were shown to be sufficient to produce a macroscopic fracture plane oriented perpendicular to the applied compressive stress.

In Stage 1 of failure (Figure 8.5.a), two grain randomly failed because their tensile strength had been exceeded. During the next iteration (Figure 8.5.b) the Young's modulus in these debonded grains was reduced, the local compressive stresses redistributed to adjoining grains, and the bead adjacent to the removed bead in the upper left, also failed. By Stage 3 (Figure 8.5.c), fracturing was no longer a random process but had localized on either side of the growing fracture in a direction orthogonal to the compressive load.

The explanation for this observed fracture pattern was that compression-induced tensile stress concentrations were large enough to preferentially fracture grains orthogonal to the applied load. Once the load-bearing capacity of the grain was reduced in Figure 8.5, an approximation to the two-dimensional Kirsch solution for the stresses around a circular hole could be used to predict that a tensile stress concentration developed in the "region" above and below the newly-created void in the direction of the applied compressive stress (Region A, Figure 8.4), and also that a compressive stress concentration developed in the "region" at ninety degrees (Region B, Figure 8.4). At the microscale, either of these stress concentrations could have induced additional crack growth in the two-dimensional granular simulation: direct tensile fracturing could have occurred by the tensile stress concentration, or compression-induced tensile fracturing could have occurred within grains or along grain

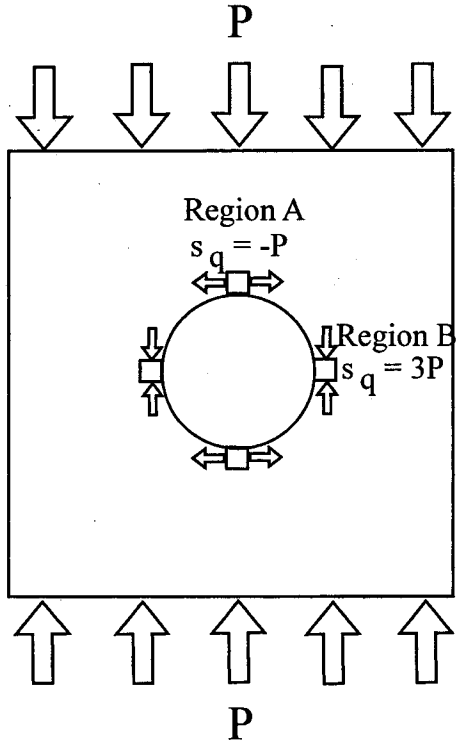

Figure 7.4 The Kirsch solution for the stresses around a circular void. A tensile stress concentration occurs in Region A and a compressive stress concentration occurs in Region B.

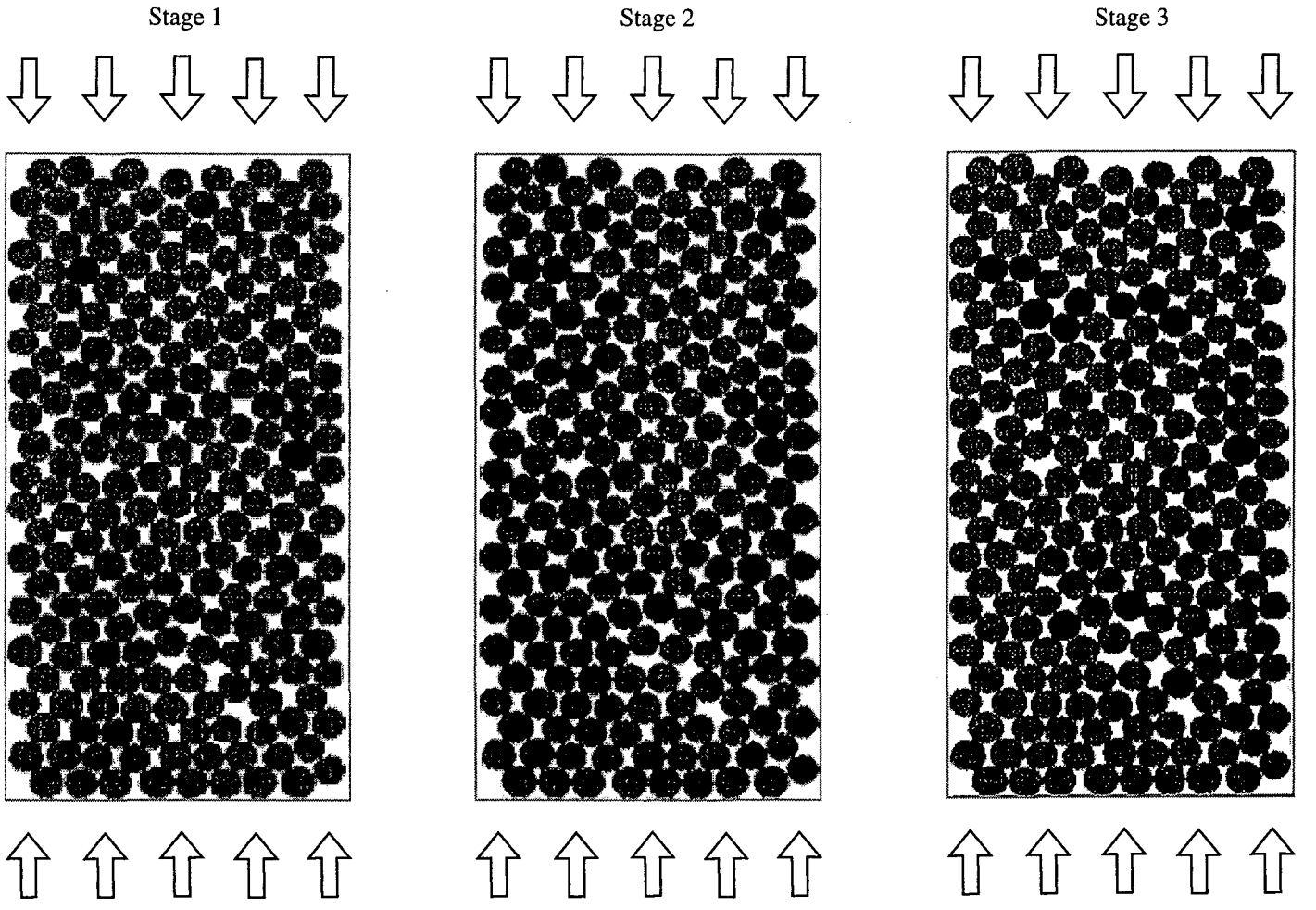

Figure 7.5 Boundary integral simulation of fracture process in granular material. a) A uniaxial compressive stress caused two grain contacts to rupture by tensile cracking. The Youngs modulus of these debonded grains were subsequently reduced. b) Increased compressive stresses were generated by this "hole" in its immediate vicinity causing additional failure in the immediate vicinity. d) Continued localization occurred and a macroscopic fracture grew perpendicular to the applied stress.

contacts by the compressive stress concentration. If direct tensile cracking occurred in adjacent grains in the direction of the compressive loading stress then the macroscopic fracture would have propagated vertically in the picture, forming an extensile fracture. Alternatively, if the indirect tensile stress debonded grains at ninety degrees to the applied load, and if these debonded grains were removed, the macroscopic fracture would have propagated perpendicular to the load.

Liu (1995) demonstrated that to create extensile rather than "nondilatational" fracturing in a randomly packed grain geometry and uniaxial compressive stress boundary conditions, a confining stress associated with an opening displacement within broken grains had to be applied to adjacent grains to prevent compression-induced tensile failure on either side of the broken grain. In the absence of grain dilatation in a randomly-packed matrix, compression-driven tensile failure was promoted, and "nondilatational" fracturing occurred (as in Figure 8.5).

8.5 Discussion

The macroscopic diagnostic feature of a "nondilatational" fracture was that the fracture plane was oriented perpendicular to the applied compressive stress, whereas an extensile fracture are known to form parallel to it. This "nondilatational" fracture can be explained first of all by the bond-strength to grain-strength ratio. Because the bond strength between beads in Bricks A and B were sufficiently small, then grain contact failure was promoted over grain cracking. Because the beads were additionally allowed to leave the sample, a stress redistribution occurred around the subsequent void. This stress redistribution resulted in a tensile stress concentration at the top and bottom of the void of Figure 8.4 (Region A) and a compressive stress concentration on the sides (Region B). It has been shown that individual grains loaded by a uniaxial compressive stress through a limited number of contact points may generate tensile stresses within the grains (Liu, et al., 1993). Removal or movement of grains may also create tensile or shear rupture of the contacts. The

development of indirect tensile stresses perpendicular to the compressive loading stress therefore created the conditions required for subsequent grain or bond failure orthogonal to the applied load, and propagation of a fracture progressed by a "nondilatational" process.

One reason why "nondilatational" fracturing has not been commonly observed in most uniaxial compression experiments was that either the bond-strength to grain-strength ratio was small, or there was no mechanism to remove debonded grains. Consequently, as soon as a crack formed, it introduced a compressive confining stress perpendicular to the load because of the opening displacement within the grain. This confinement inhibited compression-induced tensile stresses from cracking adjacent grains and grain contacts perpendicular to the applied load. Therefore, only the tensile stress concentration in the direction of the applied compressive stress was able to induce additional cracking, and a macroscopic extensile fracture formed instead.

Although the previously described tests demonstrate that bond strength may be the key variable controlling whether an extensile or "nondilatational" fracturing occurs in sintered glass bead bricks, many other microscale properties must be considered in rock systems. For example, very angular grains may be "locked" in place despite being debonded, thereby clogging the fracture process zone and inhibiting grain removal. Some type of mechanical force, like flowing groundwater, may then be required to remove these debonded grains and prevent them from redistributing a compressive load into a confining stress on adjacent grains. A high stress gradient was not necessary for "nondilatational" fracture propagation because a fracture oriented perpendicular to the applied compressive stress also propagated in a brick with a Young's modulus of 3.0 and a compressive strength of 2.6 MPa that did not contain a hole. This implied that "nondilatational" fracturing occurred in the absence of a hole-induced stress concentration.

Despite the added complexities imposed by heterogeneous granular rock, "nondilatational" fracturing may have already been observed in the laboratory and field. Tronvoll and Fjær (1994) demonstrated that if fluid was allowed to flow during compression-

driven sanding experiments, axial flow channels developed orthogonal to the applied compressive stress in poorly cemented sandstone. These authors call the fracture process "piping erosion", but it may, in fact, be none other than the failure mechanism discussed in this chapter, where water provided a mechanical force to clear the fracture zone and allowed propagation to continue.

8.6 Conclusion

In poorly-sintered glass bead bricks, fractures were observed to extend out from a borehole orthogonal to the applied compressive stress. This fracture orientation was similar to antimode I fractures such as compaction bands in sandstone (Antonellini, et al., 1994), but occurred by a newly-described mechanical mechanism consisting of grain debonding and removal by ejection from the sample. For Brick A, fracture propagation occurred along grain boundaries in a fracture zone five grain diameters wide, which may be the minimum dimension to allow debonded grains to be ejected from the sample. A boundary integral numerical simulation demonstrated that as a grain was removed from the sample, the compressive load was transferred to adjacent grains, making them more likely to undergo compression-induced tensile cracking. In the actual experiments, because tensile stresses were also generated at the grain contacts, grain debonding was possible. Consequently, the resultant breakout patterns consisted of fractures aligned orthogonal to the applied load. To discern the effect of grain-to-grain bond strength on fracture behavior, two other glass bead bricks of greater sintering were also loaded in uniaxial compression and the most highly sintered brick underwent extensile/shear failure, which was typical of borehole breakouts in rock. Because crack formation occurred between grains for Brick A and Brick B, rather than through them (creating opening displacements in Brick C), this new macroscopic fracture for granular media was called "nondilatational." Sand production may be a potentially costly example of this process in oil and natural gas reservoirs, where fluid movement into a

producing well removes debonded grains. Similar conditions are unlikely around mining excavations.

CHAPTER 9. Conclusions

One important conclusion of this dissertation is that the problem of predicting the occurrence and mineralogy of fractures in the Earth is extremely complex. Each of the independent studies reported above revealed equally important issues requiring further analysis. Consequently, to close this dissertation, Tables 9.1 and 9.2 were generated to summarize the important discoveries and unresolved issues (for a more thorough discussion of each topic, the reader is referred to the conclusions section of the cited chapter).

Understanding the metallogeny of the Carlin-type gold deposits was addressed in this dissertation by first calculating the thermodynamic properties for the metal-bearing mineral and aqueous species in the system and then calculating the phase diagrams to determine the conditions which could have led to mineral deposition. Because this study employed the HKF equation of state to extrapolate experimental thermodynamic measurements to the inferred temperatures and pressures of deposition, its validity was examined in **Chapter 2**. A fundamental incompatibility was found between the predictions for the standard partial molal volumes, heat capacities, and Gibbs free energy of formation for neutral aqueous species, but because the latter was the most important property to understanding the Carlin-type gold deposits, the HKF equation of state parameters were derived in terms of equilibrium constant data (**Chapter 3**). Based on these calculations, the thermodynamic properties of As and Sb hydroxide and sulfide complexes were found to be consistent with the correlations for nonmetal hydrogen-bearing acids and oxyanions, but no clear evidence was shown for Au-As heteropolynuclear speciation. Finally, **Chapter 4** demonstrated that mineral stability and solubility are strong functions of the oxidation state of the system. It was found that sulfidation of host rock iron could have preferentially precipitated the phases observed in the main gold ore mineralization stage.

Methods to understand and detect the occurrence of fractures were addressed in **Chapters**

Chapter 2. Evaluation of equations of state for gases, minerals, and aqueous species

- The application of the HKF equation of state to neutral aqueous species is based on the correlation in derivative properties between the Born and Onsager equations (2.16 and 2.51, respectively).
- The HKF equation of state cannot simultaneously predict the standard partial molal heat capacity, volume, and Gibbs free energy of neutral aqueous species.
- A correction for dielectric saturation and solvent compressibility do not improve this incompatibility.
- Prediction of the standard partial molal Gibbs free energy at elevated temperatures and pressures can be obtained by using underestimated heat capacity and volume thermodynamic values if the Born parameter [ω] is obtained from regression of log K_r data.

Chapter 3. Thermodynamic properties of Sb, As, and Au minerals and aqueous species

- Additional problems with the HKF equation of state for ionic species may also exist due to the incorrect assumption of a species-independent correction for dielectric saturation and solvent compressibility.
- Regression calculations show that errors in the correlations for HKF parameters are sometimes large. Extrapolation beyond the temperature range of experimental data also results in large error envelopes.
- The HKF equation of state parameters for Sb and As aqueous species are consistent with the correlations for nonmetal hydrogen-bearing acids and oxyanions.
- There is a large experimental uncertainty in $Au(HS)_2^-$. Regression calculations produced HKF parameters inconsistent with any existing correlations.
- The experiments producing the result that Au forms heteroploynuclear complexes with Sb and As did not adequately constrain the oxidation state. The HKF parameters for $H_2AuSbS_3^0$ were shown to be in error (**Chapter 4**).
- The HKF equation of state parameters for $H_2S(aq)$, HS^- were recalculated.
- The hydroxide and sulfide complexes of Sb, As, and Au were identified and their HKF equation of state parameters determined. The heat capacity of the important mineral phases were also expressed in terms of equation (2.9).

Chapter 4. Metal deposition in the Carlin-type gold deposits

- Mineral stability and solubility were calculated at 200 and 300°C and 800 bars for an idealized sulfur-rich and sulfur-poor aqueous phase.
- Both mineral stability and solubility are strongly affected by changes in oxidation potential, but are relatively insensitive to pH in neutral to acidic solutions.
- The extremely reducing conditions required to stabilize $FeSb_2$ partially explains why Sb is not correlated with As on pyrite surfaces (FeS_2).
- The hydroxide complexes of Sb and As predominate in the Carlin-type gold deposits.
- pH and oxidation are less important relative to reduction and cooling for Sb, As, and/or Au precipitation.
- Sulfidation preferentially precipitates pyrite, arsenopyrite, arsenian pyrite and gold, possibly explaining their spatial and temporal correlation. Sb would likely pass through the system undergoing sulfidation without forming a stable mineral phase.
- The mineral paragenesis observed in Carlin-type gold deposits is consistent with a fluid undergoing cooling and oxidation with time.
- Fluid mixing during the main gold ore stage (MGO) might produce Sb deposition, a result generally inconsistent with field observations.

Table 9.1.a Summary of the results of the geochemistry study.

Chapter 6. The role of compressive stresses in jointing

- Field and laboratory measurements indicated two distinct lithologic and mechanical units at a field site on Vancouver Island, British Columbia.
- The alignment of concretion fractures and sandstone joint sets implied that they formed in the same stress field.
- Fracture density was proportional to the sandstone's moduli and strength, but was inversely proportional to the concretions'.
- Tension alone could not explain the fractures in the concretions because debonding would have occurred first and would have created a stress shadow.
- Compression alone also could not explain preferential concretion fracturing without an initial stage of debonding because the Poisson's ratio of the concretions were greater.
- Three possible stress fields were identified for concretion fracturing: 1) If the sandstone Poisson's ratio was less, a tensile stress may have produced debonding, followed by compression-driven fracturing; 2) If the sandstone Poisson's ratio was less then compressive stresses could have generated tensile stresses within the concretion, with a smaller stress shadow that would have allowed a limited number of concretion fractures following debonding; and/or 3) the Poisson's ratio was very similar, in which case fracturing was entirely controlled by the maximum compressive stress.
- Because some concretions were fractured without an initial stage of debonding possibility 3) was at least operative for some of the concretion fractures.
- Joints at the field site were too closely spaced to have been generated by tensile stresses alone.
- Tensile stresses necessary to reduce the minimum compressive confining stress acting perpendicular to a fracture face could have been generated during burial or anticline formation, but an unidentified tectonic compressive stress would have been required in the direction of fracture growth.

Chapter 7. Seismic fracture detection

- Amplitude anisotropy was significantly larger than velocity anisotropy in rock cores.
- Fractures were identified by a reduction in amplitude perpendicular to fracture alignment in laboratory measurements.
- Thin sections confirmed the presence of fractures perpendicular to the minimum seismic amplitude, but also showed that squirt flow was operative in porous sedimentary beds.
- A nonwelded interface model could replicate both the magnitude and frequency dependence of the fracture sets in the cores, but required a time correction for effects not accounted for the nonwelded interface model (e.g. squirt flow mechanisms).
- The importance of this method to field scale fractures is further limited by the complexity of field conditions.

Chapter 8. A new fracturing method for granular media

- In weakly cemented glass bricks, fractures were found to propagate perpendicular to the direction of the applied compressive stress.
- SEM photography confirmed that this fracturing mechanism proceeded by a process of grain contact rupturing and expulsion from the sample.
- A boundary integral code was used to verify that the removal of a grain resulted in a compressive stress concentration at the tip of the growing fracture, and which promoted further grain debonding.
- Fracturing in well cemented bricks proceeded by a process similar to borehole breakout experiments in sandstones suggesting that the bond strength to grain strength ratio may have been a controlling factor.
- Based on experimental data provided elsewhere it was inferred that this new fracturing mechanism is important in oil and natural gas reservoirs where a fluid flowing into a well could remove debonded grains, allowing a similar stress redistribution and fracture growth.

Table 9.1.b Summary of the results of the geomechanics study.

Chapter 2. Evaluation of equations of state for gases, minerals, and aqueous species
- The cause of the disparity between the HKF equation of state predictions and high temperature experimental standard partial molal heat capacities and volumes of neutral species.

Chapter 3. Thermodynamic properties of Sb, As, and Au minerals and aqueous species
- The cause of the inconsistencies between the HKF standard partial molal Gibbs free energy for HS^- and high temperature spectroscopic measurements.
- The relative importance of several species including: $Sb_2(OH)_6^0$; $H_6As_2O_6^0$; and $H_3As_3S_6^0$.
- Correlations between thermodynamic properties for metal sulfide complexes.
- The existence and HKF parameters for Au-As-Sb heteropolynuclear complexes.

Chapter 4. Metal deposition in the Carlin-type gold deposits
- Molar volumes of gudmundite, kermesite, berthierite, and seinäjoikite.
- Phase diagrams for the temperature where sulfidation would have produced the observed mineralogy, diagrams for the entire paragenetic sequence (i.e. complete temperature and pressure range), and diagrams exploring other depositional mechanisms.
- Equation of state parameters for the complete metallogeny of the deposit (e.g. Ag and Hg) to further constrain key variables such as the oxidation potential.
- Speciation and reaction path simulations to determine the temperature, pressure, and source rock assemblage which would have produced the observed fluid inclusions.
- Comparison between observed mineralogies and those calculated from reaction path simulations for every possible depositional mechanism.
- Detailed field and petrographic analysis of phase relationships to constrain depositional models.
- Calculation of errors at each step of the study.

Chapter 6. The role of compressive stresses in jointing
- The moduli and strength of the rock at the time of fracturing.
- The failure envelope for rock which fails by compression-driven extensile fracturing.
- The controls on the spacing of fractures under compressive driving stresses.
- The origin of the compressive driving stresses at Vancouver Island.
- The paleo-stress field within a given structural setting.

Chapter 7. Seismic fracture detection
- Method to distinguish between fracture-induced and other attenuation mechanisms.

Chapter 8. A new fracturing method for granular media
- The transitional mode and stress between nondilatational and extensile failure.
- The effect of the stress field on nondilatational fracturing versus compaction band formation (i.e. does this result primarily occur under uniaxial (or biaxial) stress?).
- The failure process for the case where the ejection of debonded grains is restricted.
- The importance of other factors such as grain shape and size.

Table 9.2 Issues requiring additional study.

5 through 8. **Chapter 6** demonstrated that compression-driven extensile fracturing likely contributed to jointing at a field site on Vancouver Island. This result emphasizes the need for additional research into its mechanics under geologically-realistic boundary conditions. Next, **Chapter 7** showed that seismic amplitudes decrease dramatically across fracture interfaces, but models which could be used to distinguish fracture-induced from other forms of attenuation require additional research. Finally, in **Chapter 8**, a new, nondilatational fracturing mechanism was discovered which probably causes sand generation in oil and natural gas reservoirs.

CHAPTER 10. References

10.1 References for Chapter 1

Akhmedzhanova, G. M., Nekrasov, I.Y., Tikhomirova and A.A. Konyushok, 1988. Solubility of gold in sulfide-arsenide solutions at 200-300 degrees C. Transactions (Doklady Akademii Nauk SSSR): Earth Sciences Section, V. 300, p. 189-191.

Alvarez, A.A. and D.C. Noble, 1988. Sedimentary rock-hosted disseminated precious metal mineralization at the Purisima Concepcion, Yauricocha District, Central Peru. Economic Geology, V. 83, p. 1368-1378.

Arehart, G.B., Kesler, S.E., O'Neil, J.R., and K.A. Foland, 1992. Evidence for the supergene origin of alunite in sediment-hosted micron gold deposits, Nevada. Economic Geology, V. 87, p. 263-270.

Arehart, G.B., Foland, K.A., Nasser, C.W., and S.E. Kesler, 1993a. 40Ar/39Ar, K/Ar and fission track geochronology of sediment-hosted disseminated deposits at Post-Betze, Carlin Trend, northeastern Nevada. Economic Geology, V. 88, p. 622-646.

Arehart, G.B., S.L. Chryssoulis, and S.E. Kesler, 1993. Gold and arsenic in iron sulfides from sediment-hosted disseminated gold deposits; implications for depositional processes. Economic Geology, V. 88, p. 171-185.

Arehart, G.B., 1996. Characteristics and origin of sediment-hosted disseminated gold deposits: A review. Ore Geology Reviews, V.11, p. 383-403.

Armstrong, A.K., Theodore, T.G., Kotlyar, B.B., Lauha, E.G., Griffin, G.L., Lorge, D.L., and E.W. Abbot, 1997. Preliminary facies analysis of Devonian autochthonous rocks that host gold along the Carlin trend, Nevada. *In* Carlin-type gold deposits field conference (Vikre, Thompson, Christensen, Parrat (*eds.*)). Society of Economic Geologists Guidebook Series, V. 28, p. 53-73.

Ashley, R.P., Cunningham, C.G., Bostick, N.H., Dean, W.E., and I.-M. Chou, 1991. Geology and geochemistry of three sedimentary-rock-hosted disseminated gold deposits in Guizhou Province, People's Republic of China, V. 6, p. 133-151.

Bagby, W.C. and B.R. Berger, 1985. Geological characteristics of sediment-hosted disseminated precious-metal deposits in the western United States. *In* Geology and Geochemistry of epithermal systems, Reviews in Economic Geology; V. 2; p. 169-202.

Bakken, B.E. and M. Einaudi, 1986. Spatial and temporal relation between wall rock alteration and gold mineralization, main pit, Carlin mine Nevada, USA. *In* Gold '86, p. 388-403.

Benning, L.G. and T.M. Seward, 1996. Hydrosulphide complexing of Au (I) in hydrothermal solutions from 150-400°C and 500-1500 bar. Geochimica et Cosmochimica Acta, V. 60, p. 1849-1871.

Cheng, Q, Hattori, K, Fan, Jizhang, and S. Wang, 1994. Exploration history and geology of disseminated gold deposits at the Maoling in Proterozoic sedimentary rocks in North China Platform. Journal of Geochemical Exploration, V. 51, p. 93-108.

Cline, J.S., Hofstra, A., Landis, G., and R. Rye, 1997. *In* Carlin-type gold deposits field conference (Vikre, Thompson, Christensen, Parrat (*eds.*)). Society of Economic Geologists Guidebook Series, V. 28, p. 155-166.

Coney, P.J., 1979. Tertiary evolution of the Cordilleran metamorphic core complexes. *In* Cenozoic paleogeography of the western United States. Society of Economic Paleontologists and Mineralogists Pacific Section Symposium, V. 3, p. 15-28.

Coney, P.J. and T.A. Harms, 1984. Cordilleran metamorphic core complexes: Cenozoic extensional relics of Mesozoic compression. Geology, V. 12, p. 550-554.

Cunningham, C.G., Ashley, R.P., Chou, I.-M., Zushu, H., Chaoyuan, W. and L. Wenkang, 1998. Newly discovered sedimentary rock-hosted disseminated gold deposits in the People's Republic of China. Economic Geology, V. 83, p. 1462-1467.

Emsbo, P., Hutchinson, R.W., Hofstra, A.H., Volk, J.A., Bettles, K.H., Baschuck, G.J., Collins, T.M., Lauha, E.A., and J.L. Borhauer, 1997. Newly discovered Devonian sedex-type base and precious metal mineralization, northern Carlin trend, Nevada. *In* Carlin-type gold deposits field conference (Vikre, Thompson, Christensen, Parrat (*eds.*)). Society of Economic Geologists Guidebook Series, V. 28, p. 109-117.

Faure, G., 1986. Principles of isotope geology. Wiley, New York.

Ferdock, G.C., Castor, S.B., Leonardson, R.W., and T. Collins, 1997. Mineralogy and paragenesis of ore stage mineralization in the Betze gold deposit, Goldstrike Mine, Eureka County, Nevada. *In* Carlin-type gold deposits field conference (Vikre, Thompson, Christensen, Parrat (*eds.*)). Society of Economic Geologists Guidebook Series, V. 28, p. 75-86.

Fiero, B., 1986. Geology of the Great Basin. University of Nevada Press, Reno, NV, 198 pp.

Gammons, C.H., 1997. Thermochemical sulfate reduction: A key step in the origin of sediment-hosted disseminated gold deposits. *In* Carlin-type gold deposits field conference (Vikre, Thompson, Christensen, Parrat (*eds.*)). Society of Economic Geologists Guidebook Series, V. 28, p. 141-143.

Gammons, C.H. and H.L. Barnes, 1989. The solubility of Ag_2S in near-neutral aqueous sulfide solutions at 25 to 300 degrees C. Geochimica et Cosmochimica Acta, V. 53, p. 279-290.

Gammons, C.H. and A.E. Williams-Jones, 1997. Chemical mobility of gold in the porphyry-epithermal environment. Economic Geology, V. 92, p. 45-59.

Gans, P.B., Mahood, G.A., and E. Schermer, 1989. Synextensional magmatism in the Basin and Range Province: A case study from the eastern Great Basin. Geological Society of America Special Paper, V. 233, 53 pp.

Hall, C.M., Simon, G., and S.E. Kesler, 1997. Age of mineralization at the Twin Creeks SHMG deposit, Nevada. *In* Carlin-type gold deposits field conference (Vikre, Thompson, Christensen, Parrat (*eds.*)). Society of Economic Geologists Guidebook Series, V. 28, p. 151-154.

Hausen, D.M. and W.C. Park, 1985. Observations on the association of gold mineralization with organic matter in Carlin-type gold ores. Denver Region Exploration Geologists Society Symposium. V. 3, p. 119-136.

Hayashi, K.-I. and H. Ohmoto, 1991. Solubility of gold in NaCl- and H2S-bearing aqueous solutions at 250-350 degrees C. Geochimica et Cosmochimica Acta, V. 55, p. 2111-2126.

Helgeson, H.C., Kirkham, D.H., and G.C. Flowers, 1981. Theoretical prediction of the thermodynamic behavior of aqueous electrolytes at high pressures and temperatures: IV. Calculation of activity coefficients, osmotic coefficients, and apparent molal and standard and relative partial molal properties to 600°C and 5 kb. American Journal of Science, V281, p. 1249-1516.

Helz, G.R., Tossell, J.A., Charnock, J.M., Pattrick, R.A.D., Vaughan, D.J., and C.D., Garner, 1995. Oligomerization in As (III) sulfide solutions; theoretical constraints and spectroscopic evidence. Geochimica et Cosmochimica Acta , V. 59, p. 4591-4604.

Hofstra, A.H., 1997. Isotopic composition of sulfur in Carlin-type gold deposits: Implications for genetic models. *In* Carlin-type gold deposits field conference (Vikre, Thompson, Christensen, Parrat (*eds.*)). Society of Economic Geologists Guidebook Series, V. 28, p. 119-129.

Hofstra, A.H., Daly, W.E., Birak, D.J., and T.C. Doe, 1991. Geologic framework and genesis of Carlin-type gold deposits in the Jerritt Canyon District, Nevada, USA. *In* Brazil Gold '91: The economics, geology, geochemistry and genesis of gold deposits, p. 77-87.

Hudec, M.R., 1992. Mesozoic structural and metamorphic history of the central Ruby Mountains metamorphic core complex, Nevada. Geological Society of America Bulletin, V. 104, p. 1086-1100.

Ilchik, R.P., Brimhall, G.H., and H.W. Schull, 1986. Hydrothermal maturation of indigenous organic matter at the Alligator Ridge gold deposits. Economic Geology, V. 81, p. 113-130.

Ilchik, R.P. and M.D. Barton, 1997. An amagmatic origin of Carlin-type gold deposits. Economic Geology, V. 92, p. 269-288.

Jewell, P.W. and W.T. Parry, 1987. Geology and hydrothermal alteration at the Mercur deposit, Utah. Economic Geology, V. 82, p. 1958-1966.

Johnson, J.W., Oelkers, E.H. and H.C. Helgeson, 1992. SUPCRT92; a software package for calculating the standard molal thermodynamic properties of minerals, gases, aqueous species, and reactions from 1 to 5000 bar and 0 to 1000 degrees C. Computers and Geosciences, V. 18, p. 899-947.

Kuehn, C.A. and A.W. Rose, 1992. Geology and geochemistry of wall-rock alteration at the Carlin gold deposit, Nevada. Economic Geology, V. 87, p. 1697-1721.

Kuehn, C.A. and A.W. Rose, 1995. Carlin gold deposits, Nevada; origin in a deep zone of mixing between normally pressured and overpressured fluids. 1995. Economic Geology, V. 90, p. 17-36.

Kulik, D.A., Dmitrieva, S.V., Chudnenko, Karpov, I.K., Sinitsyn, V.A., Aja, S.U., Khordorivski, M.S., and Yu.A. Shibetsky, 1997. Selektor-A: Integrated program and database to calculate environmental geochemical equilibria by Gibbs energy minimization.

King, P.B., 1977. The evolution of North America. Princeton University Press, New Jersey, 197 pp.

Madrid, R.J., 1987. Stratigraphy of the Roberts Mountain allochthon in north-central Nevada. Unpublished Ph.D. dissertation, Stanford University, 332 p.p.

Madrid,R.J., Bagby, W.C. and B.M. Bakken, 1988. Gold occurrence and its relation to vein and mineral paragenesis in selected sedimentary-rock-hosted, Carlin-type gold deposits, Nevada. Proceedings of Bicentennial Gold '88.

Murphy, J.B., Oppliger, G.L., Brimhall, G.H. and A. Hynes, 1999. Mantle plumes and mountains. American Scientist, V. 87, p. 146-153.

Nekrasov, I.Y., Konyushok, A.A. and V.I. Sorokin, 1982. Form of gold (I) in antimony-bearing sulfide solutions. Transactions (Doklady Akademii Nauk SSSR): Earth Sciences Section, V. 264, p. 207-210.

Nekrasov, I.Y. and A.A. Konyushok, 1982. Heteropolynucleate gold complexes in antimony-bearing sulfide solution. Transactions (Doklady Akademii Nauk SSSR): Earth Sciences Section, V. 266, p. 185-188.

Nekrasov, I.Y., 1996. Geochemistry, Mineralogy, and Genesis of Gold Deposits, Nauka Publishers, Moscow, 329 pp.

Noble, D., Weiss, S., Odt, D., Carr, J. and P. Lechler, 1996. Trace-element evidence for multiple hydrothermal fluid compositions at Sterling, a Carlin-type gold deposit in southwestern Nevada. *In* Geochemical Workshop on Carlin-Type Gold Deposits '96.

Oppliger, G.L., Murphy, J.B., and G.H. Brimhall, 1997. Is the ancestral Yellowstone hotspot responsible for the Tertiary "Carlin" mineralization in the Great Basin of Nevada?. Geology, V. 25, p. 627-630.

Osterberg, M.W., 1990. Geology and geochemistry of the Chimney Creek gold deposit, Humboldt County, Nevada. Unpublished Ph.D. thesis, University of Arizona, 173 pp.

Parry, W.T., Wilson, P.N., and R. Presnell, 1997. Clay alteration and age of sediment-hosted disseminated gold deposits in the fold and thrust belt, Utah. *In* Carlin-type gold deposits field conference (Vikre, Thompson, Christensen, Parrat (*eds.*)). Society of Economic Geologists Guidebook Series, V. 28, p. 185-191.

Peters, S.G., Leonardson, R.W., Ferdock, G.C., and E.A. Lauha, 1997. Breccia types in the Betze orebody, Goldstrike Mine, Eureka County, Nevada. *In* Carlin-type gold deposits field conference (Vikre, Thompson, Christensen, Parrat (*eds.*)). Society of Economic Geologists Guidebook Series, V. 28, p. 87-100.

Phillips, G.N. and R. Powell, 1993. Link between gold provinces. Economic Geology, V. 88, p. 1084-1098.

Powell, R., Will, T.M., and G.N. Fillips, 1991. Metamorphism in Archaen greenstone belts: Calculated fluid composition sand implications for gold mineralization. Journal of Metamorphic Petrology, V. 9, p. 141-150.

Radtke, A.S. and B.J. Scheiner, 1970. Studies of hydrothermal gold deposition I. Carlin gold deposits, Nevada: The role of carbonaceous materials in gold deposition. Economic Geology, V. 65, p. 87-102.

Radtke, Arthur S. Geology of the Carlin gold deposit, Nevada. U.S. Geological Survey Professional Paper, V. 1267, 124 pp.

Rock, N.M.S. and D.I. Groves, 1988. Can lamprophyres resolve the genetic controversy over mesothermal gold deposits?. Geology, V. 16, p. 538-541.

Rodriguez, B.D., 1997. Deep regional resisitivity structure across the Carlin trend. *In* Carlin-type gold deposits field conference (Vikre, Thompson, Christensen, Parrat (*eds.*)). Society of Economic Geologists Guidebook Series, V. 28, p. 39-45.

Schenberger, D. M. and H.L. Barnes, 1989. Solubility of gold in aqueous sulfide solutions from 150 to 350 degrees C. Geochimica et Cosmochimica Acta, V. 53, p. 269-278.

Seedorff, E., 1991. Magmatism, extension, and ore deposits of Eocene to Holocene age in the Great Basin--Mutual effects and preliminary proposed genetic relationships. *In* Geology and ore deposits of the Great Basin, V. 1, p. 133-178.

Seward, 1973. Thio complexes of gold and the transport of gold in hydrothermal ore solutions. Geochimica et Cosmochimica Acta, V. 37, p. 379-399.

Shawe, D.R., 1991. Structurally controlled gold trends imply large gold resources in Nevada. *In* Geology and ore deposits of the Great Basin, V. 1, p. 199-212.

Simon, G., Kesler, S.E., and S. Chryssoulis, 1999a. Geochemistry and textures of gold-bearing arsenian pyrite, Twin Creeks, Nevada: Implications for deposition of gold in Carlin-type deposits. Economic Geology, V. 94, p. 405-422.

Simon, G., Hui, H., Penner-Hahn, J.E., and S.E. Kesler, 1999b. Oxidation state of gold and arsenic in gold-bearing arsenian pyrite: A XANES, EXAFS and TEM study. American Mineralogist, in press.

Stenger, D.P., Kesler, S.E., Peltonen, D.R., and C.J. Tapper, 1998. Deposition of gold in Carlin-type deposits: The role of sulfidation and decarbonatization Twin Creeks, Nevada. Economic Geology and the Bulletin of Economic Geologists, V. 93, p. 201-215.

Stewart, J.H., 1980. The Geology of Nevada. Nevada Bureau of Mines Special Publication, V. 4, 136 pp.

Suleimenov, O.M. and R.E. Krupp, 1994. Solubility of hydrogen sulfide in pure water and NaCl solutions, from 20 to 320C and at saturation pressures. Geochimica et Cosmochimica Acta, V. 58, p. 2433-2444.

Sverjensky, D.A., Shock, E.L. and H.C. Helgeson, 1997. Prediction of the thermodynamic properties of aqueous metal complexes to 1000 degrees C and 5 kb. Geochimica et Cosmochimica Acta, V. 61, p. 1359-1412.

Tanger, J.C. and H.C. Helgeson, 1988. Calculation of the thermodynamic and transport properties of aqueous species at high pressures and temperatures: Revised equations of state for the standard partial molal properties of ions and electrolytes. American Journal of Science, V. 288, p. 19-98.

Teal, L. and M. Jackson, 1997. Geologic overview of the Carlin trend gold deposits and descriptions of recent deep discoveries. *In* Carlin-type gold deposits field conference (Vikre, Thompson, Christensen, Parrat (*eds.*)). Society of Economic Geologists Guidebook Series, V. 28, p. 3-37.

Turner, S.J., Fklindell, P.A., Hendri, D., Hardjana, I., P.F. Lauricella, Lindsay, R.P., Marpaung, B. and G.P. White, 1994. Sediment-hosted gold mineralization in the Ratatok district, North Sulawesi, Indonesia. Journal of Geochemical Exploration, V. 50, p. 317-336.

Wedepohl, K.H. Handbook of Geochemistry, 1978. Springer, Berlin.

Wooden, J.L., Tosdal, R.M., and R.W. Kistler, 1997. Pb and Sr mapping of the crustal structure in the northern Great Basin. *In* Carlin-type gold deposits field conference (Vikre, Thompson, Christensen, Parrat (*eds.*)). Society of Economic Geologists Guidebook Series, V. 28, p. 47-51.

10.2 References for Chapter 2

Anderson, G. M., 1996. Thermodynamics of natural systems. John Wiley .

Bjerrum, N., 1926. Untersuchungen über ionenassoziation. Der einfluss der ion mass auf die aktivität der ionen bei mittleren assoziationsgraden. Kgl. Danske Vidensk, V. 7, p. 1-48.

Born, V.M., 1920. Volumen und hydratationswärme der ionen: Zeitschr. Physik, V. 1, p. 45-48.

Burden, R.L. and J.D. Faires, 1989. Numerical Analysis. PWS-Kent Publishing Company, Boston, MA. 729 p.

Castellan, G.W., 1983. Physical Chemistry. Addison-Wesley.

Drummond, S.E., 1981. Boiling and mixing of hydrothermal fluids: effects on mineral deposition. Ph.D. thesis, Pennsylvania State University, 400 p.

Fletcher, P., 1993. Chemical thermodynamics for earth scientists. Longman Group UK Ltd.

Graybill, F.A. and H.K. Iyer, 1994. Regression Analysis: Concepts and Applications. Duxbury Press, Belmont, CA. 701 p.

Harvey, A.H., Levelt Sengers, J.M.H. and J.C. Tanger, 1991. Unified description of infinite-dilution thermodynamic properties for aqueous solutions. Journal of Physical Chemistry, V. 95, p. 932-937.

Helgeson, H.C., 1969. Thermodynamics of hydrothermal systems at elevated temperatures and pressures. American Journal of Science, V. 267, p. 729-804.

Helgeson, H.C., Kirkham, D.H., Nesbitt, H.W., and D.K. Bird, 1978. Summary and critique of the thermodynamic properties of rock-forming minerals. American Journal of Science, V. 278A, p. 1-299.

Helgeson, H.C. and D.H. Kirkham, 1974. Theoretical prediction of the thermodynamic behavior of aqueous electrolytes at high pressures and temperatures: I. Summary of the thermodynamic/electrostatic properties of the solvent. American Journal of Science, V. 274, p. 1089-1198.

Helgeson, H.C., Kirkham, D.H., and G.C. Flowers, 1981. Theoretical prediction of the thermodynamic behavior of aqueous electrolytes at high pressures and temperatures: IV. Calculation of the activity coefficients, osmotic coefficients, and apparent molal and standard and relative partial molal properties to 600°C and 5 kb. American Journal of Science, V. 281, p. 1249-1516.

Hnedkovsky, L., Wood, R.H., and V. Majer, 1996. Volumes of solutions of CH_4, CO_2, H_2S, and NH_3 at temperatures from 298.15 K to 705 K and pressures to 35 MPa. Journal of Chemical Thermodynamics, V. 28, p. 125-142.

Hnedkovsky, L. and R.H. Wood, 1997. Apparent molar heat capacities of aqueous solutions of CH_4, CO_2, H_2S, and NH_3 at temperatures from 304 K to 704 K at a pressure of 28 MPa. Journal of Chemical Thermodynamics, V. 29, p. 731-747.

Johnson, J.W., Oelkers, E.H., and H.C. Helgeson, 1992. SUPCRT92: A software package for calculating the standard partial molal thermodynamic properties of minerals, gases, aqueous species, and reactions from 1 to 5000 bar and 0 to 1000° C. Computers and Geosciences, V. 18, p. 899-947.

Laarhoven, P.J.and E.H.L. Aarts, 1987. Simulated annealing : theory and applications. Kluwer Academic Publishers.

Maier, C.G. and K.K. Kelley, 1932. An equation for the representation of high temperature heat content data. American Chemical Society Journal, V. 54, p. 3243-3246.

O'Connell, J.P., Sharygin, A.V. and R.H. Wood, 1996. Infinite dilution partial molar volumes of aqueous solutes over wide ranges of conditions. Industrial and Chemical Engineering Research, V. 35, p. 2808-2812.

Onsager, L., 1936. Electric moments of molecules and liquids. Journal of the American Chemical Society, V. 58, p. 1486-1493.

Pitzer, K.S., 1995. Thermodynamics. McGraw-Hill, Inc.

Quist, A.S. and W.L. Marshall, 1968. Ionization equilibria in ammonia-water solutions to 700° and to 4000 bars. Journal of Physical Chemistry, V. 72, p. 3123-3128.

Seber, G.A.F. and C.J. Wild, 1989. Nonlinear Regression. John Wiley and Sons, New York, NY. 768 p. (21-25; 191-194)

Shock, E.L. and H.C. Helgeson, 1988. Calculation of the thermodynamic and transport properties of aqueous species at high pressures and temperatures: Correlation algorithms for ionic species and equation of state predictions to 5 kb and 1000° C. Geochimica et Cosmochimica Acta, V. 52, p. 2009-2036.

Shock, E.L., Helgeson, H.C., and D.M. Sverjensky, 1989. Calculation of the thermodynamic and transport properties of aqueous species at high pressures and temperatures: Standard partial molal properties of inorganic neutral species. Geochimica et Cosmochimica Acta, V. 53, p. 2157-2183.

Shock, E.L., et al., 1992. Calculation of the thermodynamic properties of aqueous species at high pressures and temperatures-effective electrostatic radii, dissociation constants and standard partial molal properties to 1000 degrees Celsius and 5000 bars. Journal of the Chemical Society-Faraday Transactions, V. 88, p. 803-826.

Shock, E.L., Sassani, D.C., Willis, M., and D.A. Sverjensky, 1997. Inorganic species in geologic fluids: Correlations among standard partial molal thermodynamic properties of aqueous ions and hydroxide complexes. Geochimica et Cosmochimica Acta, V. 61, p. 907-950.

Simkin, B.Y. and I.I. Sheikhet, 1995. Quantum chemical and statistical theory of solutions: a computational approach. Ellis Horwood.

Sverjensky, D.A., Shock, E.L., and H.C. Helgeson, 1997. Prediction of the thermodynamic properties of aqueous metal complexes to 1000° C and 5 kb. Geochimica et Cosmochimica Acta, V. 61, p. 1359-1412.

Tanger, J.C. and H.C. Helgeson, 1988. Calculation of the thermodynamic and transport properties of aqueous species at high pressures and temperatures: Revised equations of state for the standard partial molal properties of ions and electrolytes. American Journal of Science, V. 288, p. 19-98.

Walther, J.V. and H.C. Helgeson, 1977. Calculation of the thermodynamic properties of aqueous silica and the solubility of quartz and its polymorphs at high pressures and temperatures. American Journal of Science, V. 277, p. 1315-1351.

10.3 References for Chapter 3

Akeret, R., 1953. Ueber die Löslichkeit von Antimon (3) Sulfid, Ph.D. dissertation, Prom. Nr. 2271, Eidgenossische Technische Hochschule, Zurich.

Akhmedzhanova, G. M., Nekrasov, I.Y., Tikhomirova, V.I., and Konyushok, A.A., 1988. Solubility of gold in sulfide-arsenide solutions at 200-300 degrees C. Transactions (Doklady Akademii Nauk SSSR): Earth Sciences Section, V. 300, p. 189-191.

Akinfiev, N.N., Zotov, A.V., and Nikonorov, A.P., 1993. Thermodynamic analysis of equilibria in the system As(III)-S(II)-O-H. Geochemistry International, p. 109-121.

Akinfiev, N.N., Zotov, A.V., and Shikina, N.D., 1994. Experimental investigation and thermodynamic correlation in the Sb(III)-S(II)-O-H system. Geochemistry International, p. 27-40.

Anderson, E. and Storey, L.G., 1922. Studies on certain physical properties of arsenic trioxide in water solutions. Journal of the American Chemical Society, V. 45, p. 1102-1105.

Arntson, R.H., Dickson, F.W., and Tunell, G., 1966. Stibnite (Sb_2S_3) solubility in sodium sulfide solutions. Science, V. 153, p. 1673-1674.

Babko, A.K. and Listeskaya, G.S., 1956. Equilibrium reactions of formation of thiosalts of tin, antimony, and arsenic in solution. Journal of Inorganic Chemistry, USSR, V. 1, p. 95-107.

Baes, C.F. and R.E. Mesmer, 1976. The Hydrolysis of Cations. Wiley.

Barbero, J.A., McCurdy, K.G., and Tremaine, P.R., 1982. Apparent molal heat capacities and volumes of aqueous hydrogen sulfide and sodium hydrogen sulfide near 25°C: The temperature dependence of H2S ionization. Canadian Journal of Chemistry, V. 60, p. 1872-1880.

Barker, W.W. and Parks, T.C., 1986. The thermodynamic properties of pyrrhotite and pyrite: a re-evaluation. Geochimica et Cosmochimica Acta, V. 50, p. 2185-2194.

Barrett, T.J., Anderson, G.M., and Lugowski, J., 1988. The solubility of hydrogen sulfide in 1-5 m NaCl at 25-95°C and 1 atm. Geochimica et Cosmochimica Acta, V. 52, p. 807-811.

Barton, M.D., 1980. The Ag-Au-S System. economic Geology, V. 75, p. 303-316.

Barton, P.B., 1969. Thermochemical study of the system Fe-As-S. Geochimica et Cosmochimica Acta, V. 33, p. 841-857.

Belevantsev, V.I., Gushchina, L.V., and Obolenskii, A.A., 1998. Solubility of stibnite, Sb_2S_3(cr): A revision of proposed interpretations and refinements. Geochemistry International, V. 36, p. 58-64.

Belevantsev, V.I., Pescchevskii, and Shamovskaya, G.I., 1981. Gold(I) complexes in aqueous solution. Isvest. sib. Otd. Nauk SSSR, Ser. Khim, V. 1, p. 81-87.

Benning, L.G., and Seward, T.M., 1996. Hydrosulphide complexing of Au(I) in hydrothermal solutions from 150-400°C and 500-1500 bar. Geochimica et Cosmochimica Acta, V. 60, p. 1849-1871.

Clarke, C.W. and Glew, D.N., 1971. Aqueous nonelectrolyte solutions. Part VIII. Deuterium and hydrogen sulfide solubilities in deuterium oxide and water. Canadian Journal of Chemistry, V. 49, p. 691-698.

De Cugnac-Pailliotet, A. and Pouradier, J., 1972. Proprietes thermodynamiques du sulfure d'or. C.R. Acad. Sc., Ser. C., V 275, p. 551-554.

Driesner, T., Seward, T.M., and Tironi, I.G., 1998. Molecular dynamics simulation study of ionic hydration and ion association in dilute and 1 molal aqueous solutions from ambient to supercritical conditions. Geochimica et Cosmochimica Acta, V. 62, p. 3095-3107.

Drummond, S.E., 1981. Boiling and mixing of hydrothermal fluids: chemical effects on mineral precipitation. Ph.D. thesis, Pennsylvania State University, 400 p.

Dubey, K.P. and Ghosh, S., 1962. Formation of thiosalt from antimonous sulfide. Zeit. Anorg. Chem., V. 319, p. 204-207.

Eary, L. E., 1992. The solubility of amorphous As_2S_2 from 25 to 90°C. Geochimica et Cosmochimica Acta , V. 56, p. 2267-2280.

Ellis, A.J. and Giggenbach, W., 1971. Hydrogen sulphide ionization and sulphur hydrolysis in high temperature solution. Geochimica et Cosmochimica Acta, V.35, p. 247-260.

Ellis, A.J. and McFadden, I.M., 1972. Partial molal volumes of ions in hydrothermal solutions. Geochimica et Cosmochimica Acta, V. 36, p. 413-426.

Gibert, F., Pascal, M.L., and Pichavant, M., 1998. Gold solubility and speciation in hydrothermal solutions: Experimental study of the stability of hydrosulphide complex of gold $Au(HS)^0$ at 350 to 450°C and 500 bars. Geochimica et Cosmochimica Acta, V. 62, p. 2931-2947.

Glushko, V.P. (*ed.*), 1978-1982. Thermodynamic properties of individual substances. Nauka, Moscow.

Gout, R, Pokrovski, G, Schott, J., and Zwick, A., 1997. Raman spectroscopic study of arsenic speciation in aqueous solutions up to 275 degrees C. Journal of Raman Spectroscopy, V. 28, p. 725-730.

Grigor'yeva, T.A. and Sukneva, L.S., 1982. Effects of sulfur and of antimony and arsenic sulfides on the solubility of gold. Geochemistry International, p. 153-158.

Haas, J.L., 1976. Physical properties of the co-existing phases and the thermodynamics of the H2O component in boiling NaCl solutions. USGS Bulletin, 1421-A, 73 p.

Hayashi, K. and Ohmoto, H., 1991. Solubility of gold in NaCl- and H_2S-bearing aqueous solutions at 250-350°C. Geochimica et Cosmochimica Acta , V. 55, p. 2111-2126.

Helgeson, H.C., Kirkham, D.H., and Flowers, G.C., 1981. Theoretical prediction of the thermodynamic behavior of aqueous electrolytes at high pressures and temperatures: IV. Calculation of the activity coefficients, osmotic coefficients, and apparent molal and standard and relative partial molal properties to 600°C and 5 kb. American Journal of Science, V. 281, p. 1249-1516.

Helz, G.R., Tossell, J.A., Charnock, J.M., Pattrick, R.A.D., Vaughan, D.J., and Garner, C.D., 1995. Oligomerization in As (III) sulfide solutions; theoretical constraints and spectroscopic evidence. Geochimica et Cosmochimica Acta , V. 59, p. 4591-4604.

Johnson, J.W., Oelkers, E.H., and Helgeson, H.C., 1992. SUPCRT92; a software package for calculating the standard molal thermodynamic properties of minerals, gases, aqueous species, and reactions from 1 to 5000 bar and 0 to 1000 degrees C. Computers and Geosciences, V. 18, p. 899-947.

Kolpakova, N.N., 1982. Laboratory and field studies of ionic equilibria in the Sb_2S_3-H_2O-H_2S system. Geochemistry International, V. 19, p. 46-64.

Kozintseva, T.N., 1964. Solubility of hydrogen sulfide in water at elevated temperatures. Geochemistry International, p. 750-756.

Krupp, R.E., 1988. Solubility of stibnite in hydrogen sulfide solutions, speciation, and equilibrium constants, from 25 to 350°C. Geochimica et Cosmochimica Acta , V. 52, p. 3005-3015.

Kulik, D.A., Dmitrieva, S.V., Chudnenko, K.V., Karpov, I.K., Sinitsyn, V.A., Aja, S.U., Khordorivski, M.S., and Shibetsky, Y.A., 1997. Selektor-A: Integrated Program and Database to Calculate Environmental Geochemical Equilibria by Gibbs Energy Minimization. User's Manual. Brooklyn-Kiev, 278 p.

Kryukov, P.A. and Starostina, L.I., 1978. The first ionization constants of hydrogen sulfide at temperatures 150°C. Izvestija Sibirskogo Otdelenia AN SSSR, V. 14, p. 87-93.

Learned, R.E., 1966. The solubilities of quartz, quartz-cinnabar, and cinnabar-stibnite in sodium sulfide solutions and their implications for ore genesis. Ph.D. dissertation, University of California, Riverside.

Lee, B.I. and Kesler, M.G., 1975. A generalized thermodynamic correlation based on a three-parameter corresponding states. AICHE Journal, V. 21, p. 510-527.

Lee, J.I. and Mather, A.E., 1977. Solubility of hydrogen sulfide in water. Berichte der Bunsen-Gussellschaft für Physicalische Chemie, V. 81, p. 1021-1023.

Letnikov, F.A. and Vilor, N.V., 1981. Gold in Hydrothermal Processes. Nedra, Moscow.

Linke, W.F., 1958. Solubilities of Inorganic and Metal-Organic Compounds. ACS, p. 234-240.

Maier, C.G. and Kelley, K.K., 1932. An equation for the representation of high temperature heat content data. American Chemical Society Journal, V. 54, p. 3243-3246.

Mironova, G.D. and Zotov, A.V., 1981. Solubility studies of the stability of As (III) sulfide complexes. Geochemistry International, p. 46-54.

Mironova, G.D., Zotov, A.V., and Gul'ko, N.I., 1984. Determination of the solubility of orpiment in acid solutions at 25-150°C. Geochemistry International, p. 53-59.

Mironova, G.D., Zotov, A.V., and Gul'ko, N.I., 1991. The solubility of orpiment in sulfide solutions at 25-150°C and the stability of the arsenic sulfide complexes. Geochemistry International, p. 61-73.

Murray, R.C. and Cubiciotti, D., 1983. Thermodynamics of aqueous sulfur species to 300°C and potential-pH diagrams. Journal of the Electrochemical Society, V. 130, p. 866-869.

Nagakawa, R., 1971. Solubility of orpiment (As2S3) in Tamagawa Hot Springs, Akita Prefecture. Nippon Kagaku Zaishi, V. 92, p. 159.

Naumov, G.B., Ryzhenko, B.N. and I.L. Khodakovsky, 1974. Handbook of Thermodynamic Data. USGS-WRD-74-001, 328 p.

Nekrasov, I.Y., Konyushok, A.A., and Sorokin, V.I., 1982. Form of gold (I) in antimony-bearing sulfide solutions. Transactions (Doklady Akademii Nauk SSSR): Earth Sciences Section, V. 264, p. 207-210.

Nekrasov, I.Y. and Konyushok, A.A., 1982. Heteropolynucleate gold complexes in antimony-bearing sulfide solution. Transactions (Doklady Akademii Nauk SSSR): Earth Sciences Section, V. 266, p. 185-188.

Norton, D.L., 1964. Geological and geochemical investigations of stibnite deposits. Ph.D. dissertation, University of California, Riverside.

Ovchinnikov, L.N., Kozlov, Y.D., and Rafal'skiy, R.P., 1982. The solubility of stibnite in chloride solutions at elevated temperatures. Geochemistry International, V. 19, p. 56-63.

Pan, P. and Wood, S.A., 1994. Solubility of Pt and Pd sulfides and Au metal in aqueous bisulfide solutions: II. Results at 200 to 350°C and saturated vapor pressure. Mineralium Deposita, V. 29, p. 373-390.

Pauling, L., 1927. The sizes of ions and the structure of ionic crystals. American Chemical Society Journal, V. 49, p. 765-790.

Pokrovski, G., Gout, R., Schott, J., Zotov, A., and Harrichoury, J., 1996. Thermodynamic and stoichiometry of As (III) hydroxide complexes at hydrothermal conditions. Geochimica et Cosmochimica Acta, V. 60, p. 737-749.

Popova, M. Y., Khodakovsky, I.L., and Ozerova, N.A., 1975. Measurement of the thermodynamic parameters of antimony hydroxo-complexes and hydroxofluoride complexes up to 200 degrees C. Geochemistry International, V. 12, p. 223.

Renders, P. J., and Seward, T.M., 1989. The stability of hydrosulphido- and sulphido-complexes of Au(I) and Ag(I) at 25°C. Geochimica et Cosmochimica Acta, V. 53, p. 245-253.

Seal, R.R., Robie, R.A., Barton, P.B., and Hemingway, B.S., 1992. Superambient heat capacities of synthetic stibnite, berthierite, and chalcostibnite: Revised thermodynamic properties and implications for phase equilibria. Economic Geology, V. 87, p. 1911-1918.

Selleck, F.T., Carmichael, L.T., and Sage, B.H., 1952. Phase behavior in the hydrogen sulfide- water system. Industrial and Engineering Chemistry, V. 44, p. 2219-2226.

Seward, T.M., 1973. Thio complexes of gold and the transport of gold in hydrothermal ore solutions. Geochimica et Cosmochimica Acta, V. 37, p. 379-399.

Shaw, H.R. and Wones, D.R., 1964. Fugacity coefficients for hydrogen gas between 0 and 1000°C, for pressures to 3000 atm. American Journal of Science, V. 262, p. 918-929.

Shenberger, D.M. and Barnes, H.L., 1989. Solubility of gold in aqueous sulfide solutions from 150 to 350°C. Geochimica et Cosmochimica Acta, V. 53, p. 269-278.

Shikina, N.D. and Zotov, A.V., 1991. Thermodynamic properties of $Sb(OH)_3^0$ up to 723.15 K and 1000 bar. Geochemistry International, p. 97-103.

Shikina, N.D. and Zotov, A.V., 1996. Stoichiometry of the neutral antimony hydroxocomplex. Geokhimiya, p. 1242-1244.

Shikina, N.D. and Zotov, A.V., 1999. Solubility of stibnite (Sb_2S_3) in water and hydrogen sulfide solutions at temperatures of 200-300°C and under vapor-saturated conditions and pressure of 500 bar. Geochemistry International, p. 82-86.

Shikina, N.D., Zotov, A.V., and Kartashova, L.F., 1988. The behavior of Sb in the Sb-H_2O-H_2 system at elevated temperatures. Geochemistry International, p. 105-109.

Shock, E.L. and H.C. Helgeson, 1988. Calculation of the thermodynamic and transport properties of aqueous species at high pressures and temperatures: Correlation algorithms for ionic species and equation of state predictions to 5 kb and 1000° C. Geochimica et Cosmochimica Acta, V. 52, p. 2009-2036.

Shock, E.L., Helgeson, H.C., and Sverjensky, D.A., 1989. Calculation of the thermodynamic and transport properties of aqueous species at high pressures and temperatures: Standard partial molal properties of inorganic neutral species. Geochimica et Cosmochimica Acta, V. 53, p. 2157-2183.

Shock, E.L., Oelkers, E.H., Johnson, J.W., Sverjensky, D.A, and Helgeson, H.C., 1992. Calculation of the thermodynamic and transport properties of aqueous species at high pressures and temperatures: Effective electrostatic radii to 1000C and 5 kb. Journal of the Chemical Society of London, Faraday Transactions, V. 88, p. 803-826.

Shock, E.L., Sassani, D.C., Willis, M., and Sverjensky, D.A., 1997. Inorganic species in geologic fluids: Correlations among standard partial molal thermodynamic properties of aqueous ions and hydroxide complexes. Geochimica et Cosmochimica Acta, V. 61, p. 907-950.

Spycher, N.F. and Reed, M.H., 1989. As(III) and Sb(III) sulfide complexes; an evaluation of stoichiometry and stability from existing experimental data. Geochimica et Cosmochimica Acta, V. 53, p. 2185-2194.

Sretenskaya, N.G., 1977. Dissociation of hydrogen sulfide acid under pressure. Geokhimiya, V. 3, p. 430-438.

Stranski, I.N., Plieth, K., and Zoll, I., 1958. Über die Auflösung, die Loslichkeit und die Unwandlung der beiden Arsenik Modifikationen in Wasser und wäßrigen Lösungen. Zeit Electrochem., V. 62, p. 366-372.

Sulemeinov, O.M. and Krupp, R.E., 1994. Solubility of hydrogen sulfide in pure water and in NaCl solutions, from 20 to 320°C and at saturation pressures. Geochimica et Cosmochimica Acta, V. 58, p. 2433-2444.

Suleimenov, O.M. and Seward, T.M., 1997. A spectrophotometric study of sulfide ionization in aqueous solutions. Geochimica et Cosmochimica Acta, V. 61, p. 5187-5198.

Sverjensky, D.A., Shock, E.L. and Helgeson, H.C., 1997. Prediction of the thermodynamic properties of aqueous metal complexes to 1000 degrees C and 5 kb. Geochimica et Cosmochimica Acta, V. 61, p. 1359-1412.

Tanger, J.C. and Helgeson, H.C., 1988. Calculation of the thermodynamic and transport properties of aqueous species at high pressures and temperatures: Revised equations of state for the standard partial molal properties of ions and electrolytes. American Journal of Science, V. 288, p. 19-98.

Tossell, J. A., 1994. The speciation of antimony in sulfidic solutions; a theoretical study. Geochimica et Cosmochimica Acta, V. 58, p. 5093-5104.

Tossell, J. A., 1996. The speciation of gold in aqueous solution; a theoretical study. Geochimica et Cosmochimica Acta, V. 60, p. 17-29.

Tossell, J. A., 1997. Theoretical studies on arsenic oxide and hydroxide species in minerals and in aqueous solution. Geochimica et Cosmochimica Acta , V. 61, p. 1613-1623.

Tsonopoulos, C., Coulson, D.M., and Inman, L.B., 1976. Ionization constants of water pollutants. Journal of Chemical and Engineering Data, V. 21, p. 190-193.

Wagman, D.D., Evans, W.H., Parker, V.B., Schumm, R.H., Halow, I., Bailey, S.M., Churney, K.L., and Nuttall, R.L, 1982. The NBS tables of chemical thermodynamic properties.

Selected values for inorganic and C1 and C2 organic substances in SI units. Journal of Physical and Chemical Reference Data, V. 11, supplement 2, p. 1-392.

Webster, J. G., 1990. The solubility of As_2S_3 and speciation of As in dilute and sulphide-bearing fluids at 25 and 90°C. Geochimica et Cosmochimica Acta. V. 54, p. 1009-1017.

Wei, D. and Saukov, A.A., 1961. Physicochemical factors in the genesis of antimony deposits. Geochem., V. 6, p. 510-516.

Winkler, L.W., 1906. Gesetzmässigkeit bei der absorption der gase in flüssigkeiten, Z. Phys. Chem., V. 55, p. 344-354.

Wood, S.A., 1989. Raman spectroscopic determination of the speciation of ore metals in hydrothermal solutions: I. Speciation of antimony in alkaline sulfide solutions at 25°C. Geochimica et Cosmochimica Acta, V. 53, p. 237-244.

Wood, S.A., Pan, P, Zhang, Y, and Mucci, A., 1994. The solubility of Pt and Pd sulfides in bisulfide solutions: I. Results at 25-90°C and 1 bar pressure. Mineralium Deposita, V. 29, p. 309-317.

Zotov, A.V. and Baranova, N.N., 1995. The solubility of Au_2S and AuAgS in near-neutral sulphide solutions at temperatures of 25 and 80°C and pressures of 1 and 500 bars. In Water-Rock Interaction, Kharaka and Chudaev, p. 773-776.

Zotov, A.V. and Baranova, N.N., Dar'yina, T.G., Bannykh, and Kolotov, V.P., 1985. The stability of $Au(OH)_0$ in water at 300-500°C and 500-1500 atm. Geochemistry International, V. 5, p. 156-161.

Zotov, A.V., Kudrin, A.V., Levin, K.A., Shikina, N.D., and Var'yash, L.D. Experimental studies of the solubility and complexing of selected ore elements (Au, Ag, Cu, Mo, As, Sb, Hg) in aqueous solutions. *In* Fluids in the Crust (Shmulovich, Yardley, and Gonchar, *eds.*), p. 95-137.

10.4 References for Chapter 4

Arehart, G.B., S.L. Chryssoulis, and S.E. Kesler, 1993. Gold and arsenic in iron sulfides from sediment-hosted disseminated gold deposits; implications for depositional processes. Economic Geology, V. 88, p. 171-185.

Ballyntyne, J.M. and Moore, J.N., 1988. Arsenic geochemistry in geothermal systems. Geochimica et Cosmochimica Acta, V. 52, p. 475-483.

Ilchik, R.P. and M.D. Barton, 1997. An amagmatic origin of Carlin-type gold deposits. Economic Geology, V. 92, p. 269-288.

Johnson, J.W., Oelkers, E.H. and H.C. Helgeson, 1992. SUPCRT92; a software package for calculating the standard molal thermodynamic properties of minerals, gases, aqueous species, and reactions from 1 to 5000 bar and 0 to 1000 degrees C. Computers and Geosciences, V. 18, p. 899-947.

Kuehn, C.A. and A.W. Rose, 1995. Carlin gold deposits, Nevada; origin in a deep zone of mixing between normally pressured and overpressured fluids. 1995. Economic Geology, V. 90, p. 17-36.

Naumov, G.B., Ryzhenko, B.N. and I.L. Khodakovsky, 1974. Handbook of Thermodynamic Data. USGS-WRD-74-001, 328 p.

Simon, G., Kesler, S.E., and S. Chryssoulis, 1999. Geochemistry and textures of gold-bearing arsenian pyrite, Twin Creeks, Nevada: Implications for deposition of gold in Carlin-type deposits. Economic Geology, V. 94, p. 405-422.

Stenger, D.P., Kesler, S.E., Peltonen, D.R., and C.J. Tapper, 1998. Deposition of gold in Carlin-type deposits: The role of sulfidation and decarbonatization Twin Creeks, Nevada. Economic Geology and the Bulletin of Economic Geologists, V. 93, p. 201-215.

White, D.E., 1981. Active geothermal systems and hydrothermal ore deposits. Economic Geology 75th Anniversary Volume, p. 392-423.

Williams-Jones, A.E. and Normand, C., 1997. Controls on mineral paragenesis in the system Fe-Sb-S-O. Economic Geology, V. 92, p.308-324.

10.5 References for Chapter 6

Astin, T. R., 1986. Septarian crack formation in carbonate concretions from shales and mudstones. Clay Minerals 21, 617-631.

Atkinson, B.K. and Meredith, P. G. 1987. The theory of subcritical crack growth with applications to minerals and rocks. In: Atkinson, B.K. (Ed.), Fracture Mechanics of Rock. Academic Press, pp. 111-166.

Atkinson, R. H., 1978. Suggested methods for determining hardness and abrasiveness of rocks. International Journal of Rock Mechanics and Mining Sciences and Geomechanics Abstracts 15, 89-97.

Bieniawski, Z. T., 1978. Suggested methods for determining tensile strength of rock materials. International Journal of Rock Mechanics and Mining Sciences and Geomechanics Abstracts 15, 99-103.

Bieniawski, Z. T., 1979. Suggested methods for determining the uniaxial compressive strength and deformability of rock materials. International Journal of Rock Mechanics and Mining Sciences and Geomechanics Abstracts 16,135-140.

Costin, L.S., 1987. Time-dependent deformation and failure. In: Atkinson, B.K. (Ed.), Fracture Mechanics of Rock. Academic Press, pp. 167-215.

Cruikshank, K.M., Zhao, G., and Johnson, A.M., 1991. Analysis of minor fractures associated with joints and faulted joints. Journal of Structural Geology 13, 865-886.

Eidelman, A. and Reches, Z., 1992. Fractured pebbles--a new stress indicator. Geology 20, 307-310.

England, T. D. J., 1990. Late Cretaceous to Paleogene evolution of the Georgia Basin, southwestern British Columbia. Ph.D. thesis, Memorial University of Newfoundland.

England, T. D. J., and Calon, T.J., 1991. The Cowichan fold and thrust system, Vancouver Island, southwestern British Columbia. Geological Society of America Bulletin 103, 336-362.

England, T. D. J., Currie, L.D., Massey, N.W.D., Roden-Tice, M.K. and Miller, D.S., 1997. Apatite fission-track dating of the Cowichan fold and thrust system, southern Vancouver Island, British Columbia. Canadian Journal of Earth Sciences 34, 635-645.

Eshelby, J.D., 1957. The determination of the elastic field of an ellipsoidal inclusion and related problems. Proceedings of the Royal Society of London, Series A 241, 376-396.

Gramberg, J. 1989. A Non-Conventional View on Rock Mechanics and Fracture Mechanics. A. A. Balkema, Rotterdam.

Hounslow, M.W., 1997. Significance of localized pore pressures to the genesis of septarian concretions. Sedimentology 44, 1133-1147.

Hucka, V., 1965. A rapid method for determining the strength of rocks in situ. International Journal of Rock Mechanics and Mining Sciences and Geomechanics Abstracts 2, 127-134.

Jaeger, J. C. and Cook, N.G.W., 1963. Pinching-off and disking of rock. Journal of Geophysical Research 68, 1759-1765.

Jaeger, J. C. and Cook, N.G.W., 1979. Fundamentals of Rock Mechanics. Methuen and Co.

Hilbert, L.B., Hwong, T.K., Cook, N.G.W., Nihei, K. and L.R. Myer. Effects of strain amplitude on the static and dynamic nonlinear deformation of Berea sandstone. 1st North American Rock Mechanics Symposium, 497-504.

Kemeny, J. and Cook, N.G.W., 1985. Formation and stability of steeply dipping joint sets. 26th Symposium on Rock Mechanics, 471-478.

Kemeny, J. and Cook, N.G.W. 1987. Determination of rock fracture parameters from crack models for failure under compression. 28th Symposium on Rock Mechanics, 367-374.

Lorenz, J.C., Teufel, L. W. and Warpinski, N. R. 1991a. Regional Fractures I: a mechanism for the formation of regional fractures at depth in flat-lying reservoirs. American Association of Petroleum Geologists Bulletin 75, 1714-1737.

Lorenz, J.C. and Finley, S. J. 1991b. Regional fractures II: fracturing of Mesaverde reservoirs in the Piceance Basin, Colorado. American Association of Geologists Bulletin 75, 1738-1757.

Maltman, A., 1994. The geological deformation of sediments. Chapman & Hall, London.

Marshall, J.D., 1982. Isotopic composition of displacive fibrous calcite veins: reversals in pore-water composition trends during burial diagenesis. Journal of Sedimentary Petrology 52, 615-630.

McCarroll, D., 1987. The Schmidt hammer in geomorphology; five sources of instrument error. Technical Bulletin--British Geomorphological Research Group 36, 16-27.

Monger, J.W.H. and Journeay, J.M., 1994. Basement geology and tectonic evolution of the Vancouver region. Geological Survey of Canada Bulletin 481, 3-25.

Mustard, P.S., 1994. The Upper Cretaceous Nanaimo Group, Georgia Basin. Geological Survey of Canada Bulletin 481, 27-95.

Nur, A., 1982. The origin of tensile fracture lineaments. Journal of Structural Geology 4, 31-40.

Olson, J.E., 1993, Joint pattern development: Effect of subcritical crack growth and mechanical interaction. Journal of Geophysical Research 98, 12251-12265.

Olson, J.E. and Pollard, D.D., 1989. Inferring paleostresses from natural fracture patterns: A new method. Geology 17, 345-348.

Olson, J.E. and Pollard, D.D., 1991. The initiation and growth of en echelon veins. Journal of Structural Geology 13, 595-608.

Paterson, M.S., 1978. Experimental rock deformation--the brittle field. New York, Springer-Verlag.

Pollard, D.D. and Segall, P., 1987. Theoretical displacements and stresses near fractures in rock. In: Atkinson, B.K. (Ed.), Fracture Mechanics of Rock. Academic Press, pp. 247-349.

Poole, R. W., and Farmer, I.W. , 1980. Consistency and repeatability of Schmidt hammer rebound data during field testing. International Journal of Rock Mechanics and Mining Sciences and Geomechanics Abstracts 17, 167-171.

Price, N. J., 1974. The development of stress systems and fracture patterns in undeformed sediments. Proceedings of the Third International Conference of the Society of Rock Mechanics, No. 3, Vol. 1, Part A, Advances in rock mechanics, 487-519.

Price, N.J. and Cosgrove, J.W. 1990. Analysis of Geologic Structures. Cambridge University Press.

Raiswell, R., 1971. The growth of Cambrian and Liassic concretions. Sedimentology 17, 147-171.

Raiswell, R., 1976. The microbiological formation of carbonate concretions in the upper Lias of NE England. Chemical Geology 18, 227-244.

Raiswell, R., 1987. Non-steady state microbiological diagenesis and the origin of concretions and nodular limestones. In: Geological Society Special Publication No. 36, Diagenesis of Sedimentary Sequences, pp. 41-54.

Raiswell, R., 1988. Evidence for surface reaction-controlled growth of carbonate concretions in shales. Sedimentology 35, 571-575.

Renshaw, C.E. and Pollard, D.D., 1994. Numerical simulation of fracture set formation: a fracture mechanics model consistent with experimental observations. Journal of Geophysical Research 99, 9359-9372.

Renshaw, C.E. and Pollard, D.D., 1995. An experimentally verified criterion for propagation across unbounded frictional interfaces in brittle, linear elastic materials. International Journal of Rock Mechanics and Mining Sciences and Geomechanics 32, 237-249.

Rinne, R.W., 1973. Geology of the Duke Point-Kulleet Bay area, Vancouver Island, B.C. M.S. thesis, Oregon State University.

Secor, D., 1965. Fluid pressure in jointing. American Journal of Science 263, 633-728.

Segall, P. and Pollard, D. D. 1983. Joint formation in granitic rocks of the Sierra Nevada. Geological Society of America Bulletin 94, 563-575.

Suppe, J., 1985. Principles of Structural Geology. Prentice-Hall, Inc.

Touloukian, Y.S., W.R. Judd and R.F. Roy, 1989. Physical properties of rocks and minerals. CINDAS Data Series on Material Properties V. II-2.

Turner, A., 1999. Micro-fractures in siliceous quartzites failed in triaxial extension: Part I. Observations and their interpretation. Journal of Structural Geology (*submitted*).

Weiss, N.A., 1993. Elementary Statistics. Addison-Wesley Publishing.

Wu, H. and Pollard, D. D. 1995. An experimental study of the relationship between joint spacing and layer thickness. Journal of Structural Geology 17, 887-905.

10.6 References for Chapter 7

Cadoret, T., Marion, D., and Zinszner, B., 1995, Influence of frequency and fluid distribution on elastic wave velocities in partially saturated limestones: Journal of Geophysical Research, 100, No. B6, 9789-9803.

Crampin, S., 1981, A review of wave motion in anisotropic and cracked elastic media: Wave Motion, 3, 343-391.

Dvorkin, J., Mavko, G., and Nur, A., 1995, Squirt flow in fully saturated rocks: Geophysics, 60, No. 1, 97-107.

Dvorkin, J., and Nur, A., 1993, Dynamic poroelasticity: A unified model with squirt and Biot mechanisms: Geophysics, 59, 428-438.

Brun Hilbert, B.L., Bessinger, B.A., and Cook, N.G.W., 1995. Effects of bedding planes and discontinuities on the sorptivity and permeability of rock. American Geophysical Union 1995 Fall Meeting, V. 76, p. 599.

Hudson, J.A., 1981, Wave speeds and attenuation of elastic waves in material containing cracks: Geophysical Journal of the Royal Astronomical Society, 64, 133-150.

Johnston, D.H., Toksoz, M.N., and Timur, A., 1979, Attenuation of seismic waves in dry and saturated rocks, II, Mechanisms: Geophysics, 44, No. 4, 691-711.

Larner, K., 1993, Dip-moveout error in transversely isotropic media with linear velocity variation with depth: geophysics, 58, 883-888.

Lo, T., Coyner, K.B., and Toksoz, M.N., 1986, Experimental determination of elastic anisotropy of Berea sandstone, Chicopee shale, and Chelmsford granite: Geophysics, 51, 164-171.

O'Connell, R.J., and Budiansky, B., 1974, Seismic velocities in dry and saturated cracked solids: Journal of Geophysical Research, 79, 5412-5426.

Pyrak-Nolte, L. J., 1997, The seismic response of fractures and the interrelations among fracture properties: International Journal of Rock Mechanics and Mining Sciences and Geomechanics Abstracts, 33, No. 8, 785-802.

Pyrak-Nolte, L.J., Myer, L.R., and Cook, N.G.W., 1990a, Anisotropy in seismic velocities and amplitudes from multiple parallel fractures: Journal of Geophysical Research, 95, No. B7, 11345-11358.

Pyrak-Nolte, L.J., Myer, L.R., and Cook, N.G.W., 1990b, Transmission of seismic waves across single natural fractures: Journal of Geophysical Research, 95, No. B6, 8617-8638.

Pyrak-Nolte, L.J., Myer, L.R., Cook, N.G.W., and Witherspoon, P.A., 1987, Hydraulic and mechanical properties of natural fractures in low permeability rock: Proceedings of the 6th International Congress on Rock Mechanics, 1, 225-232.

Remy, J.M., Bellanger, M., and Homand-Etienne, F., 1994, Laboratory velocities and attenuation of P-waves in limestones during freeze-thaw cycles: Geophysics, 59, No. 2, 245-251.

Schoenberg, M. and Haugen, G.U., 1995, Fracture Characterization: Proceeding of the Third SEGJ/SEG International Symposium, 31-38.

Schoenberg, M., and Sayers, C.M., 1995, Seismic anisotropy of fractured rock: Geophysics, 60, No. 1, 204-211.

Schoenberg, M., 1980, Elastic wave behavior across linear slip surfaces: Journal of the Acoustical Society of America, 68, No. 5, 1516-1521.

Thomsen, L., 1986, Weak elastic anisotropy: Geophysics, 51, No. 10, 1954-1966.

Tsvankin, I., 1995, P-wave signatures and notation for transversely isotropic media: an overview: Geophysics, 61, No. 2, 467-483.

Walsh, J.B., 1995, Seismic attenuation in partially saturated rock: Journal of Geophysical Research, 100, No. B8, 15407-15424.

10.7 References for Chapter 8

Antonellini, M. A., Mollema, P. N., Aydin, A., and D. D. Pollard, Compaction bands; a structural analog for anti-mode I cracks in eolian sandstone (abstract), *Abstracts with Programs - Geological Society of America, 26*, 184, 1994.

Berge, P. A., Bonner, B. P., and J. G. Berryman, Ultrasonic velocity-porosity relationships for sandstone analogs made from fused glass beads, *Geophysics, 60*, 108-119, 1995.

Dvorkin, J., Mavko, G., and A. Nur, The effect of cementation on the elastic properties of granular material, *Mechanics of Materials, 12*, 207-217, 1991.

Ewy, R. T. and N. G. W. Cook, Deformation and fracture around cylinderical openings in rock--I. Observations and analysis of deformations, *International Journal of Rock Mechanics, Mining Science, and Geomechanics Abstracts, 27*, 387-408, 1990a.

Ewy, R. T. and N. G. W. Cook, Deformation and fracture around cylinderical openings in rock--II. Initiation, growth and interaction of fractures, *International Journal of Rock Mechanics, Mining Science, and Geomechanics Abstracts, 27*, 409-427, 1990b.

Haimson, B. C. and C. G. Herrick, In situ stress evaluation from borehole breakouts, experimental studies, *Proceedings of the 26th United States Symposium on Rock Mechanics, 26*, 1207-1218, 1985.

Jaeger, J. C. and N. G. W. Cook, *Fundamentals of Rock Mechanics*, 593 pp., Chapman & Hall, London, UK, 1979.

Liu, Z., Myer, L. R,. and N. G. W. Cook, Micromechanics of granular materials--Numerical simulation of the effects of heterogeneities, *International Journal of Rock Mechanics, Mining Science, and Geomechanics Abstracts, 30*, 1281-1284, 1993.

Liu, Z., Numerical simulation of microscopic and deformation and failure of clastic media, Ph.D.dissertation, 196 pp., University of California at Berkeley, June 1995.

Myer, L. R., Kemeny, J. M., Zheng, Z., Suarez-Rivera, R., Ewy, R. T., and N. G. W. Cook, Extensile cracking in porous rock under differential compressive stress, *Applied Mechanics Review*, *45*, 263-280, 1992.

Myer, L.R., Kemeny, J.M., Cook, N.G.W., Liu, Z., and Nihei, K., Micromechanics of non-linear macroscopic deformation and fracture of rocks under differential compression, in *Fracture of Brittle Disordered Materials: Concrete, Rock and Ceramics*, p. 151-167, 1995.

Tronvoll, J. and E. Fjær, Experimental study of sand production from perforation cavities, *International Journal of Rock Mechanics, Mining Science, and Geomechanics Abstracts*, *31*, 393-410, 1994.

Zheng, Z., Kemeny, K., and N. G. W. Cook, Analysis of borehole breakouts, *Journal of Geophysical Research*, *94*, 7171-7182, 1989.

Zoback, M. D., Moos, D., Mastin, L., and R. N. Anderson, Wellbore breakouts and in situ stress. *Journal of Geophysical Research*, *90*, 5523-5530, 1985.

APPENDIX A. Revised HKF Equation of state parameters for SiO_2(aq)

A.1 Introduction

Because silicification was an important process in the development of the Carlin-type gold deposits, future reaction path simulations must utilize accurate thermodynamic data for both the aqueous and solid phases of SiO_2. Recent experimental data provided by Rimstidt (1997) indicates that the data used by Shock, et al. (1989) to constrain the HKF equation of state parameters for SiO_2(aq) underestimates the solubility of quartz at 25°C. Although this is a low temperature error (and thus unimportant for the Carlin-type gold deposits), the role of SiO_2(aq) in low temperature processes required a re-eveluation in this study.

A.2 Calculations

The HKF equation of state parameters for aqueous silica are listed in the first row of Table A.1 (Shock, et al., 1989). The standard partial molal Gibbs free energy of formation [$\Delta G^o_{f_{\mathrm{Pr}Tr}}$] and the Born function parameter [$\omega_{\mathrm{Pr}Tr}$] in the table were taken from Walther and Helgeson (1977) and the other parameters were regressed graphically from experimental solubility data for α-quartz shown in Figure A.1, excluding the data of Brisco (1937), Siffert (as reported by Wey (1961)), Stöber (1967), the recent experiments of Rimstidt (1997), and the low temperature data of Van Lier, et al. (1960) and Siever (1962). Although these HKF parameters values were used along with the thermodynamic properties of α-quartz from the SUPCRT database (Johnson, et al., 1992) to successfully predict its solubility at high temperatures along the vapor saturation curve of water (the dashed line), there is a discrepancy by as much as 0.4 log units between these predictions and the excluded data at low temperatures.

The disparity in low temperature data is based on the assumption of Walther and Helgeson (1977) that the fine grains of quartz used in the studies of Van Lier, et al. (1960)

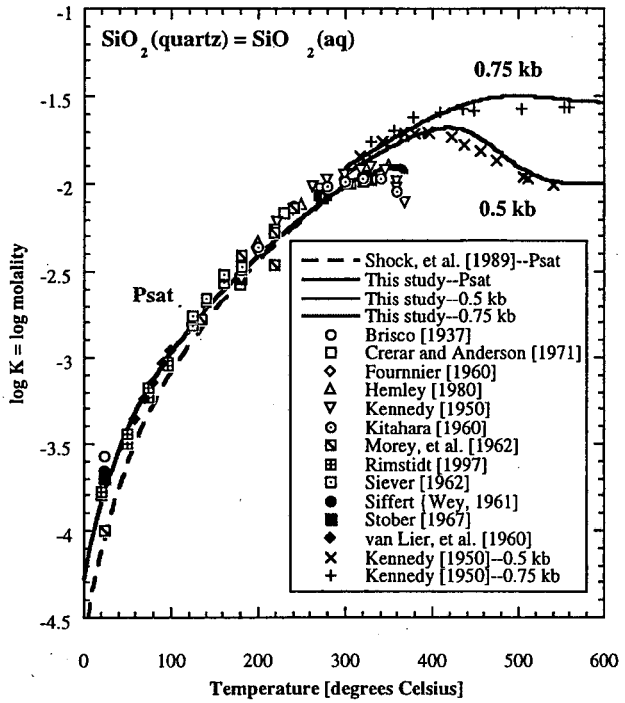

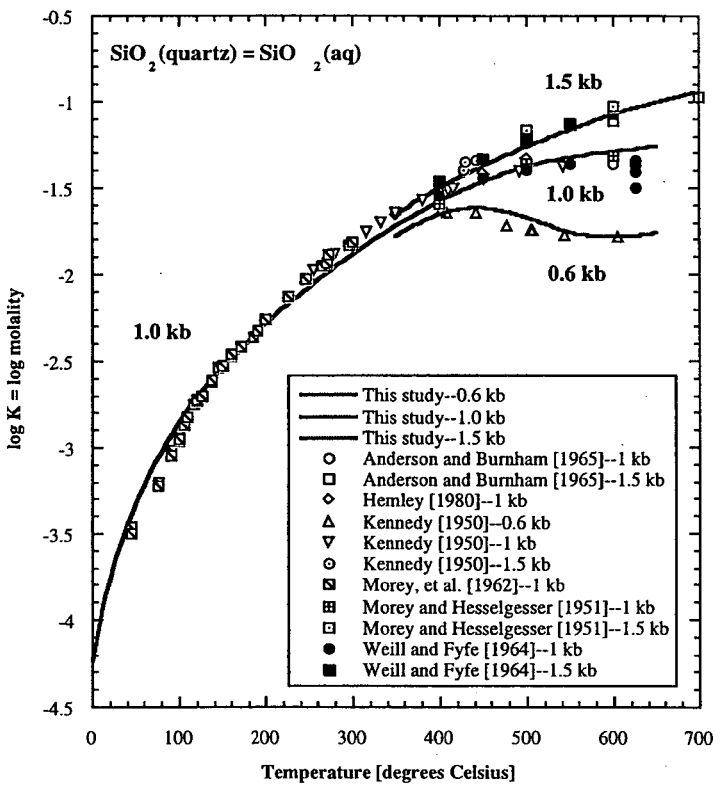

Figure A.1 The solubility of quartz as SiO_2(aq). The lines represent the predictions of the HKF equation of state using the parameters derived in this study (except as noted).

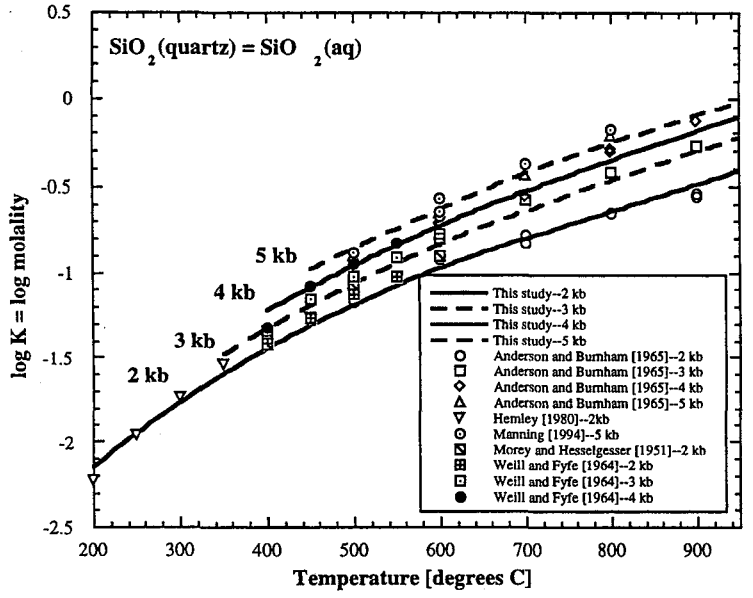

Study	$\Delta G°_f$ [a]	$S°$ [b]	$C_{pr}°$ [b]	$V°$ [c]	a_1 [d] x 10	a_2 [a] x 10^{-2}	a_3 [e]	a_4 [f] x 10^{-4}	c_1 [b]	c_2 [f] x 10^{-4}	ω [a] x 10^{-5}
Shock, et al. (1990)	-199190	18.0	-76.1	16.1	1.9	1.7	20.0	-2.7	29.1	-51.2	0.1291
This study	-199540	14.8± 0.90	-61.8	16.1	1.9	1.7	20.0	-2.7	29.5± 0.65	-44.5± 4.41	0.1064± 0.0012

a. cal mol^{-1} b. cal mol^{-1} K^{-1} c. cm^3 mol^{-1} d. cal mol^{-1} bar^{-1} e. cal K mol^{-1} bar^{-1} f. cal K mol^{-1}

Table A.1 Comparison of equations of state parameters and standard molal properties at 25° C and 1 bar for SiO_2(aq)

and Siever (1962) created abnormally high solubilities and should therefore be excluded from regression calculations. To assess this hypothesis, the effect of particle size on solubility was ascertained in this study using the Ostwald-Freundlich equation:

$$\frac{c_r}{c_\infty} = \exp\left(\frac{2\gamma_{\alpha-quartz}\overline{V}_{\alpha-quartz}}{RTr_{\alpha-quartz}}\right) \qquad (A.1)$$

where [c_r] is the solubility at a radius [$r_{\alpha-quartz}$], [c_∞] is the solubility at a radius [$r_{\alpha-quartz}$], [$\gamma_{\alpha-quartz}$] is the interfacial surface energy, and [$\overline{V}_{\alpha-quartz}$] is the molal volume (Iler, 1955). The surface energy of α-quartz in water was taken to be approximately 86 cal/m^2, the molal volume was assumed to be 22.688 cm3/mol (Walther and Helgeson, 1977), and the particles were assumed to be spherical. Figure A.2 shows the effect of particle size on the solubility of α-quartz assuming that the solubility at zero surface area was the 6 ppm responsible for the [$\Delta G^o_{f_{PrTr}}$] reported by Shock, et al. (1989). Solubility increases significantly only below the 0.1 μm particle size; however the particle sizes used in the experiments of Van Lier, et al. (1960), Siever (1962), and Rimstidt (1997) were 1-50 μm, >2 μm, and 50-400 μm, respectively.

These results suggest that the excluded data is reliable and consistent and that the results of Morey, et al. (1962) and Mackenzie and Gees (1971) may instead be the source of error. Rimstidt (1997) argued that although the two experiments which reported solubilities at 6 ppm or lower were supposedly based on equilibration from supersaturated conditions, that equilibration was probably approached from undersaturation, with the low solubilities reflecting this disequilibration.

Based on Figure A.2, the experimental data selected to represent the revised [$\Delta\overline{G}^o_{f_{PrTr}}$] of SiO_2(aq) was the new experimental results of Rimstidt (1997). The [$\Delta\overline{G}^o_{f_{PrTr}}$] of SiO_2(aq) was determined from the law of mass action:

$$\log K = \log a_{SiO_{2(aq)}} = \log\left(m_{SiO_{2(aq)}}\gamma_{SiO_{2(aq)}}\right) \qquad (A.2)$$

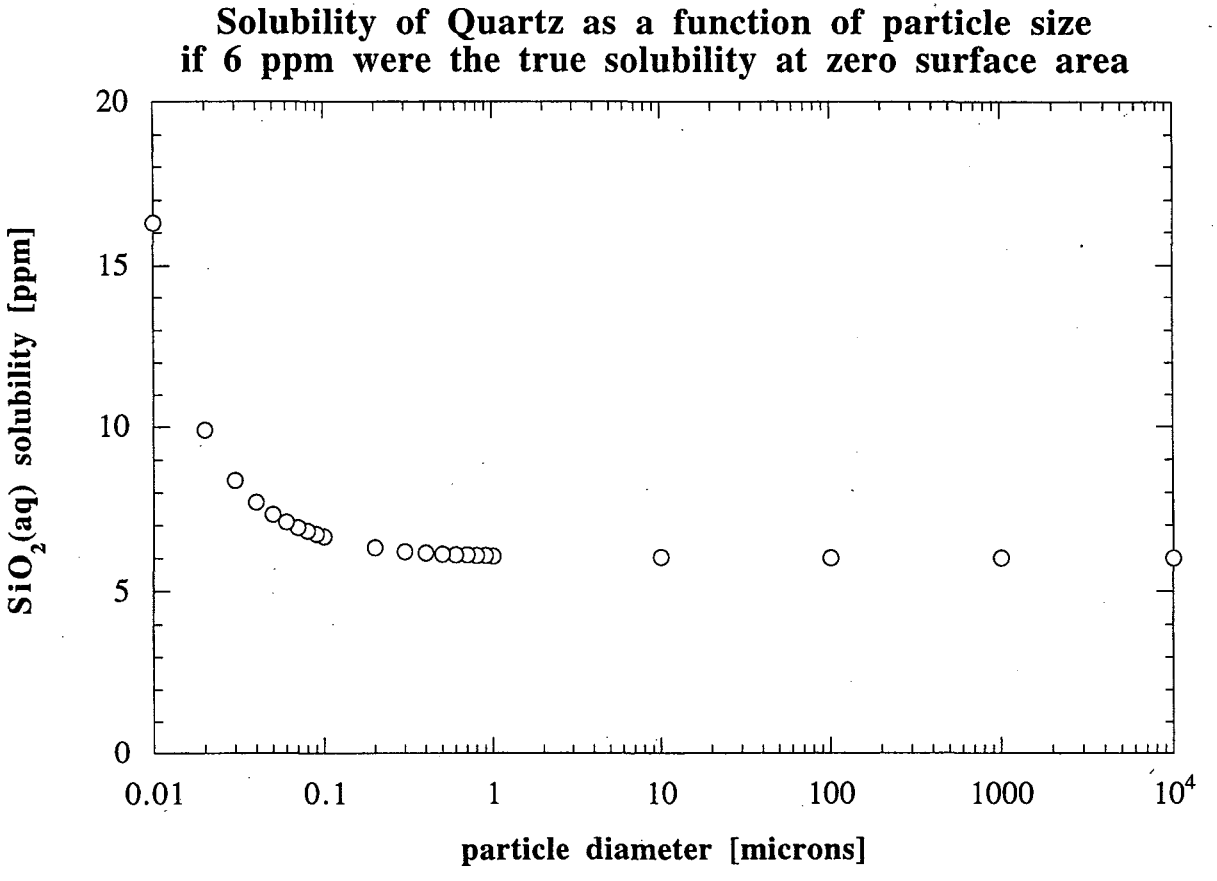

Figure A.2 The effect of particle size on the solubility of quartz

assuming the activity coefficient of the neutral species was approximately equal to one:

$$\Delta\overline{G}^{o}_{f(SiO_2(aq))_{PrTr}} = -2.303RT\log m_{SiO_{2(aq)}} + \Delta\overline{G}^{o}_{f(SiO_2(s))_{PrTr}}. \qquad (A.3)$$

The standard partial molal entropy [$\overline{S}^{o}_{PrTr}$] and the HKF parameters [c_1], [c_2], and [ω_e] were then obtained by regression. Because the new experiments did not greatly alter the predictions at elevated pressures the HKF parameters [a_1], [a_2], [a_3], and [a_4] were retained from the analysis of Shock, et al. (1989). This led to calculation of the standard partial molal volume [$\overline{V}^{o}$] and heat capacity [$\overline{C}^{o}_{p}$] via equations (6.30) and (6.31), respectively. These updated predictions of log K_r are displayed in Figure A.1.

A.3 Conclusions

Because many of the thermodynamic properties of the SiO_2(s) polymorphs were based on the thermodynamic properties of SiO_2(aq) at low temperatures, their properties also require revision; however, this is beyond the scope of the present investigation.

A.4 References

Anderson, G.M. and C.W. Burnham, 1965. The solubility of quartz in supercritical water. American Journal of Science, V. 263, p. 494-511.

Briscoe, H.V.A., Mathews, J.W., Holt, P.F., and P.M. Sanderson, 1937. Some new characteristics of certain industrial dusts. Transactions of the Institution of Mining and Metallurgy, V. 46, p. 291-302.

Crerar, D.A. and G.M. Anderson, 1971. Solubility and solvation of quartz in dilute hydrothermal solutions. Chemical Geology, V. 8, p. 107-122.

Fournier, R.O., 1960. Solubility of quartz in water in the temperature interval from 25°C to 300°C. Geological Society of America Bulletin Abstract, V. 71, p. 1867-1868.

Hemley, J.J., Montoya, J.W., Marinenko, J.W. and R.W. Luce, 1980. Equilibria in the system Al_2O_3-SiO_2-H_2O and some general implications for alteration/mineralization processes. Economic Geology, V. 75, p. 210-228.

Iler, R.K., 1979. The Chemistry of Silica Solubility: Polymerization, Colloid and Surface Properties, and Biochemistry, Wiley.

Johnson, J.W., Oelkers, E.H., and H.C. Helgeson, 1992. SUPCRT92: A software package for calculating the standard partial molal thermodynamic properties of minerals, gases, aqueous species, and reactions from 1 to 5000 bar and 0 to 1000° C. Computers and Geosciences, V. 18, p. 899-947.

Kennedy, G.C., 1950. A portion of the system silica-water. Economic Geology, V. 45, p. 629-653.

Kitahara, S., 1960a. The solubility of quartz in water at high temperatures and pressures. Review of Physical Chemistry of Japan. V. 30, p. 109-114.

Kitahara, S., 1960b. The solubility equilibrium and the rate of solution of quartz in water at high temperatures and high pressures. V. 30, p. 115-130.

Kitahara, S., 1960c. The polymerization of silicic acid obtained by the hydrothermal treatment of quartz and the solubility of amorphous silica. Review of Physical Chemistry of Japan. V. 30, p. 131-137.

Manning, C.E., 1994. The solubility of quartz in H_2O in the lower crust and upper mantle. Geochimica et Cosmochimica Acta, V. 58, p. 4831-4839.

Morey, G.W., Fournier, R.O., and J.J. Rowe, 1962. The solubility of quartz in water in the temperature interval from 25° to 300°C. Geochimica et Cosmochimica Acta, V. 26, p. 1029-1043.

Rimstidt, J.D., 1997. Quartz solubility at low temperatures. Geochimica et Cosmochimica Acta, V. 61, p. 2553-2558.

Shock, E.L., Helgeson, H.C., and D.M. Sverjensky, 1989. Calculation of the thermodynamic and transport properties of aqueous species at high pressures and temperatures: Standard

partial molal properties of inorganic neutral species. Geochimica et Cosmochimica Acta, V. 53, p. 2157-2183.

Siever, R., 1962. Silica solubility 0°-200°C, and the diagenesis of siliceous sediments. Journal of Geology, V. 70, p. 127-150.

Stöber, W., 1967. Formation of silicic acid in aqueous suspensions of different silica modifications. Advances in Chemistry Series, V. 67, p. 161-182.

Van Lier, J.A., de Bryun, P.L., and J.T.G. Overbeek, 1960. The solubility of quartz. Journal of Physical Chemistry, V. 64, p. 1675-1682.

Walther, J.V. and H.C. Helgeson, 1977. Calculation of the thermodynamic properties of aqueous silica and the solubility of quartz and its polymorphs at high pressures and temperatures.. American Journal of Science, V. 277, p. 1315-1351.

Weill, D.F. and W.S. Fyfe, 1964. The solubility of quartz in H_2O in the range 1000-4000 bars and 450-550°C. Geochimica et Cosmochimica Acta, V. 28, p. 1243-1255.

Ernest Orlando Lawrence Berkeley National Laboratory
One Cyclotron Road | Berkeley, California 94720

Prepared for the U.S. Department of Energy under Contract No. DE-AC03-76SF00098